Formation of nanostructured anodic films on iron and their electrode applications

鉄へのナノ構造アノード酸化皮膜の形成と電極応用

2021

Doctoral Thesis

Laras Fadillah

Laboratory of Interfacial Electrochemistry
Graduate School of Chemical Sciences and Engineering
Hokkaido University, Japan

Table of Contents

Abstract

Laras Fadillah
Graduate School of Chemical Sciences and Engineering
Hokkaido University

Anodizing of valve metals such as Ti, Nb, Ta, W and Al has become a subject of scientific interest in recent years in view of possibilities to form self-organized nanoporous and nanotubular anodic films on metal substrate. An extension of anodizing process to oxidizable metals such as Fe opens the way for applications of nanostructured oxides to cost-effective electrochemical devices such as those used in energy conversion and storage systems. The current thesis focusses on anodizing of Fe and electrochemistry of self-organized nanotubes/nanopores in order to estimate the possibility of application in energy conversion and storage. Anodic iron oxide has not been extensively explored so far in electrochemical devices among which hematite (Fe_2O_3) is a promising photoanode for water splitting and negative electrode material for lithium ion battery. The objective of the present study is the fundamental understanding of the growth of anodic nanopores/nanotubes on iron implicating the studies on iron single crystals for evaluation on how the anodic film grows depending on facet index number. The modification of the anodic film growth by addition of an alloying element is studied to control full transition between nanopores and nanotubes in order to meet the requirements of high surface area for desired applications and physicochemical parameters such as bandgap engineering. Further, the functionality of nanostructured anodic iron oxide films for photocatalytic water splitting and lithium ion battery applications is investigated.

This dissertation includes seven chapters, and the organization is explained bellow.

The background of this study including the details of anodizing process and specific objectives of this dissertation are described in Chapter 1. Chapter 2 consists of theoretical and practical details of the techniques used in the present study. Chapter 3 describes investigations of the effect of crystallographic orientation of iron on anodizing process. Anodizing of iron (100), (110) and (111) single crystals in ethylene glycol electrolyte containing 1.5 mol dm^{-3} water and 0.1 mol dm^{-3} ammonium fluoride leads to formation of anodic nanopores/nanotubes where the nanopores are essentially composed of oxide nanotubes separated by iron fluoride cell boundaries. The

nanoporous/nanotubular film formation apparently depends on the index number of facets on which the anodic film is formed. The film formation on (100) facet is associated with extended gas evolution upon anodizing and consequently corresponds to a shift of current-time curve towards higher current density values comparing with those formed on higher index number facets. The nanotubes formed on (100) facet have a general chemical formula of $Fe_2O_3 \cdot FeF_2$, whereas those formed on higher index number are composed of $Fe_3O_4 \cdot FeF_2$. The anodic films formed on Fe (110) and Fe (111) are essentially amorphous whereas the one formed on (100) facet shows high degree of crystallinity. The results are discussed in view of anisotropic properties of iron.

In Chapter 4, the effect of alloying of sputter-deposited Fe with 9 at.% tungsten on the growth of nanoporous anodic oxide is studied in ethylene glycol electrolyte containing 0.1 mol dm^{-3} ammonium fluoride and 1.5 mol dm^{-3} water. The classic nanoporous anodic film (Al_2O_3-like) is developed on pure Fe while the transition of nanopores to nanotubes (TiO_2-like) is observed for anodizing of Fe-W alloy. The pores/nanotubes having average diameter 50-110 nm and 30-60 nm are formed on pure Fe and Fe-W alloy at voltage 40-60 V, respectively. Both nanoporous/nanotubular anodic films grow in line with the field assisted flow model with a few fundamental details: i) transition of nanopores to nanotubes occurs upon anodizing of Fe-W alloy, ii) significant reduction of the cell size (nanotube diameter) is obtained on Fe-W alloy, iii) relatively thick layer is produced at Fe-W alloy/oxide interface. The primary reason of this transition to nanotubes as well as chemical changes is discussed in view of effective modification of the cell boundary region with tungsten species, probably WF_6 compound, upon growth of anodic film under influence of high electric field strength. The possible reason of developing the space in between nanotubes is faster kinetics of WF_6 reaction with water. Alloying of iron is one of the effective ways to modify the nanostructure of the anodic film on iron.

Furthermore, the functionality of Fe-W oxides as photoanode is demonstrated in Chapter 5. The nanotubes-type anodic film with 800 nm in length and barrier-type with 540 nm length is grown by modifying anodization conditions, including the water content and anodizing time. The following thermal treatment from 300 - 400 °C for 30 min enhances the crystallinity of the films. the photocatalytic activity of Fe-W oxides is compared with that of Fe oxides, the results demonstrate that the activity is highly enhanced by the addition of tungsten species. The possible explanation is attributed to the efficient separation of the photoinduced electron–hole pairs and large surface area of the

uniform nanotube arrays.

The performance of anodic nanoporous/nanotubular films grown on iron for lithium ion battery application is examined and the results are summarized in Chapter 6. The iron oxide nanotubes formed by anodizing of polycrystalline iron in ethylene glycol electrolyte containing 0.1 mol dm^{-3} of ammonium fluoride and 1.5 mol dm^{-3} of water are thermally treated at 350-500 ^{o}C in order to control the crystallographic structure of the oxide. An increase of crystallinity, the increased ratio of hematite (Fe_2O_3) to magnetite (Fe_3O_4) and elimination of the fluorides are observed with an increase in annealing temperature. The differential capacity plots of $dQ \cdot dE^{-1}$ reveal quasi-reversible lithiation/delithiation process through Li_2O formation. The anodic nanotubes/nanopores annealed at 500 ^{o}C exhibit relatively high areal capacity of 3.5 mA h cm^{-2} at a charge/discharge current density of 20 μA cm^{-2} assembled in the half-cell of lithium ion battery. The better electrochemical performance is found for nanotubes/nanopores having higher degree of crystallinity, high ratio of hematite (Fe_2O_3) to magnetite (Fe_3O_4) and eliminated fluorides. The cycling stability tests supported with optical microscopy observations of the negative electrode assembled in electrochemical cell for *in-situ* measurements indicate adhesion problems, leading to gradual degrease of rate capability mainly caused by the detachment of oxide.

Finally, the main findings of this dissertation are summarized, and future prospects are given in Chapter 7

Chapter 1 Introduction and Literature Survey

1.1. Introduction

On December 29th 1959, the physicist Richard Feynman was given a lecture at an American Physical Society meeting at Caltech with the tittle "There's plenty of Room at the Bottom". In this lecture he predicted that if we can control the matter in the microscale, we can get plenty of excellent properties and realize plenty of change in them. He also suggested that it would be possible to make nanoscale machine that can "arrange the atom the way we want" and do chemical synthesis by mechanical manipulation.

Since then, plenty of techniques were introduced to design and control the microstructures of the materials. Among the microstructures formed, free-standing nanoporous and nanotubular oxides are the most promising shapes in terms of functionality and applications. Anodizing is one of the facile and straightforward processes to growth such microstructures, In 1995, Masuda and Fukuda reported the porous anodic aluminum oxide with self-organized hexagonal array by two step anodizing [3]. Afterward, anodizing has attracted much attention as one of key fabrication process of nanomaterials for a range of nanodevices and nanobiosensors, in addition to the traditional importance for corrosion protection of metals and the improved aesthetic appearance of the metal components. Anodizing of aluminum, which forms self-organized Al_2O_3 nanoporous films, is of interest for aerospace, biomedical, architecture and nanotechnology applications, as well as templates for the fabrication of nanomaterials in the form of nanowires, nanopores, and nanotubes [3-9]. On the other hand, self-organized nanotubes were produced by anodizing of titanium that has many applications including solar cells, photocatalysts and biomaterials, because of the useful semiconductor properties of TiO_2 and unique morphology of 1-dimensional nanotube. Moreover, self-ordered porous structures were also successfully designed by anodizing of zirconium and tungsten [10-12]. While many studies on formation, properties and applications of anodic films on valve metals are available because of ready and efficient film growth in aqueous electrolytes, limited studies have been conducted on anodizing of non-valve metals including iron.

1.2. Anodic Films

Anodizing is a process that results in the formation of oxide film on a metallic substrate. In general, most metals; except noble metals are covered with a very thin air-formed oxide, Fig 1.1 a. The structure of this oxide has an impact to the oxide that formed by anodization [13, 14]. When a metal (M) is exposed to a sufficiently high anodic voltage in an electrolyte containing water, oxidation of metals takes place. In the first stages of anodization, a compact film is formed, due to the large amount of water in the environment, Fig 1.1 b. The $MO_{n/2}$ layer formation occurs at the metal/film interface by migration of oxide ions inwards in the oxide film under the high electric field as can be written as Eq. (1.1) [15]:

$$M + nO^{2-} \rightarrow MO_{n/2} + 2ne^{-} \quad (1.1)$$

and at the film/electrolyte interface by outward migration of cations that react with water in the electrolyte (1.3) [15]:

$$M^{n+} + n/2H_2O \rightarrow MO_{n/2} + nH^{+} \quad (1.3)$$

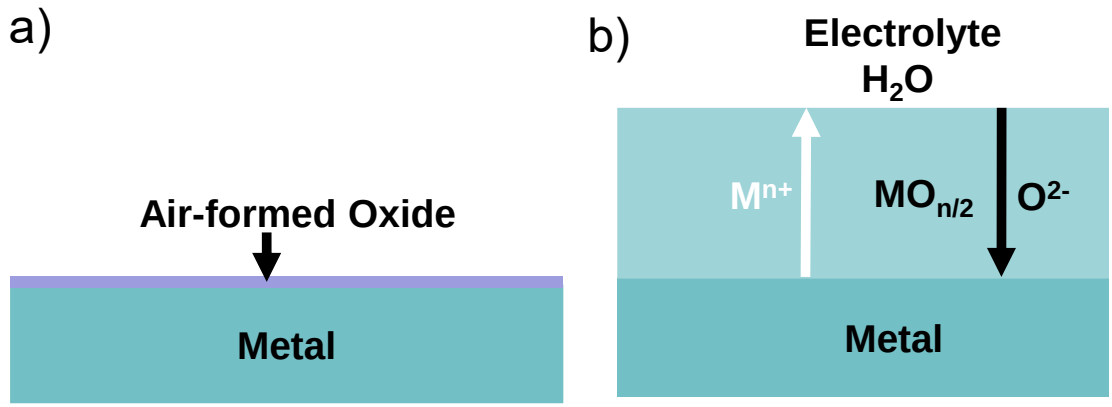

Figure 1.1 Schematic diagram of (a) thin air-formed oxide and (b) the oxidation on the first step of anodizing processes.

The properties of metal oxide, $MO_{n/2}$, will be determined by the underlying metal. If the MO is easy to dissolve then the metal will not be protected and it will be degraded. The opposite is if the MO is not dissolved, a barrier layer is formed resulting compact film that may protect the underlying metal from further corrosion.

1.2.1. Types of Anodic Oxide Films

As mentioned above, the microstructures of the oxides are depending on the metal/alloy substrate and the parameters used for anodizing, such as the composition of electrolyte, anodizing time, applied voltages and current density. Three morphological types of films can be produced by anodizing metals: barrier-type, nanoporous-type, and nanotubular-type [16-18].

Barrier-type Anodic Films

Barrier-type films are formed in the electrolytes, in which almost no dissolution of substrate species proceeds. Defects always exist in the barrier layer and the population densities of the defect are on the order of 10^8 to 10^{10} m^{-2} [19]. Defects population depends on the substrate surface condition and the film thickness. The generation of the defects is essentially related with local heterogeneities in the metal substrate [20]. The presence of such defects might cause the reduction of current efficiency during the anodizing processes. During the growth of barrier-type films at 100 % Faradaic efficiency, formation voltage increases linearly with time under the galvanostatic condition until the dielectric breakdown of the anodic film occurs at a certain voltage. The breakdown voltage depends on the type of metallic substrate and electrolyte used. The barrier-type films are compact and thin, usually in the order of hundred nanometers, and use as applications for capacitors and corrosion protection. Barrier-type anodic films formed on Al, Nb, Ta, and W are usually amorphous and the thickness of those anodic films are proportional to the formation voltage before reaching to dielectric breakdown [9, 21-25].

Xu et al. reported that growth of barrier-type or porous-type films on aluminum depends on the effective current efficiency in a specific electrolyte [26]. The growth efficiency of the barrier-type alumina film decreases with a decrease in current density and the pH of the electrolyte employed. For low current densities than a critical value, film formation at the film/electrolyte interface involves field-induced dissolution and the formation of a porous layer commences. In the case of aluminum anodizing, this critical current density for the formation of a porous film depends on the electrolyte concentration, temperature, and pH of the electrolyte [26]. Extensive studies on barrier-type anodic alumina films show that these films are not pure oxides of aluminum, but contain a small amount of electrolyte-derived anion species that significantly influence the properties of resultant anodic films. In addition, the distribution and extent of the depth of these species within the film is complex. Shimizu et al. [27] and Skeldon et al.

[28] have reported that the distribution of incorporated species is determined by the transport number of metals ions as well as by the relative migration rates of incorporated species during the growth of barrier films. Boron, phosphate, chromium, molybdenum, and tungsten species are usually incorporated into the anodic films and they show different distribution in the resultant barrier-type anodic films owing to their different migration rates. Such species can be used as tracers for the investigation of ion transport processes during the film growth [17, 27-31]. It is well-known that phosphate is incorporated within outer two-third of the anodic alumina film and an inner one-third is usually a phosphate-free, relatively pure alumina region. Investigations of the barrier-type anodic films on aluminum in phosphate electrolyte revealed that phosphorous species migrate inwards at a rate of ~ 0.5 times that of O^{2-} [32-34].

The incorporation and different depth distributions of various electrolyte anion-derived species are strongly correlated with the ionic transport process in growing anodic oxides. Extensive research work on the growth of barrier-type anodic film on aluminum has been done to clarify whether the growth proceeds owing to the migration of metal cation through the film to react with electrolyte species, or due to the migration of oxide anions across the film to react with the metal at the metal/film interface, or due to the migration of both cations or anion species. Hoar and Mott reported that hydroxyl ions also carry the ionic current during film growth and the outer region of the film materials are usually hydrated while Brock and Wood suggested that only oxide anions are mobile as no hydration is found in glycerol-based organic electrolytes [35, 36].

It is well known that the growth of amorphous barrier-type films proceeds by high field conduction mechanisms, where transportation of ionic species occurs under the electric field of 10^6-10^7 V cm^{-1} and new film material is formed at the film/electrolyte and metal/film interfaces by outward migration of metal cations and inward migration of electrolyte-derived anion species, respectively, as shown in Fig. 1.1. In contrast to aluminum, films formed on some metals such as zirconium and hafnium are crystalline and growth proceeds predominantly by the migration of O^{2-} ions, with a minor contribution from zirconium cations Zr^{4+} [37]. Films formed on titanium show a transition from amorphous to a mixture of amorphous and crystalline oxide at relatively low voltages less than 10 V [13]. The current density, J_i, during amorphous film growth is related to the electric field by the following eq.1.3 [38],

$$J_i = \mathrm{A}\exp(\mathrm{B}E) \tag{1.3}$$

where E is the electric field, A and B are constants that depend on temperature. The electric field E is further related to the anodizing voltage, V, and film thickness, d, by the following equation.

$$V = Ed \tag{1.4}$$

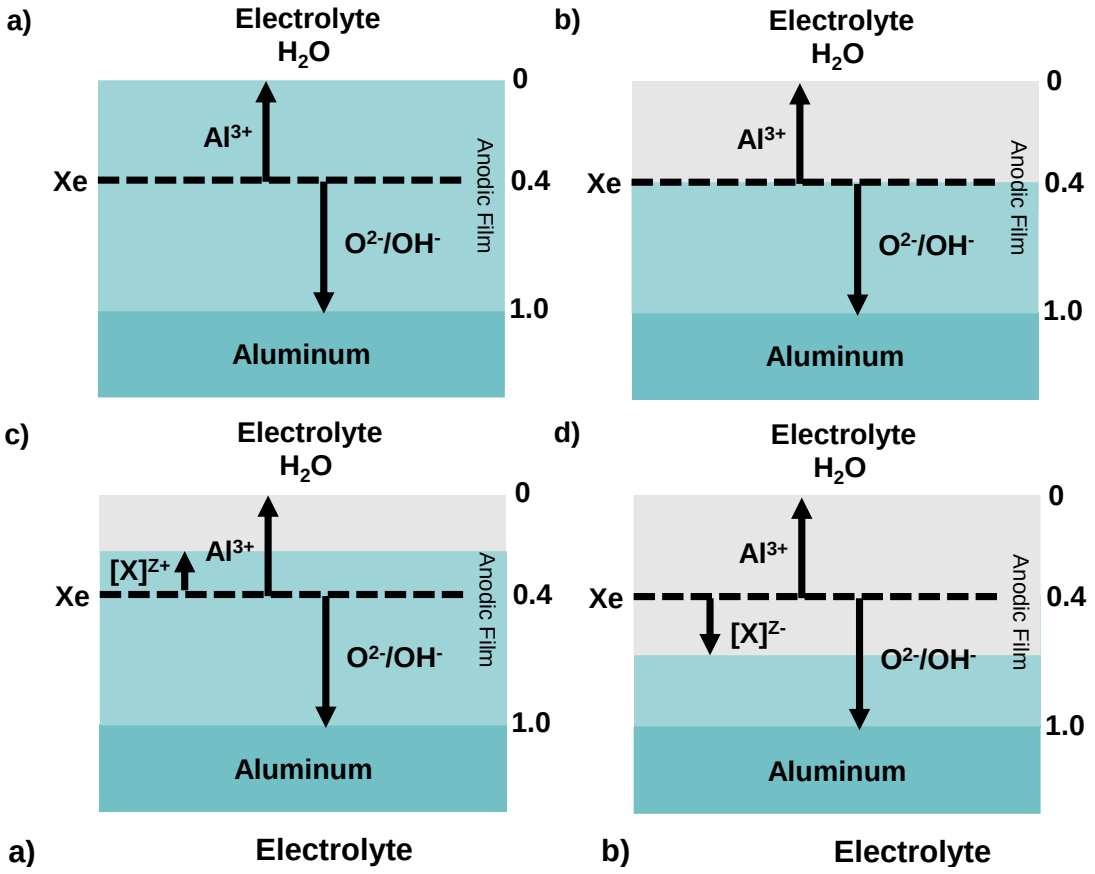

Figure 1.2 Schematic diagram of immobile Xenon tracer experiments to determine the migration of electrolytes species during the barrier-type films formed in aqueous electrolytes galvanostatically at 100 % Faradaic efficiency; (a) impurity-free anodic alumina film, (b) anodic alumina film containing an immobile electrolyte species that contaminate the outer 0.4 of the film, (c) anodic alumina film containing electrolyte species migrating outwards that contaminate < 0.4 of the film thickness and, (d) anodic alumina film containing electrolyte species migrating inwards that contaminate > 0.4 of the film thickness [44].

Various tracer techniques such as ion implantation, micro-analytical, and radioactive techniques have also been employed to understand the ionic transport processes [35, 36, 39, 40]. It is now well known that aluminum cations transport number is approximately 0.4 under 100 % Faradaic efficiency [41]. Later studies on barrier-type film on aluminum suggested that electrolyte-derived species are incorporated within the film at a constant rate under constant current film growth and electrolytes-derived species

could be immobile, migrate outwards or inwards at different rates [42-44]. Wood et al. presented a model for the incorporation of electrolyte-derived species during the growth of barrier type anodic films in aqueous electrolytes at constant current density [43] as shown in Fig. 1.2. They concluded that the amount of electrolyte-derived species to aluminum is independent of the Faradaic efficiency, but depends on the mobility of species.

Porous-type Anodic Films

The formation behavior of compact barrier films is relatively simple in terms of electrochemical theories with the film thickness is controlled by formation voltage. In contrast, the formation behavior and the formation mechanism of self-organized porous oxide films have attracted much debate in recent years. These films on aluminum are formed in certain acidic and alkaline electrolytes, such as phosphoric acid, oxalic acid, sulfuric acid, and borax that have the capability of partially dissolving the film. In potentiostatic anodizing, the current decreases continuously when a barrier type anodic film is formed at high current efficiency, while a steady current appears when a porous anodic film is developed. The porous-type anodic films comprise a relatively thick porous layer with numbers of cylindrical pores normal to the metal substrate and a thin barrier layer sandwiched between the metal substrate and the porous layer (Fig. 1.3 a). Various film parameters, including barrier layer thickness and cell sizes, are directly proportional to anodizing voltage. These films are usually formed by anodizing at a constant voltage or constant current. The typical voltage vs time and current density vs time responses during porous film growth are shown in Fig. 1.3 b. and c.

When a constant current is applied to the growth of porous film, the cell voltage rises linearly with time until the maximum is reached, and then decreases gradually to a steady sate voltage. Linear non-steady rise of potential is associated with thickening of a barrier layer and then, pores start to develop when the voltage-time curve is deviated from the slope of the linear voltage rise. At the steady-state constant voltage, thickening of porous layer proceeds with the barrier layer thickness remained constant. In anodizing at a constant voltage, an initial rapid current rise is observed, followed by a decrease in current density to a minimum value. Thereafter, current rises to local maximum before reaching to steady state.

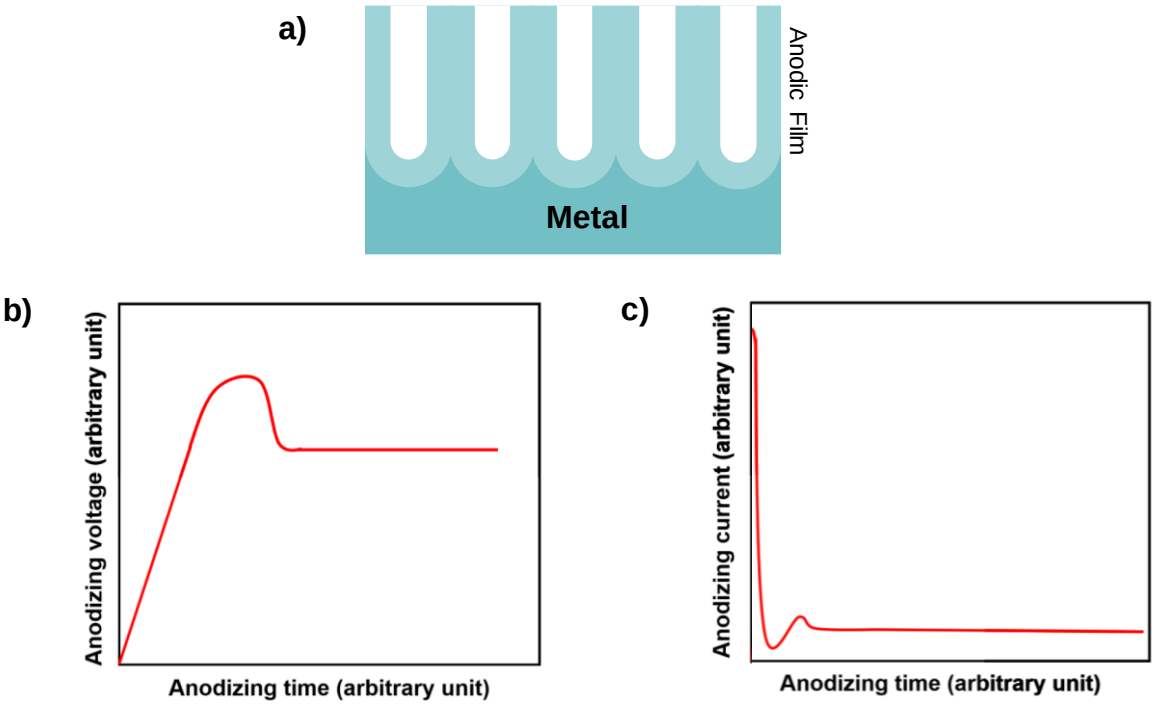

Figure 1.3 a) Schematic illustration of nanoporous-type films and typical voltage-time and current density-time responses during anodizing at: b) constant current condition and c) constant voltage condition.

Nanotubular-type Anodic Films

In addition to barrier and porous-type anodic films, self-organized ordered nanotubular anodic films on titanium [43], zirconium [44], niobium [45], tantalum [46], and iron [47] have also attracted significant attention because of their unique properties in various fields, including energy conversion, photocatalysis and biomedical devices, since the observation of titanium surface by Assefpour-Dezeuly et al. in 1984 [48] and formation of self-organized nanotubes on titatnium by Zwilling et al. [49-52] in fluoride-containing electrolytes. Among various porous morphologies, nanotubular morphology provides an extra degree of freedom in its wall thickness that can be tuned in addition to the diameter and length of nanotubes to obtain the required properties. Furthermore, nanotubes provide a large surface area than nanowires of the same diameter and length. The morphology of nanotubes depends on applied voltage, duration, temperature, and fluoride concentration. While voltage, duration, and fluoride concentration primarily control the nanotube length, diameter, and growth rate, the electrolyte composition including water content, pH, viscosity, and conductivity also affect the nanotube properties. Apart from the parameter optimization of nanotubes growth for specific applications, several studies have been conducted for the investigation of growth mechanism and efforts have been made to understand the transitional from nanoporous

to the nanotubular structure. The nanotubes are typically formed under constant potential in fluoride-containing nonaqueous electrolyte; such as glycerol and ethylene glycol and in aqueous electrolytes [53-56]. Recent direct observation on the formation of nanotubes on titanium and zirconium in non-aqueous electrolytes have proved that transition from nanoporous to nanotubular films starts along the cell boundaries [57-59]. The formation of the fluoride-rich layer along the cell boundaries can be explained by their fast migration rate compared with oxide anions [60, 61]. These fluoride species are then preferentially dissolved into the electrolyte, thus forming the nanotubes. A schematic of fluoride enrichment and dissolution is shown in Fig. 1.4.

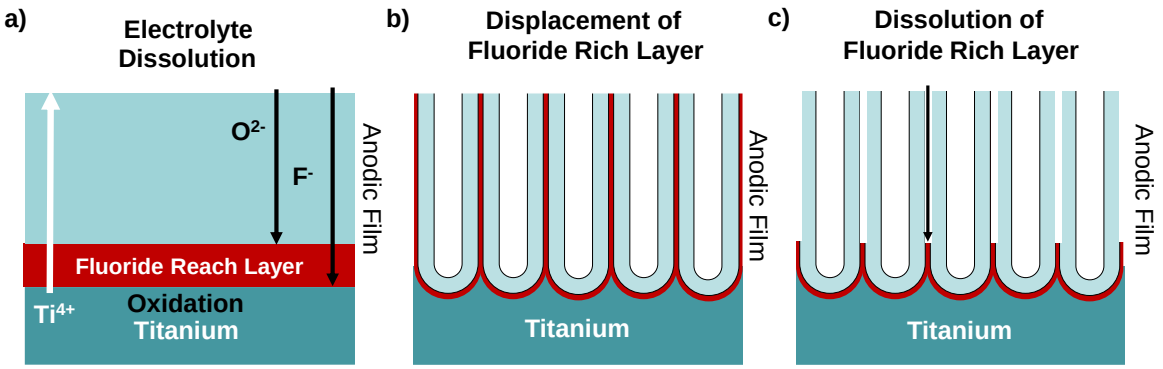

Figure 1.4 Schematic illustration of TiO_2 nanotubes formation (a) formation of fluoride richlayer, (b) displacement of fluoride rich layer and c) dissolution of fluoride rich layer. [1, 2]

1.3. Iron-based Anodic Films

Iron (Fe) is one of the most abundant metals in earth and the practically most important metal. Iron can be oxidized to various kind of iron oxides, including magnetite (Fe_3O_4), maghemite (γ-Fe_2O_3), and hematite (α-Fe_2O_3). The ordered micro/nanostructures (nanotubes, nanopores, nanowires, nanoparticles, etc.) of the iron oxides are technologically crucial for many research activities in magnetic, environmental, biomedical and material studies; including humidity and gas sensors, photocatalysts, magnetic storage devices, lithium ion batteries, and electrodes for electrochemical capacitors [62-68]. Nanoporous/nanotubular iron oxides film can be prepared by a polymer precursor method, thermal oxidation of iron, electrospinning, hydrothermal process, and very recently besides valve metals the self-organized nanoporous/nanotubular oxide films have been grown on iron and stainless steels by anodizing in organic electrolytes containing fluorides and small amounts of water [47, 69-74].

Anodizing of iron has been explored in the past decade [75, 76]. Anodization of iron to produce nanoporous films like anodic Al_2O_3 and nanotubular films like anodic TiO_2 is however relatively new [69-73, 77-86]. Concerning the growth mechanism of porous anodic alumina [87], oxide flow is assumed, originating from the stress-induced plasticity of the oxide barrier layer. To minimize the stress, the oxide behaves visco-plasticity and continuously being pushed upwards from metal oxide interface, forming scalloped structure which will then develop into pores.

The transition from nanoporous to nanotubular structure occurs with increasing the electrolyte temperature. According to La Tempa [88], the transformation from nanoporous to nanotubular was observed when the electrolyte temperature was increased from 35 ^oC to 55 ^oC. Another method is by modifying the electrolyte composition. The use of organic electrolytes provides the formation of thick anodic films with high growth efficiency on iron and stainless steel and improves the uniformity of the self-ordered porous or nanotubular array. Hence, for the efficient fabrication of nanoporous and nanotubular anodic oxide films on iron, understanding of growth behavior of the porous films and the inter-relationship between structure, composition, and morphology of the anodic films on iron is of crucial importance [72].

1.3.1. Anodizing in Fluoride-containing Electrolytes

As mentioned above modifying the composition of the electrolyte is important to control the morphology on anodic films. Extensive studies on the formation of titania nanotubes in HF-based aqueous electrolytes showed that nanotubes could be grown only up to few hundreds of nm, consequently reducing the growth efficiency. This limited growth may be assumed to be the result of fast dissolution process during anodizing. Thus, nanotube length is limited to 500 nm for acidic and 2 μm for neutral aqueous electrolytes containing fluoride [49]. In contrast, TiO_2 nanotubes of 1 mm thickness were reported at 60 V in ethylene glycol electrolytes containing 0.5 wt. % ammonium fluoride and 3 % water [89]. Therefore, organic electrolytes with low conductivity compared with aqueous electrolytes allow the growth of nanotubes with highest efficiencies and with high degree of ordering. In addition to organic electrolytes, nanotubes growth rates on titanium are also determined by a balance between water and fluoride concentration. High fluoride concentration (> 0.1 mol dm^{-3} ammonium fluoride) enhances the dissolution of nanotubes, while the small addition of water to organic electrolytes allows sufficient rate of oxidation. In this regards, most recent studies have focused on the formation of

nanoporous and nanotubular anodic films on Ti, Al, Zr, and Fe in fluoride and water-containing glycerol/ethylene glycol electrolytes.

In anodizing of iron, there are three important parameters for nanoporous or nanotubular formation, which are listed as follow:

- Composition of the electrolyte (NH_4F and Water, in Ethylene glycol/Glycerol)
- Applied Voltage
- Anodization time (3 minutes - 4 hour)

The correlation between the film morphology and anodizing conditions reported so far is summarized in Table 1.1:

Table 1. 1. Summary of the anodizing conditions related to the type of anodic iron oxide films

Type	**Electrolyte**	**Voltage (V)/ Current Density (A/m^{-2})**
Nanopores [69]	Glycerol + 0.5 wt.% NH_4F + 0.2% 0.1M HNO_3 at 10 ^oC	90 V
Nanotubes [71]	Ethylene glycol + 0.5 wt.% NH_4F + 3vol% H_2O	50 V
Nanotubes [47]	Ethylene glycol + 0.1 wt.% NH_4F + 3vol% H_2O	50 V
Nanotubes [78]	Ethylene glycol + 0.3 wt.% NH_4F + 2 vol% H_2O	50 V
Nanotubes [73]	Ethylene glycol + 0.1 M NH_4F + 3vol% H_2O	50 V
Nanopores [90]	Ethylene glycol + 0.1 M NH_4F + 1.5 M H_2O	50 Am^{-2}
Nanopores and Nanotubes [80]	Ethylene glycol + 0.1 M NH_4F + 1.7 M H_2O	50 V
Nanopores [91]	Ethylene glycol + 0.1 M NH_4F + 3vol% H_2O	50 V
Nanopores and Nanotubes [82]	Ethylene glycol + 0.5 M NH_4F + 3wt% H_2O	50 V
Nanotubes [85]	Ethylene glycol + 0.1 M NH_4F + 1 M H_2O at 25 ^oC	40 V
Nanopores [86]	Ethylene glycol + 0.14 M NH_4F + 1.7 M H_2O at room temperature	50 V
Nanotubes [86]	Ethylene glycol + 0.14 M NH_4F + 1.7 M H_2O at 60 ^oC	50 V
Nanotubes [84]	Ethylene glycol + 0.37 wt% NH_4F + 2 M H_2O at 25 ± 2 ^oC	40 V

Multi-layer nanotubes [84]	Ethylene glycol + 0.37 wt% NH_4F + 2 M H_2O at 25 ± 2 °C	0-45 V, rate 2.5 V/s, then pulsing voltage between 20V -45 V
Wave like tubes [84]	Ethylene glycol + 0.37 wt% NH_4F + 2 M H_2O at 25 ± 2 °C	Triangular profile with voltages between 30 V -60 V
Nanopores [83]	Ethylene glycol + 0.1 M NH_4F + 0.1-2.0 M H_2O at room temperature	≤ 50 V
Nanotubes [83]	Ethylene glycol + 0.1 M NH_4F + 1.5 M H_2O at room temperature	60 V-100 V

From the table above, we understand that the concentration of NH_4F is important to control the morphology of the anodic film on iron. The presence of F^- adjacent to the bottom of the pore will induce further dissolution of the oxide. Water concentration also significantly affects the resultant film morphology and growth efficiency. Shahzad, et al. [83] discussed the growth mechanism that is dependent on the water concentration (Figure 1.5); at lower water concentration a barrier layer is thick and the metal/film interface is flat, not scalloped, and at high water concentration a layer of nanopores or nanotubes can be formed. The transformation from nanopores to nanotubular can be explained by the preferential dissolution of fluoride-rich layer at the cell boundaries.

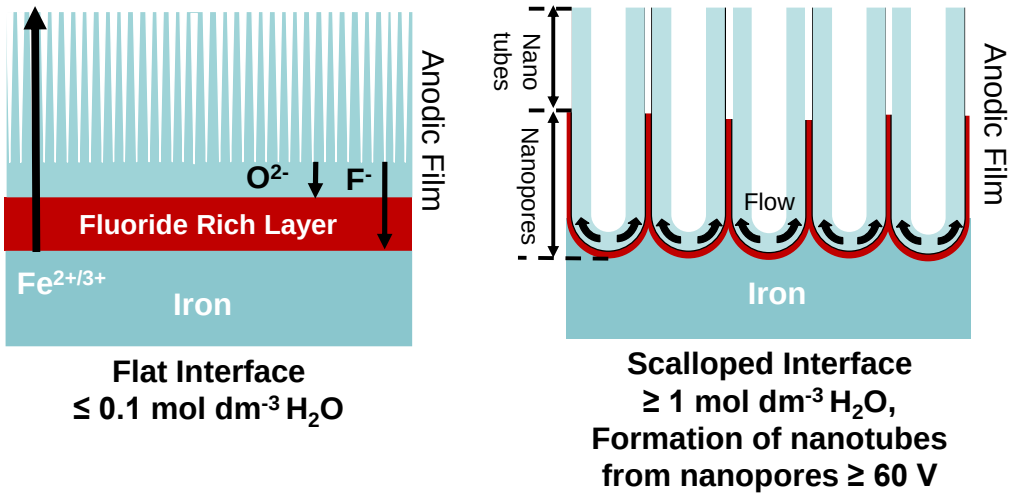

Figure 1.5 Schematic illustrations of the change in film morphology of the anodic films on iron in the ethylene glycol electrolytes containing 0.1 mol dm^{-3} ammonium fluoride (a) flat metal/film interface at water concentration ≤ 1 mol dm^{-3} water, (b) scalloped metal/film interface at water concentration ≥1 mol dm^{-3} water and formation of nanotubes at cell boundaries ≥ 60 V.

1.3.2. The Influence of Crystal Orientation on Formation of Anodic Films

In the past decade, the ability to control the morphology of anodic films by choosing the proper crystallographic orientation of the aluminum and titanium substrate has been proposed. Beck et al. demonstrated that the large scale of perfect hexagonal packed pores in anodic alumina can be obtained by using the coarse-grained microstructure in aluminum [92]. The correlation between the size of the regions with perfect hexagonal pore ordering in the anodic alumina porous structure and the crystallographic orientation of the Al substrate has been shown: the largest mean domain size and, as a consequence, the best transverse positional order have been observed for aluminum foils with (100) texture [93]. Clement, et al. demonstrated, the structure of anodic alumina formed in sulfuric acid on the surface of the single crystals of aluminum with (111), (110), and (100) orientations was analyzed [94]. According to scanning electron microscopy (SEM) measurements the smallest fraction of defects (dislocations and high- and low-angle grain boundaries) has been found for the (100) substrate. Obtained results have been explained in terms of minimizing the anodic alumina/Al interface energy. According to previously reported data [95], anodic alumina with the best transverse positional order of the pores is formed on (100)- oriented Al grains, whereas pore arrangement in the films grown on Al(110) does not show any resemblance to a hexagonal pattern. A theoretical description of this phenomenon has been performed by numerical simulations of the pore growth process involving different ratios of the formation of free and bound forms of Al^{3+} ions at the Al/anodic alumina interface.[96] An alternative explanation proposed for the influence of the crystallographic orientation of the Al substrate on the ordering of the amorphous anodic alumina porous structure involves the anisotropy of aluminum oxidation rates, which governs long-range transverse orientational pore ordering.[97] Indeed, the mosaicist of the porous structure was found to be minimal in the case of anodic alumina grown on Al(111) faces with 6-fold symmetry, whereas in the case of the 4-fold symmetry Al(100) crystal two equivalent options for the arrangement of a hexagonal lattice of pores were shown.

On anodic titania, the crystallographic orientation of the titanium substrate can affect the film thickness, donor concentration, electronic conductivity, the rate of ion transfer reactions and electron transfer reaction [98-101]. A combination of electrochemical analysis with electron backscatter diffraction (EBSD) has been performed to study the correlation between the crystallographic orientations of the Ti

metal substrate and the electrochemical behavior of the compact anodic oxide formed [100]. The anodic film thickness and its crystallinity were analyzed. Thin crystalline oxide with electronical conductivity are formed on lower index facet (001), whereas thicker oxides with less crystalline and lower electronic conductivity grow on higher index facet (hk0). As a consequence of the high electron conductivity on growing anodic films on (001) facet, an electronic current also flows through the film in addition to the ionic current. Therefore, a competition between anodic film growth and other electrochemical oxidation side reactions occurs and results on the presence of oxygen evolution reaction [102]. For TiO_2 on Ti(001), anodic oxygen evolution comes to pass at potentials of >4 V, while on higher index Ti(hk0) facets, only an ion transfer reaction (oxide growth) observed during anodizing; resulting in the thick nanotubes film formation [101]. Leonardi et al. showed how the growth characteristics of anodic nanotubular TiO_2 films, produced in an aqueous electrolyte solution of 1 M (NH_4) H_2PO_3 and 0.5 wt % NH_4F, can be tailored by controlling the orientation of the underlying Ti metal substrate. It was found that open or partially capped amorphous TiO_2 nanotubes form on Ti(hk0) grains, where growth of thick nanotubular oxide films is permitted. On Ti (001) grains, the anodic films exhibited large degree of structural crystalline disorder with mixed anatase and rutile phase [103-105]. Except for this research, one paper reported exceptional nanotube growth on the Ti(001) surface [106]. The results reported therein, even though interesting, there are several contradictory theories and experimental results concerning the influence of the crystallographic orientation of the titanium substrate on the morphology of anodic nanotubular titania films.

The effects of crystallographic structure of iron on anodizing process has not been studied so far either on grains of polycrystalline iron or iron single crystals, however the crystallographic structure of oxides grown on passive film iron has been a subject of immense debate for the last few decades in corrosion community. For the passive films on iron, the presence of Fe_2O_3 or Fe_3O_4 has been proposed [107-109]. Nagayama et al. found that the passive oxide can be composed of Fe_3O_4 inner-layer and Fe_2O_3 outer-layer [76, 110, 111]. Several reports suggested that the passive films may be amorphous having FeOOH like structure [112-117]. The other studies showed that passive oxide is composed of Fe_2O_3 or Fe_3O_4 [118, 119]. Toney et al. [120] and Davenport et al. [121] evaluated the structure of passive oxide formed on iron single crystals of (001) and (110) by means of *in-situ* surface X-ray diffraction technique, and found that the passive oxide has the LAMM phase, analogous to Fe_2O_3 or Fe_3O_4. The oxide formed on (100) plane

was less defective and has larger crystallites than that formed on (110) single crystal surfaces as shown in Figu.1.6 [120, 121]. Takabatake et al. found that the passive film on iron has bi-layered structure, with Fe_3O_4 as an inner-layer and Fe_2O_3 as an outer-layer, varying in the thickness proportion of -inner to -outer layers depending on the surface energy of the substrate related to its crystallographic orientation [122]. The mechanical properties of passive oxides formed on iron (100) and (110) single crystals were conducted by Seo and Chiba, the hardness of the passive iron (100) orientation was lower by 10% than the passive iron of (110) orientation [123]. Taking into account the nature of oxide formed on iron, immensely investigated by corrosion community, one may expect that the structure of oxide formed by anodizing may also depend on the crystallographic structure of metal on which it is formed.

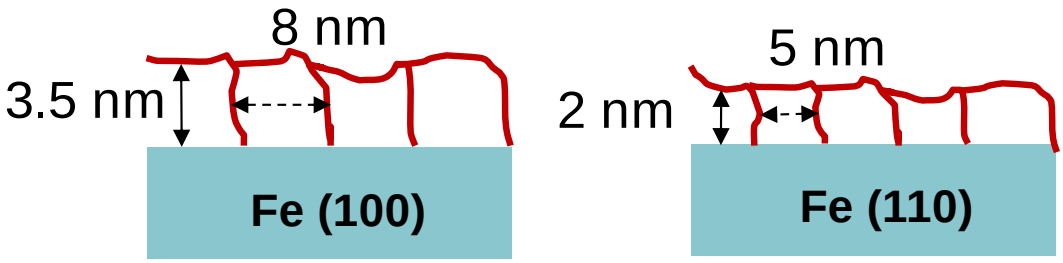

Figure 1.6 Schematic illustrations of the change in film morphology of the anodic films grown on (100) and (110) orientation [119].

1.3.3. Tracer Study

Various mechanisms have been proposed to explain the growth of nanoporous or naotubular films [33, 83, 87, 124-127]. Hoar and Mott suggested that pore formation was associated with the field-induced and thermally assisted dissolution of anodic alumina at the pore base [33]. O' Sullivan and Wood proposed that field-assisted dissolution is accelerated by the polarization of Al-O bonds [7, 33]. Cherki and Sielka employed the ^{18}O tracers to investigate the mechanisms of dissolution, transport, and growth associated with oxygen during the formation of porous films and estimated that 40 % of ionic current is carried by aluminum ions, while about 60 % is transported by oxide anions. They also found that pore formation causes the loss of aluminum cations to the electrolyte, resulting reduced growth efficiency close to 60 % for porous film formation [124].

The field-assisted ejection of aluminum cations to the electrolyte was first confirmed by Xu et al. using a xenon inert marker [24]. Sato gave the concept of plastic flow and mechanical breakdown of the oxide film and estimated that electrostriction

stresses at the pore bottom are 100 times higher than that acting on the pore walls and proposed that stresses at the pore bottom are sufficient for plastic flow of oxide materials from pore base [125]. In addition to the experimental study, the various mathematical model is have also been developed, based on ionic transport processes and interfacial reactions, as well as on the effects of surface energy, and elastic stress[128, 129].

In 2006, Manchester group proposed a flow mechanism based on direct experimental evidence, to explain the mechanism of pore generation and development in porous anodic alumina films. They found an increase in thickness of porous anodic films relative to that of metal consumed by an expansion factor of 1.35 during anodizing in 0.4 M sulfuric and phosphoric acids. This value of expansion factor exceeded the expected value of 1.16 based on purely field-assisted dissolution model. They estimated that increased film thickness is equal to pore volume. They predicted that plastic flow of alumina beneath the pore in the presence of ion transport and compressive stresses displace the material from the barrier layer towards the cell wall region and this contributes to an increased thickness of porous film relative to that of metal consumed [130]. Houser and Hebert in 2009, proposed a model for the potential distribution in porous anodic alumina films during steady state growth using computational approach [87]. Manchester group also conducted a series of tracer experiments and they incorporated tungsten tracer into the sputtered-deposited aluminum substrate prior to anodizing in phosphoric acid electrolyte [131, 132]. They found from direct TEM observations that tungsten band is distorted, flowing upwards toward the cell wall regions from the pore base as pore develops. These findings are contradictory to the field-assisted dissolution model of pore development, indicating the flow of film material owing to the plasticity and high compressive stresses in the barrier layer of porous anodic alumina films. A schematic diagram, indicating flow mechanism is shown in Figure 1.7, which shows the incorporation of tungsten tracer into the barrier layer and its subsequent migration towards the pore wall.

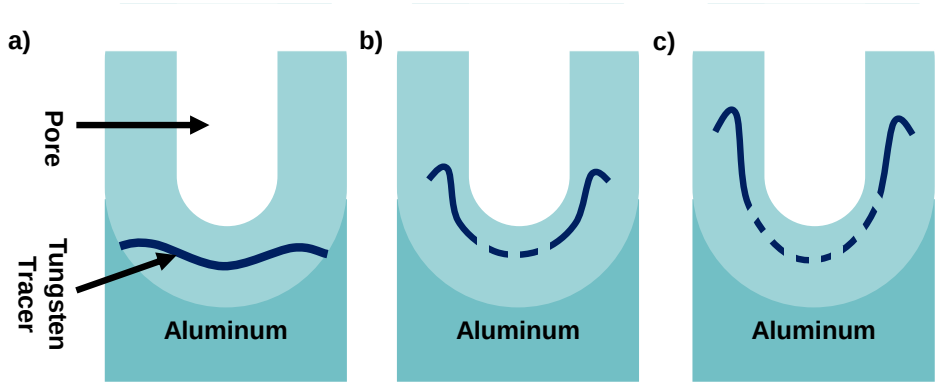

Figure 1.7 Schematic diagram illustrating the migration of tungsten tracer band during growth of porous film on aluminum; (a) tungsten tracer in the barrier layer and (b, c) migration of tungsten tracer towards the walls from pore base during pore growth [131].

1.4. The Application of Anodic Films Formed on Iron and Its Alloys

1.4.1. Photoelectrochemical study

The process of photoelectrochemical decomposition of water using semiconductor photoelectrodes was first reported in 1972 by Fujishima and Honda. Titanium dioxide (TiO_2) was used to absorb ultraviolet (UV) radiation and internally generate an electric potential due to the separation of charges within the material. By applying a small outside bias potential, it was observed that water is electrochemically split into hydrogen and oxygen gases. Titanium dioxide allow to absorb UV light of < 414 nm, which is only a small portion of the total solar spectrum, because TiO_2 band gap is relatively high (3.2 eV). Thus, it is unable to show sufficient efficiency to split water. This limitation indicates that titanium dioxide cannot itself stand up to the task of photoelectrochemically generating hydrogen.

A great deal of effort has been invested into devising photoelectrochemical cell (PEC) systems that will generate hydrogen efficiently at low cost. When a semiconductor electrode becomes illuminated, it absorbs photons with energies (hν) greater than its band gap energy (E_g),

$$h\nu \geq E_g \tag{1.5}$$

where h is Planck's constant (4.14×10^{-15} eV s) and ν is the frequency of the light. The frequency may be obtained from the wavelength (λ) by the relationship,

$$c = \lambda\nu \tag{1.6}$$

The band gap is the energy difference between the material's valence and conduction bands. Materials with band gaps greater than 4 eV are considered as insulators; those with little or no band gap are considered metals. Semiconductors lie in between. When photon energy is absorbed, electrons from the valence band are excited up into the conduction band and a positively charged hole is left in the valence band. n-type semiconductors have upward band bending at potentials more positive than the flat band potential, as shown in Figure 1.8. The excited electron moves to the back of the electrode, while hole moves to the surface. The standard electrolysis reaction is;

$$4H_2O \rightarrow 4H^+ + 4OH^- \quad (1.7)$$

$$\text{photo anode material} + \text{sunlight} \rightarrow 4h^+ + 4e^- \quad (1.8)$$

$$4OH^- + 4h^+ \rightarrow O_2 + 2H_2O \quad (1.9)$$

$$4H^+ + 4e^- \rightarrow 2H_2 \quad (1.10)$$

The overall reaction is:

$$H_2O + \text{photoanode} + \text{sunlight} \rightarrow H_2 + 1/2O_2 \quad (1.11)$$

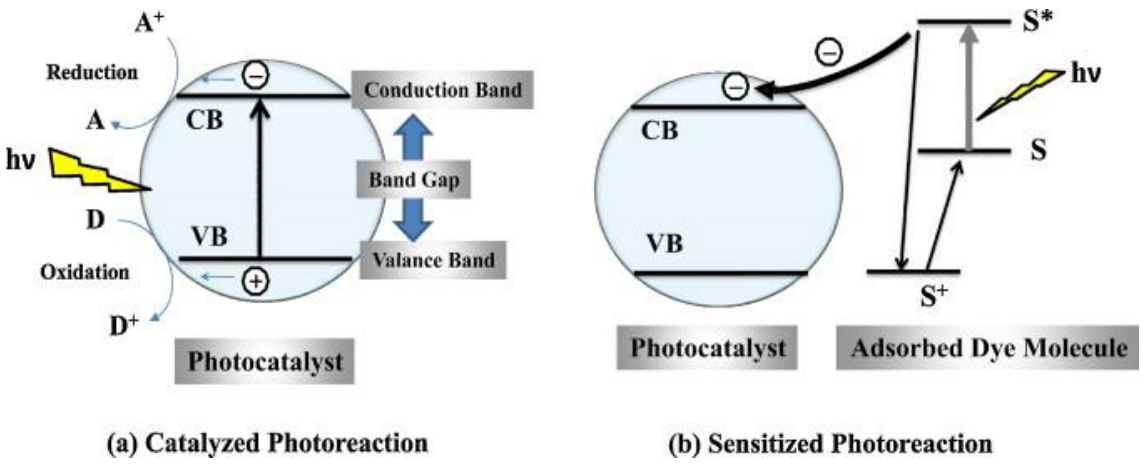

Figure 1.8 Schematic presentation of photocatalytic processes [133].

Iron oxide, among other iron oxides, is commonly found as rust, which is formed from iron (Fe) in the presence of water. However, it may be produced as the anhydrous form which has been found to be a cheap and useful semiconductor material. α-Fe_2O_3 has a band gap of 2.0 to 2.2 eV and may absorb electromagnetic radiation with wavelengths up to 621 nm which is in the visible portion of the solar spectrum. Its band gap makes it a perfect candidate as the top junction for hybrid multijunction PECs because it will absorb in the same range as the portion of the multijunction it replaces. The problem with pure iron oxides is that it is a resistive semiconductor, and therefore the introduction of dopants or combination of higher valence to make it more n-type, or lower valence to

make it more p-type, has also been investigated to enhance its electrical characteristics. On the other hand, WO_3 itself has emerged as a promising candidate as combining materials with iron oxide photocatalyst, due to its suitable physical and chemical properties. The effective utilization of this n-type material in solar water splitting was first presented in 1976 by Hodes et al. Since then, significant research contributions have been reported. However, WO_3 with a band gap of 2.6–2.8 eV can only absorb a maximum of ~12% of the incident solar light [134]. A combination of different semiconductor materials; such as, WO_3/TiO_2 [135], $TiO_2/Fe2O_3$ [136] and Fe_2O_3/WO_3 [137-139] proved to increase the semiconductor performance in many ways such as the increase of optical absorption, charge separation enhancement, faster surface kinetics, and the modification of the electronic structure between both materials [137].

1.4.2. Lithium Ion Battery

Lithium batteries are playing an important role among of energy storage technologies, because of their high specific per unit weight and also per unit volume compared to other batteries available on the market (Figure 1.9), such as lead-acid (Pb-acid), and nickel-metal hydride (Ni-MH) batteries. The use of Pb-acid batteries is restricted only to starting, lighting, and ignition in automobiles applications, while Ni-Cd batteries continue as the most suitable technologies for high-power applications (for example, power tools). Since their introduction in 1991, lithium-ion battery (Li-ion battery or LIB) has transformed portable electronic devices, such as laptops, cell phones, digital cameras and other consumer electronics.

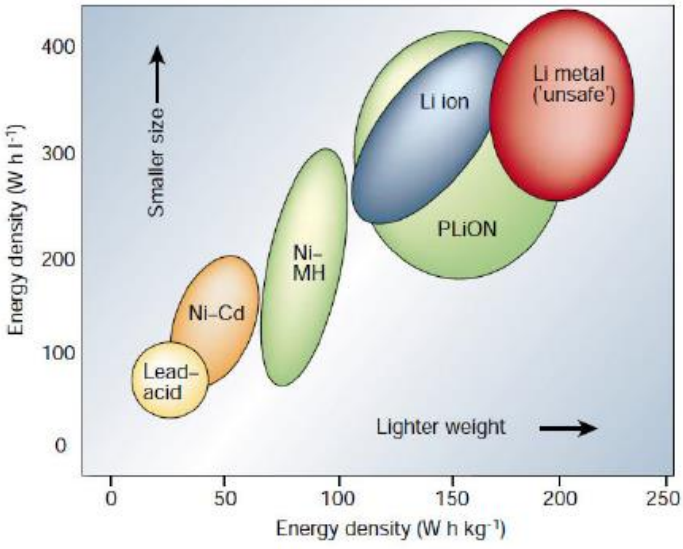

Figure 1.9 Comparison of the different battery technologies in terms of volumetric and gravimetric energy density [140].

The first commercialized LIBs were developed by Sony Corporation in 1991 with a graphite negative electrode, a $LiCoO_2$ positive electrode and the electrolyte, and have been dominant in the Li-ion battery market for 20 years due to their high energy density and long cycle life. However, this combination is not suitable for large scale batteries for vehicle and grid use. Firstly, the high cost of $LiCoO_2$ is due to scarcity and not environmental friendliness of cobalt resources. Secondly, there are potential safety hazards in such a system which will greatly enlarge in large-scale batteries. The safety hazards arise from the strongly oxidizing delithiated $Li_{1-x}CoO_2$ cathode in the charged state, which can release O_2, and the reducing lithiated graphite negative electrode, coupled with a flammable electrolyte, that commonly co-exist in a LIBs system. Furthermore, lithium-alloyed metals such as Al, Bi, Cd, Mg, Sn, and Sb also used due to high and fast storage capacities produced, despite that extensive volume expansion limits the cycle life of the batteries [141, 142]. To overcome these problems, the use of the metal oxides had been proposed. The most-publicized metal oxide negative electrode are based on titanium for example titanium dioxide [143, 144], $Li_4Ti_5O_{12}$ [145-147] or Na_2Ti_3O [148-150] which does not demonstrate large volumetric changes during lithiation/delithiation process. However, the used of this electrode limited only at low energy density. Other metal oxides for instance tin dioxide[151] have been investigated as an negative electrode in lithium batteries. However, the continuous aggregation of the elemental particles upon lithiation/delithiation in these electrode leads to rapid capacity degradation. This can be avoided by the use of transition metal oxides, for which the elemental transition metal does not alloy with lithium. So far, transition metals specifically, nickel oxide [152-154], copper oxide[155, 156], cobalt oxides[157-159], manganese oxide [160-162], zinc oxide [163], iron oxide [164] have been investigated as negative electrode for lithium ion batteries.

Iron Oxide for Lithium Ion Battery

Iron oxide is one of the most interesting and important transition metal oxides for application in LIBs due to its relatively high theoretical capacity of 1007 mAh g^{-1} for Fe_2O_3 [165, 166] and 926 mAh g^{-1} for Fe_3O_4 [167-169] and it has multiple electron valence states; Fe^0, Fe^{2+} and Fe^{3+} to provide rich redox pairs, and have abundance and environmental friendliness, and been studied as candidate negative electrode material since first reported as conversion-type material. The chemical reaction for the lithiation process on the iron oxides may be described as follow [170-172] , [173-175]:

$$Fe_2O_3 + xLi^+ + xe^- \rightarrow Li_xFe_2O_3 \quad (1.12)$$

$$Li_x\ Fe_2O_3 + (2-x)Li^+ + (2-x)e^- \rightarrow Li_2Fe_2O_3 \quad (1.13)$$

$$Fe_3O_4 + xLi^+ + xe^- \rightarrow Li_xFe_3O_4 \quad (1.14)$$

$$Li_xFe_3O_4 + (2-x)Li^+ + (2-x)e^- \rightarrow Li_2Fe_3O_4 \quad (1.15)$$

Despite so many advantegous of iron oxides for LiBs application, iron oxide still suffers from rapid capacity fading and poor cycle stability due to the electrode pulverization and volume expansion during lithiation/delithiation process. To improve the electrochemical performance of electrode materials, nanostructured engineering has been considered as a promising avenue towards the development of high-performance LIBs with high energy density, high power density, long cycle life, and improved safety. In general, nanostructures can provide reduced distance for ion and electron transport, larger electrode/electrolyte contact area, and good accommodation ability of the volume changes. Therefore, a wide variety of nanoarchitectured iron oxides with differing morphologies has been extensively explored, such as such as 1D (nanorods [176-180], nanowires [181], and nanotubes [165, 182, 183]), 2D (nanosheets [184, 185], Fe_2O_3 nanoflakes [186-188]) and 3D (nanoparticles [189-191], mesostructured Fe_2O_3 [192], Fe_2O_3 hollow microcubes [193], multi-shell Fe_2O_3 hollow spheres [194], porous Fe_2O_3 nanocubes [195], flower-like structures[196-198], Fe_2O_3 nano-assembled spindles[199], self-assembled Fe_3O_4 nanoparticle clusters [200], hierarchical Fe_3O_4 hollow microspheres [201, 202]) studied as negative electrode with good capacity and improved cyclability.

1.5. Objectives and Content of This Thesis

This thesis comprises work related to developing and establishing structures of anodic iron oxide materials. The objective of the present study is the fundamental understanding of the growth of anodic nanopores/nanotubes on iron implicating the studies on iron single crystals for evaluation on how the anodic film grows depending on facet index number and the modification of the anodic film growth by addition of an alloying element is studied to the control full transition between nanopores and nanotubes in order to meet the requirements of high surface area for desired applications and physicochemical parameters such as bandgap engineering. Further, the functionality of nanostructured anodic iron oxide films for photocatalytic water splitting and lithium ion battery applications is investigated.

This thesis consists of total seven chapters. **Chapter 1** describes the brief introduction of anodizing of iron, as well as scientific background behind the formation of various types of anodic films and their growth mechanisms, the state-of-the-art and objectives presented in the present introduction chapter. The **Chapter 2** elaborates the details of different characterization methods used to assess the fabricated nanopores/nanotubular films and its application on photoelectrochemical study and also lithium ion batteries.

In **Chapter 3**, the effect of crystallographic orientation of iron on anodizing processes in organic electrolyte is studied. The objective of this chapter is to evaluate how the crystallographic orientation of iron affects the growth of anodic films on individual single crystals for BCC iron. In **Chapter 4**, the anodizing of Fe-W alloy was studied for the first time. The main interest in this study was to examine the influence of tungsten species on the growth process of formed oxide. The results were compared with that of anodizing of pure Fe for a better understanding the growth mechanism of the anodic iron oxide films. Furthermore, the influence of anodizing conditions, especially water contain and anodizing voltage was analyzed.

In **Chapter 5**, the photochemical characteristics of Fe-W oxides of controlled thickness and structure grown by anodizing sputter-deposited Fe-W in a fluoride containing solution, followed by annealing at different temperatures are examined. The results are compared to the nanoporous iron oxide to understand the effect of WO_3 to the photocatalytic activity on the iron oxides. DRS analysis, photocurrent measurements, and photodegradation on methylene blue were also performed to explore the influence of Fe_2O_3-WO_3 hybridization on the photocatalytic performance. The **Chapter 6** focuses to explore the influence of crystallographic structure of anodic iron oxide to the areal capacity, efficiency and stability as negative electrode for lithium ion batteries (LIBs).

Finally, **Chapter 7** contains the main conclusions of the results of the previous chapters as well as the perspectives and also includes prospects for future work.

References:

1. Masuda, H. and K. Fukuda, *Ordered Metal Nanohole Arrays Made by a Two-Step Replication of Honeycomb Structures of Anodic Alumina.* Science, 1995. **268**(5216): p. 1466.
2. Keller, F., M.S. Hunter, and D.L. Robinson, *Structural Features of Oxide Coatings on Aluminum.* Journal of The Electrochemical Society, 1953. **100**(9): p. 411-419.
3. Ono, S., et al., *Controlling Factor of Self-Ordering of Anodic Porous Alumina.* Journal of The Electrochemical Society, 2004. **151**(8): p. B473-B478.
4. Pringle, J.P.S., *A Very Precise Sectioning Method for Measuring Concentration Profiles in Anodic Tantalum Oxide.* Journal of The Electrochemical Society, 1972. **119**(4): p. 482-491.
5. Young, L., *Anodic oxide films.* 1961, London; New York (N.Y.): Academic Press.

6. Jessensky, O., F. Müller, and U. Gösele, *Self‐Organized Formation of Hexagonal Pore Structures in Anodic Alumina.* Journal of The Electrochemical Society, 1998. **145**(11): p. 3735-3740.
7. O, J.P., et al., *The morphology and mechanism of formation of porous anodic films on aluminium.* Proceedings of the Royal Society of London. A. Mathematical and Physical Sciences, 1970. **317**(1531): p. 511-543.
8. Tsuchiya, H., et al., *Self-Organized High-Aspect-Ratio Nanoporous Zirconium Oxides Prepared by Electrochemical Anodization.* Small, 2005. **1**(7): p. 722-725.
9. Tsuchiya, H., et al., *Self-organized porous TiO_2 and ZrO_2 produced by anodization.* Corrosion Science, 2005. **47**(12): p. 3324-3335.
10. Kikuchi, T., et al., *Fabrication of porous tungsten oxide via anodizing in an ammonium nitrate/ethylene glycol/water mixture for visible light-driven photocatalyst.* Applied Surface Science, 2017. **422**: p. 130-137.
11. Habazaki, H., et al., *Crystallization of anodic titania on titanium and its alloys.* Corrosion Science, 2003. **45**(9): p. 2063-2073.
12. Tanvir, M.T., et al., *Influence of silicon on the growth of barrier-type anodic films on titanium.* Electrochimica Acta, 2007. **52**(24): p. 6834-6840.
13. Kowalski, D., D. Kim, and P. Schmuki, *TiO_2 nanotubes, nanochannels and mesosponge: Self-organized formation and applications.* Nano Today, 2013. **8**(3): p. 235-264.
14. Thompson, G.E. and G.C. Wood, *5 - Anodic films on aluminium*, in *Treatise on Materials Science and Technology*, J.C. Scully, Editor. 1983, Elsevier. p. 205-329.
15. Skeldon, P., et al., *Fundamental studies elucidating anodic barrier-type film growth on aluminium.* Thin Solid Films, 1985. **123**(2): p. 127-133.
16. Ono, S., K. Kuramochi, and H. Asoh, *Effects of electrolyte pH and temperature on dielectric properties of anodic oxide films formed on niobium.* Corrosion Science, 2009. **51**(7): p. 1513-1518.
17. Richardson, J.A. and G.C. Wood, *A study of the pitting corrosion of Al byscanning electron microscopy.* Corrosion Science, 1970. **10**(5): p. 313-323.
18. Richardson, J.A., G.C. Wood, and A.J. Breen, *The interpretation of impedance measurements on oxide-coated aluminium part 1. A correction procedure for "wet" measurements.* Thin Solid Films, 1973. **16**(1): p. 81-97.
19. Franklin, R.W., *Structure of Non-porous Anodic Films on Aluminium.* Nature, 1957. **180**(4600): p. 1470-1471.
20. Stirland, D.J. and R.W. Bicknell, *Studies of the Structure of Anodic Oxide Films on Aluminum, I.* Journal of The Electrochemical Society, 1959. **106**(6): p. 481-485.
21. Leach, J.S.L. and P. Neufeld, *Pore structure in anodic Al_2O_3 films.* Corrosion Science, 1969. **9**(6): p. 413-IN6.
22. Dorsey, G.A., *The Characterization of Anodic Aluminas: I . Composition of Films from Acidic Anodizing Electrolytes.* Journal of The Electrochemical Society, 1966. **113**(2): p. 169-172.
23. Takahashi, H. and M. Nagayama, *Electrochemical behaviour and structure of anodic oxide films formed on aluminium in a neutral borate solution.* Electrochimica Acta, 1978. **23**(3): p. 279-286.
24. Xu, Y., G.E. Thompson, and G.C. Wood, *Mechanism of anodic film growth on aluminium.* Transactions of the IMF, 1985. **63**(1): p. 98-103.
25. Shimizu, K., G.E. Thompson, and G.C. Wood, *The duplex nature of anodic barrier films formed on aluminium in aqueous borate and borate-glycol solutions.* Thin Solid Films, 1981. **85**(1): p. 53-59.
26. Skeldon, P., et al., *Barrier-type anodic films on aluminium in aqueous borate solutions: 2—Film compositions by Rutherford backscattering spectroscopy and nuclear reaction methods.* Surface and Interface Analysis, 1983. **5**(6): p. 252-263.
27. Shimizu, K., et al., *Anodic oxide films on tantalum: Incorporation and mobilities of electrolyte-derived species.* Philosophical Magazine B, 1996. **73**(3): p. 461-485.
28. Habazaki, H., et al., *Anodic film formation on a sputter-deposited Al-30at%Mo alloy.* Corrosion Science, 1995. **37**(9): p. 1497-1509.
29. Shimizu, B.K., et al., *A novel marker for the determination of transport numbers during anodic barrier oxide growth on aluminium.* Philosophical Magazine B, 1991. **64**(3): p. 345-353.
30. Shimizu, K., et al., *Incorporation and migration of Cr^{3+} and $PO^{3-}{}_4$ species in anodic alumina.* Corrosion Science, 1999. **41**(10): p. 1971-1976.
31. Takahashi, H., K. Fujimoto, and M. Nagayama, *Effect of pH on the Distribution of Anions in Anodic Oxide Films Formed on Aluminum in Phosphate Solutions.* Journal of The Electrochemical Society, 1988. **135**(6): p. 1349-1353.

32. Abd Rabbo, M.F., J.A. Richardson, and G.C. Wood, *A study of barrier film growth on aluminium in solutions of film-promoting and aggressive ions using secondary ion mass spectrometry*. Corrosion Science, 1976. **16**(10): p. 689-702.
33. Hoar, T.P. and N.F. Mott, *A mechanism for the formation of porous anodic oxide films on aluminium.* Journal of Physics and Chemistry of Solids, 1959. **9**(2): p. 97-99.
34. Brock, A.J. and G.C. Wood, *Hydroxyl ion and proton mobility during anodic oxidation of aluminium.* Electrochimica Acta, 1967. **12**(4): p. 395-412.
35. Davies, J.A., et al., *The Migration of Metal and Oxygen during Anodic Film Formation.* Journal of The Electrochemical Society, 1965. **112**(7): p. 675-680.
36. Güntherschulze, A. and H. Betz, *Die Bewegung der Ionengitter von Isolatoren bei extremen elektrischen Feldstärken.* Zeitschrift für physik, 1934. **92**(5-6): p. 367-374.
37. Lewis, J.E. and R.C. Plumb, *Studies of the Anodic Behavior of Aluminum: I . The Direction of lonic Movement.* Journal of The Electrochemical Society, 1958. **105**(9): p. 496-498.
38. Diggle, J.W., T.C. Downie, and C.W. Goulding, *A Study of the Formation and Dissolution of Porous Anodic Oxide Films on Aluminum: Behavior of the Porous Layer.* Journal of The Electrochemical Society, 1969. **116**(10): p. 1347-1351.
39. Bailey, G. 1978, University of Manchester.
40. Bernard, W.J., *Ionic Movement during the Growth of Anodic Oxide Films on Aluminum.* Journal of The Electrochemical Society, 1962. **109**(11): p. 1082-1084.
41. Wood, G.C., et al., *A Model for the Incorporation of Electrolyte Species into Anodic Alumina.* Journal of The Electrochemical Society, 1996. **143**(1): p. 74-83.
42. Randall, J.J. and W.J. Bernard, *A radiotracer study of the anodization of aluminum in aqueous phosphate solutions.* Electrochimica Acta, 1975. **20**(9): p. 653-661.
43. Macak, J.M. and P. Schmuki, *Anodic growth of self-organized anodic TiO_2 nanotubes in viscous electrolytes.* Electrochimica Acta, 2006. **52**(3): p. 1258-1264.
44. Berger, S., et al., *Enhanced self-ordering of anodic ZrO_2 nanotubes in inorganic and organic electrolytes using two-step anodization.* physica status solidi (RRL) – Rapid Research Letters, 2008. **2**(3): p. 102-104.
45. Ou, J.Z., et al., *Elevated Temperature Anodized Nb_2O_5: A Photoanode Material with Exceptionally Large Photoconversion Efficiencies.* ACS Nano, 2012. **6**(5): p. 4045-4053.
46. Wei, W., J.M. Macak, and P. Schmuki, *High aspect ratio ordered nanoporous Ta_2O_5 films by anodization of Ta.* Electrochemistry Communications, 2008. **10**(3): p. 428-432.
47. Rangaraju, R.R., et al., *Nanostructured anodic iron oxide film as photoanode for water oxidation.* Journal of Physics D: Applied Physics, 2009. **42**(13): p. 135303.
48. fAssefpour-Dezfuly, M., C. Vlachos, and E.H. Andrews, *Oxide morphology and adhesive bonding on titanium surfaces.* Journal of Materials Science, 1984. **19**(11): p. 3626-3639.
49. Roy, P., S. Berger, and P. Schmuki, *TiO_2 Nanotubes: Synthesis and Applications.* Angewandte Chemie International Edition, 2011. **50**(13): p. 2904-2939.
50. Crawford, G.A., N. Chawla, and J.E. Houston, *Nanomechanics of biocompatible TiO_2 nanotubes by Interfacial Force Microscopy (IFM).* Journal of the Mechanical Behavior of Biomedical Materials, 2009. **2**(6): p. 580-587.
51. Park, M.-W. and K.-Y. Chun, *Effects of anodization growth of TiO_2-nanotube array membrane on photo-conversion efficiency of dye-sensitized solar cell.* Electronic Materials Letters, 2009. **5**(1): p. 7-11.
52. Zwilling, V., et al., *Structure and physicochemistry of anodic oxide films on titanium and TA6V alloy.* Surface and Interface Analysis, 1999. **27**(7): p. 629-637.
53. Macák, J.M., H. Tsuchiya, and P. Schmuki, *High-Aspect-Ratio TiO_2 Nanotubes by Anodization of Titanium.* Angewandte Chemie International Edition, 2005. **44**(14): p. 2100-2102.
54. Albu, S.P., et al., *250 µm long anodic TiO_2 nanotubes with hexagonal self-ordering.* physica status solidi (RRL) – Rapid Research Letters, 2007. **1**(2): p. R65-R67.
55. Ghicov, A., et al., *Titanium oxide nanotubes prepared in phosphate electrolytes.* Electrochemistry Communications, 2005. **7**(5): p. 505-509.
56. Tsuchiya, H., et al., *Self-organized porous WO_3 formed in NaF electrolytes.* Electrochemistry Communications, 2005. **7**(3): p. 295-298.
57. Muratore, F., et al., *Comparison of nanotube formation on zirconium in fluoride/glycerol electrolytes at different anodizing potentials.* Electrochimica Acta, 2011. **58**: p. 389-398.
58. Valota, A., et al., *Influence of water content on nanotubular anodic titania formed in fluoride/glycerol electrolytes.* Electrochimica Acta, 2009. **54**(18): p. 4321-4327.
59. Berger, S., et al., *The origin for tubular growth of TiO_2 nanotubes: A fluoride rich layer between tube-walls.* Surface Science, 2011. **605**(19): p. L57-L60.

60. Albu, S.P., et al., *Formation of Double-Walled TiO_2 Nanotubes and Robust Anatase Membranes.* Advanced Materials, 2008. **20**(21): p. 4135-4139.
61. Habazaki, H., et al., *Fast migration of fluoride ions in growing anodic titanium oxide.* Electrochemistry Communications, 2007. **9**(5): p. 1222-1227.
62. Hardee, K.L. and A.J. Bard, *Semiconductor Electrodes: V . The Application of Chemically Vapor Deposited Iron Oxide Films to Photosensitized Electrolysis.* Journal of The Electrochemical Society, 1976. **123**(7): p. 1024-1026.
63. Beermann, N., et al., *Photoelectrochemical Studies of Oriented Nanorod Thin Films of Hematite.* Journal of The Electrochemical Society, 2000. **147**(7): p. 2456-2461.
64. Kennedy, J.H. and K.W. Frese, *Photooxidation of Water at α-Fe_2O_3 Electrodes.* Journal of The Electrochemical Society, 1978. **125**(5): p. 709-714.
65. Sun, H.-T., et al., *NO2 gas sensitivity of sol-gel-derived α-Fe_2O_3 thin films.* Thin Solid Films, 1995. **269**(1): p. 97-101.
66. Pelino, M., et al., *Silica effect on α-Fe_2O_3 humidity sensor1Presented at the 2nd East Asia Conference on Chemical Sensors, Xi'an, P.R. China, 1995.1.* Sensors and Actuators B: Chemical, 1998. **46**(3): p. 186-193.
67. Jiao, F., et al., *α-Fe_2O_3 Nanowires. Confined Synthesis and Catalytic Hydroxylation of Phenol.* Chemistry Letters, 2003. **32**(8): p. 770-771.
68. Piazza, S., et al., *Photoelectrochemical investigation of passive layers formed on Fe in different electrolytic solutions.* Corrosion Science, 2004. **46**(4): p. 831-851.
69. Prakasam, H.E., et al., *Synthesis and photoelectrochemical properties of nanoporous iron (III) oxide by potentiostatic anodization.* Nanotechnology, 2006. **17**(17): p. 4285-4291.
70. Albu, S.P., A. Ghicov, and P. Schmuki, *High aspect ratio, self-ordered iron oxide nanopores formed by anodization of Fe in ethylene glycol/NH4F electrolytes.* physica status solidi (RRL) − Rapid Research Letters, 2009. **3**(2 - 3): p. 64-66.
71. Mohapatra, S.K., et al., *Water photooxidation by smooth and ultrathin α-Fe_2O_3 nanotube arrays.* Chemistry of Materials, 2009. **21**(14): p. 3048-3055.
72. Habazaki, H., et al., *Galvanostatic growth of nanoporous anodic films on iron in ammonium fluoride−ethylene glycol electrolytes with different water contents.* The Journal of Physical Chemistry C, 2010. **114**(44): p. 18853-18859.
73. Rangaraju, R.R., et al., *An investigation on room temperature synthesis of vertically oriented arrays of iron oxide nanotubes by anodization of iron.* Electrochimica Acta, 2010. **55**(3): p. 785-793.
74. Konno, Y., et al., *Formation of Self-Organized Nanoporous Anodic Films on Carbon Steel.* ECS Transactions, 2013. **50**(37): p. 183-190.
75. Nagayama, M.i. and M. Cohen, *The anodic oxidation of iron in a neutral solution: I . The nature and composition of the passive film.* Journal of The Electrochemical Society, 1962. **109**(9): p. 781-790.
76. Nagayama, M. and M. Cohen, *The Anodic Oxidation of Iron in a Neutral Solution: II . Effect of Ferrous Ion and pH on the Behavior of Passive Iron.* Journal of The Electrochemical Society, 1963. **110**(6): p. 670-680.
77. Jagminas, A., et al., *Compositional and structural characterization of nanoporous films produced by iron anodizing in ethylene glycol solution.* Applied Surface Science, 2011. **257**(9): p. 3893-3897.
78. Zhang, Z., M.F. Hossain, and T. Takahashi, *Fabrication of shape-controlled α-Fe_2O_3 nanostructures by sonoelectrochemical anodization for visible light photocatalytic application.* Materials Letters, 2010. **64**(3): p. 435-438.
79. Cheng, H., et al., *Electrochemical fabrication and optical properties of periodically structured porous Fe_2O_3 films.* Electrochemistry Communications, 2012. **20**: p. 178-181.
80. Lee, C.-Y., et al., *Anodic Nanotubular/porous Hematite Photoanode for Solar Water Splitting: Substantial Effect of Iron Substrate Purity.* ChemSusChem, 2014. **7**(3): p. 934-940.
81. Konno, Y., et al., *Factors influencing the growth behaviour of nanoporous anodic films on iron under galvanostatic anodizing.* Journal of Solid State Electrochemistry, 2012. **16**(12): p. 3887-3896.
82. Schrebler, R., et al., *Electrochemically Grown Self-Organized Hematite Nanotube Arrays for Photoelectrochemical Water Splitting.* Journal of The Electrochemical Society, 2014. **161**(14): p. H903-H908.

83. Shahzad, K., et al., *Ex situ evidence for the role of a fluoride-rich layer switching the growth of nanopores to nanotubes: A missing piece of the anodizing puzzle*. ChemElectroChem, 2018. **5**(4): p. 610-618.
84. Mushove, T., T.M. Breault, and L.T. Thompson, *Synthesis and Characterization of Hematite Nanotube Arrays for Photocatalysis.* Industrial & Engineering Chemistry Research, 2015. **54**(16): p. 4285-4292.
85. Momeni, M.M., Y. Ghayeb, and F. Mohammadi, *Fe_2O_3 nanotube films prepared by anodisation as visible light photocatalytic.* Surface Engineering, 2015. **31**(6): p. 452-457.
86. Wang, L., et al., *Anodic self-organized transparent nanotubular/porous hematite films from Fe thin-films sputtered on FTO and photoelectrochemical water splitting.* Research on Chemical Intermediates, 2015. **41**(12): p. 9333-9341.
87. Houser, J.E. and K.R. Hebert, *The role of viscous flow of oxide in the growth of self-ordered porous anodic alumina films.* Nature Materials, 2009. **8**(5): p. 415-420.
88. LaTempa, T.J., et al., *Temperature-Dependent Growth of Self-Assembled Hematite (α-Fe_2O_3) Nanotube Arrays: Rapid Electrochemical Synthesis and Photoelectrochemical Properties.* The Journal of Physical Chemistry C, 2009. **113**(36): p. 16293-16298.
89. Paulose, M., et al., *TiO_2 Nanotube Arrays of 1000 μm Length by Anodization of Titanium Foil: Phenol Red Diffusion.* The Journal of Physical Chemistry C, 2007. **111**(41): p. 14992-14997.
90. Santamaria, M., et al., *Physicochemical characterization and photoelectrochemical analysis of iron oxide films.* Journal of Solid State Electrochemistry, 2013. **17**(12): p. 3005-3014.
91. Rozana, M., et al., *Effect of Applied Voltage on the Formation of Self-Organized Iron Oxide Nanoporous Film in Organic Electrolyte via Anodic Oxidation Process and their Photocurrent Performance.* Advanced Materials Research, 2014. **1024**: p. 99-103.
92. Grigor'ev, S.V., et al., *Two-dimensional spatially ordered Al_2O_3 systems: Small-angle neutron scattering investigation.* JETP Letters, 2007. **85**(9): p. 449-453.
93. Beck, G. and K. Petrikowski, *Influence of the microstructure of the aluminum substrate on the regularity of the nanopore arrangement in an alumina layer formed by anodic oxidation.* Surface and Coatings Technology, 2008. **202**(21): p. 5084-5091.
94. Beck, G. and R. Bretzler, *Regularity of nanopores in anodic alumina formed on orientated aluminium single-crystals.* Materials Chemistry and Physics, 2011. **128**(3): p. 383-387.
95. Ng, C.K.Y. and A.H.W. Ngan, *Precise Control of Nanohoneycomb Ordering over Anodic Aluminum Oxide of Square Centimeter Areas.* Chemistry of Materials, 2011. **23**(23): p. 5264-5268.
96. Cheng, C., et al., *Simulation and experiment of substrate aluminum grain orientation dependent self-ordering in anodic porous alumina.* Journal of Applied Physics, 2013. **113**(20): p. 204903.
97. Napolskii, K.S., et al., *Origin of long-range orientational pore ordering in anodic films on aluminium.* Journal of Materials Chemistry, 2012. **22**(24): p. 11922-11926.
98. Kudelka, S. and J.W. Schultze, *Photoelectrochemical imaging and microscopic reactivity of oxidised Ti.* Electrochimica Acta, 1997. **42**(18): p. 2817-2825.
99. Kudelka, S., A. Michaelis, and J.W. Schultze, *Effect of texture and formation rate on ionic and electronic properties of passive layers on Ti single crystals.* Electrochimica Acta, 1996. **41**(6): p. 863-870.
100. König, U. and B. Davepon, *Microstructure of polycrystalline Ti and its microelectrochemical properties by means of electron-backscattering diffraction (EBSD).* Electrochimica Acta, 2001. **47**(1): p. 149-160.
101. Davepon, B., et al., *Crystallographic orientation of single grains of polycrystalline titanium and their influence on electrochemical processes.* Surface and Coatings Technology, 2003. **169-170**: p. 85-90.
102. Vanhumbeeck, J.-F. and J. Proost, *Current understanding of Ti anodisation: functional, morphological, chemical and mechanical aspects.* Corrosion Reviews, 2009. **27**(3): p. 117-204.
103. Likodimos, V., et al., *Phase Composition, Size, Orientation, and Antenna Effects of Self-Assembled Anodized Titania Nanotube Arrays: A Polarized Micro-Raman Investigation.* The Journal of Physical Chemistry C, 2008. **112**(51): p. 20574-20574.
104. Leonardi, S., et al., *TiO_2 nanotubes: Interdependence of substrate grain orientation and growth characteristics.* The Journal of Physical Chemistry C, 2012. **116**(1): p. 384-392.
105. Leonardi, S., et al., *TiO_2 Nanotubes: Interdependence of Substrate Grain Orientation and Growth Rate.* ACS Applied Materials & Interfaces, 2015. **7**(3): p. 1662-1668.
106. Crawford, G.A. and N. Chawla, *Tailoring TiO2 nanotube growth during anodic oxidation by crystallographic orientation of Ti.* Scripta Materialia, 2009. **60**(10): p. 874-877.

107. Iitaka, I., S. Miyake, and T. Iimori, *Examination of passive iron by electron diffraction.* Nature, 1937. **139**(3508): p. 156-156.
108. Mayne, J.E.O. and M.J. Pryor, *392. The mechanism of inhibition of corrosion of iron by chromic acid and potassium chromate.* Journal of the Chemical Society (Resumed), 1949(0): p. 1831-1835.
109. Cohen, M., *An Electron Diffraction Study of Films Formed by Sodium Nitrite Solution on Iron.* The Journal of Physical Chemistry, 1952. **56**(4): p. 451-453.
110. Foley, C.L., J. Kruger, and C.J. Bechtoldt, *Electron diffraction studies of active, passive, and transpassive oxide films formed on iron.* Journal of The Electrochemical Society, 1967. **114**(10): p. 994-1001.
111. Kuroda, K., et al., *Electron diffraction study of the passive film on iron.* Journal of The Electrochemical Society, 1982. **129**(10): p. 2163-2169.
112. O'Grady, W.E., *Mössbauer study of the passive oxide film on iron.* Journal of The Electrochemical Society, 1980. **127**(3): p. 555-563.
113. Eldridge, J. and R.W. Hoffman, *A mössbauer spectroscopy study of the potential dependence of passivated iron films.* Journal of The Electrochemical Society, 1989. **136**(4): p. 955-961.
114. Kerkar, M., J. Robinson, and A.J. Forty, *In situ structural studies of the passive film on iron and iron/chromium alloys using X-ray absorption spectroscopy.* Faraday Discussions of the Chemical Society, 1990. **89**(0): p. 31-40.
115. Long, G.G., et al., *Structure of passive films on iron using a new surface-EXAFS technique.* Journal of Electroanalytical Chemistry and Interfacial Electrochemistry, 1983. **150**(1): p. 603-610.
116. Gui, J. and T.M. Devine, *In situ vibrational spectra of the passive film on iron in buffered borate solution.* Corrosion Science, 1991. **32**(10): p. 1105-1124.
117. Rubim, J.C. and J. Dünnwald, *Enhanced Raman scattering from passive films on silver-coated iron electrodes.* Journal of Electroanalytical Chemistry and Interfacial Electrochemistry, 1989. **258**(2): p. 327-344.
118. Davenport, A.J. and M. Sansone, *High resolution in situ XANES investigation of the nature of the passive film on iron in a pH 8.4 borate buffer.* Journal of The Electrochemical Society, 1995. **142**(3): p. 725-730.
119. Ryan, M.P., R.C. Newman, and G.E. Thompson, *An STM study of the passive film formed on iron in borate buffer solution.* Journal of The Electrochemical Society, 1995. **142**(10): p. L177-L179.
120. Toney, M.F., et al., *Atomic structure of the passive oxide film formed on iron.* Physical Review Letters, 1997. **79**(21): p. 4282-4285.
121. Davenport, A.J., et al., *The structure of the passive film that forms on iron in aqueous environments.* Journal of The Electrochemical Society, 2000. **147**(6): p. 2162-2173.
122. Takabatake, Y., et al., *Grain-Dependent Passivation of Iron in Sulfuric Acid Solution.* Journal of The Electrochemical Society, 2014. **161**(14): p. C594-C600.
123. Seo, M. and M. Chiba, *Nano-mechano-electrochemistry of passive metal surfaces.* Electrochimica Acta, 2001. **47**(1): p. 319-325.
124. Cherki, C. and J. Siejka, *Study by Nuclear Microanalysis and O_{18} Tracer Techniques of the Oxygen Transport Processes and the Growth Laws for Porous Anodic Oxide Layers on Aluminum.* Journal of The Electrochemical Society, 1973. **120**(6): p. 784-791.
125. Sato, N., K. Kudo, and T. Noda, *The anodic oxide film on iron in neutral solution.* Electrochimica Acta, 1971. **16**(11): p. 1909-1921.
126. Siejka, J. and C. Ortega, *An O_{18} Study of Field - Assisted Pore Formation in Compact Anodic Oxide Films on Aluminum.* Journal of The Electrochemical Society, 1977. **124**(6): p. 883-891.
127. Thompson, G.E., *Porous anodic alumina: fabrication, characterization and applications.* Thin Solid Films, 1997. **297**(1): p. 192-201.
128. Parkhutik, V.P. and V.I. Shershulsky, *Theoretical modelling of porous oxide growth on aluminium.* Journal of Physics D: Applied Physics, 1992. **25**(8): p. 1258-1263.
129. Singh, G.K., et al., *Formation of nanoscale pore arrays during anodization of aluminum.* Europhys. Lett., 2005. **70**(6): p. 836-842.
130. Garcia-Vergara, S.J., et al., *A flow model of porous anodic film growth on aluminium.* Electrochimica Acta, 2006. **52**(2): p. 681-687.
131. Skeldon, P., et al., *A Tracer Study of Porous Anodic Alumina.* Electrochemical and Solid-State Letters, 2006. **9**(11): p. B47-B51.
132. Garcia-Vergara, S.J., et al., *Stress generated porosity in anodic alumina formed in sulphuric acid electrolyte.* Corrosion Science, 2007. **49**(10): p. 3772-3782.
133. Mohamed, H.H. and D.W. Bahnemann, *The role of electron transfer in photocatalysis: Fact and fictions.* Applied Catalysis B: Environmental, 2012. **128**: p. 91-104.

134. Mao, A., et al., *Hematite modified tungsten trioxide nanoparticle photoanode for solar water oxidation.* Journal of Power Sources, 2012. **210**: p. 32-37.
135. Wang, J., et al., *Preparation and photoelectrochemical characterization of WO_3/TiO_2 nanotube array electrode.* Journal of Materials Science, 2011. **46**(2): p. 416-421.
136. Luan, P., et al., *Effective charge separation in the rutile TiO_2 nanorod-coupled α-Fe_2O_3 with exceptionally high visible activities.* Scientific Reports, 2014. **4**(1): p. 6180.
137. Kronawitter, C.X., et al., *A perspective on solar-driven water splitting with all-oxide hetero-nanostructures.* Energy & Environmental Science, 2011. **4**(10): p. 3889-3899.
138. Sivula, K., F.L. Formal, and M. Grätzel, *WO_3−Fe_2O_3 Photoanodes for Water Splitting: A Host Scaffold, Guest Absorber Approach.* Chemistry of Materials, 2009. **21**(13): p. 2862-2867.
139. Jin, T., et al., *WO_3 nanoneedles/α-Fe_2O_3/cobalt phosphate composite photoanode for efficient photoelectrochemical water splitting.* Applied Catalysis B: Environmental, 2014. **148-149**: p. 304-310.
140. Tarascon, J.M. and M. Armand, *Issues and challenges facing rechargeable lithium batteries.* Nature, 2001. **414**(6861): p. 359-367.
141. Mekonnen, Y., A. Sundararajan, and A.I. Sarwat. *A review of cathode and anode materials for lithium-ion batteries*. in *SoutheastCon 2016*. 2016.
142. Zhang, W.-J., *A review of the electrochemical performance of alloy anodes for lithium-ion batteries.* Journal of Power Sources, 2011. **196**(1): p. 13-24.
143. Kowalski, D., et al., *Electrochemical synthesis of 1D core-shell Si/TiO2 nanotubes for lithium ion batteries.* Journal of Power Sources, 2017. **361**: p. 243-248.
144. Wei, W., et al., *High energy and power density TiO2 nanotube electrodes for 3D Li-ion microbatteries.* Journal of Materials Chemistry A, 2013. **1**(28): p. 8160-8169.
145. Chen, Z., et al., *Titanium-Based Anode Materials for Safe Lithium-Ion Batteries.* Advanced Functional Materials, 2013. **23**(8): p. 959-969.
146. Ohzuku, T., *Zero-Strain Insertion Material of Li, $Li_{1/3}Ti_{5/3}O_4$ for Rechargeable Lithium Cells.* Journal of The Electrochemical Society, 1995. **142**(5): p. 1431.
147. Bresser, D., et al., *The importance of "going nano" for high power battery materials.* Journal of Power Sources, 2012. **219**: p. 217-222.
148. Senguttuvan, P., et al., *$Na_2Ti_3O_7$: Lowest Voltage Ever Reported Oxide Insertion Electrode for Sodium Ion Batteries.* Chemistry of Materials, 2011. **23**(18): p. 4109-4111.
149. Pan, H., et al., *Sodium Storage and Transport Properties in Layered $Na_2Ti_3O_7$ for Room-Temperature Sodium-Ion Batteries.* Advanced Energy Materials, 2013. **3**(9): p. 1186-1194.
150. Yan, Z., et al., *A tightly integrated sodium titanate-carbon composite as an anode material for rechargeable sodium ion batteries.* Journal of Power Sources, 2015. **274**: p. 8-14.
151. Chen, J.S., L.A. Archer, and X. Wen Lou, *SnO_2 hollow structures and TiO_2 nanosheets for lithium-ion batteries.* Journal of Materials Chemistry, 2011. **21**(27): p. 9912-9924.
152. Jang, J.-H., et al., *Understanding conversion mechanism of NiO anodic materials for Li-ion battery using in situ X-ray absorption near edge structure spectroscopy.* Journal of Power Sources, 2016. **304**: p. 189-195.
153. Matsubara, K., et al., *Enhanced conductivity and gating effect of p-type Li-doped NiO nanowires.* Nanoscale, 2014. **6**(2): p. 688-692.
154. bai, Z., et al., *Direct large-scale synthesis of 3D hierarchical mesoporous NiO microspheres as high-performance anode materials for lithium ion batteries.* Nanoscale, 2014. **6**(6): p. 3268-3273.
155. Zhang, R., et al., *Synthesis of CuO nanowire arrays as high-performance electrode for lithium ion batteries.* Materials Letters, 2015. **139**: p. 55-58.
156. Zhang, Q., et al., *In Situ Synthesis of CuO and Cu Nanostructures with Promising Electrochemical and Wettability Properties.* Small, 2014. **10**(5): p. 935-943.
157. Chen, C., et al., *Controllable synthesis of Cu-doped CoO hierarchical structure for high performance lithium-ion battery.* Journal of Power Sources, 2016. **314**: p. 66-75.
158. Cao, K., et al., *Ultra-High Capacity Lithium-Ion Batteries with Hierarchical CoO Nanowire Clusters as Binder Free Electrodes.* Advanced Functional Materials, 2015. **25**(7): p. 1082-1089.
159. Binitha, G., et al., *3D Interconnected Networks of Graphene and Flower-Like Cobalt Oxide Microstructures with Improved Lithium Storage.* Advanced Materials Interfaces, 2016. **3**(1): p. 1500419.
160. Deng, Y., et al., *Recent advances in Mn-based oxides as anode materials for lithium ion batteries.* RSC Advances, 2014. **4**(45): p. 23914-23935.
161. Cao, K., et al., *Reconstruction of Mini-Hollow Polyhedron Mn_2O_3 Derived from MOFs as a High-Performance Lithium Anode Material.* Advanced Science, 2016. **3**(3): p. 1500185.

162. Zhong, K., et al., *MnO powder as anode active materials for lithium ion batteries.* Journal of Power Sources, 2010. **195**(10): p. 3300-3308.
163. Pelliccione, C.J., et al., *In Situ XAFS Study of the Capacity Fading Mechanisms in ZnO Anodes for Lithium-Ion Batteries.* Journal of The Electrochemical Society, 2015. **162**(10): p. A1935-A1939.
164. Zhang, L., H.B. Wu, and X.W. Lou, *Iron-Oxide-Based Advanced Anode Materials for Lithium-Ion Batteries.* Advanced Energy Materials, 2014. **4**(4): p. 1300958.
165. Liu, J., et al., *Iron Oxide-Based Nanotube Arrays Derived from Sacrificial Template-Accelerated Hydrolysis: Large-Area Design and Reversible Lithium Storage*. Chemistry of Materials, 2010. **22**(1): p. 212-217.
166. Chen, J.S., et al., *Top-Down Fabrication of α-Fe_2O_3 Single-Crystal Nanodiscs and Microparticles with Tunable Porosity for Largely Improved Lithium Storage Properties.* Journal of the American Chemical Society, 2010. **132**(38): p. 13162-13164.
167. Muraliganth, T., A. Vadivel Murugan, and A. Manthiram, *Facile synthesis of carbon-decorated single-crystalline Fe3O4nanowires and their application as high performance anode in lithium ion batteries.* Chemical Communications, 2009(47): p. 7360-7362.
168. Luo, J., et al., *Three-Dimensional Graphene Foam Supported Fe_3O_4 Lithium Battery Anodes with Long Cycle Life and High Rate Capability.* Nano Letters, 2013. **13**(12): p. 6136-6143.
169. Li, B., et al., *Superparamagnetic Fe3O4 nanocrystals@graphene composites for energy storage devices.* Journal of Materials Chemistry, 2011. **21**(13): p. 5069-5075.
170. Cheng, F., et al., *Functional Materials for Rechargeable Batteries.* Advanced Materials, 2011. **23**(15): p. 1695-1715.
171. Cheng, F., et al., *Template-Directed Materials for Rechargeable Lithium-Ion Batteries.* Chemistry of Materials, 2008. **20**(3): p. 667-681.
172. Wang, Z., et al., *Assembling carbon-coated α-Fe_2O_3 hollow nanohorns on the CNT backbone for superior lithium storage capability.* Energy and Environmental Science, 2012. **5**(1): p. 5252-5256.
173. Wang, J., et al., *Nano-sized Fe_3O_4/carbon as anode material for lithium ion battery.* Materials Chemistry and Physics, 2014. **148**(3): p. 699-704.
174. He, Y., et al., *Structure and electrochemical performance of nanostructured Fe3O4/carbon nanotube composites as anodes for lithium ion batteries.* Electrochimica Acta, 2010. **55**(3): p. 1140-1144.
175. Wang, L., et al., *Electrospinning synthesis of C/Fe_3O_4 composite nanofibers and their application for high performance lithium-ion batteries.* Journal of Power Sources, 2008. **183**(2): p. 717-723.
176. Wu, C., et al., *Synthesis of Hematite (α-Fe_2O_3) Nanorods: Diameter-Size and Shape Effects on Their Applications in Magnetism, Lithium Ion Battery, and Gas Sensors.* The Journal of Physical Chemistry B, 2006. **110**(36): p. 17806-17812.
177. Liu, H., et al., *Electrochemical performance of α-Fe2O3 nanorods as anode material for lithium-ion cells.* Electrochimica Acta, 2009. **54**(6): p. 1733-1736.
178. Song, Y., et al., *Large-Scale Porous Hematite Nanorod Arrays: Direct Growth on Titanium Foil and Reversible Lithium Storage.* The Journal of Physical Chemistry C, 2010. **114**(49): p. 21158-21164.
179. Lin, Y.-M., et al., *α-Fe_2O_3 Nanorods as Anode Material for Lithium Ion Batteries.* The Journal of Physical Chemistry Letters, 2011. **2**(22): p. 2885-2891.
180. Cherian, C.T., et al., *Electrospun α-Fe_2O_3 nanorods as a stable, high capacity anode material for Li-ion batteries.* Journal of Materials Chemistry, 2012. **22**(24): p. 12198-12204.
181. Liu, H., D. Wexler, and G. Wang, *One-pot facile synthesis of iron oxide nanowires as high capacity anode materials for lithium ion batteries.* Journal of Alloys and Compounds, 2009. **487**(1): p. L24-L27.
182. Chen, J., et al., *α-Fe_2O_3 Nanotubes in Gas Sensor and Lithium-Ion Battery Applications.* Advanced Materials, 2005. **17**(5): p. 582-586.
183. Wang, Z., et al., *α-Fe_2O_3 nanotubes with superior lithium storage capability.* Chemical Communications, 2011. **47**(28): p. 8061-8063.
184. Wu, M.-S., Y.-H. Ou, and Y.-P. Lin, *Iron Oxide Nanosheets and Nanoparticles Synthesized by a Facile Single-Step Coprecipitation Method for Lithium-Ion Batteries.* Journal of The Electrochemical Society, 2011. **158**(3): p. A231.
185. Jang, B., et al., *Direct Synthesis of Self-Assembled Ferrite/Carbon Hybrid Nanosheets for High Performance Lithium-Ion Battery Anodes.* Journal of the American Chemical Society, 2012. **134**(36): p. 15010-15015.
186. Reddy, M.V., et al., *α-Fe_2O_3 Nanoflakes as an Anode Material for Li-Ion Batteries.* Advanced Functional Materials, 2007. **17**(15): p. 2792-2799.

187. Chun, L., et al., *Hematite nanoflakes as anode electrode materials for rechargeable lithium-ion batteries.* Electrochimica Acta, 2010. **55**(9): p. 3089-3092.
188. Lei, D., et al., *α-Fe_2O_3 nanowall arrays: hydrothermal preparation, growth mechanism and excellent rate performances for lithium ion batteries.* Nanoscale, 2012. **4**(11): p. 3422-3426.
189. Wu, X.-L., et al., *α-Fe_2O_3 Nanostructures: Inorganic Salt-Controlled Synthesis and Their Electrochemical Performance toward Lithium Storage.* The Journal of Physical Chemistry C, 2008. **112**(43): p. 16824-16829.
190. Zhang, P., Z.P. Guo, and H.K. Liu, *Submicron-sized cube-like α-Fe_2O_3 agglomerates as an anode material for Li-ion batteries.* Electrochimica Acta, 2010. **55**(28): p. 8521-8526.
191. Duan, X., et al., *Facet-induced formation of hematite mesocrystals with improved lithium storage properties.* Chemical Communications, 2012. **48**(100): p. 12204-12206.
192. Wang, J., et al., *Three-Dimensionally Mesostructured Fe_2O_3 Electrodes with Good Rate Performance and Reduced Voltage Hysteresis.* Chemistry of Materials, 2015. **27**(8): p. 2803-2811.
193. Xiao, H., et al., *Template-free synthesis of hollow α-Fe_2O_3 microcubes for advanced lithium-ion batteries.* Journal of Materials Chemistry A, 2013. **1**(6): p. 2307-2312.
194. Xu, S., et al., *α-Fe_2O_3 multi-shelled hollow microspheres for lithium ion battery anodes with superior capacity and charge retention.* Energy & Environmental Science, 2014. **7**(2): p. 632-637.
195. Zhang, L., et al., *Porous Fe_2O_3 nanocubes derived from MOFs for highly reversible lithium storage.* CrystEngComm, 2013. **15**(45): p. 9332-9335.
196. Han, Y., et al., *Preparation and electrochemical performance of flower-like hematite for lithium-ion batteries.* Electrochimica Acta, 2011. **56**(9): p. 3175-3181.
197. Zeng, S., et al., *Facile Route for the Fabrication of Porous Hematite Nanoflowers: Its Synthesis, Growth Mechanism, Application in the Lithium Ion Battery, and Magnetic and Photocatalytic Properties.* The Journal of Physical Chemistry C, 2008. **112**(13): p. 4836-4843.
198. Ma, X.-H., et al., *Facile synthesis of flower-like and yarn-like α-Fe_2O_3 spherical clusters as anode materials for lithium-ion batteries.* Electrochimica Acta, 2013. **93**: p. 131-136.
199. Banerjee, A., et al., *Superior lithium storage properties of α-Fe_2O_3 nano-assembled spindles.* Nano Energy, 2013. **2**(5): p. 890-896.
200. Lee, S.H., et al., *Self-Assembled Fe_3O_4 Nanoparticle Clusters as High-Performance Anodes for Lithium Ion Batteries via Geometric Confinement.* Nano Letters, 2013. **13**(9): p. 4249-4256.
201. Wang, B., et al., *Self-Supported Construction of Uniform Fe_3O_4 Hollow Microspheres from Nanoplate Building Blocks.* Angewandte Chemie International Edition, 2013. **52**(15): p. 4165-4168.
202. Ma, F.-X., et al., *Formation of Uniform Fe_3O_4 Hollow Spheres Organized by Ultrathin Nanosheets and Their Excellent Lithium Storage Properties.* Advanced Materials, 2015. **27**(27): p. 4097-4101.

Chapter 2 Characterization Techniques

"We never know how good something is, until we know what it is capable of". The same situation also applied in this thesis. Every samples which we produce, should pass the process of characterization and this work is no exception. Naturally in thin films-related work, the microstructure is important. Thus, the Chapter begins with detailed information on how we can see the microstructure of the thin films, (even what components made the microstructure) by two common electron microscopy methods, namely scanning electron microscopy and transmission electron microscopy. This is followed by characterization techniques that allow us to "touch" and reveal the state of nanoscale surface, that is, X-ray diffraction, X-ray photoelectron spectroscopy, Raman spectroscopy, glow discharge optical emission spectroscopy and time of flight-secondary ion mass spectroscopy. Later on, in this Chapter, I will introduce one of the main characterization techniques used in photocatalysis and lithium ion batteries-related studies, as well as specific and detailed descriptions of the measurement setups used throughout the project.

2.1. Morphological Characterization

Conventional optical microscopy have an usage limit, which unable to investigate image smaller than ordo micron due to diffraction of light comes into play, thus the image cannot be focused to a point in the optical microscopy [1]. To overcome this problem, the use radiation with substantially shorter wavelength is needed. Electrons are the perfect choice as a probe, due to its dual wave-particle enables their usage as "light" in microscopy. There are two basic types of electron microscopy: Scanning Electron Microscopy (SEM) and Transmission Electron Microscopy (TEM).

2.1.1 Scanning Electron Microscopy

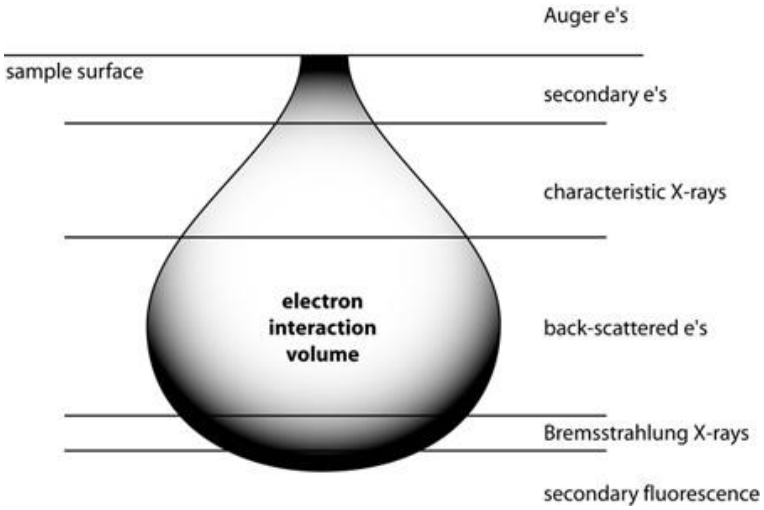

Figure 2.1 Generation of electrons and X-rays as a result of electron beam-solid interactions [2].

Scanning electron microscope (SEM) is a powerful instrument for the examination and analysis of the microstructure characteristics of materials surface. As its name says, the SEM produces the image by scanning the electron beam across the specimen point by point. In the imaging system there is a deflection system which causes the beam to move to a series of discrete locations along a line and then along another line below the first, and so on, until a rectangular "raster" is generated on the specimen. With a small electron probe, the investigation of a small area of material can be performed. Basically, a SEM consists of an electron gun, lens system, electron collector, visual and recording in computerized. The electron gun, located on the top of the column, generates and accelerates electrons to energies in the range of 0.1 – 30 kV. There are several types of electron guns normally used: thermionic emitters (made of tungsten and LaB_6), cold and thermal or Schottky field emitters. The field emitters are being used especially in the modern SEMs due to their enhanced performance, reliability and lifetime.

Upon the bombardment, the electron beam-solid interactions produce various kinds of excitations, as shown in Figure 2.1, secondary electrons, backscattered electrons, Auger electrons, as well as X-rays. These different excitations, which can be detected by a state-of-the-art SEM's different types of detectors and analyzers. As imaging modes are concerned, only secondary electron and backscattered electron signals contain information about topography. The two, however, originate from different process and have different energies. Thus, they are captured using different detectors and carry different information.

Primary electrons, the electrons bombarding the sample, may lose some of their energy upon colliding and interacting with the sample. This process is known as inelastic scattering and occurs by interaction with electrons of the sample. From the principle of conservation of energy, the energy lost from the primary electrons will be compensated as a "gain" in energy of the electrons of the sample. If these are the outer-shell electrons, weakly bound to an atomic nucleus, most of the energy will be retained as kinetic energy, allowing the electrons to escape and travel through the solid as secondary electrons (SE). SE typically have kinetic energies of less than 100 eV and the average distance they can travel in the solid is limited to just one or two nm. This property provides excellent information about the surface structure as the secondary electrons that can be detected have to be created very close to the surface. Secondary electrons are thus able to produce the so-called topographical contrast of the samples studied.

Backscattered electrons (BSE), on the other hand, are elastically scattered primary electrons. Hence, BSE escape from the sample with energies only slightly smaller than the primary electron energy (i.e. higher energy than SE). Since elastic scattering is strongly dependent on the details of atoms the electrons collide with (e.g. atomic mass, crystal orientation, defects etc.), BSE can provide information about microstructural parameters of materials. For typical use of SEM, BSE offer good composition contrast if different chemical elements are present in a sample. Together, BSE and SE can be used interchangeably in an SEM to obtain topographical information complemented with some compositional information.

The interaction of primary electrons and the sample also creates the emission of X-rays resulting from electronic shell transitions in the sample (Figure 2.2). The emitted X-rays, which may originate from several microns deep within the sample, carry energy characteristics of the element emitted from (i.e. every element has its own set of characteristic peaks in its X-ray emission spectrum). Thus, detection and measurement of these energies permits quantitative elemental analysis known as energy dispersive X-ray spectroscopy (EDS).

SEM has been an instrumental tool for the work presented in this thesis. While the charging effect by itself is not damaging the sample, it nonetheless creates distorted and poor resolution images due to the built-up of electrons on the surface, creating an electric field, which in turn deflects the incoming electron beam in undesirable ways.

2.1.2 Electron Backscatter Diffraction (EBSD)

Rich information provided by BSE outlined above spurred a class of techniques called electron backscatter diffraction (EBSD) [3]. Specifically, EBSD is employed to characterize microstructural-crystallographic parameters in bulk materials such as crystal orientation, grain morphology and defects. A bulk material is crucial for EBSD to provide a high enough number of scattered electrons to be detected. In EBDS, a tilted sample is irradiated with a beam of electrons which interact with the atoms in the crystal lattice. Some of the BSE leave at the Bragg condition from the sample crystal planes and form the so-called Kikuchi patterns as shown on Figure 2.2. These patterns relate to each of the diffracting planes in the lattice and thus a crystal orientation map can be constructed [4]. This map provides essential information of the crystalline state of the sample, such as grain orientation and grain boundaries.

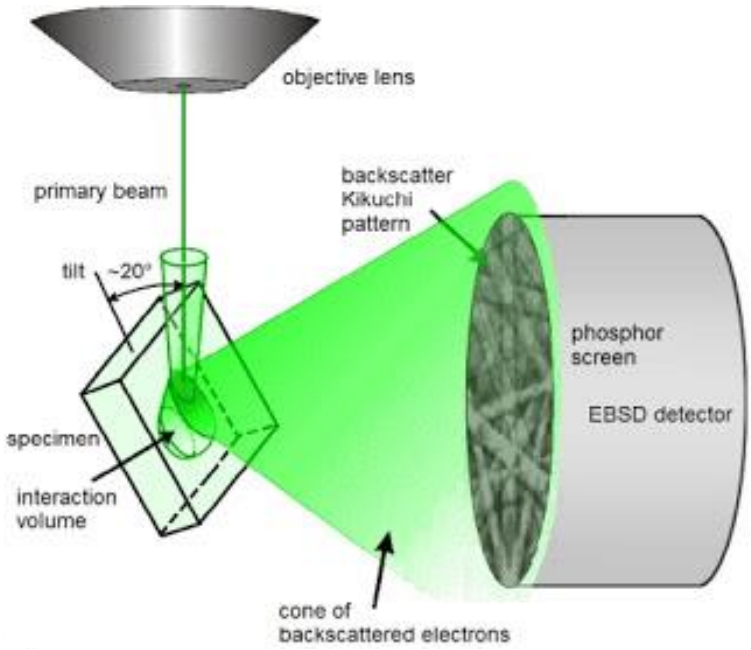

Figure 2.2 Kikuchi diffraction in the SEM [5].

In this thesis, Backscatter Kikuchi Diffraction (BKD) is employed to reveal the microstructural details of the single crystal bulk iron studied in Chapter 3. Specifically, determination of the orientation after mechanical polishing and electropolishing was conducted.

2.1.3 Cross Sectional TEM sample preparation: Focused Ion Beam (FIB)

The focused ion beam (FIB) techniques are most powerful sample preparation for TEM observation; which required very thin specimens to be investigated. Below 100 nm thick; on the term of "electron transparent" is essential. FIB allows to produce a very large thin area; FIB also allows us to select the target area very precisely. Compared to other methods, FIB preparation is fast and reliable. Last but not least, the FIB preparation techniques are virtually independent from the nature of the material, which means that most materials including ceramics, metals or even biological materials, can be prepared using this technique. With all those advantages, FIB preparation techniques have become the most powerful TEM sample preparation techniques over the last two decades. Nowadays FIB techniques can be used not only as preparation tools but also make material and failure analysis of isolated, sub-micron electrically tested structures possible.[6, 7]

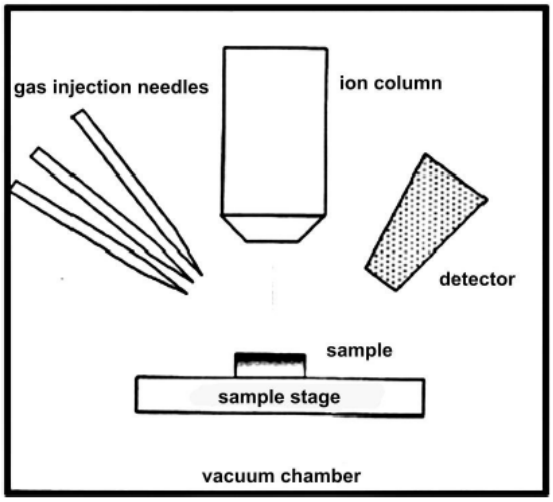

Figure 2.3 Schematic diagram of the FIB instrument [8].

As shown if Figure 2.3, the conventional FIB instrument consists of a vacuum system and a chamber, a liquid metal ion source (normally gallium), an ion column, a sample stage, detectors, gas delivery system, and a computer to run the complete instrument. A gallium (Ga) reservoir is positioned in contact with a sharp Tungsten (W) needle, later on the gallium wets the tungsten needle tip. A high extraction field more than10^8 V/cm, is used to pull the liquid gallium into a sharp cone about 5-10 nm radius size. Finally, ions are emitted as a result of field ionization and post-ionization and then accelerated down the FIB column [9]. As source, this liquid metal ion source (LMIS) of

Ga is used because of two advantages: (i) it has a low melting point therefore the liquid state may exist near room temperature, and (ii) it can be focused to a very small probe size (<10nm in diameter).

Conventional and lift out techniques are two common FIB-based sample preparation techniques. In the conventional technique, the specimens are picked up from the bulk specimen and then mounted on a cross section of Cu plate. Afterwards, it can be thinned and used as TEM specimens. Detailed explanation about conventional methods can be found in [10]. On the other hand, in the lift out technique the specimens will be milled to an electron-transparent membrane, and later on the membrane will be attached to a TEM grid using a manipulator. There are also two additional sub-techniques, ex-situ and in-situ lifts out. In the ex-situ lift out technique, the attachment process is done outside the FIB instrument while in the latter technique, it is done inside the FIB instrument [11-14].

All TEM specimens in this study were prepared by in situ lift out technique using a Hitachi FB-2100 focused ion beam (FIB) system employing a Ga^+ ion beam. The process consisted of two steps; milling the specimens and re-thinning the attached lamella at TEM grid. The samples were first covered by carbon and platinum and in the FIB chamber it was covered by tungsten to protect the surface layer of the specimens from Ga ion bombardment. Next, the lamella was cut trace by trace on both sides. After the lamella reached a thickness of about 500 nm, it was cut on the bottom and both left and right sides. At the right and the left sides small parts of the area were left to make sure the lamella was still fixed by the bulk specimen. The lamella was then tilted for 15^o by the user and one side of the lamella is attached to a micromanipulator. The lamella was made completely free from the bulk specimens by cutting all of the rest connected side and was attached to the micromanipulator to be transported to the TEM grid later on. In the second process, the lamella was attached to TEM grid, which is normally made of copper or molybdenum. Afterwards, the lamella was thinned on both sides until the thickness is less than 100 nm.

2.1.4 Transmission Electron Microscopy (TEM)

As seen in Figure 2.4, electrons which pass through the specimen can be used in investigations [15] by TEM. Back in 1932, the first TEM was developed by Knoll and Ruska and four years later the first commercial TEM was developed by Siemens and Halske in Germany in 1936. After World War II, TEMs have become widely available from several commercial companies, namely Siemens, Zeiss, Hitachi, JEOL, Philips (now FEI) and RCA.

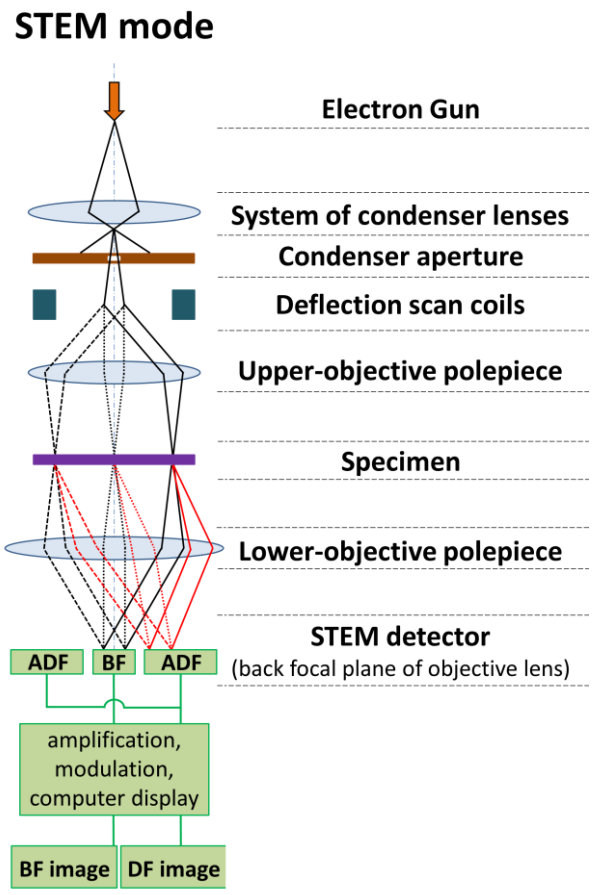

Figure 2.4 Schematic drawing of a TEM with STEM capability [15].

A conventional TEM consists of an electron source, illumination system, specimen stage, imaging system, projection system and viewing screen to view the image. Furthermore, a modern TEM is equipped with analytical equipments such as energy dispersive X-rays and electron energy-loss spectroscopy. There are three types of electron emission guns in TEMs; thermionic, Schottky and field emission. In conventional TEM instruments, two-three condenser lenses (C1, C2) are located above the specimen. In normal TEM mode, those lenses are adjusted to illuminate the specimen with a parallel beam. Below the specimen, an objective lens will form images and also diffraction

patterns. The next lens is an intermediate lens which is important to produce either the diffraction pattern or an image on the viewing screen. Since electrons cannot be “seen”, a viewing screen, normally coated with a material such as ZnS will translate electron intensity to light intensity ($\lambda \approx 550$nm). Furthermore, both the diffraction patterns and images, can be recorded onto photographic emulsion or Charge-Coupled Device (CCD) cameras with high sensitivity, which are available nowadays.

Two conventional imaging techniques in TEM are the bright-field (BF) and the dark-field (DF) imaging. Both transmitted and diffracted beam will make contrast. This condition rises because the diffracted intensity recombines with the transmitted intensity at the viewing screen and produces contrast. When the objective aperture is used to block all diffracted beam and allow only the direct transmitted beams, the BF image will be formed. When the direct transmitted beams are tilted and the objective aperture is used to block it, the formed image is called as the DF image (Figure 2.5).

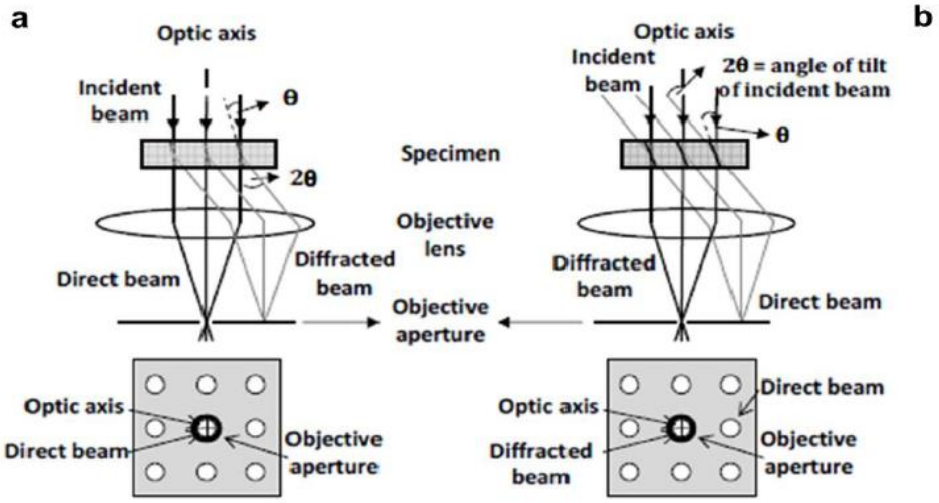

Figure 2.5 Condition for (a) bright- and (b) dark-field imaging [16].

2.1.5 Scanning Transmission Electron Microscopy (STEM) and Energy Dispersive X-Ray (EDX) Analysis

A modern TEM can also have scanning capability, known as scanning TEM (STEM), which allows the specimen to be scanned point by point with a small probe of electrons. In order to obtain a small probe with a diameter of ≈ 0.2–5 nm, a large aperture angle α must be used. Two additional pairs of scan coils below the condenser lenses allow the raster process to be performed. Besides producing secondary electron signal, TEM can also produce bright field images, dark field and annular dark field (ADF) images. Annular detector is positioned below the specimen that will collect electrons diffracted in large angles allow to present variety mode (see Fig. 2.6).

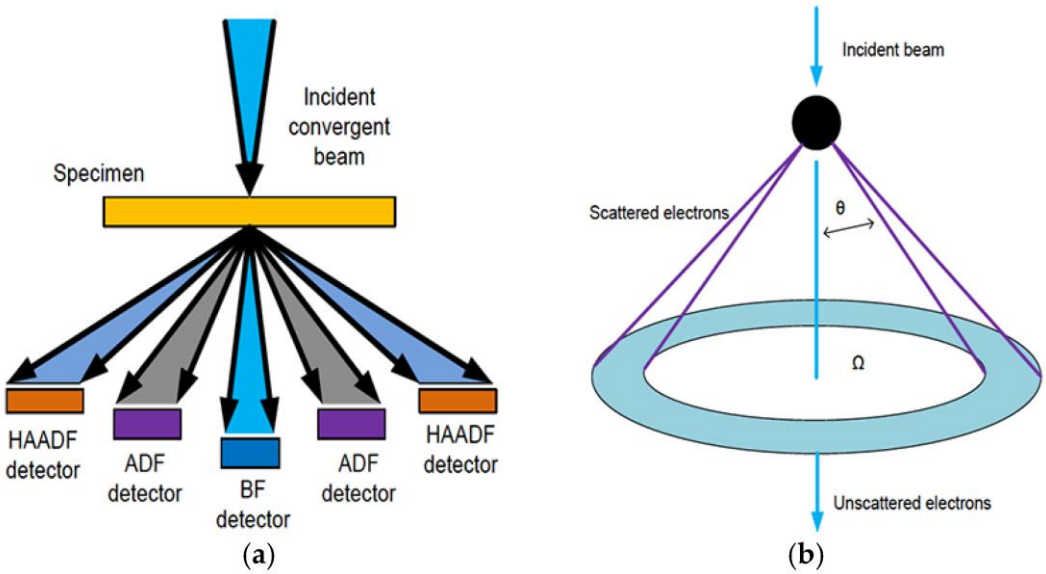

Figure 2.6 (a) Schematic of the HAADF, conventional annular dark-field (ADF) and BF detectors in a STEM; and (b) electron scattering by a single isolated atom in STEM [17].

The strong Coulomb interaction of the negatively charged electrons with the positive potential of an atom core, leads to high angle scattering as described in Rutherford scattering as follow:

$$\frac{d\sigma(\theta)}{d\Omega} = \frac{e^4 Z^2}{16(E_o)^2 \sin^4\frac{\theta}{2}} \tag{2.1}$$

where,

$\frac{d\sigma(\theta)}{d\Omega}$ = differential scattering cross sections as a function of scattering angle

E_o = incident beam energy

e = electron charge

Z = atomic number of the scattering nucleus

As seen in Eq. 2.1, these diffracted electrons are very sensitive to increasing Z (atomic number) and the contrast is approximately proportional to Z^2. Based on that formula, heavier elements will be brighter in ADF STEM images compared to the lighter elements. This effect is even more pronounced when the electrons are diffracted in a very large angle (>50 mrad). The technique is known as high-angle annular dark-field or HAADF imaging, or Z-contrast imaging, which has been introduced by Crewe and co-workers [18].

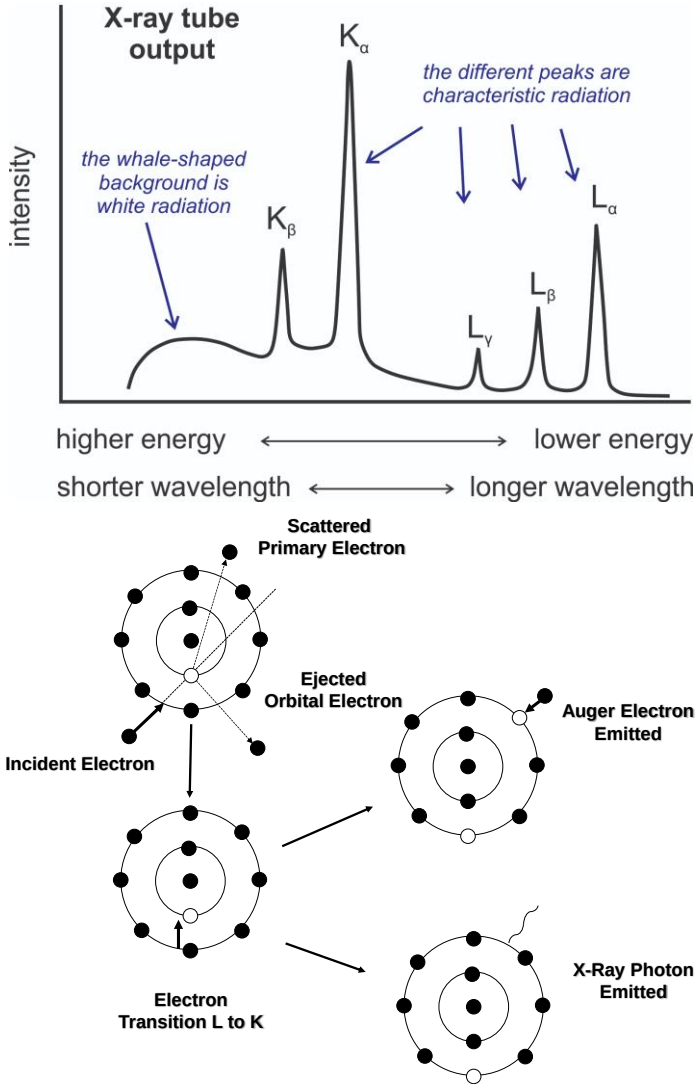

Figure 2.7 Characteristic X-ray and excitation process [19].

The electron beam also generates X-rays photons in the beam-specimen interaction, which have energies characteristic for each element in the specimen and can be used in STEM analysis (Figure 2.7). These characteristic X-rays are emitted from inner shell electrons of a specimen atom. They are referred to as characteristic X-rays since the energy of an emitted X-ray is related to the energy differences between the sharply defined levels of the atom. When the beam electron interacts with an inner-shell electron, it knocks out the bound electron, which leaves the atom in an excited state with a hole in the electron shell. During subsequent deexcitation, an electron transition involves a change in energy, and the energy released from the atom can manifest itself either in the form of an X-ray or an ejected (Auger) electron. These X-rays will be captured by energy-dispersive spectrometers (EDS). These spectrometers use lithium-drifted silicon Si (Li) solid state X-ray detectors or intrinsic or high-purity Ge (HPGe) EDS detectors. A detailed explanation about the principle of EDS can be found in literature [20]. In this study, STEM and EDX observation were carried out using JEOL, JEM-ARM200F scanning transmission electron microscope (STEM) with energy dispersive X-ray spectrometry (EDS) facilities at the Research Institute for Electronic Sciences, Hokkaido University, Japan.

2.1.6 High Resolution Transmission Electron Microscopy

By definition, high-resolution transmission electron microscopy (HRTEM) is one of imaging mode of the TEM; which allows the imaging of the crystallographic structure of a sample at an atomic scale. In contrast to the conventional imaging mode in CTEM which relies on a diffraction contrast, the image formation in HRTEM relies on phase-contrast resulting from an interference of several beams. In this case, to understand the image formation and the interpretation of the object structure on the atomic scale, one needs to understand the interactions of the electron beam with the crystal, the influenced of the lens aberrations and the wave transferred by microscope.

As mentioned before, the image formation in a high-resolution electron microscope is an interference phenomenon. A parallel, coherent incident beam is diffracted by the thin crystal placed in the object plane of the objective lens. The aberrations of real lenses deform the electron waves and decrease the resolution of the microscope. These aberrations are defocus, spherical aberration, chromatic aberration, astigmatism and coma.

Besides receiving detailed crystallite structure in atomic scale such as defects, grains and crystal growth, the high resolution TEM image can also be used to inform the exact positions of atomic columns with respect to black and white contrast on the micrograph. But unfortunately, the direct interpretation is possible only where the final image correspondence to the projected potential of the whole specimen. In real crystal, the interaction of the crystal with the incident electron beam and also the transfer of the intensity of the image are not linear.

The position of the maxima and minima of interference with respect to the atomic columns depends on the crystal thickness and on the defocus of the objective lens, in which both values are often very difficult to determine. To overcome that problem, creating model of the corresponding crystal and simulating its interaction with the electrons and obtaining the wave function emerging from the crystals are necessary. Later, the image of this wave function is calculated and compared to the result form the experimental micrograph. Detailed explanation about the high resolution TEM can be found in the literatures [21-23].

2.2. Analytical Composition

2.2.1 X-ray Diffraction

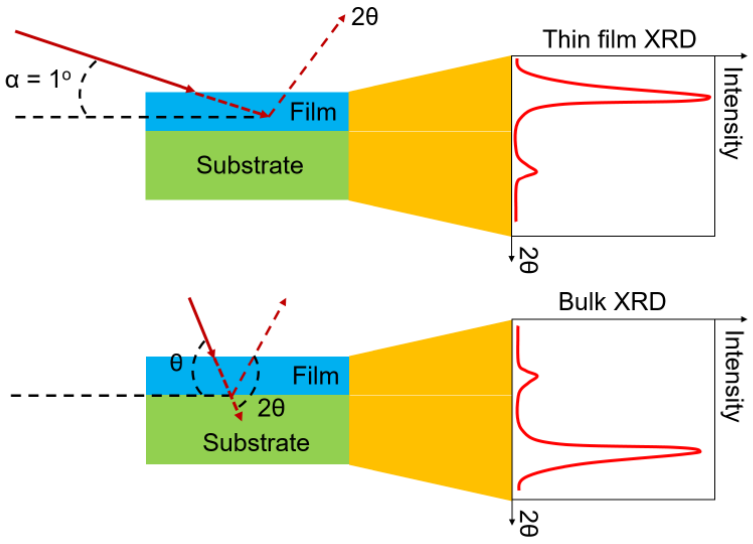

Figure 2.8 Schematic diagram illustrating the glazing incidence and bulk modes of X-ray diffraction measurements [24].

The phases in the anodic films were identified by a Rigaku, RINT-2000 X-ray diffractometer using Cu Kα irradiation (λ = 0.15418 nm). The diffraction occurs only under conditions of constructive interference when Bragg's law is satisfied. In bulk XRD

mode, also known as θ-2θ or Bragg-Brentano geometry, the incident angle of X-ray onto the specimen surface is maintained at the same angle as the detecting angle. However, this mode produces a weak signal from a surface thin film and the intense signal from the substrate. For the analysis of thin anodic films in this study, grazing incidence XRD (GIXRD) was used to minimize the contribution of the substrate material, in which the incidence angle (alpha) is fixed at a small value and only the detecting angle (2θ) was varied. Fig. 2.8 shows the schematic of thin film and bulk modes of XRD. In the present study, both θ-2θ and α-2θ (α = 1°) modes were employed to obtain information of the individual phases within the film material. The quantitative analysis of the phases on the XRD pattern in this thesis is done using the Rietveld method on GSAS software. Rietveld refinement requires a reference structure file of the identified phase, and chi-square method were used to minimize the difference between the observed pattern and calculated profiles. During the fitting, the phase weight can be calculated by modifying values of scale factors, number of formula units per unit cell, and the unit cell volume [25].

2.2.2 X-Ray Photoelectron Spectroscopy (XPS)

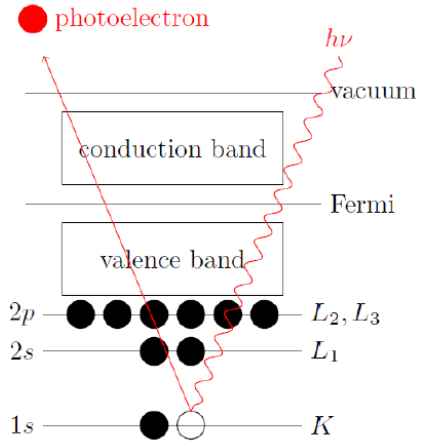

Figure 2.9 XPS photoelectron mechanism [26].

X-ray photoelectron spectroscopy (XPS) relies on the photoelectric effect to reveal the surface chemistry of a sample. When electrons are emitted by a material that irradiated by photons it can produce photoelectric effects. In a typical experiment, X-rays with specific energy (e.g. Mg Kα with energy of 1253.6 eV) are used to irradiate the sample. As the photons interact with the material, energy is transferred from the photons to the electrons in the material. If the energy is sufficient to overcome the binding energy, electrons will be emitted from the material. These electrons are called photoelectrons (Figure 2.9), whose kinetic energies can be described by:

$$E_{kin} = h\nu - E_{bind} - \emptyset_s \quad (2.2)$$

where $h\nu$ is the energy of the photon, E_{bind} is the binding energy of the photoelectrons and $\emptyset_s$ is the spectrometer work function which is defined by the spectrometer used. As the mean free path of photoelectrons is very short, only a small portion of them, i.e. the ones originating from the top-most layer of the material being analyzed, can exit the material and reach the detector without further energy loss. Thus, XPS is a very surface sensitive technique. XPS spectra can then be constructed by plotting the energy and number of electrons emitted from the material. Since each element possesses its own unique set of binding energies, XPS spectra can be used to identify elements present on the surface of a material. Furthermore, the chemical state of the elements (e.g. oxidized state) can also be determined since depending on whether an element is bound to another species or not, it will possess slightly different binding energies of its electrons. This difference in energies is due to electron transfer between the different species, which depends on their relative electron affinities. Finally, a relative elemental quantification can also be obtained by integrating the area of different peaks in the spectrum. The unique surface elemental information provided by XPS is valuable especially for the oxides grown on alloy systems, (see Chapter 4). The XPS analysis presented in this thesis was carried by our collaborator form Warsaw University.

2.2.3 Raman Spectroscopy

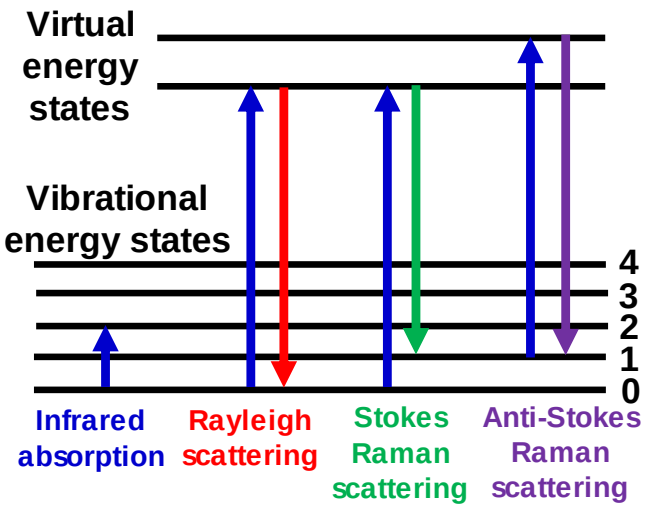

Figure 2.10 Energy level diagram showing the states involved in Raman signal [27].

Raman spectroscopy is the technique to observe rotational, vibrational, and other lower frequencies modes in system. This spectroscopy relies on inelastic scattering and/or Raman scattering of monochromatic light, from visible, near infrared or near ultraviolet laser. The laser interacts with molecular vibration, phonon or other excitation in the system; results on the shifted of energy of the laser photon to up or down. The energy shifting gifts the information about the vibrational mode in the system. Infrared spectroscopy yields similar, but complementary information. Raman spectroscopy is more often used in chemistry field, because of the vibrational information give specific chemical bond and symmetry of molecule.

The Raman effect occurs when light infringed upon molecule and interacts with the electron cloud and the bonds of the molecule. For the spontaneous Raman effect, a photon will excite the molecule from the ground state to a virtual energy state. When the molecule relaxes, the molecule will emit a photon and returns to a different state. The energy differences between the original state and the new state undergo to shift the emitted photon's frequency away from the excitation wavelength. If the new vibrational state of the molecule is more energetic than the initial state, the emitted photon will be shifted to the lower frequency for the total energy of the system to remain balanced. The frequency shifted is labelled as a Stokes shift. On the contrary, anti-Stokes shift is labeled from the emitted photon shifting to higher frequency, due to less energetic of final vibrational state than the initial state. (Figure 2.10) Raman scattering is an example of an inelastic scattering because of the energy transfer between the photons and the molecule during their interaction. Molecular polarization potential changed or the deformation of the electron cloud on the vibrational coordinate is required to exhibit the Raman effect. The Raman scattering intensity is determined by amount of polarization change, while the pattern of shifted frequency is determined by rotational and vibrational states of the samples. [28, 29] The Raman spectra in this study were collected at Faculty of Engineering, Hokkaido University, using Horiba XploRA Raman microscope (Kyoto, Japan); equipped with an Olympus microscope (Tokyo, Japan).

2.2.4 Glow Discharge Optical Emission Spectrometry (GDOES)

Glow discharge optical emission spectroscopy (GDOES) is the technique to for the depth profiling of thin films. The rapid analysis without using an ultrahigh vacuum, high sensitivity to all elements of periodic table including hydrogen, high accuracy, and excellent depth resolution allow us to obtain the information from nanometers to the few

micrometers of film materials. GDOES has also proven its capability of rapid analysis of film thickness from a few nanometers up to several hundred micrometers, being suitable for depth profile analysis of both barrier-type and porous type anodic films.

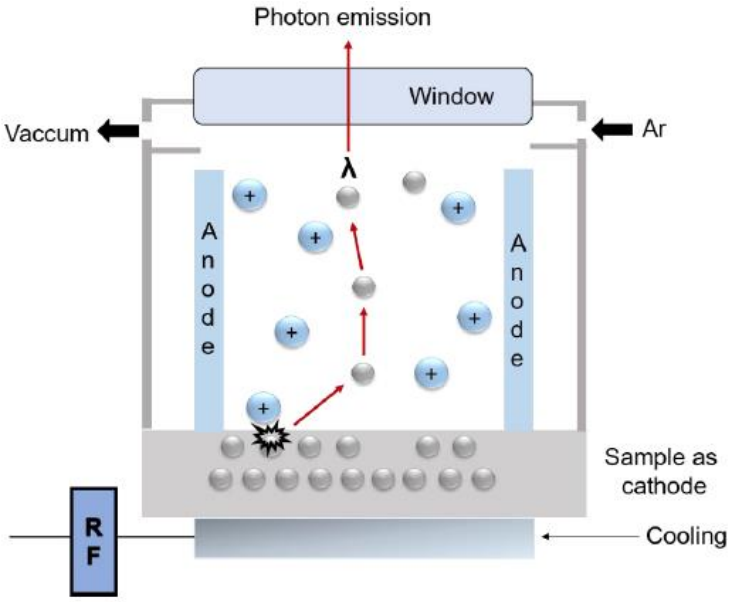

Figure 2.11 Schematic diagram illustrating GDOES sputtering and emission process [25].

A schematic illustration of GDOES process is shown in Fig. 2.11. When a voltage applied in GDOES, electrons are accelerated toward the anode and then they collide with gas atoms (Ar/Ne). The energy from the collisions were remove the electron from the gas atoms, and generated ions are accelerated toward the samples as cathode. These ions impinge the surface of the samples and sputtered the sample atoms from the surface. The sputtered atoms then diffuse into the excitation regions of the plasma where they can undergo excitation via some collisional processes, and then the photons can be detected with optical emission spectrometry. This study uses Jobin-Yvon 5000 RF GDOES instrument for depth profile analysis. The RF power of 13.56 MHz and 35 W was used for elemental depth profile analysis of anodized films formed on iron at various water concentrations. It is well known that fluorine atomic lines (F-I) as well as ionic lines (F-II) are hardly observed in the argon-glow discharge plasma, whereas they can be emitted by using neon plasma [30]. Therefore, porous anodic films on bulk iron were sputtered in a neon atmosphere of 1100 Pa to excite the most intense fluorine line of 685.6 nm instead of normally used argon gas when depth profile of fluorine was needed at a power of 50 W, with a data acquisition time of 0.05s. A copper anode of 4 mm diameter and a polychromator was employed for the detection of emission intensity from the sputtered elements.

2.2.5 Time of Flight – Secondary Ion Mass Spectroscopy (ToF-SIMS)

Time of Flight (ToF)- Secondary ion mass spectrometry (SIMS) was first introduced in the 1980s [31]. 60 years ago, the SIMS technique was first used to analyze oxides and metals. As reviewed by Benninghoven et al. (1987) [32], The use of ToF technique was to provide spatially resolved information on the SIMS as an ion-optical collection system to preserve the spatial relationship of the desorbed ions. Nowadays, the SIMS technique has been improved extensively and can be used in various kind of operational modes [33-35].

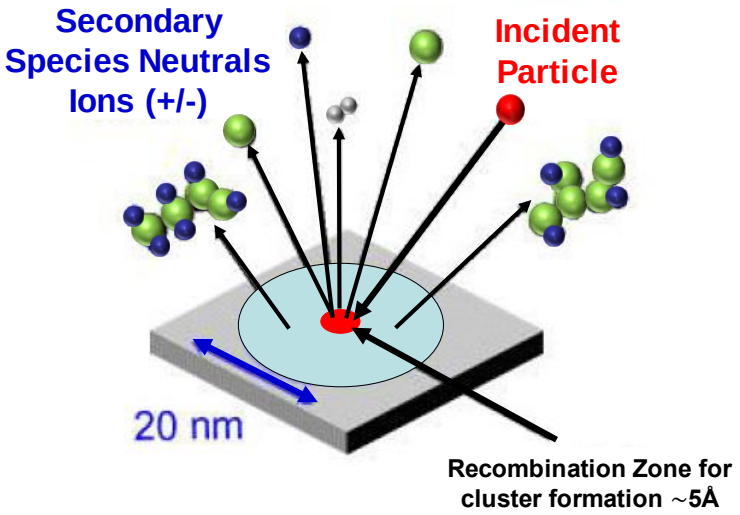

Figure 2.12 Schematic representation of secondary ion generation [36].

SIMS is a technique that analyzes ejected ions from the surface of sample material by energetic ion bombardment. The SIMS technique uses focused ion beam of primary ions which impinge upon the surface. The atomic collisions transfer the primary ions energy to the target atoms, so that a collision cascade occurs. And then, the primary ions set an atom in motion, both by direct or indirect collisions of atoms in motion with other target atoms (Figure 2.14). The energy produced is transferred back to the surface which allows surface atoms and molecules of approximately the top 2-3 molecular layers to overcome their surface binding energy [37]. The sputtered atoms or molecules from the target surface are named as the secondary ions. Secondary ions come off neutrally charged, however a small portion generated can be ionized, which subsequently analyzed as positive or negative ions. Depending on the ion mass to charge ratio m/z, dynamic and static mode SIMS can be introduced. Static SIMS is performed with low primary ion doses, while dynamic SIMS is performed at high primary ion doses. Approximately

below 1% of the top monolayer is impacted by primary ions on static SIMS, to produce elemental or molecular distribution of secondary ions. The principle of Time of Flight (ToF) mass analysis mass spectrometry is based on the fact that ions with different masses travel with different velocities. Essentially, desorbed secondary ions from the target surface by energetic particle bombardment are accelerated and then the ions are traveled to the detector. The TOF analyzer separates the secondary ions from how long time it takes to travel through the length of the field free Time of Flight (ToF) tube. The time interval needed is related to the mass and charge of the accelerated secondary ions.

Normally, the lighter secondary ions are faster than the heavier ones where the mass spectrum could be recorded. The mass spectrum then used to obtain composition, distribution and molecular information of surface constituents [38]. With ToF-SIMS techniques, spatially resolved images; with a spatial resolution less than 100 nm, of molecular species with weight up to 1000 Daltons can be produced [39]. Furthermore, ToF-SIMS has so many advantages; parallel detection of multiple samples with excellent mass resolution, monolayer sensitivity and the ability to record the location of atoms and molecules, as well as the ions, lipids, and metabolites. In TOF-SIMS, the uses of pulsed primary ion beam is to achieves greater precise mass-to-charge measurements [40]. The ToF-SIMS presented in this thesis was carried out using TOF SIMS 5, ION-TOF GmbH; by our collaborator form University of Warsaw.

2.3. Photoelectrochemical Measurement

2.3.1 Photocurrent & Photodegradation Measurement

Photocurrent is the electric current which generated by a photosensitive material device such as a photovoltaic cell, photocell, photodiode, etc. upon exposure to light as a result of either photovoltaic, photoconductive or photo-emissive effect. The general physical mechanism of light sensing can be summarized as follows: the photon excites certain molecules in the sensing element; in turn, this excitation generates secondary or higher order reaction that creates free flowing electric charges. The movement of the photon-generated electrical charge under an applied electrical field is what constitutes the photocurrent. The photocurrent is directly proportional to intensity of radiation when a suitable radiation is used and can be further enhanced by internal gain due to photons and ions interaction on applied field. Photocurrent increases with accelerating potential until saturation current is reached at which the generated photocurrent is at maximum and does

not increase further with increasing accelerating potential. On the other hand, there is a retarding potential called stopping potential at which no photocurrent is generated for a given frequency of incident light rays.

2.3.2 UV-DRS Measurement

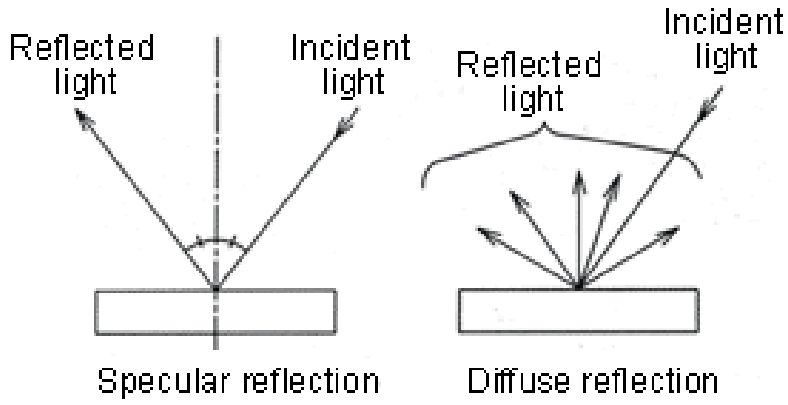

Figure 2.13 Schematic representation of reflectance measurement.

When light propagates through a material, the scattering and absorption events exist because of its constituent particles. After several scattering events, the light that exits the tissue will be nearly isotropic and is therefore considered to be diffusely reflected light. The difference between specular and diffuse reflectance is illustrated in Figure 2.13. Incoming light (black) is reflected both specularly (red) and diffusely (green). For diffuse reflectance, the source-detector separation (SDS) is defined as the distance between the incoming source beam and the point at which the diffusely reflected light is collected. We know the light cannot penetrate solid samples; however, it can be reflected on the surface of the samples. Figure 2.15 show the "specular reflection," which is attributed to the incident light reflected symmetrically to the normal, while "diffuse reflection" is attributed to the incident light scattered in different directions. Reflectance spectroscopy is almost similar to the UV/Vis spectroscopy, which use visible light to excite valence electrons to empty orbitals. UV/Vis spectroscopy technique measures transmittance of light changed as it passes through a solution, meanwhile the diffuse reflectance is measuring the relative amount of reflected light off changed of a surface. This UV DRS measurement was performed at Ohtani Lab using JASCO V-670 spectrophotometer equipped with PIN-757 integrating sphere.

2.4. Electrochemical Measurements

The electrochemical techniques used in this work are galvanostatic cycling with potential limitation (GCPL) and galvanostatic discharge-charge cycling. In this thesis, the electrochemical study was performed in two-electrode systems at a constant current density in the potential range of 2.6 - 0.01 V using PAT-Cell (EL-cell) as shown on Figure 2.14 and EC-Lab electrochemical workstation (Bio-Logic Science Instruments), respectively, with metal plate with an oxide thin film as working electrode and Li foil for a reference and counter electrodes.

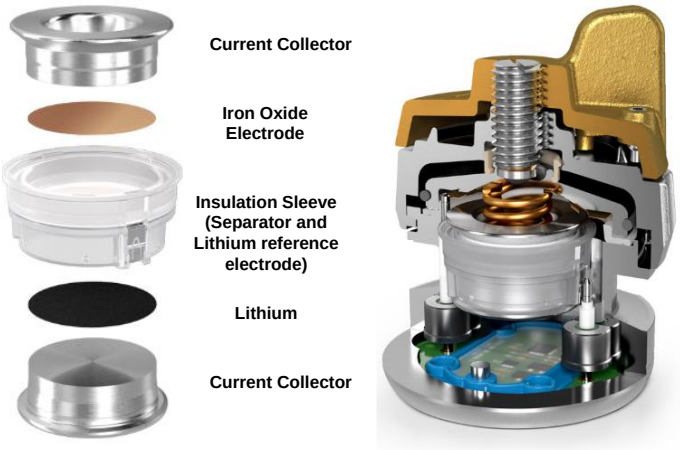

Figure 2.14. PAT-Cell core assembly [42].

In order to understand the degradation and the loss of capacity of Lithium-ion batteries, a differential capacity plot studies have been performed. The "differential capacity" curve is obtained by differentiating the capacity *Q vs.* voltage *E*. It is defined in the equation below.

$$\frac{|dQ|}{dE} = \frac{|Q_t - Q_{t-1}|}{E_t - E_{t-1}} \tag{2.2}$$

Where, Q_t, E_t are capacity and voltage values measured at a given time t. Q_{t-1}, E_{t-1} are capacity and voltage values measured at a previous time *t*-1. Differential Capacity curve can be plotted with voltage or *Q* or *vs.* other parameters. The differential capacity vs potential gives information about structural transformations during lithiation/delithiation process. The advantage of the differential capacity curve is that plateaus in the *E vs. Q* charge curve can clearly identify by the peaks in the d*Q*/d*E vs. E* curve. These peaks are associated to phase transitions of the electrode material. The cathodic and the anodic curves by differential capacity gives information about the reversibility of the electrode reaction.

Galvanostatic techniques generally apply a constant current source across the cell between working and counter electrodes and measure the potential response. Some electrochemical performances of a cell could be expressed on the galvanostatic charge-discharge curves, such as specific capacity, reaction plateau and coulombic efficiency. A charge-discharge cycle is the process of charging a rechargeable battery and discharging it as required into a load. The charge-discharge cycle is typically used to specify expected life of the batteries, as the life time is more affected by the number of charge-discharge cycles than the mere passage of time. Generally, the charge and discharge cycling number for a rechargeable battery; reflected how long does it can go through the complete process charging and discharging until its failure or starts to lose capacity. Coulombic efficiency in the other hand, describes the efficiency of electron charges transferred in a system that facilitates electrochemical reaction.

Reference:

1. Newton, R.G., *Optical theorem and beyond.* American Journal of Physics, 1976. **44**(7): p. 639-642.
2. Henry, D. *Electron-Sample Interactions*. Louisiana State University.
3. Humphreys, F.J., *Characterisation of fine-scale microstructures by electron backscatter diffraction (EBSD).* Scripta Materialia, 2004. **51**(8): p. 771-776.
4. Nishikawa, S. and S. Kikuchi, *Diffraction of Cathode Rays by Mica.* Nature, 1928. **121**(3061): p. 1019-1020.
5. Schwarzer, R., *Backscatter and transmission Kikuchi diffraction for materials science*; 2020, Herrenberg, Germany.
6. KELLER, R.R. and R.H. GEISS, *Transmission EBSD from 10 nm domains in a scanning electron microscope.* Journal of Microscopy, 2012. **245**(3): p. 245-251.
7. Yamaguchi, A., M. Shibata, and T. Hashinaga, *Transmission electron microscopy specimen preparation technique using focused ion beam fabrication: Application to GaAs metal–semiconductor field effect transistors.* Journal of Vacuum Science & Technology B: Microelectronics and Nanometer Structures Processing, Measurement, and Phenomena, 1993. **11**(6): p. 2016-2020.
8. Szot, J., et al., *Focused ion beam micromachining for transmission electron microscopy specimen preparation of semiconductor laser diodes.* Journal of Vacuum Science & Technology B: Microelectronics and Nanometer Structures Processing, Measurement, and Phenomena, 1992. **10**(2): p. 575-579.
9. Stevie, F.A., L.A. Giannuzzi, and B.I. Prenitzer, *The Focused Ion Beam Instrument*, in *Introduction to Focused Ion Beams: Instrumentation, Theory, Techniques and Practice*, L.A. Giannuzzi and F.A. Stevie, Editors. 2005, Springer US: Boston, MA. p. 1-12.
10. Giannuzzi, L.A. and F.A. Stevie, *A review of focused ion beam milling techniques for TEM specimen preparation.* Micron, 1999. **30**(3): p. 197-204.
11. Sasaki, H., et al., *Specimen preparation for high-resolution transmission electron microscopy using focused ion beam and Ar ion milling.* Journal of Electron Microscopy, 2004. **53**(5): p. 497-500.
12. Giannuzzi, L.A., et al., *FIB Lift-Out Specimen Preparation Techniques*, in *Introduction to Focused Ion Beams: Instrumentation, Theory, Techniques and Practice*, L.A. Giannuzzi and F.A. Stevie, Editors. 2005, Springer US: Boston, MA. p. 201-228.
13. Giannuzzi, L.A., et al., *Applications of the FIB lift-out technique for TEM specimen preparation.* Microscopy Research and Technique, 1998. **41**(4): p. 285-290.

14. Overwijk, M., F. Van den Heuvel, and C. Bulle‐Lieuwma, *Novel scheme for the preparation of transmission electron microscopy specimens with a focused ion beam.* Journal of Vacuum Science & Technology B: Microelectronics and Nanometer Structures Processing, Measurement, and Phenomena, 1993. **11**(6): p. 2021-2024.
15. Stevie, F.A., et al., *Application of focused ion beam lift-out specimen preparation to TEM, SEM, STEM, AES and SIMS analysis.* Surface and Interface Analysis, 2001. **31**(5): p. 345-351.
16. Nellist, P.D., *Scanning Transmission Electron Microscopy*, in *Springer Handbook of Microscopy*, P.W. Hawkes and J.C.H. Spence, Editors. 2019, Springer International Publishing: Cham. p. 2-2.
17. Williams, D.B. and C.B. Carter, *The Transmission Electron Microscope*, in *Transmission Electron Microscopy: A Textbook for Materials Science*. 1996, Springer US: Boston, MA. p. 3-17.
18. Pilz, S., et al., *Granulated silica method for the fiber preform production.* Fibers, 2017. **5**(3): p. 24.
19. Crewe, A.V. and J. Wall, *A scanning microscope with 5 Å resolution.* Journal of Molecular Biology, 1970. **48**(3): p. 375-393.
20. Goldstein, J.I., et al., *Qualitative X-Ray Analysis*, in *Scanning Electron Microscopy and X-ray Microanalysis: Third Edition*. 2003, Springer US: Boston, MA. p. 355-390.
21. Goldstein, J.I., et al., *Energy Dispersive X-ray Spectrometry: Physical Principles and User-Selected Parameters*, in *Scanning Electron Microscopy and X-Ray Microanalysis*. 2018, Springer New York: New York, NY. p. 209-234.
22. De Graef, M., *Introduction to Conventional Transmission Electron Microscopy*. 2003, Cambridge: Cambridge University Press.
23. Spence, J.C.H., *High-Resolution Electron Microscopy*. 4 ed. 2013, Oxford: Oxford University Press. 432.
24. Wagner, G., *P. R. Buseck, J. M. Cowley, L. Eyring. High-Resolution Transmission Electron Microscopy and Associated Techniques. Oxford University Press, Inc. 1992. Price £ 27.50. ISBN 0-19-507262-6 (pbk.) and ISBN 0-19-504275-1.* Crystal Research and Technology, 1993. **28**(5): p. 628-628.
25. Shahzad, K., *Formation Behavior of Nanostructured Anodic Films on Metals in Fluoride Containing Organic Electrolytes*, in *総合化学院（総合化学専攻）*. 2016, 北海道大学.
26. *Determination and Refinement of the Unit Cell*, in *Fundamentals of Powder Diffraction and Structural Characterization of Materials*. 2009, Springer US: Boston, MA. p. 407-495.
27. Laurin M. *Example: Principle of X-ray photoelectron spectroscopy (XPS), 2009,*
28. Rahman, M., et al., *Iron Oxide Nanoparticles.* 2011.
29. Turrell, G., *1 - The Raman Effect*, in *Raman Microscopy*, G. Turrell and J. Corset, Editors. 1996, Academic Press: London. p. 1-25.
30. Weng, S., et al., *Recent advances in Raman technology with applications in agriculture, food and biosystems: A review.* Artificial Intelligence in Agriculture, 2019. **3**: p. 1-10.
31. Wagatsuma, K., K. Hirokawa, and N. Yamashita, *Detection of fluorine emission lines from Grimm-type glow-discharge plasmas — use of neon as the plasma gas.* Analytica Chimica Acta, 1996. **324**(2): p. 147-154.
32. Chait, B.T. and K.G. Standing, *A time-of-flight mass spectrometer for measurement of secondary ion mass spectra.* International Journal of Mass Spectrometry and Ion Physics, 1981. **40**(2): p. 185-193.
33. Benninghoven, A., F.G. Rüdenauer, and H.W. Werner, *Secondary Ion Mass Spectrometry: Basic Concepts, Instrumental Aspects, Applications, and Trends*. 1987: J. Wiley.
34. Lockyer, N.P., *Static Secondary Ion Mass Spectrometry for Biological and Biomedical Research*, in *Electron Microscopy: Methods and Protocols*, J. Kuo, Editor. 2007, Humana Press: Totowa, NJ. p. 543-567.
35. McDonnell, L.A. and R.M.A. Heeren, *Imaging mass spectrometry.* Mass Spectrometry Reviews, 2007. **26**(4): p. 606-643.
36. Pacholski, M.L. and N. Winograd, *Imaging with Mass Spectrometry.* Chemical Reviews, 1999. **99**(10): p. 2977-3006.
37. D.W., M. *Time-of-Flight Secondary Ion Mass Spectrometry (ToF-SIMS)*. Montana State University
38. Vickerman, J.C. and D. Briggs, *ToF-SIMS : Surface Analysis by Mass Spectrometry*. 2001, [S.l.]: IM Publications.

39. Belu, A.M., D.J. Graham, and D.G. Castner, *Time-of-flight secondary ion mass spectrometry: techniques and applications for the characterization of biomaterial surfaces.* Biomaterials, 2003. **24**(21): p. 3635-3653.
40. Schwieters, J., et al., *High mass resolution surface imaging with a time‐of‐flight secondary ion mass spectroscopy scanning microprobe.* Journal of Vacuum Science & Technology A, 1991. **9**(6): p. 2864-2871.
41. Benninghoven, A., B. Hagenhoff, and E. Niehuis, *Surface MS: Probing Real-World Samples.* Analytical Chemistry, 1993. **65**(14): p. 630A-640A.
42. *EL-Cell Manual*. Available from: https://el-cell.com/support/manuals/.

Chapter 3 The Influence of Crystal Orientation on Formation of Anodic Films on Single Crystalline Iron

3.1. Introduction

The effects of applied voltage, current, temperature, and electrolyte composition are well known to influence the growth of anodic film. The crystallographic structure of oxides grown on iron has been a subject of immense debate for the last few decades by corrosion community. with the aim to understand the passivity of iron. For the passive film the presence of Fe_2O_3 or Fe_3O_4 has been proposed. [1-3] Nagayama et al. found that the passive oxide can be composed of Fe_3O_4 inner-layer and Fe_2O_3 outer-layer. [4-6] The passive film may be amorphous having FeOOH like structure. [7-13] In contrast to the above findings, the other studies showed that passive oxide is composed of Fe_2O_3 or Fe_3O_4. [14, 15] Toney et al. [16] and Davenport et al. [17] evaluated the structure of passive oxide formed on iron single crystals of (001) and (110) by means of in-situ surface X-ray diffraction technique, and found that the passive oxide has the LAMM phase, analogous to Fe_2O_3 or Fe_3O_4. The oxide formed on (001) plane was less defective, has larger crystallites and grains than that formed on (110) single crystal surface. [16, 17] Takabatake et al. found the passive film on iron has bi-layered structure, with Fe_3O_4 as an inner-layer and Fe_2O_3 as an outer-layer, varying in the proportion of -inner to -outer layers depending on the surface energy of the substrate related to its crystallographic orientation. [18] The mechanical properties of passive oxides formed on iron (100) and (110) single crystals were conducted by Seo and Chiba, the hardness of the passive iron (100) orientation was lower by 10% than the passive iron of (110) orientation. [19] Taking into account the nature of oxide formed on iron, immensely investigated by corrosion community, one may expect that the structure of oxide formed by anodizing may also depend on the crystallographic structure of metal on which it is formed.

In the present study, the author investigated the correlation of anodizing behavior when the anodization process is carried out and the nanoporous anodic film characteristics, such as the pore diameter, the wall thickness, and the thickness of nanoporous with (111), (110) and (100) orientated iron single crystals as substrate using ethylene glycol electrolytes with additions of fluorides and water. The morphology of the

formed nanoporous film was investigated by scanning electron microscopy (SEM) and a scanning transmission electron micrograph (STEM). We also determined the phase structure of the anodic iron oxide layers by X-ray diffraction (XRD), Raman Spectrometry and Auger Electron Spectroscopy (AES) analysis.

3.2. Experimental Details

Iron single crystal (100), (110) and (111) disk electrodes of 10 mm in diameter grown by Czochralski process were purchased from Goodfellows (purity 99.98%). Polycrystalline iron specimen purchased from Nilaco, Japan (purity 99.99%) was used as a reference. Before anodizing the specimens were mechanically polished with SiC grinding paper from up to 1500 grade, then polished with set of alumina suspension using 3 µm, 1 µm, and 0.05 µm. Then, specimens were electropolished in a mixture of perchloric acid and ethanol (40:60 v/v). This solution is vulnerable due to its aggressiveness and oxidizing nature and should be used below 10^{o}C. The schematic of electropolishing setup is shown in Figure 3.1. About 800 mL of ethanol was obtained in 1 L beaker containing magnetic stirrer and surrounded by ice in a bath to maintain the temperature of the beaker below 10^{o}C. 200 mL of perchloric acid was slowly added to a beaker containing ethanol and magnetic stirrer. The electropolishing was carried out in a two electrode-cell in a fume cupboard with single crystal iron and aluminum sheet serving as working and counter electrode. Electropolishing was performed at optimized 20 V applied from a power source. Stirring of the solution was also performed during electropolishing.

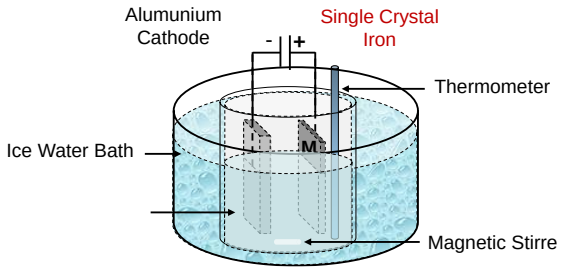

Figure 3.1 Schematic illustration of electropolishing process.

Electropolishing was carried out for 4-5 minutes. After electropolishing, the specimen was removed and rinsed thoroughly first in ethanol and then in deionized water in an ultrasonic bath for 15 min and dried in a cool air stream. Prior to anodizing the iron specimen was observed by electron backscatter diffraction (EBSD) mapping.

Iron single crystals were anodized at 60-100 V for 900 s in ethylene glycol electrolyte containing 0.1 mol dm^{-3} ammonium fluoride and 1.5 mol dm^{-3} deionized water in o-ring type electrochemical cell (V= 4 mL) with a two-electrode system using platinum counter electrode as schematically shown in Fig. 3.2. The distance between working and counter electrodes was kept constant at 2 cm, before anodizing the electrolyte was cooled down to 20 °C by a Huber K6 then the anodizing was carried out at 20 °C with the temperature of substrate controlled by Peltier element at 20±0.1°C. After anodizing, the specimens were rinsed in ethylene glycol, ethanol (99,8%), and then dried in nitrogen stream. Anodizing at selected voltage was repeated ten times on each single crystal specimen to ensure the effect of plane orientation.

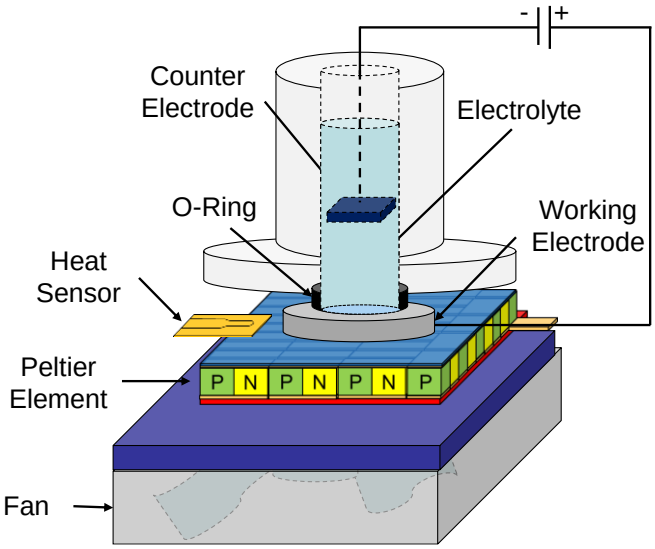

Figure 3.2 Schematic illustration of the anodizing apparatus used in single crystal study, indicating two electrode anodizing cell in a cooling condition using Peltier element.

The surfaces and cross-section of the electropolished single crystal samples and anodized specimens were observed using a JEOL JSM-6500F field emission scanning electron microscope equipped with a TSL-EBSD system. EBSD maps were analyzed with respect to grain size distribution and crystallographic texture using the OIM5.22 software. Electron-transparent sections were prepared by a Hitachi FB-2100 focused ion beam (FIB) system employing a Ga^{+} ion beam. Electron-transparent cross-sections of the anodized specimens were observed by a JEOL, JEM-ARM200F scanning transmission electron microscope (STEM) with energy dispersive X-ray spectrometry (EDS) facilities. The lattice fringes and corresponding electron diffraction spots on high-resolution transmission electron microscopy (HRTEM) images was observed by using JEOL JEM-2010 electron microscope operated at an accelerating voltages 200 kV.

Raman spectra of the anodized iron specimens were collected from 100–1200 cm^{-1} with Horiba XploRA Raman microscope (Kyoto, Japan) equipped with an Olympus microscope (Tokyo, Japan) with 100x magnification. Calibration of spectra was conducted using a silicon wafer with a main peak at 520.7 cm^{-1} as reference. The spectra were collected with a 532 nm line, solid-state lasers (12 mW at the sample); 2400 lines/mm grating in back-scattering, with exposure time 10 s with 3 integration times. The phase in the anodic films was identified by Rigaku, RINT-2000 X-ray diffractometer using Cu-Kα radiation ($\lambda = 0.15418$ nm) with a 2θ range of 10–80 degrees at a scan speed of 0.5 degree/min and collected by a tube voltage of 40 kV and 20 mA tube current. For the analysis thin film, grazing incidence XRD mode (α = ?) was used to minimize the contribution of the substrate material. Auger spectroscopy analysis was performed on iron (100) and (110) anodized samples using a JAMP-9500F spectrometer. The Auger spectroscopy point analysis used 10 kV primary electron energy, 10.2 nA beam current, with a cylindrical mirror analyzer of incidence with respect to the surface normal of 30° slope and performed at a pressure of $\sim 10^{-6}$ Pa.

3.3. Results and Discussion

3.3.1 EBSD Analysis

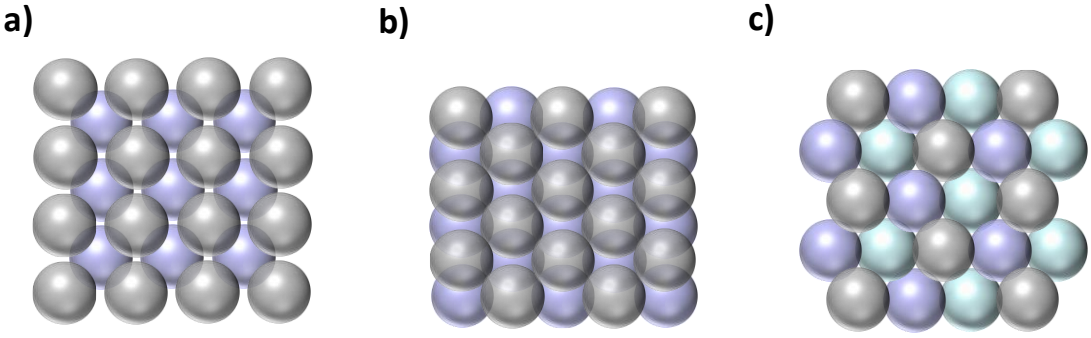

Figure 3.4 Schematic illustrations of atomic structure for iron (a) (100), (b) (110) and (c) (111) orientation, grey color represents first atomic layer, purple color represents second atomic layer and green color represent third atomic layer.

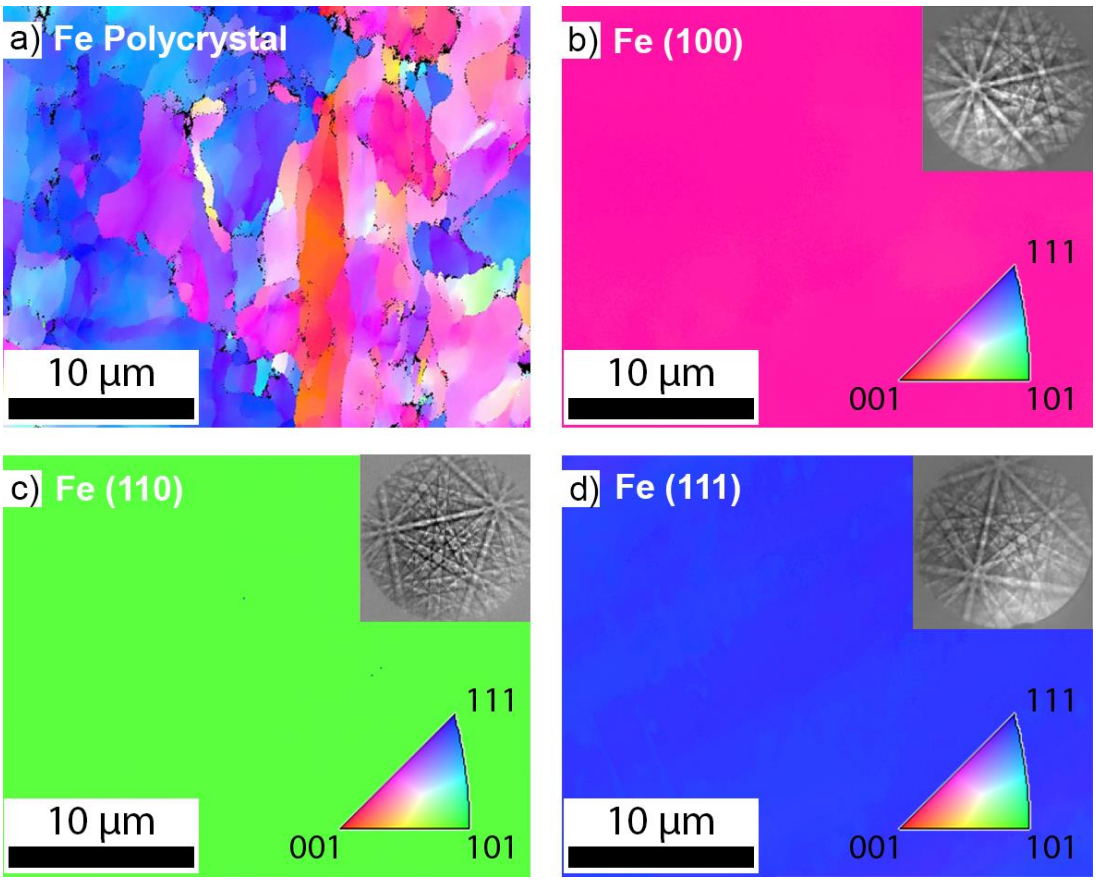

Figure 3.3 EBSD grain orientation maps of (a) polycrystalline iron and iron single crystals with (b) (100), (c) (110) and (d) (111) plan orientation.

The effect of crystallographic orientation of iron on anodic oxide growth was investigated by means of anodizing of single crystal iron grown by Czochralski method. The atomic structure of each single crystal iron having plane orientation of (100), (110) and (111) is schematically demonstrated in Fig. 3.3 with the emphasis on the first three atomic layers. The surface energy of each crystal significantly differs as a result of variations in atomic density of 1.2 x 10^{19}, 1.75 x 10^{19}, and 0.7 x 10^{19} atom m^{-2} for (100), (110) and (111) surface, respectively.

The surface state of iron specimens after polishing with 0.05 μm alumina suspension and subsequent by electropolishing was investigated by electron backscatter diffraction (EBSD) analysis. Figure 3.4 shows the inverse pole figures (IPF) and corresponding Kikuchi patterns obtained after background subtraction form each electron backscatter diffraction (EBSD) analysis of iron single crystals (100), (110) and (111). The IPF image for polycrystalline iron (Fig. 3.4a) as reference sample depicts the grain size of 2-10 μm is shown as reference sample. The IPF images for single crystals after surface pretreatment are characterized with one mono-crystalline domain indicating proper crystallographic plane exposed at solid electrolyte interface in anodizing process.

3.3.2 *j-t* curves in anodizing process

Anodizing of iron single crystals and polycrystalline reference specimen was performed at a constant voltage of 60 V in ethylene-glycol electrolyte containing 1.5 mol dm^{-3} water and 0.1 mol dm^{-3} NH_4F at 20°C for 900 s. Figure 3.5a shows the current-time (*j-t*) transients which are characterized by current spike observed in the first tens of seconds followed by quasi-steady state where the current density is nearly constant. The first stage of anodizing typically corresponds to initial barrier type-oxide formation at the metal-electrolyte interface and possible pore initiation, while the second stage is linked to steady state growth of nanoporous structure [20]. Significant differences in the current density values were found on *j-t* curves depending on indexing number of single crystal specimen. The current density in the steady state growth on iron (100) is larger than that on (110) and (111) by a factor of 1.4. This is more apparent when one compares the total charge (*Q*) passed in the anodizing process at 60 V for $Q_{Fe(100)}$= 26 C cm^{-2} with $Q_{Fe(111)}$= $Q_{Fe(110)}$=19 C cm^{-2}. The difference in anodizing on low index facet is much more pronounced at higher voltages. Figure 3.5b shows the current density as a function of voltage applied in anodizing of single crystal specimens. The slope of *j*=f(*U*) for Fe (100) is 3.06 significantly higher than that of 0.76 for Fe (110) and Fe (111) giving the current

density for low index facet larger by a factor of 2.5 at 90 V. By looking at the *j-t* transients in Fig. 3.5a one may assume that both the ionic current and electronic current may be involved in the anodizing process.

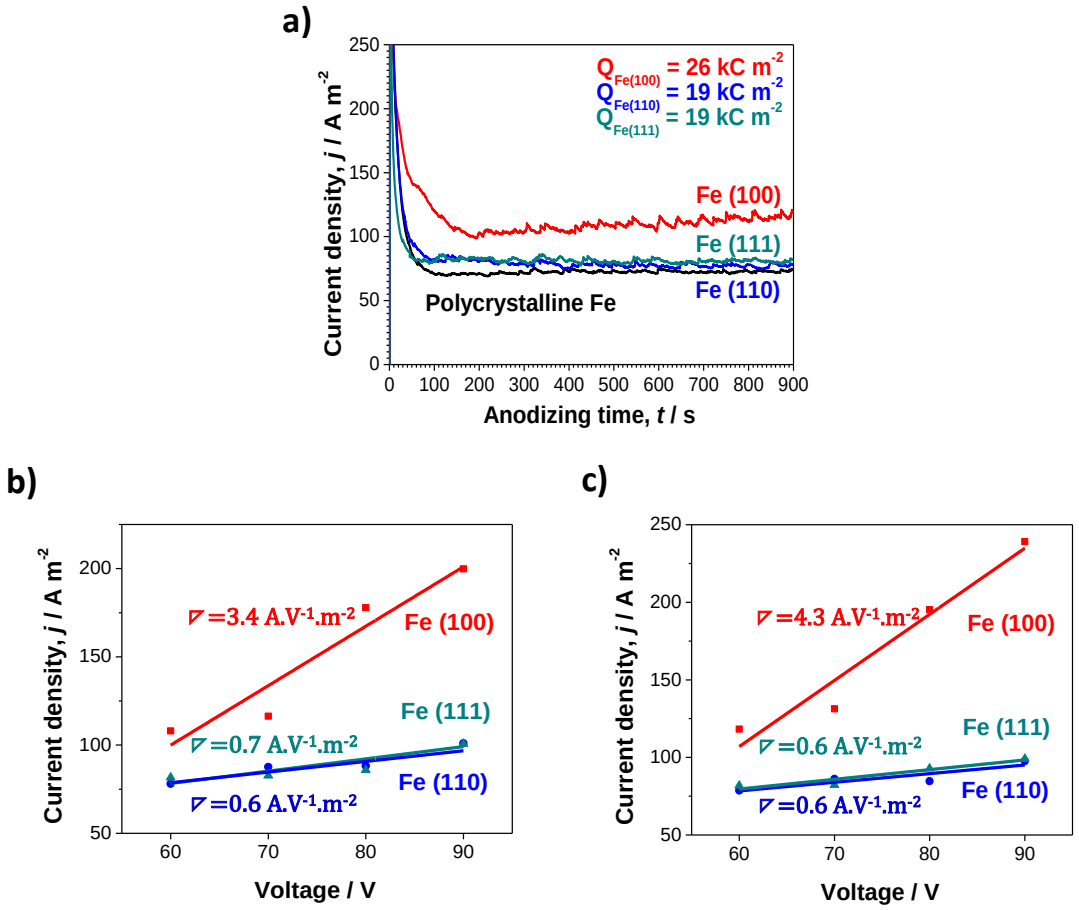

Figure 3.5 (a) Current-time (j-t) responses for poly crystalline, (100), (110) and (111) single crystal orientations of the iron substrates in an ethylene glycol electrolyte containing 1.5 mol dm^{-3} of water and 0.1 mol dm^{-3} of NH_4F at 20°C at 60 V anodizing, and current-voltages correlation at (b) 450 s and (c) 900 s on anodizing Fe(100), Fe (110) and Fe(111) shown in panel (b) and (c).

The ionic current leads to ionic migration during the oxidation process leading to film development according to reactions (3.1-3.4). Fe_3O_4, Fe_2O_3, FeF_x on both metal/film and film electrolyte interfaces according to reactions (3.1-3.6) and/or injection of ionic species to the electrolyte at film/electrolyte interface. The possible reactions at metal/film interface may be expressed as follows:

$$3Fe + 4O^{2-} \rightarrow Fe_3O_4 + 8e^- \quad (3.1)$$

$$2Fe + 3O^{2-} \rightarrow Fe_2O_3 + 6e^- \quad (3.2)$$

$$Fe + xF^- \rightarrow FeF_x + xe^- \quad (3.3)$$

$$Fe \rightarrow Fe^{x+} + xe^- \quad (3.4)$$

and consequently, at film/electrolyte interface:

$$3Fe^{x+} + 4H_2O \rightarrow Fe_3O_4 + 8H^+ + (8\text{-}3x)e^- \quad (3.5)$$

$$2Fe^{x+} + 3H_2O \rightarrow Fe_2O_3 + 6H^+ + (8\text{-}3x)e^- \quad (3.6)$$

$$2H_2O \rightarrow O_2\,(\uparrow) + 4H^+ + 4e^- \quad (3.7)$$

The presence of electronic current strongly depends on electronic structure of the developed oxide of which the conductive/resistive nature controls injection of electrons from electrolyte across the oxide to the metal back contact. If true electronic current is present, the decomposition of water takes place resulting in oxygen generation according to reaction (5). The kinetics of oxygen evolution strongly depends on electronic nature of the anodic oxide; for instance, for aluminum no oxygen evolution is typically observed due to resistive nature of Al_2O_3; for titanium, oxide formation is typically accompanied with O_2 evolution as a result of semi-conductive nature of TiO_2. The visual observation of the iron anodizing process indicated massive gas evolution during oxide formation on (100) facet, whereas very little gas evolution was observed on high index facets in Fig. 3.6. Fast kinetics of gas evolution suggest dominant role of reaction (5) in the shift of *j-t* curve towards higher current density values on iron (100).

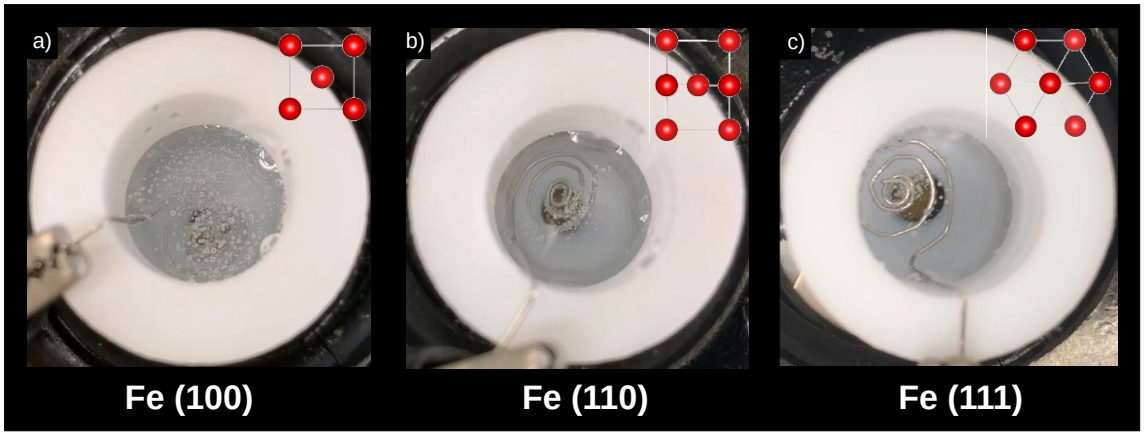

Figure 3.6 Oxygen evolution photos of three different single crystal orientations (a) Fe (100), (b) Fe (110), and (c) Fe (111) in an ethylene glycol electrolyte containing 1.5 mol dm^{-3} of water and 0.1 mol dm^{-3} of NH_4F at 20°C.

Given the truth that the temperature of the electrode was controlled by using a Peltier element, and the other anodizing parameters were precisely controlled, we can conclude that the difference in the current density is caused only by the crystallographic orientation of the iron substrate. However, on anodizing (110) and (111) crystal orientation substrate at 100 V the steady state region also breaks, leading to a continuous increase in current density with time (Figure 3.7). In fact, the electrode (iron) and bath

temperature increases during electrochemical anodization due to Joule heating. Possible explanation of the increase in the current density and higher oxygen evolution reaction on (100) crystal orientation will be explained later.

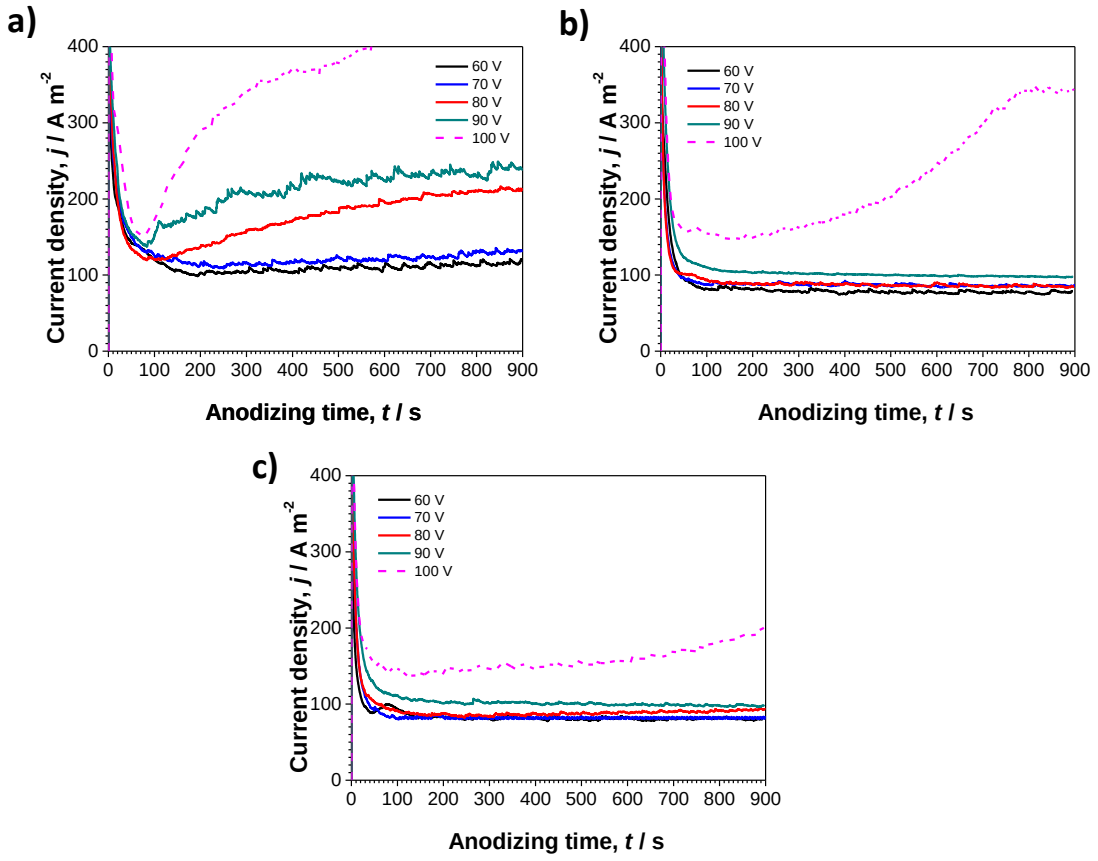

Figure 3.7 Current-time (j-t) responses for (a) (100), (b) (110) and (c) (111) single crystal orientations of the iron substrates in an ethylene glycol electrolyte containing 1.5 mol dm^{-3} of water and 0.1 mol dm^{-3} of NH_4F at 20°C at 60-100 V.

3.3.3 Morphology of anodic films

The surface morphology and corresponding cross-section images for anodic oxides formed on iron (100), (110) and (111) at 60 V depicting the presence of classic nanoporous structure analogous to that formed on polycrystalline iron surface [20, 21] are demonstrated in Fig. 3.8. The average inner-diameter of nanopore was found to be 99 ± 1 nm, 102 ± 1 nm, and 103 ± 1 nm, for anodic oxide formed on iron (100), (110) and (111), respectively. The thickness of anodic film formed on Fe (100) is 2.3 ± 0.1 μm, followed by (111) 2.2 ± 0.1 μm and (110) orientation around 2.2 ± 0.1 μm.

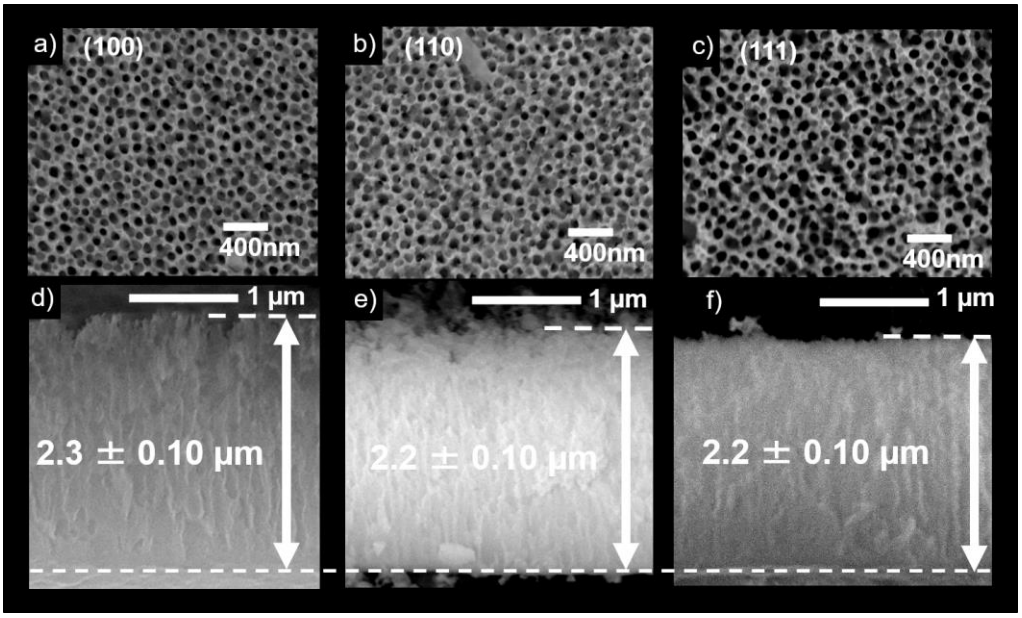

Figure 3.8 Surface and cross-section SEM images for (a,d) Fe (100) orientation, (b,e) Fe (110) orientation, and (c,f) Fe (111) orientation, anodized at 60 V in ethylene glycol electrolyte containing 1.5 mol dm^{-3} of water and 0.1 mol dm^{-3} of NH4F at 20 ^{o}C.

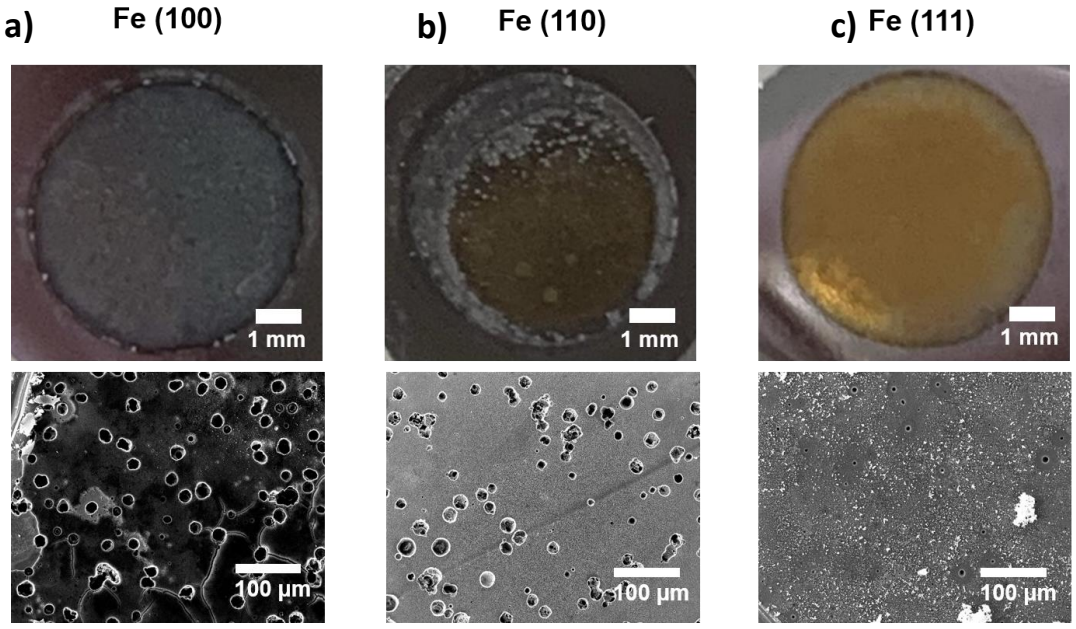

Figure 3.9 Camera pictures and SEM surface images of oxides grown on (a) Fe (100) orientation, (b) Fe (110) orientation, and (c) Fe (111) orientation, anodized at 100 V in ethylene glycol electrolyte containing 1.5 mol dm^{-3} of water and 0.1 mol dm^{-3} of NH_4F at 20 ^{o}C.

Increase in the anodizing voltage results in more apparent changes in surface morphology as well as the presence of defects on the surface depending on the indexing number of the facet (Fig. 3.9). On anodizing iron at high anodizing voltage, the pitting corrosions is present. As seen in Fig. 3.9; high anodizing voltage of 100 V is not suitable for uniform film growth. However, the (111) facet shows less significant in pitting corrosion in agreement with lower current density compared to the other facets on Fig. 3.7. For further detailed studies on the impact of exposed facet we choose the conditions at which oxygen evolution is considerably low and do not cause damages on the anodic film surface. The scanning transmission electron micrograph (STEM) of a focused ion beam (FIB) lamellas for Fe (100) and Fe (110) anodized at 60 V are shown in Fig. 3.10 a,b. The results of high angle annular dark field (HAADF) have shown that the thickness of the barrier layer is 97 and 104 nm formed on (100) and (110) facets, respectively. The inter-pore distance for anodic film formed on (110) is approximately ten nanometers thicker than that formed on (100) facet. A critical point of observation between anodic film formed on high and low index facets is the presence of roughness in the barrier-layer with dark spots on formed on (100) surface possibly associated with the higher degree of crystallinity.

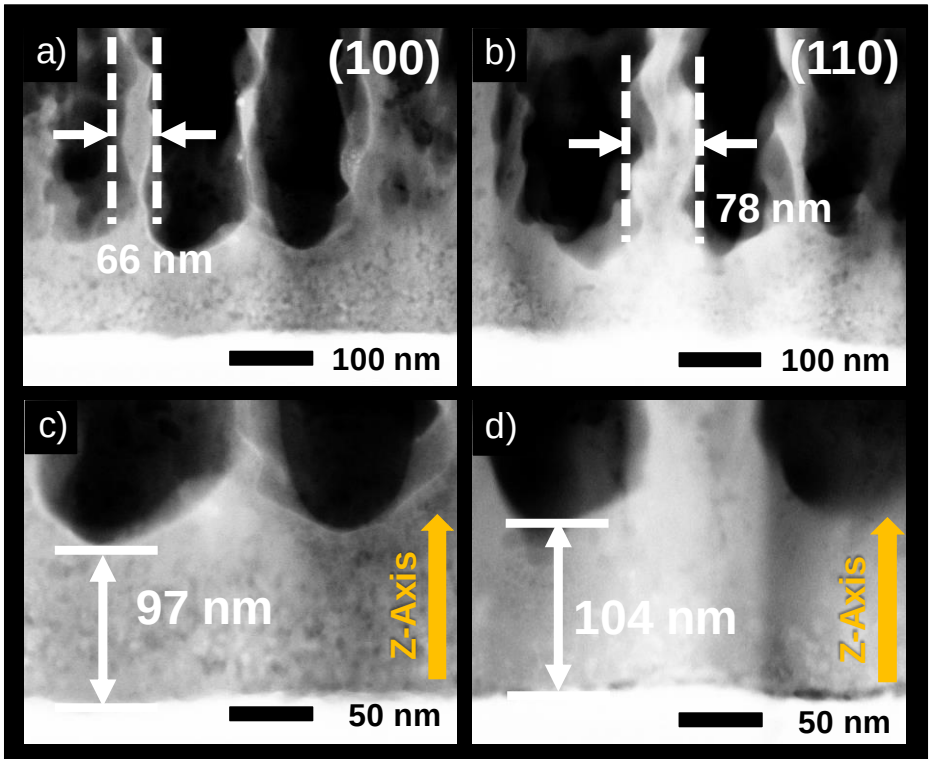

Figure 3.10 TEM images for (a,c) (100) and (b,d) (110) orientation of iron substrate anodized at 60 V in ethylene glycol electrolyte containing 1.5 mol dm^{-3} of water and 0.1 mol dm^{-3} of NH_4F at 20°C.

3.3.4 Analysis of Composition

Figure 3.11 displays the HAADF images and corresponding high-resolution energy dispersive x-ray spectrometry (EDS) elemental maps for anodic films formed at 60 V on (100) and (110) facets. The EDS maps reveal the fluorine, oxygen, and iron at the bottom regions of anodic oxides. A more detailed analysis of EDS compositional maps for oxide formed on polycrystalline iron is demonstrated elsewhere.[21].The structure of anodic film formed on iron, observed by SEM and TEM, is typically considered to be nanoporous (Al_2O_3-like nanopore). If one compares, however, TEM image with oxygen elemental map in Fig. 3.11 it is easy to understand that the true structure of oxide is nanotubular (TiO_2-like nanotube). The fluorine enrichment at the cell boundaries and at the metal/anodic-film is apparent from fluorine elemental map. Both regions are practically free from oxygen species suggesting formation of iron fluoride. The detailed compositional EDS analysis of the inner-part of barrier layer, denoted "2" in Fig. 3.11 c,d, reveal composition of 32 at.% of Fe and 65 at.% of F for film formed on (100) facet, 63 at.% of Fe and 34 at.% for film formed on (110) facet. The composition of the fluoride rich layer located at metal/anodic-film interface is in agreement with atomic ratio of 1:2 for FeF_2 compound. According to the field assisted flow model, [21]

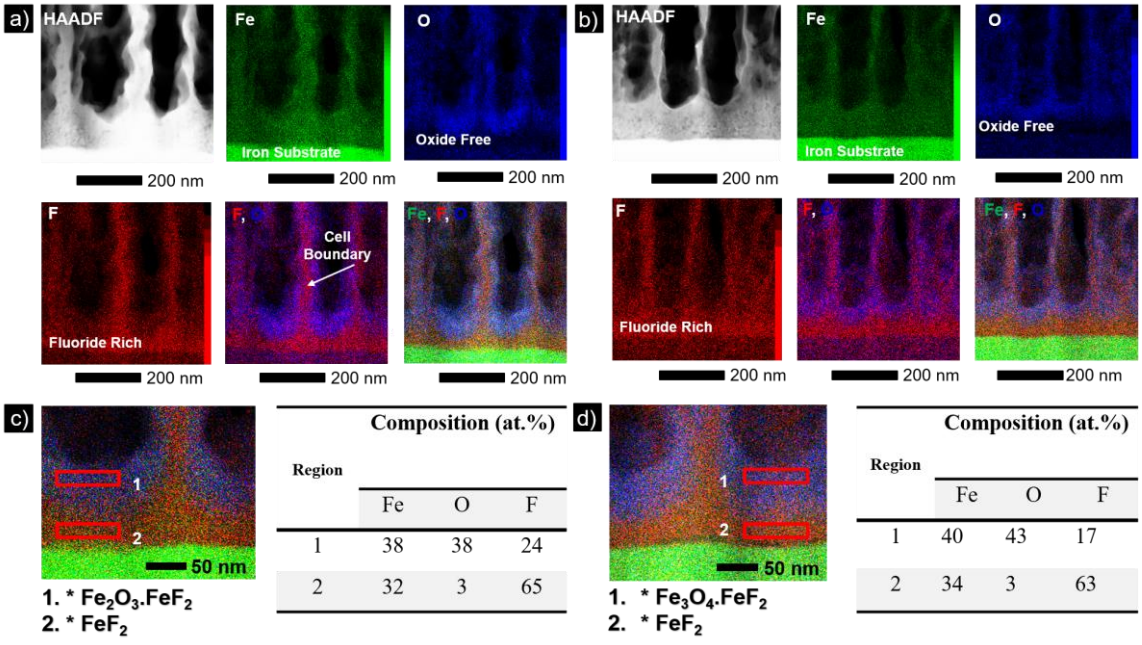

Composition (at.%)

Region	Fe	O	F
1	38	38	24
2	32	3	65

Composition (at.%)

Region	Fe	O	F
1	40	43	17
2	34	3	63

Figure 3.11 High resolution energy dispersive X-ray spectrometry (EDS) maps obtained for bottom regions of focused ion beam (FIB) cross-sections of anodic porous film formed on (a, c) (100) and (b, d) (110) single crystals at 60 V in ethylene glycol electrolyte containing 1.5 mol dm^{-3} of water and 0.1 mol dm^{-3} of ammonium fluoride for 900s at 20°C. The star symbol "*" indicates the calculated chemical composition at selected regions of nanopore/nanotube bottom region.

FeF_2 layer is switched from horizontal position to vertical position positioned at cell boundaries, well observed on superimposed iron-fluorine-oxygen EDS images in Fig. 3.11. By choosing appropriate anodizing conditions, [21] the FeF_2 may be dissolved from cell boundaries and therefore the nanopores can be further transformed into nanotubes following the shape of nanotube visible on oxygen map. The outer part of barrier-layer, which refers to the inner shell of oxide nanotube bottom, is composed of Fe, O, F with atomic ratio of 38, 38, 24 at.%, and 40, 43, 17 at.% for anodic film formed on (100) and (110) surface, respectively. If we assume that: i) all fluorine present in the outer part of barrier-layer is bounded to iron and forms iron-fluoride compound, ii) iron bounded to fluoride has an oxidation number 2+, and iii) no oxyfluorides are formed, the calculated anodic structure formed on iron (100) facet can be expressed by the following formula: $Fe_2O_3 \cdot FeF_2$. Consequently, the calculated structure of the anodic outer part of barrier-layer formed on (110) facet would be $Fe_3O_4 \cdot FeF_2$. The initial formation of FeF_3 the has been considered as a result of ions migration under high electric field conditions, however, its presence in the anodic film structure is neglected due to its faster dissolution in electrolyte over FeF_2 due to difference in solubility constants of $k_{FeF3}=5.2x10^{-1}$ mol dm^{-3} and $k_{FeF2}=8.3x10^{-3}$ mol dm^{-3} [21].

Figure 3.12a shows the X-ray diffraction (XRD) spectra for anodic oxides formed on (100), (110) and (111) single crystals. The iron with the (110) orientation shows an intense peak at 44.70º corresponding to the 110 reflection, and a weak 200 reflection is found for iron with the (100) orientation. The relatively weak 200 reflection of the (100) iron compared with the 110 reflection of the (110) iron is mainly originated from the crystal structure factor. In fact, the randomly oriented iron shows the intensity of 200 reflection that is about one tenth that of 110 reflection. The absence of 111 reflection for the (111) iron is due to the extinction rule. The anodic films formed on all three single crystal surfaces show peaks at 26.82° corresponding to 110 reflection of FeF_2 (ICSD no. 81-2271) (Fig. 3.12b). The 2θ peaks at 35.40° and 56.94° for anodic films formed on (110) and (111) single crystals may be indexed to 311 and 511 reflection of Fe_3O_4 (ICSD no. 75-1372). The obvious presence of FeOOH for anodic films formed on (110) and (111) iron (ICSD no. 75-1594) with 119 peak at 11.90°, and other peaks that overlap with those observed for Fe_3O_4 35.30° (211 reflection) and 56.61° (251 reflection) cannot be excluded. Surprisingly, additional peaks at 24.10°, 33.10° and 35.60° appear on the

diffraction pattern obtained for anodic film formed on (100) single crystal, and could be assigned to 012, 104 and 110 reflection of Fe_2O_3 (ICSD no. 80-2377). The Fe_2O_3 diffraction peaks are essentially absent for anodic films formed on high index number single crystals which can be more clearly seen on magnified pattern in Fig. 3.12c. The formation of Fe_2O_3 on (100) iron surface and Fe_3O_4 on (110) and (111) iron surfaces, detected by XRD, is in agreement with the stoichiometry of anodic films calculated from high resolution compositional EDS maps in Fig. 3.11.

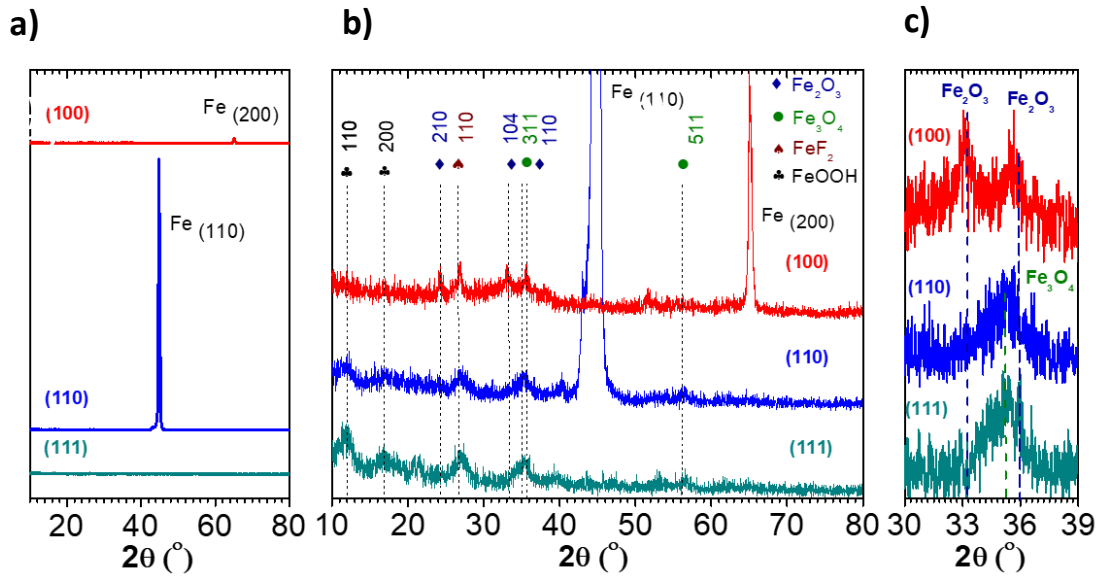

Figure 3.12 X-ray diffraction patterns for anodic porous films formed on (100), (110) and (111) single crystals at 60 V for 900 s in ethylene glycol electrolyte containing 1.5 mol dm^{-3} of water and 0.1 mol dm^{-3} of ammonium fluoride at 20°C.

3.3.5 Analysis of Crystallinity

Figure 3.13 shows high resolution TEM images obtained for FIB cross-sections of anodic films formed on (100) and (110) iron single crystals. Comparing both TEM micrographs one may notice that, fundamentally, higher degree of crystallinity was observed for the film formed on (100) single crystal. The lattice fringes having 0.33 nm and 0.23 nm corresponding to (110) and (111) planes of FeF_2 were found in the inner part of barrier layer for both anodic films (ICSD no. 81-2271). The outer part of barrier-layer (Fig. 3.13 a) for film formed on iron (100) single crystal is characterized by presence of large crystalline domains with the lattice fringes of 0.37 nm, 0.25 nm and 0.27 nm which may be indexed to (012), (110) and (104) planes of Fe_2O_3, respectively (ICSD no. 80-2377). The anodic film formed on (110) single crystal is essentially of amorphous nature having a little nanocrystal with lattice fringes at 0.25 nm, 0.16 nm and 0.48 nm which may be indexed to (311), (511) and (111) planes of Fe_3O_4 (ICSD no. 75-1372).

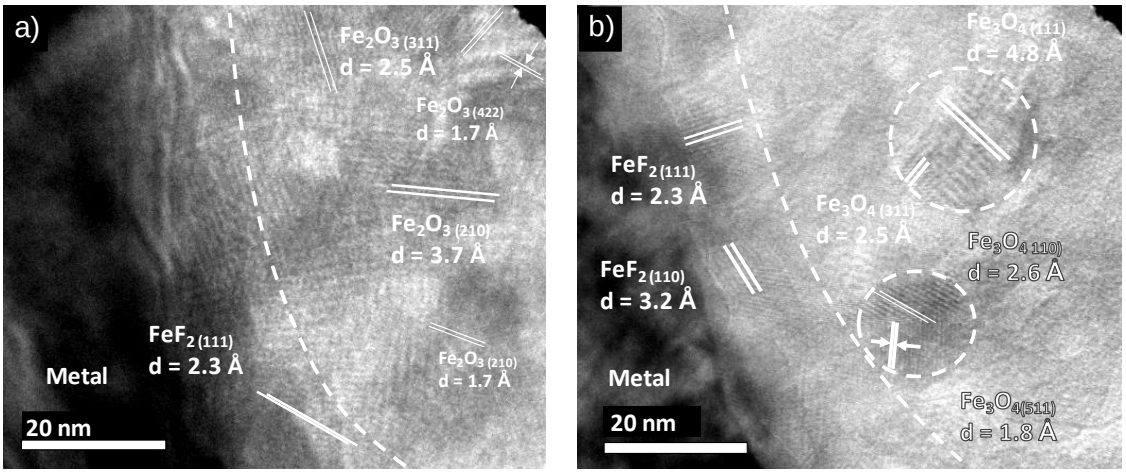

Figure 3.13 High resolution TEM images of focused ion beam (FIB) lamellas performed for iron (a) (100) and (b) (110) single crystals anodized at 60 V for 900 s in ethylene glycol electrolyte containing 1.5 mol dm^{-3} of water and 0.1 mol dm^{-3} of ammonium fluoride at 20°C.

Figure 3.14 shows Raman spectra recorded for each anodized single crystal in order to get more insight into the structural variations in anodic porous films. The spectra for anodic films formed on (110) and (111) facets show typical magnetite (Fe_3O_4) features which are attributed to the A_{1g} mode at around 700 cm^{-1}in Fig. 3.14 [22-24]. The weak spectral features at 300 and 550 cm^{-1} are assigned to the T_{1g} vibrational mode [22, 25]. The Raman spectrum for anodized (100) single crystal exhibits the spectral signatures characteristic for hematite (Fe_2O_3) in addition to the peaks associated with the presence of magnetite (Fe_3O_4). More specifically, the peaks at 229 cm^{-1} and 500 cm^{-1} are assigned to the A_{1g} modes of hematite (Fe_2O_3) [22, 23] with the remaining five peaks at 249, 295, 302, 414, and 615 cm^{-1} assigned to the E_g modes of hematite (Fe_2O_3) [22]. The strong peak seen at approximately 660 cm^{-1} has been widely observed in Raman spectra for magnetite (Fe_3O_4) or maghemite (γ-Fe_2O_3) and also attributed with the presence of hematite (Fe_2O_3) [22-25]. Except obvious differences in the chemical structure for andic porous films formed on high and low index facets, the spectrum obtained for anodized (100) single crystal is characterized by the presence of more sharp and more intense Raman peaks which is directly related to higher degree of crystallinity for anodic film formed on low index facet.

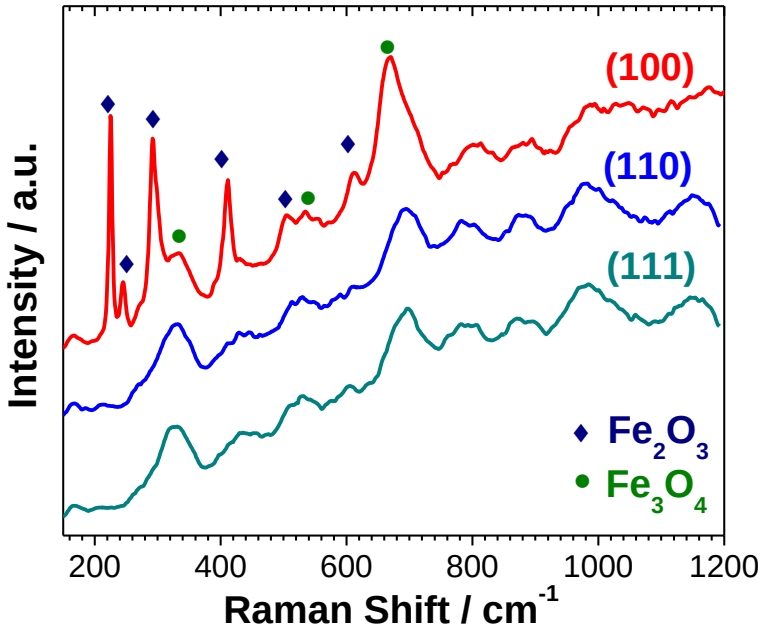

Figure 3.14. Raman spectra of anodic porous films formed on iron (100), (110) and (111) single crystals anodized at 60 V for 900 s in ethylene glycol electrolyte containing 1.5 mol dm^{-3} of water and 0.1 mol dm^{-3} of ammonium fluoride at 20°C.

Auger spectroscopy measurement have been applied to distinguish the oxidation state of oxide grown on single crystal iron (100) and (110) orientation (Figure 3.15). The spectra associated to C_{KLL}, O_{KLL} and Fe_{LMM} were obtained on the anodic films. It is known that the Fe LMM-peaks in the Auger spectra of metallic Fe, FeO, Fe_2O_3 and Fe_3O_4 are almost identical in shape [26-28]. Except typical features characteristic for Fe_xO_y compound, the Auger spectrum in Fig. 3.15b shows additional peak at ~650 eV corresponding to FeF_2. The basic curve fitting of the spectrum using standard shift peak database of Fe_2O_3, FeO, and combination of both corresponding to standard line of Fe_3O_4 could not be performed with satisfactory fitting due to complexity of the spectrum because presence of intense peak at ~650 eV. However, close inspection of the spectrum obtained for anodic film formed on Fe (100) and that formed on Fe (110) reveal higher intensity peaks at 595 and 703 eV for films formed on low index number facet whereas the peak at ~650 eV essentially remains unchanged. This suggests the contribution of Fe_2O_3 for film formed on low index number facet whereas the shape of the spectrum obtained for higher index number specimen is analogous to Fe_3O_4. Several studies have reported similar results on passive oxidation studies of Fe (100) and (110) orientation. [29-31]

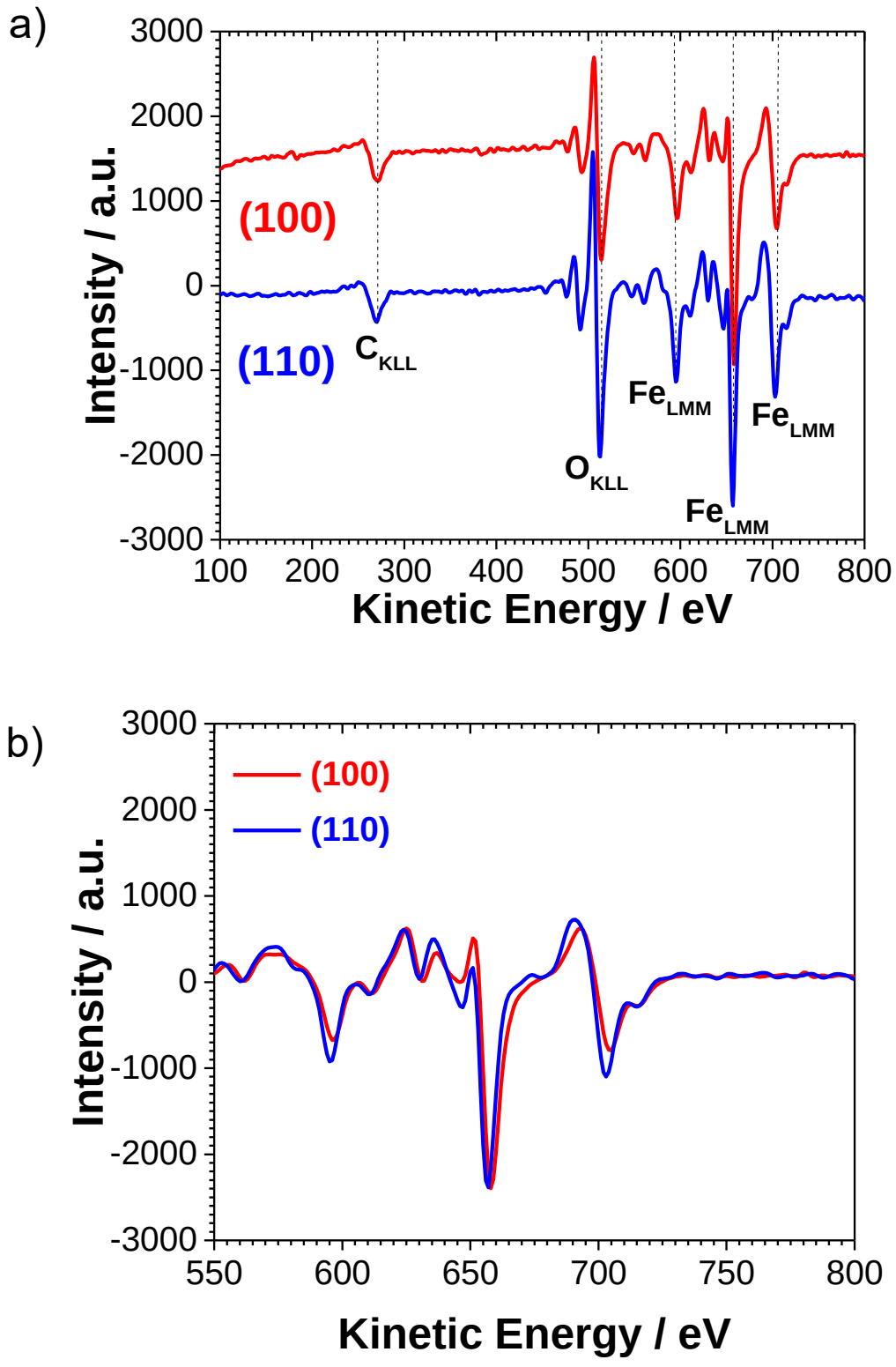

Figure 3.15 a) Wide Auger electron spectra and b) Fe_{LMM} spectra for anodic porous film formed on iron (100) and (110) single crystals anodized at 60 V for 900s in ethylene glycol electrolyte containing 1.5 mol dm^{-3} of water and 0.1 mol dm^{-3} of ammonium fluoride at 20°C.

3.3.6 Anisotropy of Iron

Anodizing of iron single crystals, with (100), (110) and (111) orientation, indicated that the anodic porous film growth depends on the index number of facet on which the film is formed. The variations in the growth may be possible if one considers following physicochemical properties of iron: i) planar atomic density and corresponding ii) surface energy, iii) magnetic anisotropy, and/or iv) electronic properties. The *j-t* transients obtained during anodizing of single crystals indicated that there is a significant difference in the formation of anodic film on (100) facet and the other single crystals. The porous anodic film formed on (100) facet is composed of $Fe_2O_3 \cdot FeF_2$ whereas that formed on higher index facet consists of $Fe_3O_4 \cdot FeF_2$. The conversion of iron into iron oxide essentially results in volume expansion which is described by Pilling-Bedworth ratio [32]. Under influence of high electric field strength, the volume change typically generates mechanical stress at the metal/oxide interface which, together with electrostriction forces, is responsible for the change of the horizontal oxide growth into vertical one developing nanoporous/nanotubular shape [33]. A relationship between internal stress and crystallization has been proposed by several authors [34-37]. High degree of crystallinity for the oxide formed on low index number facet, as evidenced by XRD and Raman spectroscopy, may be related to the presence of higher stress at the Fe(100)/oxide interface, and therefore crystallization of the oxide during the growth. The formation of nanocrystals results in modification of electronic properties of the oxide, i.e. increase of conductance which leads to electronic current increase and consequently evolution of oxygen as observed in Fig. 3.6, according to reaction (3.7). The gas evolution is typically observed for electrically conductive anodic oxides such that formed on titanium [38] in contrast to non-conductive oxides such as those formed on aluminum [33].

The anisotropy of crystal in the sense of variations in physical properties along different molecular axes such as difference in planar density shown in Fig. 3.3, should be discussed in view of its effect on the anodizing process. The surface energy of a single crystal is directly related to the planar density of the substrate because of the number of unsatisfied bonds [39, 40]. In the case of orientated iron single crystals, the calculated atomic density is 1.75×10^{19}, 1.20×10^{19}, and 0.70×10^{19} atom m^{-2} for (110), (100) and (111) surface, respectively, with the surface energy increasing in the same sequence. Our experimental results, however, show that anodizing conditions differ only on (100) surface, having the middle surface energy estimate, therefore we rule out the effect of

surface density in this particular case. The other physical properties such as elastic modulus, work function and magnetic anisotropy show dependence on the index number of the crystal [41-48]. For instance, an elastic modulus of iron (100) has been reported to be half lower than the other orientations, according to the following sequence: 129, 221 and 276 GN m^{-2} for (100), (110) and (111) orientation, respectively [41, 49]. In the anodizing process the presence of compressive-stress and tensile-stress is critical on the effects on convex geometry and therefore formation of nanoporous/nanotubular shape of anodic film. Twice lower elastic modulus value means that iron single crystal is more prone for deformation in (100) direction. The motion at the metal/film interface would therefore be dependent on the number of index facet in line with the tendency of the material towards elastic deformation. Consequently, the stress distribution would be different on (100) facet than that on the higher index number facets as a result of variations in the material motion. The magnetic anisotropy of iron is another aspect which may have an influence on the presence of magnetic field in the electrochemical cell and therefore affect electrochemical process. [42, 44, 46-48, 50] The easiest direction of magnetization of iron is (100) orientation, followed by (110) and (111) orientation [42]. In our experimental work, presented here, there is no indicator linking the magnetic anisotropy with anodizing of iron, however, the effect of magnetic field cannot be ruled out and should be explored more in depth in further work.

3.4. Conclusions

The anodic iron oxide nanopores/nanotubes were formed on iron (100), (110) and (111) single crystals in ethylene-glycol electrolyte containing 1.5 mol dm^{-3} of water and 0.1 mol dm^{-3} ammonium fluoride. It was found that anodic film growth depends on the index number of facet on which the film is formed. Based on the results obtained the following conclusions can be drawn:

1. Nanoporous/nanotubular anodic film formed on (100) iron facet was formed with electric charge ~30% larger than that on (110) and (111) single crystals. The electric charge increase was accompanied with extensive gas evolution on (100) facet.
2. Chemical composition of anodic film formed on (100) facet was $Fe_2O_3 \cdot FeF_2$ whereas film formed on higher index number was composed of $Fe_3O_4 \cdot FeF_2$, evaluated by high resolution TEM/EDS mapping of FIB lamella.
3. The anodic films formed on (111) and (110) single crystals were of amorphous nature whereas those formed on (100) facet were found to be crystalline. The

crystallization upon anodic film growth is a possible reason for modification of electronic properties followed by extensive oxygen evolution on Fe_2O_3 nanocrystals observed on (100) facet.

References:

1. Iitaka, I., S. Miyake, and T. Iimori, *Examination of passive iron by electron diffraction.* Nature, 1937. **139**(3508): p. 156-156.
2. Mayne, J.E.O. and M.J. Pryor, *392. The mechanism of inhibition of corrosion of iron by chromic acid and potassium chromate.* Journal of the Chemical Society (Resumed), 1949(0): p. 1831-1835.
3. Cohen, M., *An electron diffraction study of films formed by sodium nitrite solution on iron.* The Journal of Physical Chemistry, 1952. **56**(4): p. 451-453.
4. Nagayama, M. and M. Cohen, *The Anodic Oxidation of Iron in a Neutral Solution: II . Effect of Ferrous Ion and pH on the Behavior of Passive Iron.* Journal of The Electrochemical Society, 1963. **110**(6): p. 670-680.
5. Foley, C.L., J. Kruger, and C.J. Bechtoldt, *Electron diffraction studies of active, passive, and transpassive oxide films formed on iron.* Journal of The Electrochemical Society, 1967. **114**(10): p. 994-1001.
6. Kuroda, K., et al., *Electron diffraction study of the passive film on iron.* Journal of The Electrochemical Society, 1982. **129**(10): p. 2163-2169.
7. O'Grady, W.E., *Mössbauer study of the passive oxide film on iron.* Journal of The Electrochemical Society, 1980. **127**(3): p. 555-563.
8. Eldridge, J. and R.W. Hoffman, *A mössbauer spectroscopy study of the potential dependence of passivated iron films.* Journal of The Electrochemical Society, 1989. **136**(4): p. 955-961.
9. Kerkar, M., J. Robinson, and A.J. Forty, *In situ structural studies of the passive film on iron and iron/chromium alloys using X-ray absorption spectroscopy.* Faraday Discussions of the Chemical Society, 1990. **89**(0): p. 31-40.
10. Hoffman, R.W., *Study of passivity of iron by in situ methods: Mossbauer and EXAFS*, in *Passivity of Metals and Semiconductors*, M. Froment, Editor. 1983, Elsevier. p. 147-162.
11. Long, G.G., et al., *Structure of passive films on iron using a new surface-EXAFS technique.* Journal of Electroanalytical Chemistry and Interfacial Electrochemistry, 1983. **150**(1): p. 603-610.
12. Gui, J. and T.M. Devine, *In situ vibrational spectra of the passive film on iron in buffered borate solution.* Corrosion Science, 1991. **32**(10): p. 1105-1124.
13. Rubim, J.C. and J. Dünnwald, *Enhanced Raman scattering from passive films on silver-coated iron electrodes.* Journal of Electroanalytical Chemistry and Interfacial Electrochemistry, 1989. **258**(2): p. 327-344.
14. Ryan, M.P., R.C. Newman, and G.E. Thompson, *An STM study of the passive film formed on iron in borate buffer solution.* Journal of The Electrochemical Society, 1995. **142**(10): p. L177-L179.
15. Davenport, A.J. and M. Sansone, *High resolution in situ XANES investigation of the nature of the passive film on iron in a pH 8.4 borate buffer.* Journal of The Electrochemical Society, 1995. **142**(3): p. 725-730.
16. Toney, M.F., et al., *Atomic structure of the passive oxide film formed on iron.* Physical Review Letters, 1997. **79**(21): p. 4282-4285.
17. Davenport, A.J., et al., *The structure of the passive film that forms on iron in aqueous environments.* Journal of The Electrochemical Society, 2000. **147**(6): p. 2162-2173.
18. Takabatake, Y., et al., *Grain-Dependent Passivation of Iron in Sulfuric Acid Solution.* Journal of The Electrochemical Society, 2014. **161**(14): p. C594-C600.
19. Seo, M. and M. Chiba, *Nano-mechano-electrochemistry of passive metal surfaces.* Electrochimica Acta, 2001. **47**(1): p. 319-325.
20. Fadillah, L., et al., *The role of tungsten species in the transition of anodic nanopores to nanotubes formed on iron alloyed with tungsten.* Electrochimica Acta, 2019. **309**: p. 274-282.
21. Shahzad, K., et al., *Ex situ evidence for the role of a fluoride-rich layer switching the growth of nanopores to nanotubes: A missing piece of the anodizing puzzle.* ChemElectroChem, 2018. **5**(4): p. 610-618.

22. Jubb, A.M. and H.C. Allen, *Vibrational spectroscopic characterization of hematite, maghemite, and magnetite thin films produced by vapor deposition.* ACS Applied Materials & Interfaces, 2010. **2**(10): p. 2804-2812.
23. Chamritski, I. and G. Burns, *Infrared- and Raman-Active phonons of magnetite, maghemite, and hematite: A computer simulation and spectroscopic study.* The Journal of Physical Chemistry B, 2005. **109**(11): p. 4965-4968.
24. Bersani, D., P.P. Lottici, and A. Montenero, *Micro-Raman investigation of iron oxide films and powders produced by sol–gel syntheses.* Journal of Raman Spectroscopy, 1999. **30**(5): p. 355-360.
25. Gasparov, L.V., et al., *Infrared and Raman studies of the Verwey transition in magnetite*. Physical Review B, 2000. **62**(12): p. 7939-7944.
26. Sault, A.G., *Quantitative analysis of Auger lineshapes of oxidized iron.* Applied Surface Science, 1994. **74**(3): p. 249-262.
27. Kovač, J., et al., *Auger electron spectroscopy depth profiling of Fe-oxide layers on electromagnetic sheets prepared by low temperature oxidation.* Applied Surface Science, 2007. **253**(9): p. 4132-4136.
28. Ruby, C. and J. Fusy, *Oxidation of ultrathin iron layers grown on Cu(111).* Applied Surface Science, 1996. **99**(4): p. 393-400.
29. Smentkowski, V.S. and J.T. Yates, *The adsorption of oxygen on Fe(110) in the temperature range of 90 to 920 K.* Surface Science, 1990. **232**(1): p. 113-128.
30. Langell, M. and G.A. Somorjai, *The composition and structure of oxide films grown on the (110) crystal face of iron.* Journal of Vacuum Science and Technology, 1982. **21**(3): p. 858-866.
31. Roosendaal, S.J., A.M. Vredenberg, and F.H.P.M. Habraken, *Oxidation of iron: The relation between oxidation kinetics and oxide electronic structure.* Physical Review Letters, 2000. **84**(15): p. 3366-3369.
32. Pilling, N., *The oxidation of metals at high temperature.* J. Inst. Met., 1923. **29**: p. 529-582.
33. Kowalski, D., D. Kim, and P. Schmuki, *TiO_2 nanotubes, nanochannels and mesosponge: Self-organized formation and applications.* Nano Today, 2013. **8**(3): p. 235-264.
34. Leach, J.S.L. and B.R. Pearson, *Crystallization in anodic oxide films.* Corrosion Science, 1988. **28**(1): p. 43-56.
35. Vermilyea, D.A., *Nucleation of Crystalline Ta_2O_5 During Field Crystallization.* Journal of The Electrochemical Society, 1957. **104**(9): p. 542.
36. Nagahara, K., et al., *Change in the structure and dielectric properties of niobium anodic oxide films during potentiostatic anodizing.* Electrochemistry, 2004. **72**: p. 624-632.
37. Su, Z., et al., *Formation of crystalline TiO_2 by anodic oxidation of titanium.* Progress in Natural Science: Materials International, 2013. **23**(3): p. 294-301.
38. Habazaki, H., et al., *Crystallization of anodic titania on titanium and its alloys.* Corrosion Science, 2003. **45**(9): p. 2063-2073.
39. Beck, G. and R. Bretzler, *Regularity of nanopores in anodic alumina formed on orientated aluminium single-crystals.* Materials Chemistry and Physics, 2011. **128**(3): p. 383-387.
40. Sacco, L., et al., *Investigation of porous anodic alumina templates formed by anodization of single-crystal aluminum substrates.* Thin Solid Films, 2018. **660**: p. 213-220.
41. Courtney, T.H., *Mechanical Behavior of Materials: Second Edition*. 2005: Waveland Press.
42. Kronmüller, H. and S.S.P. Parkin, *Handbook of magnetism and advanced magnetic materials*. 2007, Hoboken, NJ: John Wiley & Sons.
43. Derry, G.N., M.E. Kern, and E.H. Worth, *Recommended values of clean metal surface work functions.* Journal of Vacuum Science & Technology A, 2015. **33**(6): p. 060801.
44. Hall, R.C., *Single-crystal magnetic anisotropy and magnetostriction studies in iron-base alloys.* Journal of Applied Physics, 1960. **31**(6): p. 1037-1038.
45. Liu X., S.M.M., Sooryakumar R., Prinz G. A., Farrow R. F. C., Harp G., *Exchange stiffness, magnetization, and spin waves in cubic and hexagonal phases of cobalt*. Phys. Rev. B, 1996. **53**(18): p. 12166.
46. Hillebrands, B., P. Baumgart, and G. Güntherodt, *In situ Brillouin scattering from surface-anisotropy-dominated Damon-Eshbach modes in ultrathin epitaxial Fe(110) layers.* Physical Review B, 1987. **36**(4): p. 2450-2453.
47. Rupp, G., et al., *Surface magnons in anisotropic ferromagnetic films.* Journal of Magnetism and Magnetic Materials, 1984. **45**(2): p. 404-408.
48. Ueda, Y. and M. Takahashi, *Structure and magnetic properties in single-crystal iron film electrodeposited on a (110) copper crystal.* Journal of Magnetism and Magnetic Materials, 1988. **71**(2): p. 212-218.

49. Yamamoto, M., *On the elastic constants of iron single crystals.* Journal of the Japan Institute of Metals, 1943. **7**(8): p. 346-348.
50. Liu X, S.M., Sooryakumar R., Prinz G. A., Farrow R. F. C., and G. Harp, *Exchange stiffness, magnetization, and spin waves in cubic and hexagonal phases of cobalt.* Phys. Rev. B, 1996. **53**(18): p. 12166.

Chapter 4 The Influence of Alloying Element to Anodic Films on Iron

4.1. Introduction

Anodizing of iron is practically more complex in processing in relation to other valve metals, due to difficulty of keeping the passive state of iron. Growth of porous anodic film is therefore not favored in aqueous electrolytes since at high potential, formation of soluble ferrate ions is promoted [1, 2] as well as anodic gas generation. The key for growth of thick porous anodic layer on iron is therefore good control over the passivity/corrosion which can be effectively provided in organic electrolytes containing small amounts of water and fluorides. The morphology of the anodic layer is mainly controlled by the voltage/current in the anodizing process. In ethylene glycol electrolyte containing 0.1 mol dm^{-3} ammonium fluoride and 1.5 mol dm^{-3} water, the nanopores (Al_2O_3-like) and nanotubes (TiO_2-like) can be formed on iron. The nanoporous-type anodic film is preferentially formed on iron, possibly due to relatively slow kinetics of dissolution of fluoride-enriched cell boundary regions [3]. The partial transition of nanopores into nanotubes is typically observed at enhanced voltages/currents. The primary reason of this transition is formation of fluoride rich layer at metal/anodic-film interface [4] and its transfer to the cell boundary region, once the porous film grows by field assisted plastic flow [3]. Although the formation of nanopores on aluminum is quite well understood, some features of the nanotubular film formation are still the subject of debate. The transport number of cations during film growth is dependent upon the oxide composition and electric field [5-7] . The relatively high contribution of both cations and anions to ionic current is characteristic of the amorphous anodic oxides. The anodic films are contaminated with electrolyte anion species, and their distributions in the anodic films are also dependent upon their mobilities. Thus, the incorporated anions are often used as a tracer for the investigation of ionic transport process during film growth [3, 8-13].

In the present study, the anodizing of Fe-W alloy was studied for the first time. The results were compared with that of anodizing of pure Fe for a better understanding the growth mechanism of the anodic films. Moreover, the influence of operating conditions, especially anodizing voltage on the geometry of nanopores including pore diameter, is

analyzed. The primary interest in this study was to examine the influence of tungsten on the growth process as well as chemical changes of formed oxide.

4.2. Experimental Details

Magnetron-sputtered Fe and Fe-W (9 at.%) films having the thickness of approximately 550 nm were used for anodizing. The target consisted of 99.99 % pure iron disk of 100 mm in diameter and one 99.9 % tungsten disk of 20 mm in diameter placed on the sputter erosion region of the iron disk. Sputter deposition was carried out in 99.99% pure argon atmosphere at 2.5×10^{-3} Torr with the current 0.5 A and voltage 350 V for 15 min. The surface image of Fe and Fe-W are shown on Figure 4.1. The thickness of the alloy deposit was 550 nm (Fig. 4.1c). The composition of the alloy was evaluated by electron probe micro analyzer (EPMA) and equaled to 9 at.% tungsten.

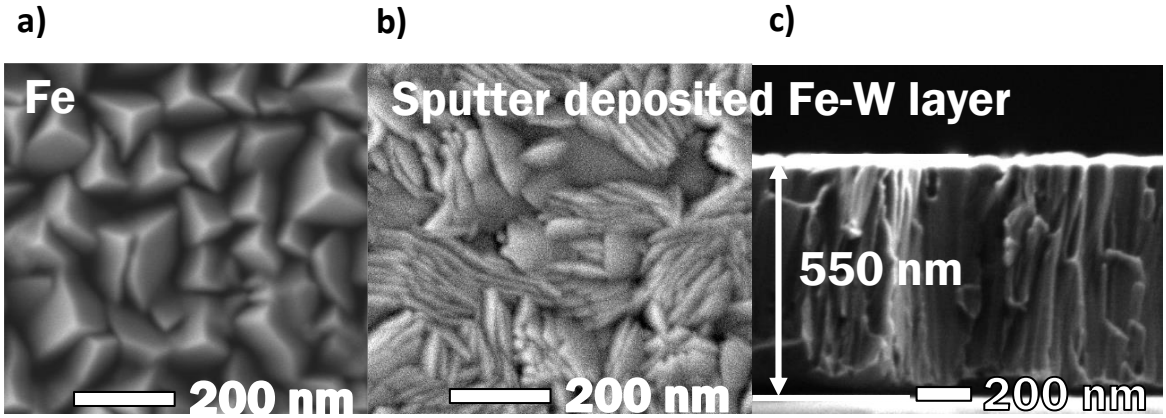

Figure 4.1 Surface SEM images of magnetron sputter deposited (a) Fe and (b) Fe-W and (c) cross section SEM image of Fe-W at 2.5×10^{-3} Torr with the current 0.5 A and voltage 350 V for 15 min.

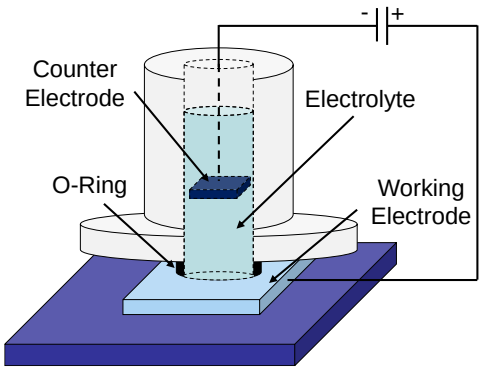

Figure 4.2 Schematic illustration of the anodizing apparatus used in this study at room temperature.

The Fe and Fe-W alloys were anodized at 40-60 V for 300 s in ethylene glycol electrolyte containing 0.1 mol dm^{-3} ammonium fluoride and 1.5 mol dm^{-3} deionized water at room temperature in o-ring type cell with a two-electrode system using platinum counter electrode without stirring of electrolyte. The schematic illustration of the anodizing cells is shown in Figure 4.2. After anodizing, the specimens were rinsed in ethylene glycol, ethanol, and then dried in the air stream.

The surface morphology and cross sections of the specimens were examined by a Zeiss Sigma 500 field emission scanning electron microscope (SEM) instrument. Elemental depth profiles of the specimens were obtained by a Horiba Jobin Yvon 5000 RF glow discharge optical emission spectrometer (GDOES) in neon atmosphere at 800 Pa by applying 35 W RF power under a pulse mode. The data were recorded at a sampling interval 0.02 s. The diameter of sputtered area was 4 mm. The cross-sections of anodic films were examined by a JEOL, JEM-ARM200F scanning transmission electron microscope (STEM) with energy dispersive X-ray spectrometry (EDS) facilities. Electron-transparent sections were prepared by a Hitachi FB-2100 focused ion beam (FIB) system employing a Ga^+ ion beam. X-ray photoelectron spectroscopy (XPS) measurements were acquired using a Kratos Axis Supra spectrometer, equipped with a monochromatic Al Kα radiation (1486.7 eV) source. The instrument work function was calibrated to give a BE of 84.0 eV ± 0.1 eV for the $4f_{7/2}$ line of metallic gold and the spectrometer dispersion was adjusted to give a BE of 932.62 eV for the Cu $2p_{3/2}$ line of metallic copper. Energy resolution was examined on silver sample. Survey (wide) spectra were collected with a quality corresponding to the full width at half maximum (FWHM) parameter for Ag 3d line equal to 0.71 eV at energy step size equal to 0.5 eV. For high resolution spectra the FWHM parameter for Ag 3d line was equal to 0.58 eV at step size of 0.1 eV. Kratos charge neutralizer system was used to reduce charge compensation. The peaks fitting was conducted using CasaXPS software version 2.3.18 on a Shirley background. All spectra were calibrated using the adventitious C 1s peak with a fixed value of 285.0 eV. The in-depth composition of the films was probed by using secondary-ion mass spectroscopy (SIMS). As-received samples were transferred without special pre-treatment to the analytical chamber where the pressure was 7×10^{-10} Torr. Distribution of elements was obtained with a time-of-flight SIMS apparatus (TOF SIMS 5, ION-TOF GmbH) operating in dual beam mode. Samples were sputtered by Cs^+ ions (2 keV, 135 nA), rastered over 320 μm by 320 μm area. Exposed this way, internal layers of films were analyzed with use of Bi^+ ions (at 64 μm by 64 μm central region only). The primary ion (target) current was typically 1.2 pA. Low energy electron flood gun was used to reduce sample charging during analysis. The internal mass calibration was performed using several ions from the mass range starting from C^- up to $W_2O_6^-$.

4.3. Results and Discussion

4.3.1. Influence of water concentration

Figure 4.3 shows the current density transient during anodizing Fe-W at 60 V in ethylene glycol electrolyte containing 0.1 dm^{-3} ammonium fluoride and various concentrations of water at 20 ^{o}C. The current density increases with an increase in water concentration during the constant-voltage anodizing at 60 V. The electric charge increases linearly with water concentration. As a consequence of this increase in the electric charge during anodizing, the thickness of the anodic film also increases with water concentration up to 1.5 mol dm^{-3} (Fig. 4.4).

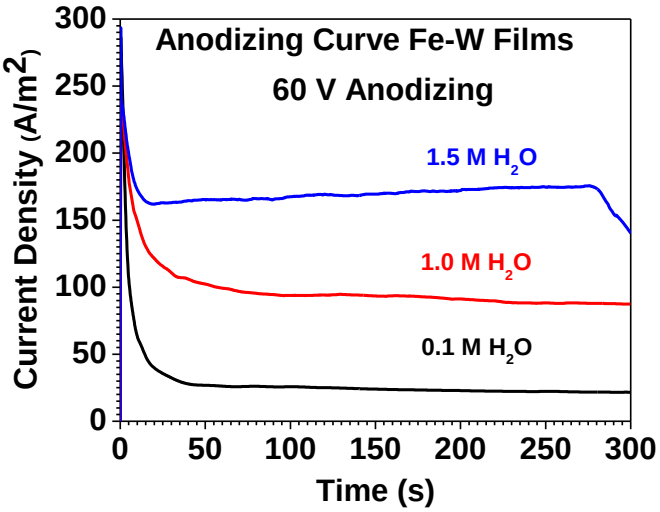

Figure 4.3 Current-time curves of Fe-W during anodizing at 60 V in ethylene glycol electrolyte containing 0.1 mol dm^{-3} ammonium fluoride and various concentrations of water at room temperature.

The surfaces and cross-sections of the anodized specimens at various water concentrations were examined by scanning electron microscopy. Fig. 4.4 shows the surface and cross-section images of the iron anodized at 60 V in the electrolyte from the lowest water concentration 0.1 mol dm^{-3} to 1.5 mol dm^{-3}. The porous anodic film is developed at all conditions and the size of pores increases with increasing water concentration. The thickness of the anodic film at 0.1 mol dm^{-3} water is 0.35 µm. On the other concentration of water, the nanotubular formation was formed, the anodic films were detached from the metal substrate in the cross-sectional scanning electron micrographs (Figs. 4.4), which probably occurred during fracturing of the anodized specimens for SEM observations.

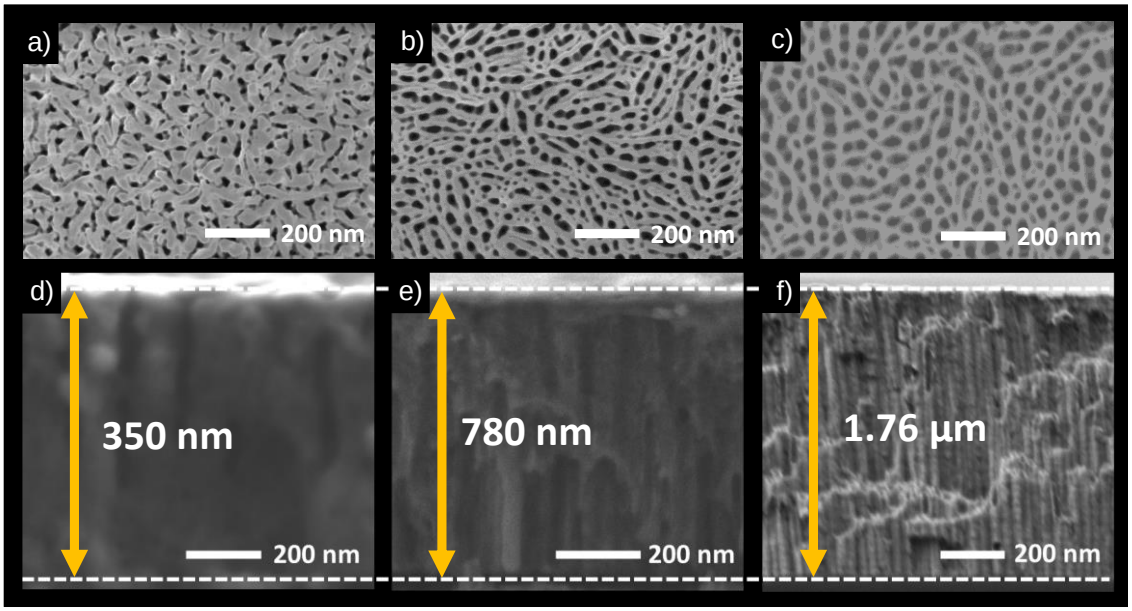

Figure 4.4 Surface and cross-section morphology SEM images for Fe-W (9 at.%) alloy anodized at 60 V in ethylene glycol electrolyte containing (a) 0.1, (b) 1 and (c) 1.5 mol dm^{-3} of water and 0.1 mol dm^{-3} of NH_4F at room temperature.

4.3.2. Influence of formation voltage

Anodizing of sputter-deposited Fe and Fe-W (9 at.%) alloy was performed at a constant voltage between 40 V and 60 V in ethylene glycol electrolyte containing 1.5 mol dm^{-3} water and 0.1 mol dm^{-3} NH_4F at room temperature for 300 s. Figure 4.5 shows the current-time (*j-t*) transients obtained during anodizing of both specimens. Two distinct stages are clearly visible on *j-t* curves Fig. 4.5.; the first stage of anodizing, observed within the first tens of seconds is characterized by rapid current drop and is typically associated with initial formation of barrier-type oxide at the alloy/electrolyte interface [5] and possible pore initiation (Fig. 4.6). The second stage of anodizing is a quasi-steady state where the current density is nearly constant. The time scale for the stage I is independent of the applied voltage, but the magnitude of current drop slightly increases with anodizing voltage. The current drop in stage I region is seven times faster for Fe-W alloy than that for pure Fe so that a quasi-steady state anodizing condition is more rapidly established on the Fe-W alloy. An initial anodizing stage is more distinct by plotting *j-t* curves in the logarithmic scale. [14, 15] This is more apparent when one looks at the *j*-log*t* graph and compares charge passed during the first stage of anodizing of 2.2 and 0.9 C cm^{-2} for Fe and Fe-W, respectively, estimated at 40 V where the contribution of oxygen evolution reaction, involved during anodizing of Fe and Fe-W alloy in this electrolyte, is significantly reduced [3].

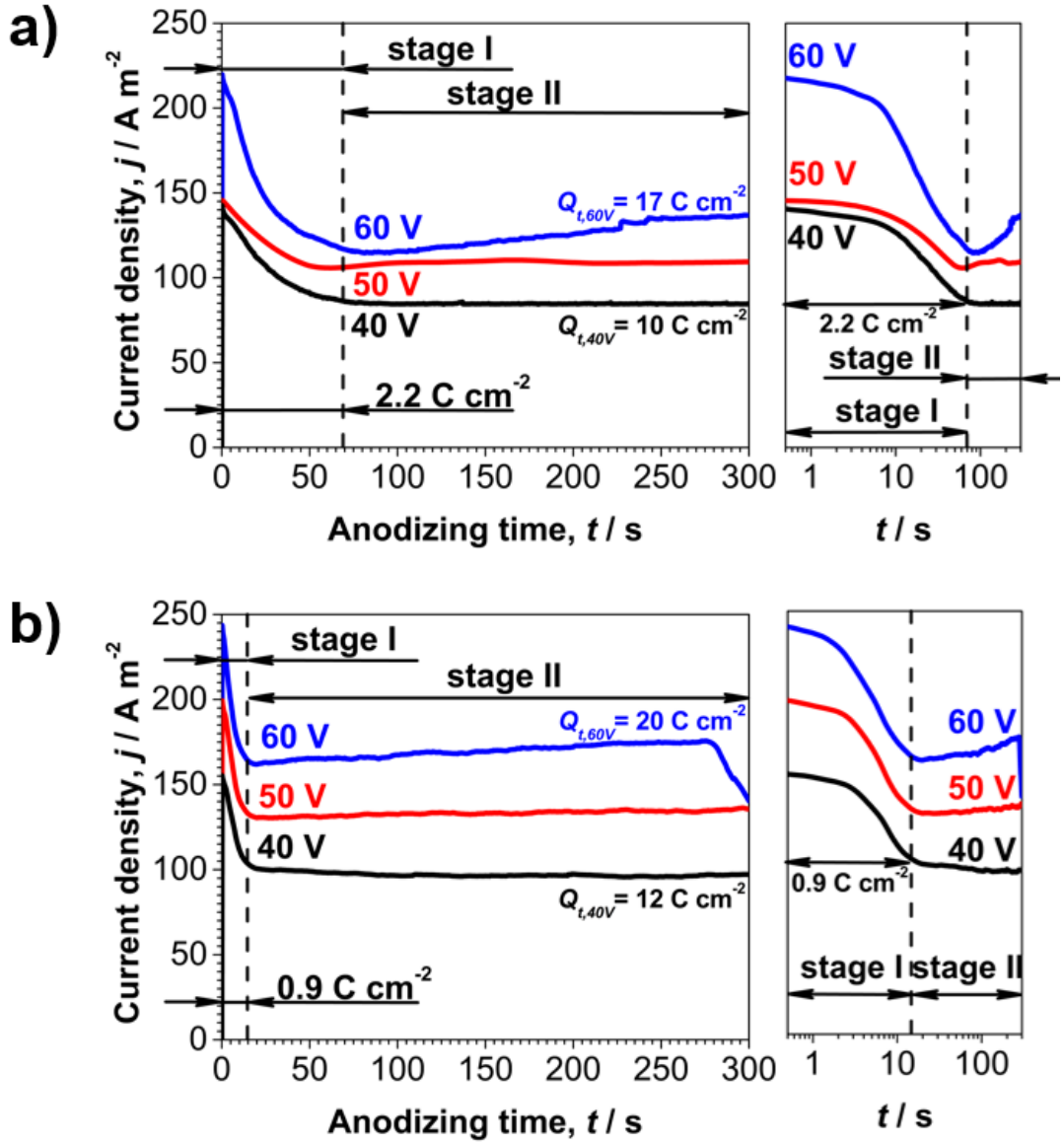

Figure 4.5 Current-time (j-t) responses for anodizing of sputter deposited (a) Fe and (b) Fe-W (9 at.%) alloy at 40 V, 50 V and 60 V in an ethylene glycol electrolyte containing 1.5 mol dm^{-3} of water and 0.1 mol dm^{-3} of NH_4F at room temperature.

During anodizing of Fe and Fe-W alloy, oxygen evolution was observed by naked eye for anodizing at 60 V and became less significant at lower voltages. The shape of *j-t* curve for Fe in Fig. 4.5a strongly depends on the applied voltage and is characterized by a steady state current density at 40 V while the current density gradually increases at 50 and 60 V probably due to Joule heat effect [3]. The current density for anodized Fe-W alloy in Fig. 4.5b is slightly higher than the current density for pure Fe in Fig. 4.5a due to the higher electric field applied over a thinner barrier layer formed on Fe-W alloy as discussed later. The total charge passed during 300 s anodizing of Fe and Fe-W at 40 V

equals to 10 and 12 C cm^{-2}, respectively. The current drop observed during last 20 s of anodizing of Fe-W alloy at 60 V results from consumption of the alloy above glass substrate and subsequent narrowing of the surface area available for oxidation of Fe-W, having negligible effect on the final structure.

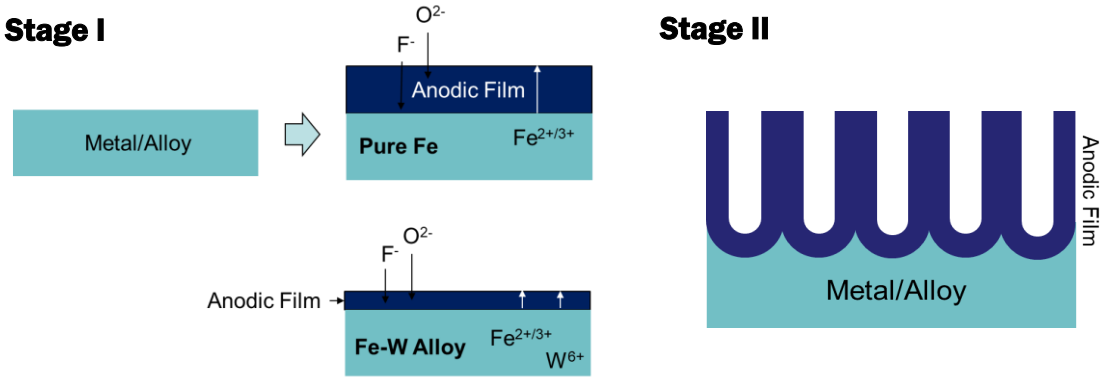

Figure 4.6 Schematic illustration of the growth mechanism of anodic Fe and Fe-W during stage I and Stage II.

The cross-section SEM images for Fe-W alloys anodized at 40-60 V for 300 s are demonstrated in Fig. 4.7 with an anodic layer formed on pure Fe at 60 V shown as a reference. The thickness of anodic layer varies with applied voltage and equals to 0.98, 1.28 and 1.76 µm for alloy anodized at 40, 50 and 60 V, respectively, aligned with higher electric field at higher anodizing voltage. The thickness variations corelate very well with the applied total electric charge (Q_t) of 12, 15 and 20 C cm^{-2} upon anodizing at 40, 50 and 60 V, respectively.

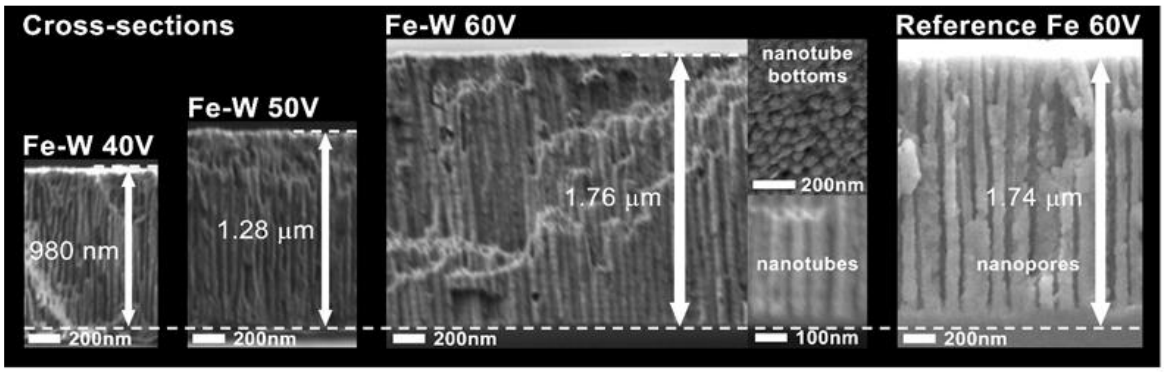

Figure 4.7 Cross-section SEM images of nanopores/nanotubes formed by anodizing of Fe-W alloy at 40, 50 and 60 V. The anodic layer formed on pure Fe at 60 V is shown as a reference. The metal/alloy layers were anodized in ethylene glycol electrolyte containing 1.5 mol dm^{-3} of water and 0.1 mol dm^{-3} of NH_4F at room temperature.

This suggests that the enhanced oxygen gas generation observed at higher anodizing voltage is due to the increased current density, not the increased current efficiency for gas generation. Anodizing of Fe-W alloy at 60 V results in formation of

1.76 μm thick anodic layer which is approximately the same as anodic film formed on pure Fe shown as a reference in Fig. 4.7. The total electric charge of 17 C cm^{-2} is required for anodic film development on pure Fe which is 15% less than that for Fe-W case at the same anodizing conditions. The slight difference in Q_t value may be related to the thickness/morphology changes and/or oxygen evolution reaction aspects.

The classic Al_2O_3-like nanopores are developed on pure Fe as expected for short anodizing time and relatively low voltage impacts according to the previous study[3]. The detailed analysis of the anodic layer formed on Fe-W alloy uncovers the shape of TiO_2-like nanotubes (Fig. 4.7). The inset of SEM image of Fe-W alloy at 60V in Fig. 4.7 shows that the bottom part of the anodic film is composed of the array of nanotubes.

The surface morphology of nanoporous/nanotubular anodic film formed by anodizing of pure Fe and Fe-W alloy at 40-60 V is shown in Fig. 4.8. The microstructure of the as-deposited substrate surface (Fig. 4.8 a,e) has an impact on the surface morphology and self-organization of pores/tubes particularly observed at lower anodizing voltages for Fe-W case where the formed nanopores/nanotubes are organized along the longitudinal grains (Fig. 4.8). Such arrangement can be clearly understood in terms of preferential nucleation of the pores in the dimples [16] of the textured alloy which slightly differs from that of pure Fe. The pore diameter and the interpore distance linearly increase with anodizing voltage 40-60 V from 50 to 110 nm and from 30 to 60 nm for anodic film formed on pure Fe and Fe-W alloy, respectively (Fig. 4.9). The effective cell size reduction is therefore observed with alloying of the iron with tungsten.

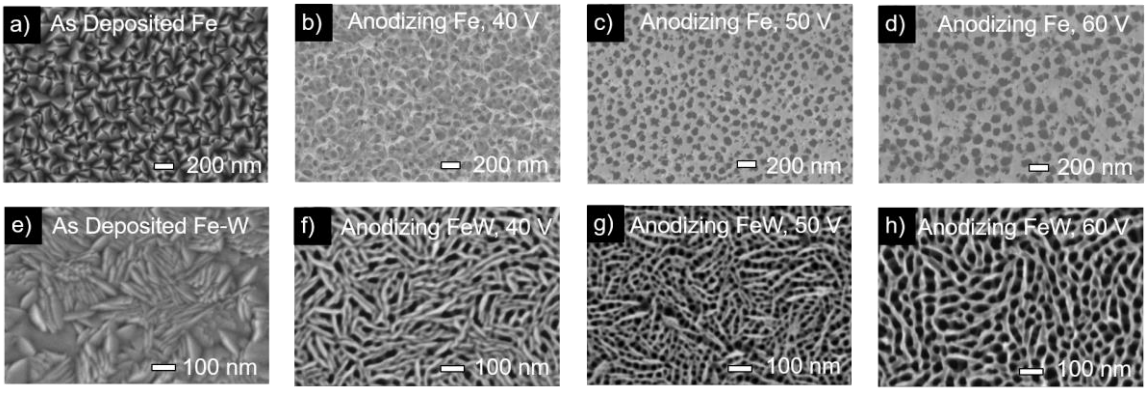

Figure 4.8 Surface morphology images for (a,e) as deposited Fe and Fe-W alloys, (b-d) Fe and (f-h) Fe-W (9 at.%) alloy anodized at 40-60 V in ethylene glycol electrolyte containing 1.5 mol dm^{-3} of water and 0.1 mol dm^{-3} of NH_4F at room temperature.

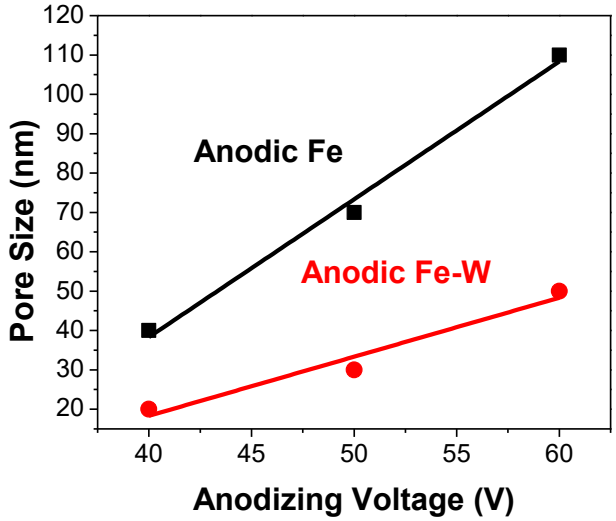

Figure 4.9 Pores size as a function of anodizing voltage for anodic films formed on Fe and Fe-W alloy anodized in ethylene glycol electrolyte containing 1.5 mol dm^{-3} of water and 0.1 mol dm^{-3} of NH_4F at room temperature.

4.3.3. Multilayer Fe/Fe-W/Fe

Since nanotubes morphology was easier developed by the addition of tungsten on the iron substrate, further investigation of the formation of anodic films for the tracer studies at various water concentration at 50 V anodizing voltage was carried out. Backscattered images from scanning electron micrographs reveal the tungsten tracer, by atomic number contrast, as a fine, light band, in the columnar-grained sputtering-deposited iron on Figure 4.10.

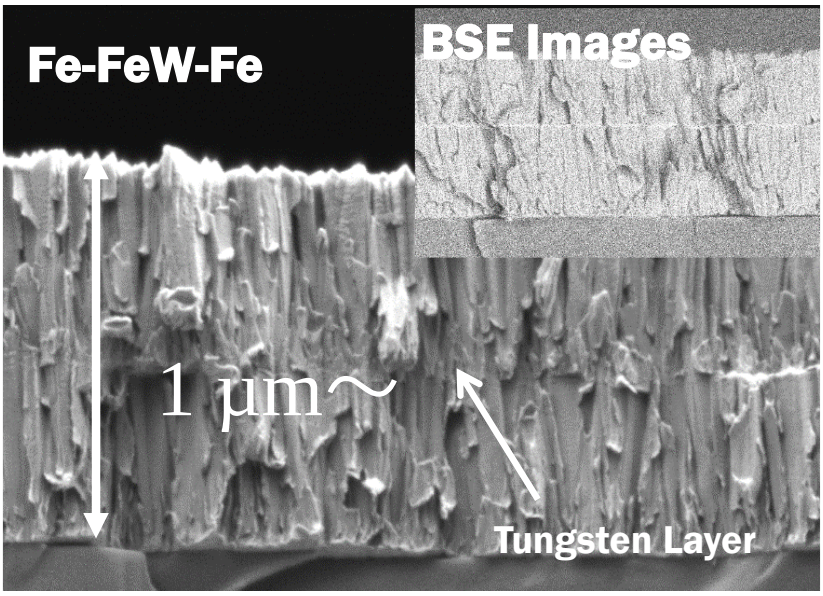

Figure 4.10 Cross-section SEM images and BSE of sputter deposited Fe/Fe-W/Fe at 2.5×10^{-3} Torr with the current 0.5 A and voltage 350 V for 15 min/5 min/15min.

Figure 4.11 show the surface and cross-section morphologies of the anodic films formed at 1.0 and 1.5 mol dm^{-3} water concentration at the 50 V. Surface morphologies, shown in Fig. 4.12, demonstrate that a nanotubes morphology is developed. However, the cross-section images show that an undefined porous morphology is always present at the bottom part of the anodic films. The formation of nanotubes will be discussed later in detail.

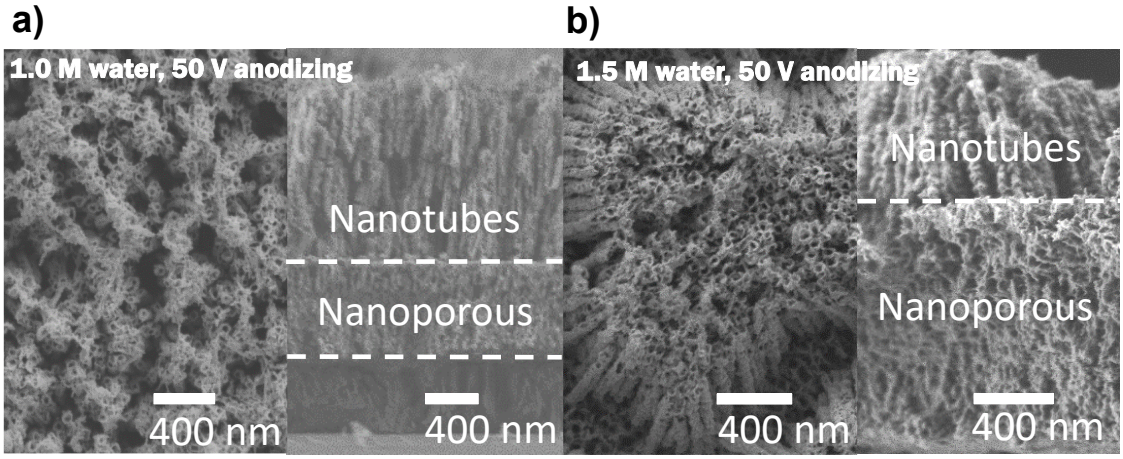

Figure 4.11 Surface morphology images for Fe/ Fe-W/Fe anodized at 50 V in ethylene glycol electrolyte containing (a) 1.0 and (b) 1.5 mol dm^{-3} of water and 0.1 mol dm^{-3} of NH_4F at room temperature.

4.3.4. Composition of anodic films

Figure 4.12 (a,b) shows GDOES elemental depth profiles, displaying the change in the optical emission intensities from oxygen, iron, fluorine and tungsten with the time of sputtering for Fe and Fe-W anodized at 60 V. The depth distribution of Fe, W and O clearly identifies the interface between alloy and formed anodic film. The total time required to sputter through the thickness of the porous anodic film is approximately 22 and 54 s for pure Fe and Fe-W alloy, respectively, resulting from different sputtering rates and variations in porosity. The GDOES depth profile revealed the incorporation of fluorine species from electrolyte and their distribution in anodic layer strongly depending on alloying element. The enrichment of fluoride in porous anodic film immediately above the metal/film interface formed on pure Fe should be associated with faster migration of F^- ions relative to that of O^{2-} ions under the high electric field during film growth [4]. The accumulation of fluorides at the metal/oxide interface for pure Fe case is evident from high resolution transmission electron microscope / energy dispersive spectroscopy (TEM/EDS) mapping studies shown in a previous study [3]. The essential difference in the elements distribution for porous films developed on Fe and Fe-W alloy is the unusual

distribution of fluorine, *i.e.* the absence of F peak at alloy/oxide interface for Fe-W system. Another interesting feature for anodic film developed on Fe-W alloy is the presence of oxygen peak at the first 10 s of sputtering time suggesting modification of surface region, both discussed in the next section of this chapter.

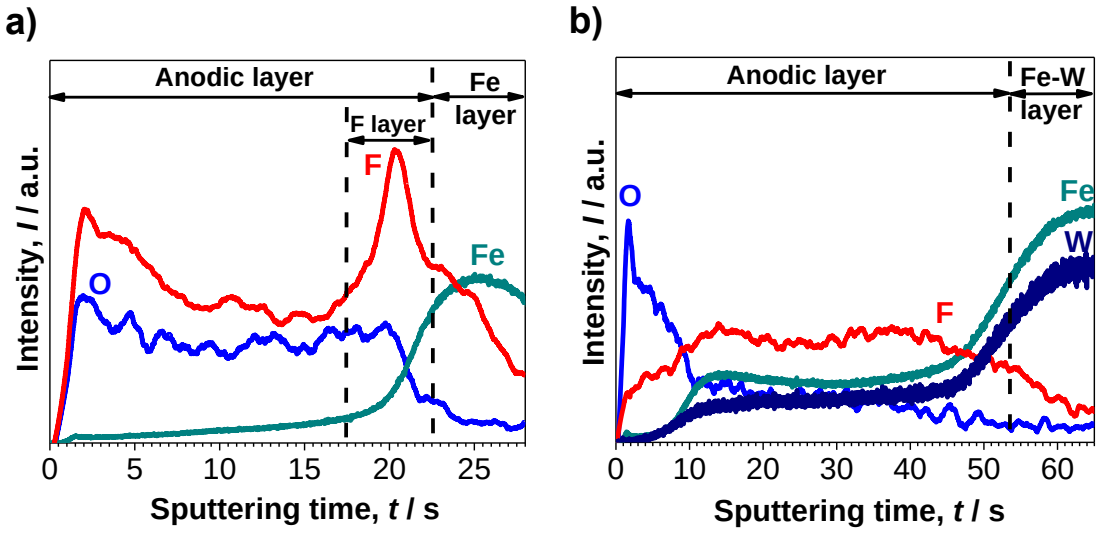

Figure 4.12 Glow discharge optical emission spectroscopy (GDOES) depth profiles for anodic layers formed at 60 V on a) pure Fe and b) Fe-W alloy.

The qualitative analysis of the surfaces for Fe and Fe-W alloy anodized at 60 V was conducted based on the XPS wide scan spectra (Fig.4.13 a.). Results allowed to confirm the presence of Fe, W, F, C and O composing nanoporous/nanotubular anodic films. The high-resolution spectra Fe 2p region of anodic films formed on Fe and Fe-W, shown in Fig. 4.13 b. and c., consist of two peaks assigned to the Fe $2p_{3/2}$ and Fe $2p_{1/2}$ spin-orbits components (Δ=13.2 eV). Determination of iron oxidation state was based on the Fe $2p_{3/2}$ region which was curve-fitted with two well resolved components located at 711.3 and 714.2 eV. According to literature data, analysis of the lower binding energy peak is not unequivocal. This peak can be related to the presence of Fe(II) and Fe(III) in FeF_2 [17-19], Fe_2O_3 [19, 20] or Fe_3O_4 [21]. In addition, binding energy of F 1s (648.8±0.2 eV) and its symmetrical shape is in accordance with the literature given for metal fluoride [17, 18, 22]. The presence of FeF_2 is consistent with identification of fluoride-rich-layer by Shahzad et al. [3] by means of TEM/EDS elemental mapping in the transition of anodic nanopores into nanotubes formed on bulk iron. The primary location of FeF_2 is the cell boundary and oxide/metal interface [3]. In the XPS spectrum a very intense signal of O 1s region was recorded. The spectrum can be resolved into

two peaks for anodic Fe or three peaks for anodic Fe-W. The high binding energy component O 1s (532.0 eV) recorded for anodic Fe is related to the presence of organic impurities, which is confirmed in C 1s region (signal from C-O, C-O-C, C-O=O, carbonates). The other peak, at 530.3 eV comes from lattice oxygen which confirm the presence of Fe_xO_y. The position of this peak slightly shifts into higher binding energy (530.5 eV) after addition of tungsten, which is similar to the O 1s values for WO_3 [23]. Additionally, 531.7 and 533.5 eV appear. High binding energy peaks can be assigned, like previously, to the presence of organic and adsorbed water, respectively. Based on the W 4f region it can be excluded that the peak around 531.7 eV is related to the presence of WO_{3-x} phase, caused by the existence of hydroxyl groups on the surface. The W 4f has well separated spin-orbit components (Δ=2.15 eV). The position of W $4f_{7/2}$ (35.8 eV) and its symmetrical shape suggest presence of only WO_3 phase [24-26].

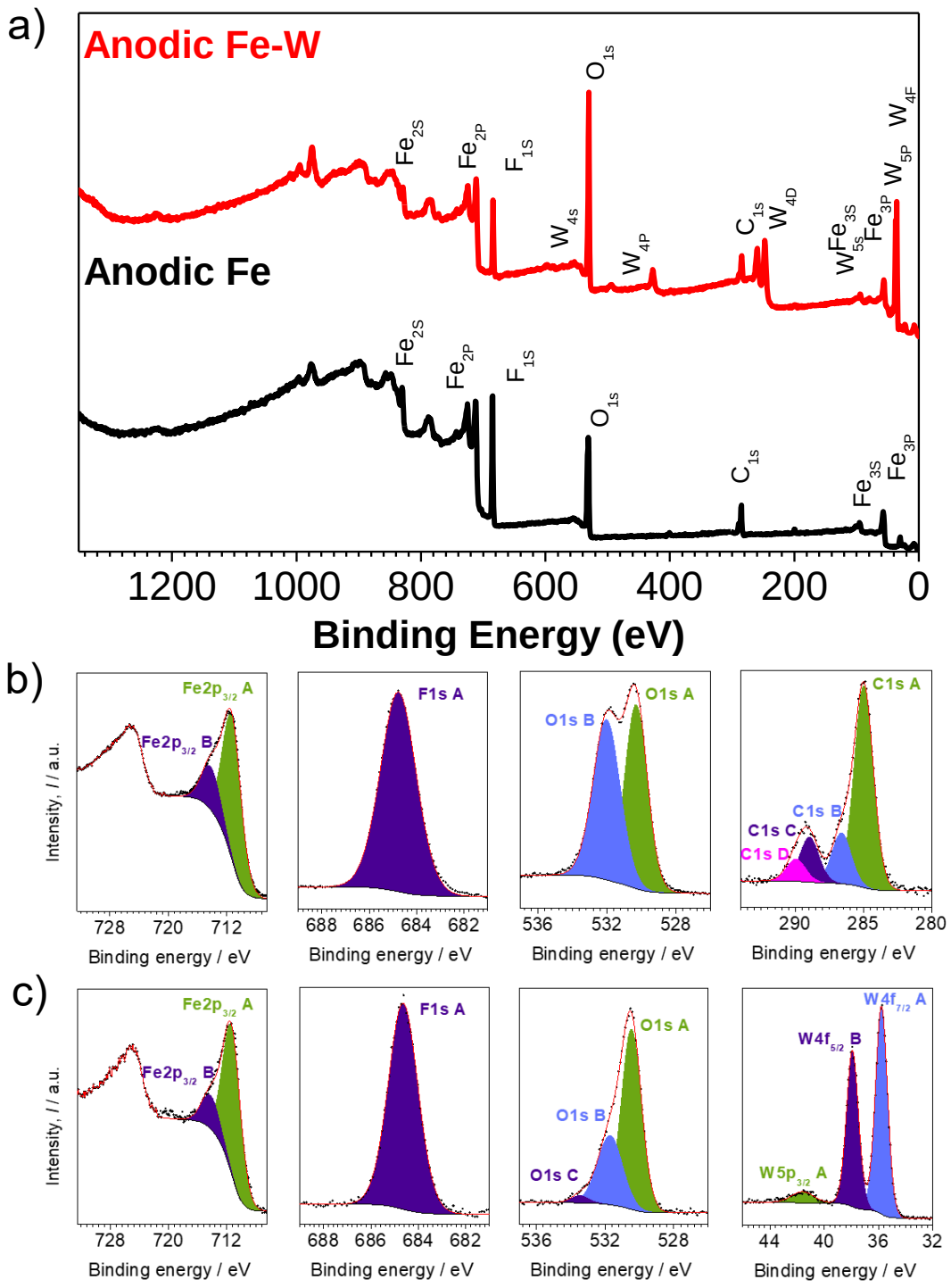

Figure 4.13 a) The wide XPS spectra and high resolution spectra of Fe 2p, F 1s, O 1s, W 4f and C 1s core level spectra for b) anodized pure Fe, c) anodized Fe-W alloy at 60 V in ethylene glycol electrolyte containing 1.5 mol dm^{-3} of water and 0.1 mol dm^{-3} of NH_4F for 300s at room temperature.

ToF-SIMS mass spectra, cumulated during the depth profiling measurement, were acquired in negative mode to avoid the influence by an external oxygen source (Fig. 4.14). The spectra show many components which can be assigned to the iron oxides, iron fluorides, tungsten oxides and tungsten oxide fluorides ion fragments. For detailed analysis the 225-325 m/z region was chosen as the most characteristic ions produced at the sample surface are WO_x clusters [27]. Anodizing of tungsten or its alloys typically results in formation of WO_3 domains in anodic film structure [28, 29]. The complexity of the spectrum is affected by the presence of oxide-fluoride forms. Tungsten has five isotopes of which four are present in the predominant quantity and relatively similar amount. This isotopic fingerprint allowed us to distinguish the contribution of individual fragments from groups of peaks that occurs at 230, 246, 271 and 293 m/z values. Figure 4.14. shows that WO_3^- and various $WO_xF_y^-$, such as WOF_4^- and $WO_2F_2^-$, could be assigned. Since WF_6 form was our main point of interest a zoomed data at 292.5-300.5 m/z range is given in Fig. 4.14 proving that WF_6 molecule is present in the film structure. The depth profile experiment allowed to monitor the content of above fragments in the nanotubular film structure. Figure 4.14 shows that various fluorides forms are stable among the film depth. A typical behavior for ToF-SIMS measurements in the depth profiling mode is the stabilization of the etching process, therefore, the content of individual fragments in the first stage undergo non-specific changes during the first 60 seconds. It is obvious that the only component that intensity change differs from the other fragments is WF_6^-. A clear disappearance of this component in the near-surface region is visible. We assume that this part of the film has been exposed to air/water and this reactive compound has decomposed as discussed in the next section of the paper.

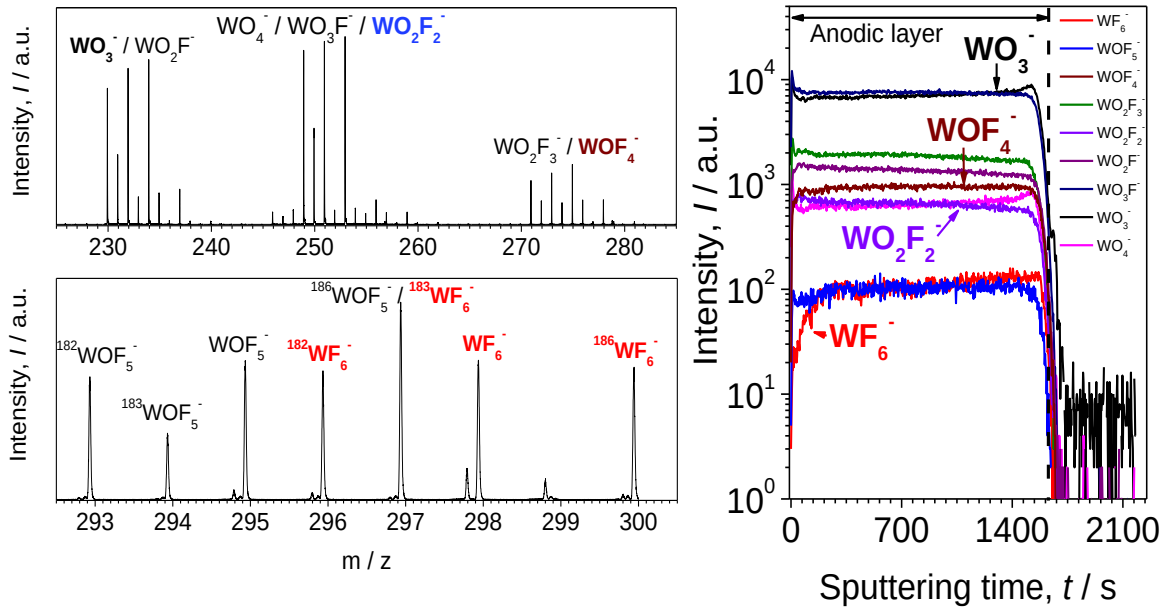

Figure 4.14 Negative ion ToF-SIMS mass spectra (a,b) and depth profile (c) for Fe-W alloy anodized at 60V in ethylene glycol electrolyte containing 1.5 mol dm^{-3} of water and 0.1 mol dm^{-3} of NH_4F for 300s at room temperature.

4.3.5. Analysis of film by STEM

The transmission electron micrograph (TEM) of a FIB lamella for Fe-W alloy anodized at 60 V is shown in Fig. 4.15. The shape of nanotubes is evident from high angle annular dark field (HAADF) images. The thickness of the anodic film is approximately 1.7 μm with the inner nanotube diameter of ~80 nm, consistent with previous SEM observations. The regions with lighter appearance on TEM micrograph (Fig. 4.15 b) are corresponding to nanotube walls composed of mixed tungsten/iron oxide containing fluorides. Relatively thick layer at the alloy/oxide interface was detected (Fig. 4.15 c). Its thickness varies across the FIB lamella from 40-130 nm as demonstrated in low resolution TEM image (Fig. 4.15 d). Such large thickness variations cannot be caused by electrochemical reaction as the high electric field is primarily localized in the barrier-layer forming uniform anodic layer depending on the applied voltage. Those thickness variations supported by unusual GDOES elemental depth distribution suggest chemical nature of its formation.

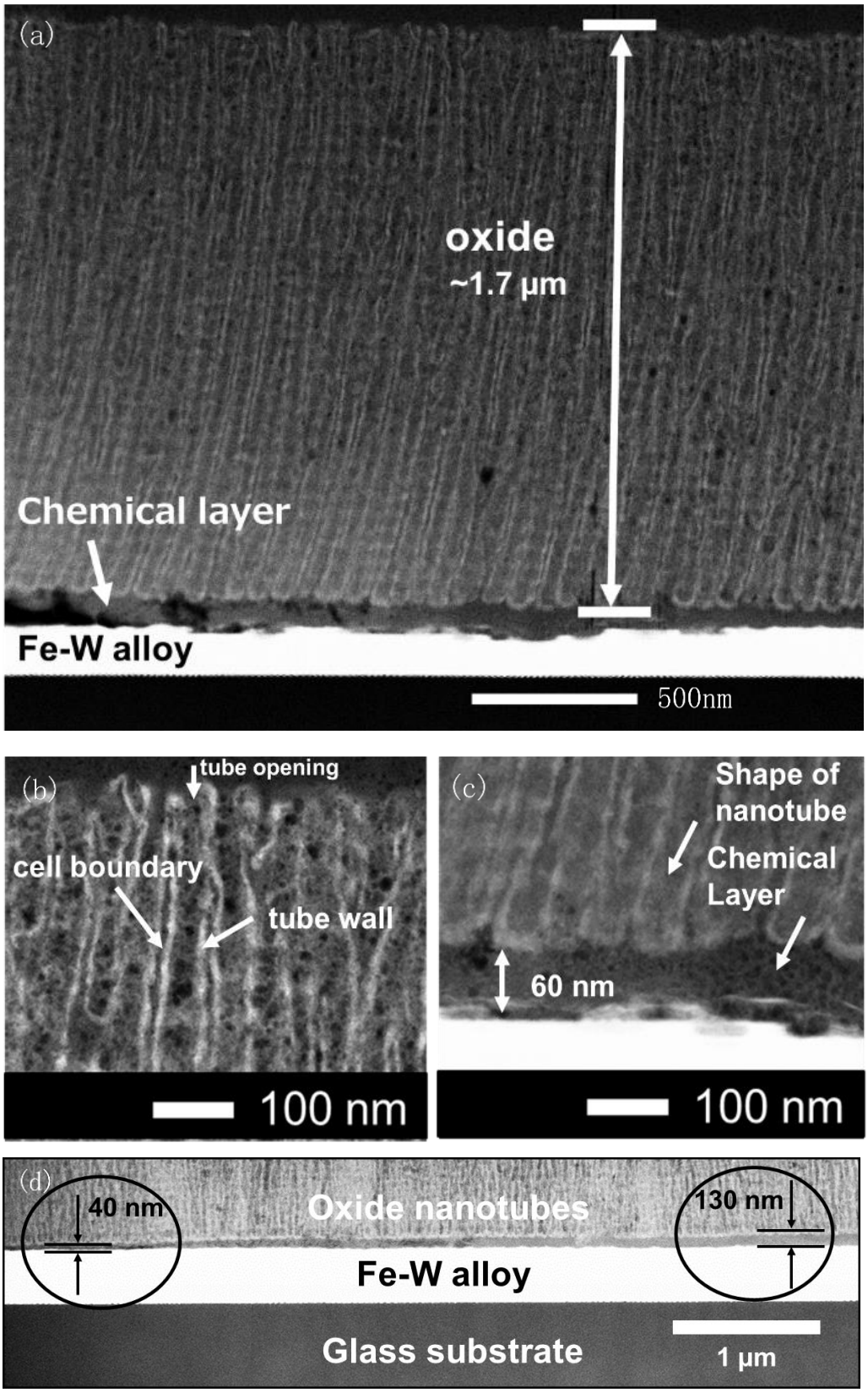

Figure 4.15 High angle annular dark field (HAADF) images of (a) full view, (b) upper side, (c,d) bottom side FIB lamella for Fe-W alloy anodized at 60 V in ethylene glycol electrolyte containing 1.5 mol dm^{-3} of water and 0.1 mol dm^{-3} of NH_4F at room temperature.

4.3.6. Growth of nanoporous/nanotubular anodic films

The above findings reveal that alloying of iron with 9 at.% of tungsten results in structural changes upon anodizing in ethylene glycol electrolyte containing 1.5 mol dm^{-3} water and 0.1 mol dm^{-3} ammonium fluoride. Essentially, two types of anodic structures are observed: Al_2O_3-like nanopores developed on pure Fe, and TiO_2-like nanotubes developed on Fe-W alloy. Schematic illustration of formed structures is demonstrated in

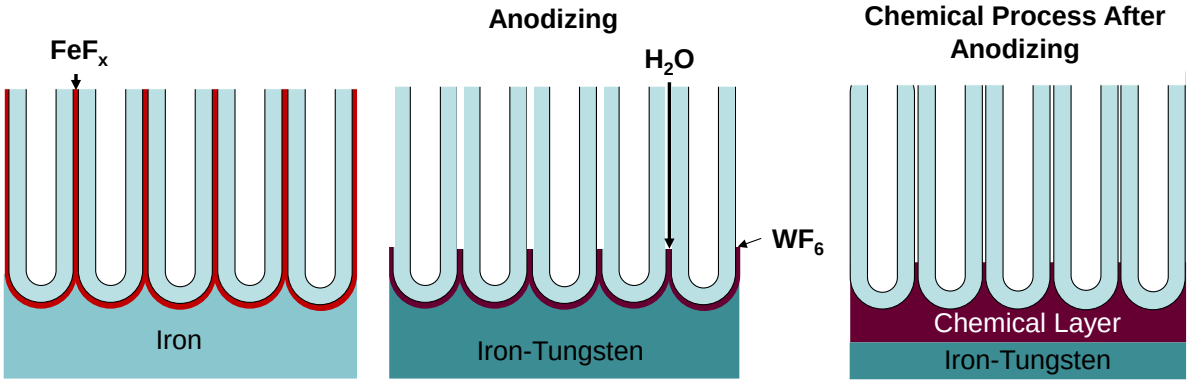

Figure 4.16 Schematic illustrations of anodic porposed growth mechanism for nanopores/nanotubes formed on a) iron, and b) iron tungsten alloy, c) illustrates post reaction with tungsten fluorides leading to formation of thick layer at metal/oxide interface.

Fig. 4.16.

Two fundamental mechanisms have been proposed for formation of nanoporous /nanotubular anodic films: i) field assisted dissolution model [30], and ii) field assisted flow model [31-33]. Very recently Shahzad et al. showed that porous anodic film on iron may grow according to both models critically depending on the water concentration in electrolyte [3]. In the classic field assisted dissolution model, the barrier-layer between metal and porous layer is kept constant under constant voltage. The formed structure is typically characterized by i) presence of less organized nanopores, ii) thick barrier-layer, and iii) flat metal/oxide interface. In the field assisted flow model, which was proposed using tungsten tracer studies [32-35], the resulting structure is typically characterized by i) presence of nanopores or nanotubes with high degree of self-organization, ii) thin barrier layer, iii) scalloped metal/oxide interface.

The key mechanism for the growth of anodic film on Fe-W alloy is the field assisted flow model, as only the plastic flow may rearrange the initial horizontal position of anodic layers into vertical position and therefore develop nanotube with the composition of the -outer and -inner shell corresponding to -bottom and -top of the barrier

layer, respectively [5]. The general growth is analogous to that formed on pure Fe in electrolyte containing 1.5 mol dm^{-3} water [3] except a few fundamental aspects: i) the transition of nanopores into nanotubes is observed by alloying with tungsten, ii) significant reduction of the cell size (nanotube diameter) is obtained on Fe-W alloy, iii) relatively thick layer is produced at alloy/oxide interface.

The nanotubes instead of nanopores are considered to be formed due to faster kinetics of WF_6 (or similar compound) dissolution. WF_6 domains and their decomposed forms have been detected on ToF-SIMS mass spectra in the nanotubular film. Taking into account fast inward-migration of F^- [4] and very slow outward-migration of W^{6+} species [36] in anodic film, the primary location of WF_6 compound should be the bottom of barrier-layer which is switched to the cell boundary position due to stress generated at the barrier-layer and material flow according to the field assisted flow model as discussed above. The difficulty in detection of WF_6 is its decomposition due to hydrolysis reaction [37] in contrast to FeF_2 which has low solubility constant of $8.3x10^{-3}$ mol dm^{-3} [38]. WF_6 is generally considered to be a gas at standard conditions [37, 39], however, may be stabilized by the oxide structure as the WF_6 domains and their decomposed forms, have been identified by ToF-SIMS analysis. The primary consequence of alloying with tungsten is therefore modification of the cell boundaries and full transition into nanotubes.

The cell size, which is corresponding to the developed nanotube diameter, is effectively modified by alloying element as demonstrated in Fig. 4.9. The reduction of cell size may be understood as an effect of thinner barrier layer formed on Fe-W alloy during the initial growth as observed in stage I of the *i-t* curves in Fig. 4.1 and therefore development of smaller in size cells by means of horizontal to vertical oxide reorganization due to material flow effect. Since the same voltage is applied, over a thinner barrier layer on Fe-W, to some extent a stronger electric field may be applied leading to morphological alternations.

The origin of a thick layer formed at metal/nanotubular-film interface observed on TEM image (Fig. 4.15a) may be misidentified and at first glance could suggest that alloying of iron with tungsten leads to change of growth mechanism from flow model into field assisted dissolution model as similar barrier layers are formed. The clear shape of developed nanotubes is however against that concept and suggest another origin of its

formation. Variations in thickness of this layer 40-130 nm (Fig. 4.15 d) suggest chemical nature of formation since electric filed located in barrier layer produces homogeneous layers of regular structure and thickness. The possible reason of the layer formation would be post reaction of WF_6 or similar compound remaining at the bottom of nanostructure, with moisture after completed anodizing process. WF_6 is typically unstable and easily hydrolyze with water though three elementary steps (4.1-4.3):

$$WF_6 + H_2O \rightarrow WOF_4 + 2HF \quad (4.1)$$

$$WOF_4 + H_2O \rightarrow WO_2F_2 + 2HF \quad (4.2)$$

$$WO_2F_2 + H_2O \rightarrow WO_3 + 2HF \quad (4.3)$$

The overall reaction is $WF_6 + 3H_2O = WO_3 + 6HF$ where 1 mol dm^{-3} WF_6 produces 6 mol dm^{-3} hydrofluoric acid. Such harsh acidic conditions may drive chemical reaction with alloy at anodic film base, and therefore thickening the layer at the alloy/nanotubular-film interface as demonstrated in Fig 4.15 c. On the Figure 4.12 also shown that the anodizing Fe/Fe-W/Fe has nanotubular on the upper part, but on the bottom part the morphology become undefined nanopores, this might be happened because of the present of HF harm the metal during anodizing. The absence of characteristic fluorine peak in the GDOES depth profile, in contrast to that for pure Fe case (Fig. 4.13), at alloy/nanotubular-film interface and consequently uniform distribution of fluorides suggest that originally formed fluoride rich layer is consumed in post reaction process. The fluoride rich layer, FeF_x formed on pure iron is practically free of oxygen species as demonstrated elsewhere[3]. The composition of the layer obtained by TEM/EDS analysis on Fe-W alloy shows 17.2, 3.4 35.4 and 44.0 at.% for Fe, W, F and O, respectively, indicating rather complex structure of the layer containing compounds such as metal oxides and metaloxyfluorides as a result of post reaction.

4.4. Conclusions

The present study shows that alloying of iron with 9 at.% tungsten has meaningful implications on the growth and resulting structure of anodic film. Based on the results obtained the following conclusions can be drawn:

1. Alloying of iron with 9 at.% of tungsten results in transition of nanoporous oxide into nanotubular nanostructure. The possible reason of this transition is faster kinetics of WF_6 reaction with water over the presence of low solubility FeF_x

species, easily developing the space in between nanotubes.

2. The pore size of the anodic films on the Fe-W alloy is smaller than that on pure Fe and the quasi-steady state anodizing condition is more rapidly established on the Fe-W alloy. Such influences of alloying with tungsten are most likely due to formation of thinner barrier layer formed on the Fe-W alloy.

3. The anodic nanopores developed on pure Fe and anodic nanotubes developed on Fe-W alloy composed of Fe_xO_y and WO_3 domains grow in line with the field assisted flow model. The thick layer formed at the alloy/oxide interface is possibly a result of chemical reaction due to exposition of structure to moisture.

References:

1. Beck, F., R. Kaus, and M. Oberst, *Transpassive dissolution of iron to ferrate(VI) in concentrated alkali hydroxide solutions.* Electrochimica Acta, 1985. **30**(2): p. 173-183.
2. Pourbaix, M., *Atlas of electrochemical equilibria in aqueous solutions.* NACA, 1984.
3. Shahzad, K., et al., *Ex situ evidence for the role of a fluoride-rich layer switching the growth of nanopores to nanotubes: A missing piece of the anodizing puzzle.* ChemElectroChem, 2018. **5**(4): p. 610-618.
4. Habazaki, H., et al., *Fast migration of fluoride ions in growing anodic titanium oxide.* Electrochemistry Communications, 2007. **9**(5): p. 1222-1227.
5. Kowalski, D., D. Kim, and P. Schmuki, *TiO_2 nanotubes, nanochannels and mesosponge: Self-organized formation and applications.* Nano Today, 2013. **8**(3): p. 235-264.
6. Prakasam, H.E., et al., *Synthesis and photoelectrochemical properties of nanoporous iron (III) oxide by potentiostatic anodization.* Nanotechnology, 2006. **17**(17): p. 4285-4291.
7. Mohapatra, S.K., et al., *Water Photooxidation by Smooth and Ultrathin α-Fe_2O_3 Nanotube Arrays.* Chemistry of Materials, 2009. **21**(14): p. 3048-3055.
8. Habazaki, H., et al., *Galvanostatic growth of nanoporous anodic films on iron in ammonium fluoride−ethylene glycol electrolytes with different water contents.* The Journal of Physical Chemistry C, 2010. **114**(44): p. 18853-18859.
9. Konno, Y., et al., *Factors influencing the growth behaviour of nanoporous anodic films on iron under galvanostatic anodizing.* Journal of Solid State Electrochemistry, 2012. **16**(12): p. 3887-3896.
10. Kure, K., et al., *Formation of self-organized nanoporous anodic films on Type 304 stainless steel.* Electrochemistry Communications, 2012. **21**: p. 1-4.
11. Albu, S.P., A. Ghicov, and P. Schmuki, *High aspect ratio, self-ordered iron oxide nanopores formed by anodization of Fe in ethylene glycol/NH_4F electrolytes.* physica status solidi (RRL) − Rapid Research Letters, 2009. **3**(2 - 3): p. 64-66.
12. Sato, N., *1989 Whitney Award Lecture: Toward a More Fundamental Understanding of Corrosion Processes.* CORROSION, 1989. **45**(5): p. 354-368.
13. Tsuchiya, H., et al., *Formation of self-organized pores on type 316 stainless steel in organic solvents.* Electrochimica Acta, 2012. **82**: p. 333-338.
14. Kowalski, D., et al., *Self-organization of TiO_2 nanotubes in mono-, di- and tri-ethylene glycol electrolytes.* Electrochimica Acta, 2016. **204**: p. 287-293.
15. Kowalski, D., et al., *Low electric field strength self-organization of anodic TiO_2 nanotubes in diethylene glycol electrolyte.* Journal of Materials Chemistry A, 2015. **3**(12): p. 6655-6661.
16. Masuda, H., et al., *Self-repair of ordered pattern of nanometer dimensions based on self-compensation properties of anodic porous alumina.* Applied Physics Letters, 2001. **78**(6): p. 826-828.
17. Bai, Y., et al., *High performance FeF_x/C composites as cathode materials for lithium-ion batteries.* Journal of Renewable and Sustainable Energy, 2013. **5**(2): p. 021402.

18. Li, L., et al., *In Situ Engineering Toward Core Regions: A Smart Way to Make Applicable FeF3@Carbon Nanoreactor Cathodes for Li-Ion Batteries.* ACS Applied Materials & Interfaces, 2017. **9**(21): p. 17992-18000.
19. Biesinger, M.C., et al., *Resolving surface chemical states in XPS analysis of first row transition metals, oxides and hydroxides: Cr, Mn, Fe, Co and Ni.* Applied Surface Science, 2011. **257**(7): p. 2717-2730.
20. Grosvenor, A.P., et al., *Investigation of multiplet splitting of Fe 2p XPS spectra and bonding in iron compounds.* Surface and Interface Analysis, 2004. **36**(12): p. 1564-1574.
21. Yamashita, T. and P. Hayes, *Analysis of XPS spectra of Fe^{2+} and Fe^{3+} ions in oxide materials.* Applied Surface Science, 2008. **254**(8): p. 2441-2449.
22. Thorpe, R., et al., *The solid state conversion reaction of epitaxial FeF2(110) thin films with lithium studied by angle-resolved X-ray photoelectron spectroscopy*. Physical Chemistry Chemical Physics, 2015. **17**(23): p. 15218-15225.
23. Shim, H.S., et al., *Electrochromic properties of tungsten oxide nanowires fabricated by electrospinning method.* Solar Energy Materials and Solar Cells, 2009. **93**(12): p. 2062-2068.
24. Green, S.V., et al., *Structure and composition of sputter-deposited nickel-tungsten oxide films.* Thin Solid Films, 2011. **519**(7): p. 2062-2066.
25. He, G.J., et al., *One pot synthesis of nickel foam supported self-assembly of $NiWO_4$ and CoWO4 nanostructures that act as high performance electrochemical capacitor electrodes.* Journal of Materials Chemistry A, 2015. **3**(27): p. 14272-14278.
26. Alov, N.V., *XPS study of MoO_3 and WO_3 oxide surface modification by low-energy Ar^+ ion bombardment.* physica status solidi c, 2015. **12**(3): p. 263-266.
27. Bittencourt, C., et al., *Characterization of WO_3 : Ag films: ToF-SIMS studies of ammonia adsorption.* Applied Surface Science, 2005. **250**(1-4): p. 21-28.
28. Garcia‐Vergara, S., et al., *Incorporation and migration of phosphorus species within anodic films on an Al‐W alloy.* Surface and Interface Analysis, 2011. **43**(5): p. 893-902.
29. Kowalski, D., Y. Aoki, and H. Habazaki, *High Proton Conductivity in Anodic ZrO_2/WO_3 Nanofilms.* Angewandte Chemie International Edition, 2009. **48**(41): p. 7582-7585.
30. Hoar, T.P. and N.F. Mott, *A mechanism for the formation of porous anodic oxide films on aluminium.* Journal of Physics and Chemistry of Solids, 1959. **9**(2): p. 97-99.
31. Garcia-Vergara, S.J., et al., *Compositional Evidence for Flow in Anodic Films on Aluminum under High Electric Fields.* Journal of The Electrochemical Society, 2007. **154**(9): p. C540-C545.
32. Garcia-Vergara, S.J., et al., *A flow model of porous anodic film growth on aluminium.* Electrochimica Acta, 2006. **52**(2): p. 681-687.
33. Houser, J.E. and K.R. Hebert, *The role of viscous flow of oxide in the growth of self-ordered porous anodic alumina films.* Nature Materials, 2009. **8**(5): p. 415-420.
34. Garcia-Vergara, S.J., et al., *Tracer studies relating to alloying element behaviour in porous anodic alumina formed in phosphoric acid.* Electrochimica Acta, 2010. **55**(9): p. 3175-3184.
35. Skeldon, P., et al., *A Tracer Study of Porous Anodic Alumina*. Electrochemical and Solid-State Letters, 2006. **9**(11): p. B47-B51.
36. Garcia-Vergar, S.J., et al., *Incorporation and migration of phosphorus species within anodic films on an Al-W alloy*. Surface and Interface Analysis, 2011. **43**(5): p. 893-902.
37. Jung, H., et al., *Elucidation of hydrolysis reaction mechanism of tungsten hexafluoride (WF_6) using first-principles calculations.* Journal of Industrial and Engineering Chemistry, 2019. **70**: p. 99-102.
38. Lide, D.R., *CRC Handbook of Chemistry and Physics, 84th Edition*. 2003: CRC Press.
39. Kajikawa, Y., et al., *Nucleation of W during Chemical Vapor Deposition from $WF_6$and SiH_4.* Japanese Journal of Applied Physics, 2004. **43**(6B): p. 3945-3950.

Chapter 5 Photoelectrochemical analysis of Fe-W anodic oxide films

5.1. Introduction

Iron oxides have been studied intensively as semiconductor materials for the photodegradation of organic matrices, as it is fairly stable in aqueous solutions, and also high availability, nontoxicity, and chromatic characteristics. Fe_2O_3 has a small band gap value of 1.6 to 2.1 eV [1-4]; this narrow band gap causes an effective absorption of the spectrum of solar light when compared to TiO_2 and WO_3 [5]. However, the slow kinetics of oxygen evolution in water splitting and short hole diffusion length in iron oxides are seen as the reasons for the lower practical conversion efficiencies [6]. WO_3 has also been intensively studied; this material is abundant and therefore cheap, non-toxic and corrosion resistant. Tungsten oxide is an n-type semiconductor, having lower energy band gap about 2.4–2.8 eV in comparison with TiO_2 and it allows to absorb a visible range of the solar light spectrum [7, 8]. Also from its high stability in acidic conditions and good charge-carrier transport properties, this semiconductor is a very attractive material for photocatalytic-purifying environmental water containing organic pollutant [9-11]. However, WO_3 could theoretically employ approximately only 12% solar light [12]. Additionally, because of indirect bandgap, WO_3 inquire a quite thick layer for harvesting light, which typically leads to enormous electron–hole recombination loss and results in reduced photoactivity[13]. One method to solve this problem is the combination of different semiconductor materials. This combination method can increase the semiconductor performance in various ways such as by optical absorption improvements, charge separation enhancement, or the modification of the electronic structure of the interface between both materials [14]. Several combined system has been successfully synthesized such are WO_3/TiO_2 [15], TiO_2/Fe_2O_3 [16] and Fe_2O_3/WO_3 [14, 17, 18].

The Fe_2O_3/WO_3 system is a good model and a promising photoanode for many reasons, because of effective operation, low cost, and environmentally friendly materials. Their beneficial energy band positions also allow the transfer of electrons from Fe_2O_3 conduction band to WO_3 and holes from WO_3 valence band into Fe_2O_3, which reduces the recombination of the electron–hole pair and results in an efficient charge separation

and better photocatalytic efficiency. Several system configurations of Fe_2O_3 and WO_3 have been proposed, including mixed films [19, 20], host–guest structure [17, 21, 22], and also modified nanowires [14, 18]. So far, the combining materials method has been successfully prepared via various procedures, for instance sol–gel [23], chemical vapor deposition [24], and hydrothermal process [25-27]. In chapter 4, the author successfully synthesized vertically aligned Fe-W oxides nanotube arrays. In this chapter the author demonstrates the photocatalytic activity of the annealed anodic nanotubular and barrier Fe-W oxides grown by anodizing sputter deposited Fe-W alloy in a fluoride containing electrolyte, tested in the aqueous MB under visible-light irradiation and compared with those of anodic nanopores iron oxide.

5.2. Experimental Details

Magnetron-sputtered iron-tungsten alloy films were deposited on flat glass. The target used for sputtering is 99.99 % pure iron disk of 100 mm in diameter and 0.5 mm thickness, which was bonded on a copper backing plate, and one 99.9 % tungsten disk of 20 mm in diameter placed on the sputter erosion region of the iron disk. The composition of the alloy was evaluated by electron probe micro analyzer (EPMA; JEOL, JXA-8530F) and equaled to 9 at.% tungsten. Two types of anodic films were formed at different anodizing conditions: (1) barrier-type anodic films with ~510 nm thickness, obtained by anodizing the sputter-deposited iron-tungsten film at a constant voltage of 60 V in ethylene glycol (99.5 % Kanto Chemical Co., Inc.) electrolyte containing 0.1 M NH_4F (97.0 % Kanto Chemical Co., Inc.) and 0.1 M H_2O for 15 s; (2) nanotubes type anodic films of ~860 nm thickness, obtained by anodizing the sputter-deposited iron-tungsten films at a constant voltage of 60 V in ethylene glycol solution containing 0.1 M NH_4F and 1.5 M H_2O for 150 s. Both anodic films (barrier-type and nanotubes-type) were annealed for 30 min in air at 300, 350, 400 and 450 °C. For comparison, nanopores-type anodic films were grown on the sputter-deposited iron films at a constant voltage of 60 V in ethylene glycol solution containing 0.1 M NH_4F and 1.5 M H_2O for 150 s.

The morphology of the fabricated materials was investigated by using a Zeiss, Sigma 500 scanning electron microscope using 1 kV accelerating voltage. X-ray diffraction (XRD) analysis was performed by Rigaku, RINT-2000 with Cu Kα radiation and collected at a tube voltage and current of 40 kV and 20 mA, respectively. Micro Raman analysis were carried out through a Renishaw in Via Raman. Microscope

spectrometer equipped with a microprobe (50×) and a CCD detector with an Nd:YAG laser of 532 nm. Glow discharge optical emission spectroscopy (GDOES) were used for depth profile analyses of the anodic films; Jobin-Yvon 5000 RF instrument in 900 Pa argon atmosphere and rf of 13.56 MHz and a power of 50 W. The wavelength signals were detected from approximately 4 mm diameter of circular area.

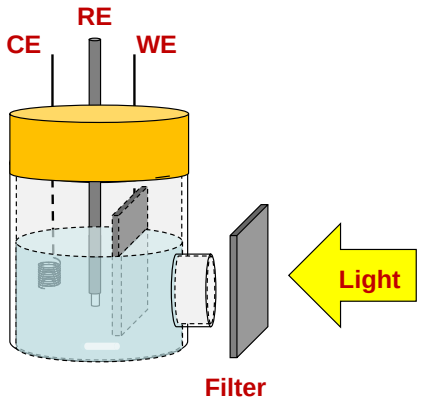

Figure 5.1 Schematic illustration of the photocurrent measurement.

Photocurrent versus voltage characteristics of the anodized iron foils (surface area ;1 cm^2) were recorded by scanning the potential from 0.1 to 10.5 V (versus Ag/AgCl) at 10 mV/s, using a potentiostat (Autolab III, Metrohm, the Netherlands). The measurement was done using a three-electrode system, with Pt rod counter electrode and Ag/AgCl/sat. KCl reference electrode in solutions containing 1 M NaOH. A xenon light source (LSP-X150, Zolix Instruments, Beijing, China) with an intensity of 100 mW/cm^2 was used as solar simulator (AM 1.5) to irradiate the annealed samples. Diffuse Reflectance Spectra (DRS) analysis was performed to characterize photo-absorption properties of samples by JASCO V-670 spectrophotometer equipped with PIN-757 integrating sphere with Barium sulphate ($BaSO_4$) powder as baseline. The obtained DRS was converted into Kubelka-Munk plot to obtain the band gap energy. 8 mL of methylene blue (MB) solution with initial concentration 5 mg L^{-1} was used to observe the photocatalytic activity of the samples. Prior to illumination on visible light, the Xenon light with an intensity of 100 mW/cm^2 was equipped by 370 nm long-pass filter OptoSigma SCF-50S-37L at interval 30 minutes. The MB solution was sonicated for 10 min to homogenize the mixture and the solution was magnetically stirred in the dark for 2 h to establish the adsorption–desorption equilibrium of MB on the surface at room temperature. During irradiation, stirring was maintained, photo degradation efficiency was computed by measuring the absorbance values of the MB solution. The concentration of MB as a function of time was calculated by the absorbency values of the original and measured samples.

5.3. Results and Discussion

5.3.1 Structural and morphological characterization

The structure of the Fe-W oxides as photoactive materials was investigated using X-ray diffraction (XRD). As mentioned in Chapter 3 and Chapter 4, the anodizing of Fe or Fe-W forms semi-crystalline iron oxide, iron fluoride species and some iron hydroxide, and the resultant films were not photoactive owing to their disordered structure. Therefore, a post annealing process is essential to remove fluorine and hydroxide from the anodic films and to crystallize fully the anodic films. Figure 5.2 displays the XRD patterns of all the annealed materials, and the results indicated that the sample annealed at 300 °C contain a very weak peaks which indexed to Fe_2O_3, but the oxide seems to be rather amorphous. The reflection of remaining iron layer beneath the anodic films corresponding to (200) peak at $2\theta=44.674°$ (COD 9013472) is present on all anodic films of Fe-W oxides. By increasing annealed temperature, the oxide crystallizes and the Fe_2O_3 (COD 9000139) and Fe_3O_4 (COD 9000139) are clearly observed after annealing at 450ºC. It is worth noting that no tungsten-containing phase was observed in the XRD patterns because of very limited amount of tungsten in the samples; however, based on the phase diagram of Fe_2O_3 and WO_3 mixture in the oxygen atmosphere and atmospheric pressure, at lower temperature (<800 °C) the mixture of Fe_2O_3 and Fe_2WO_6 might be present. [28-31]

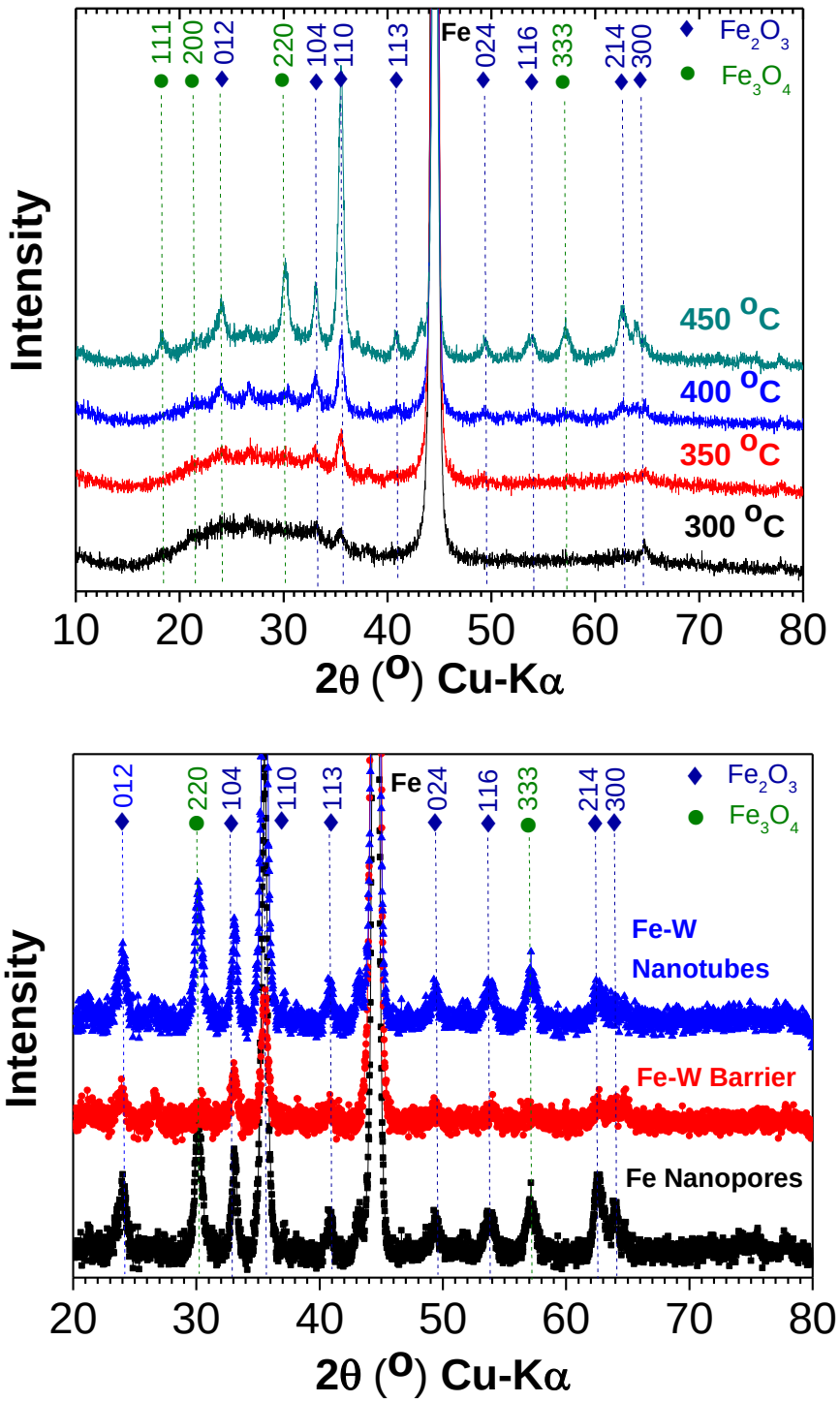

Figure 5.2 X-ray diffraction patterns relating to (a) anodic films grown on sputter-deposited Fe-W at 60 V and annealed for 30 min at different temperatures under air exposure. Growth conditions: 1.5 M H_2O for 150 s. and (b) the nanoporous film grown on Fe in ethylene glycol containing 0.1 mol dm^{-3} NH_4F, 1.5 mol dm^{-3} H_2O for 150 s, barrier film grown on Fe-W in ethylene glycol containing 0.1 mol dm^{-3} NH_4F, 0.1 mol dm^{-3} H_2O for 10 s, and nanotubes film grown on Fe-W in ethylene glycol containing 0.1 mol dm^{-3} NH_4F, 1.5 mol dm^{-3} H_2O for 150 s, and annealed for 30 min under air exposure at 450 °C.

Fig. 5.3 shows the Raman spectra of the thermal-treated porous films as a function of the annealing temperature. Again, the peaks become less broad with increasing the annealing temperature, thus better crystallization was achieved. Nevertheless, the Raman spectra are similar regardless of annealing temperature. Seven phonon lines of Fe_2O_3 are expected in the Raman spectrum: two A_{1g} modes are corresponding to 223 and 498 cm^{-1}, and another five E_g modes correspond to 247, 293, 409, and 610 cm^{-1}. A careful inspection of Fig. 5.3 shows that for samples annealed at T≥400 °C, Raman peaks are present at the wave number corresponding to all these modes. However, two other peaks are present (at 650 and 1,315 cm^{-1}) not included in the above reported list. According to the literature [32], the small peak at 650 cm^{-1} corresponds to a phonon which, in perfect Fe_2O_3 crystals, is Raman inactive and unobserved. This mode becomes active during the crystallization process owing to the symmetry breaking. The strong band at 650 cm^{-1} phonons is usually interpreted as an overtone of the 650 cm^{-1} phonons.

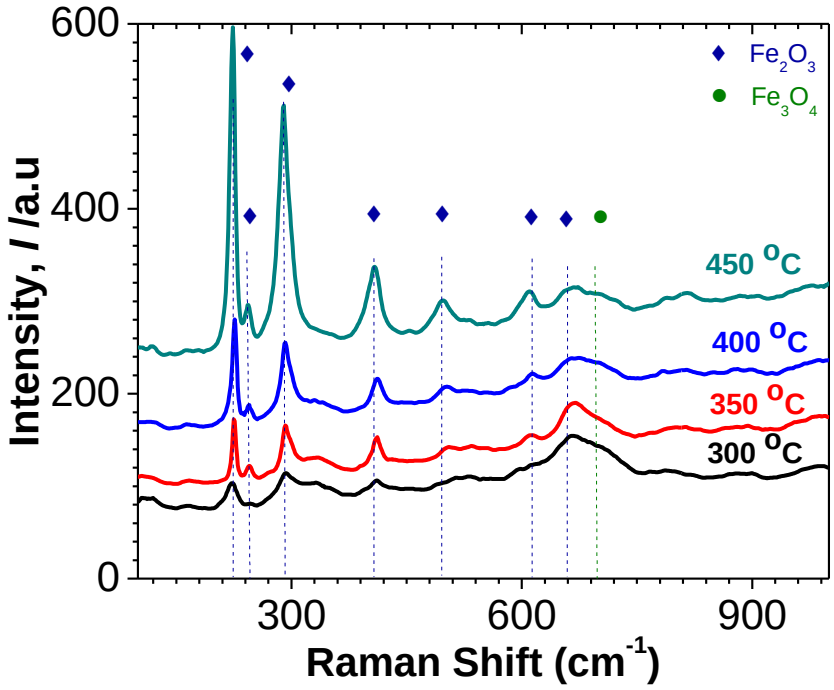

Figure 5.3 Raman spectra relating to anodic films grown on sputter deposited Fe at 60 V anodizing and annealed for 30 min at different temperatures under air exposure. Growth conditions: 1.5 M H_2O for 150 s.

In Figs. 5.4 and 5.5, the author compares the surface morphology of the barrier layers with the porous films after 30 min of annealing at different temperatures. It is interesting to mention that the surface of the barrier films in the micrographs at 300 °C has similar morphology as porous-type films, as evident that the porous type also can be produced by prolonging anodizing time on fluoride electrolyte with low water concentration (Fig. 5.4a). Nevertheless, by increasing the annealing temperature, these porous features become less visible due to higher density causing by the onset of annealing process assisted at the higher temperature (see Fig. 5.4b, c). On anodic films prepared at high water concentration; 1.5 M H_2O for 150 s, a well-defined nanoporous/nanotubular structure is present, as shown in Fig. 5.5. The thermal treatment does not change the film features even when the thermal treatment is performed at 450 °C (see Fig. 5.5 a-d).

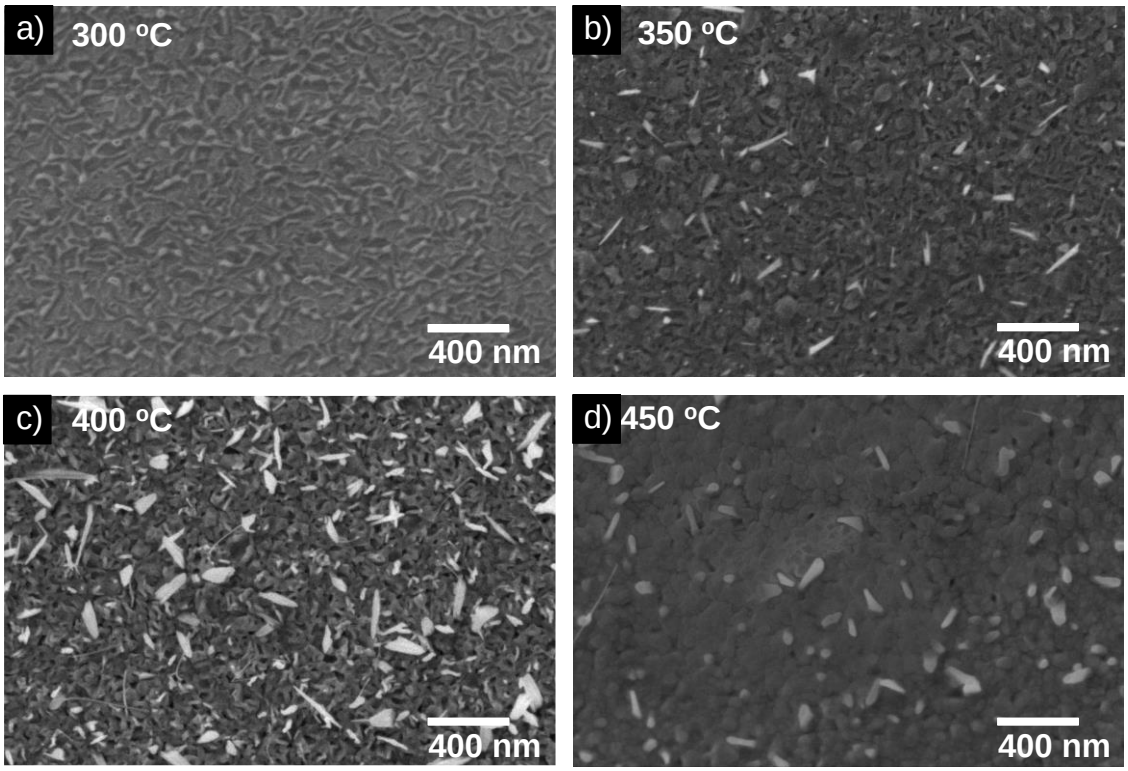

Figure 5.4 SEM images relating to anodic film grown on sputter-deposited Fe at 60 V anodizing in ethylene glycol containing 0.1 mol dm^{-3} NH_4F and 0.1 mol dm^{-3} H_2O for 30 s, and annealed for 15 min under air exposure at (a) 300 °C, (b) 350 °C, (c) 400 °C, and (d) 450 °C.

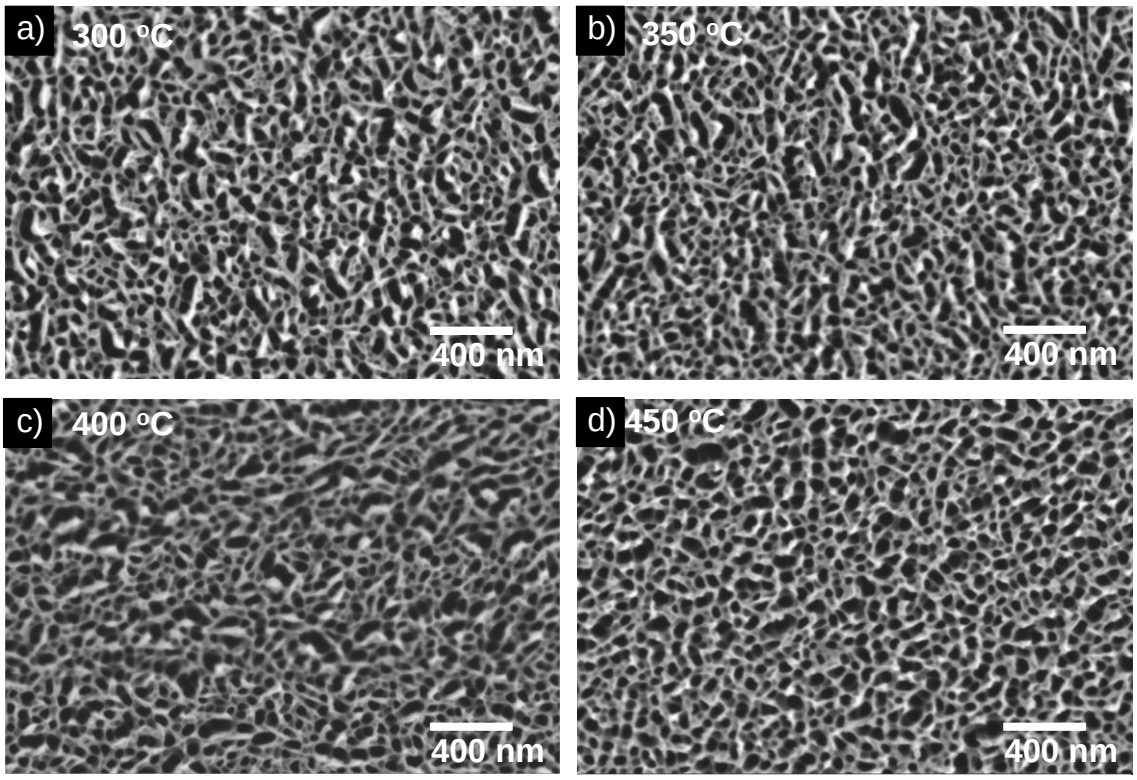

Figure 5.5 SEM images relating to anodic film grown on sputter-deposited Fe at 60 V anodizing in ethylene glycol containing 0.1 mol dm^{-3} NH_4F and 1.5 mol dm^{-3} H_2O for 150 s, and annealed for 15 min under air exposure at (a) 300 °C, (b) 350 °C, (c) 400 °C, and (d) 450 °C.

In Fig. 5.6, the author can observe the barrier-type film with 510 nm of thickness and nanotube-type film with 860 nm of thickness morphology on cross section SEM observation. In chapter 4, the author reported of the presence of chemical layer around 100 nm between the substrate and porous layer; in this chapter, the annealed iron oxide forms thicker barrier layer (thermal oxide layer) around 200 nm in thickness at the metal-film interface. The nanotubular morphology is obvious in the cross-section of the porous anodic film formed on the Fe-W, whereas the anodic film on iron is nanoporous-like (Fig. 5.6a). The annealed barrier-type anodic film is rather compact throughout the film thickness.

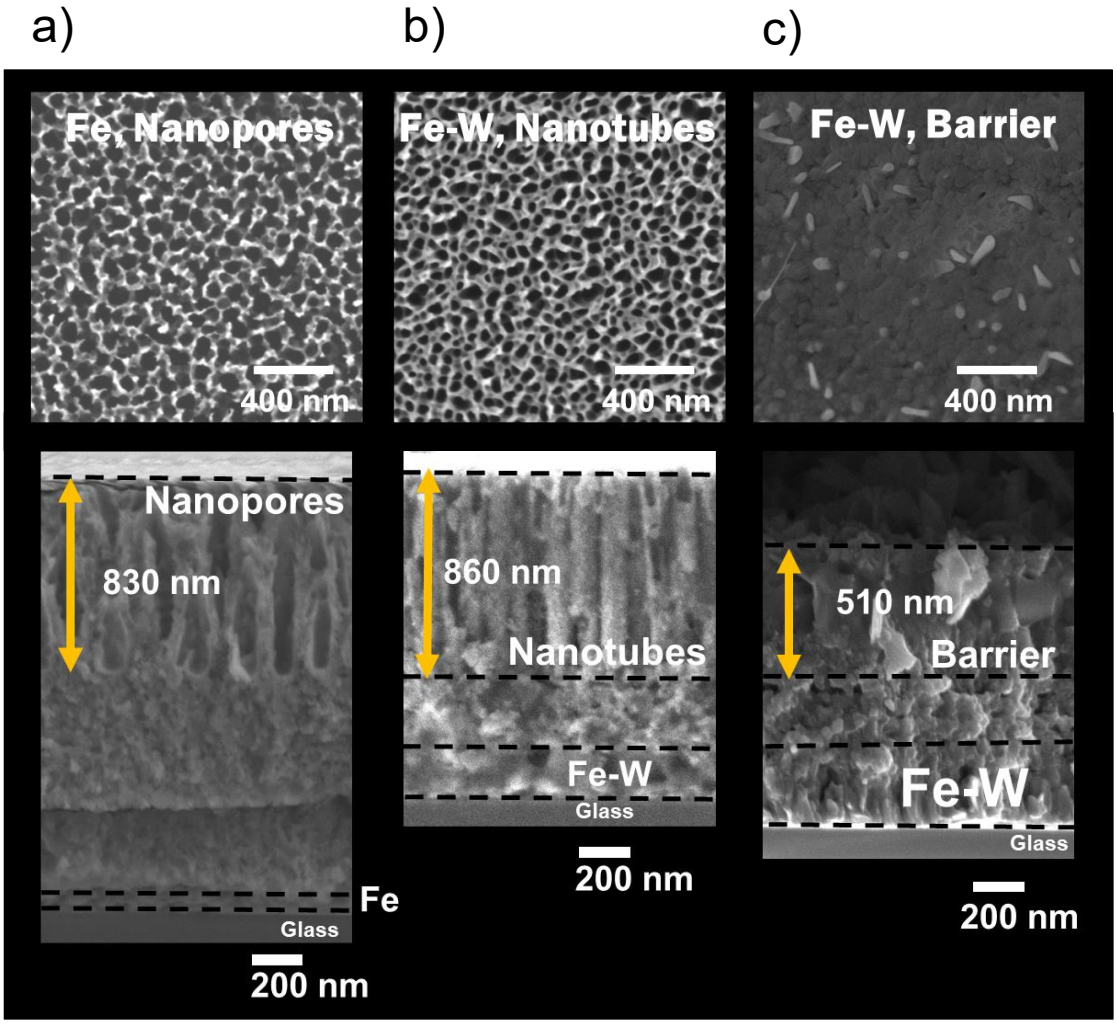

Figure 5.6 Surface and cross-section images relating to anodic film grown on sputter-deposited (a) the nanoporous film grown on Fe in ethylene glycol containing 0.1 mol dm^{-3} NH_4F, 1.5 mol dm^{-3} H_2O for 150 s, (b) nanotubes film grown on Fe-W in ethylene glycol containing 0.1 mol dm^{-3} NH_4F, 1.5 mol dm^{-3} H_2O for 150 s, and (c) barrier film grown on Fe-W in ethylene glycol containing 0.1 mol dm^{-3} NH_4F, 0.1 mol dm^{-3} H_2O for 10 s, and and annealed for 30 min under air

At chapter 4, the author understands that a chemical layer is present beneath the nanotubular anodic film grown on Fe-W. Therefore, the composition of anodic films at two different morphology annealed at high temperature was examined qualitatively by GDOES elemental depth profile analysis. According to the sputtering time required to reach the oxide/alloy interface, it is clear that the thickness of the anodic films increases by increasing the water content at anodized process. The content of tungsten is uniform in both nanotubular and barrier type films. However, on the nanotubular type films at metal-film interface, the content of tungsten is decreasing with the increasing of iron. It is known that the thickness of the iron oxide films increases with increasing the annealing temperature. A thermal oxidation process is active under air exposure leading to formation of iron oxide at the metal-film interface.

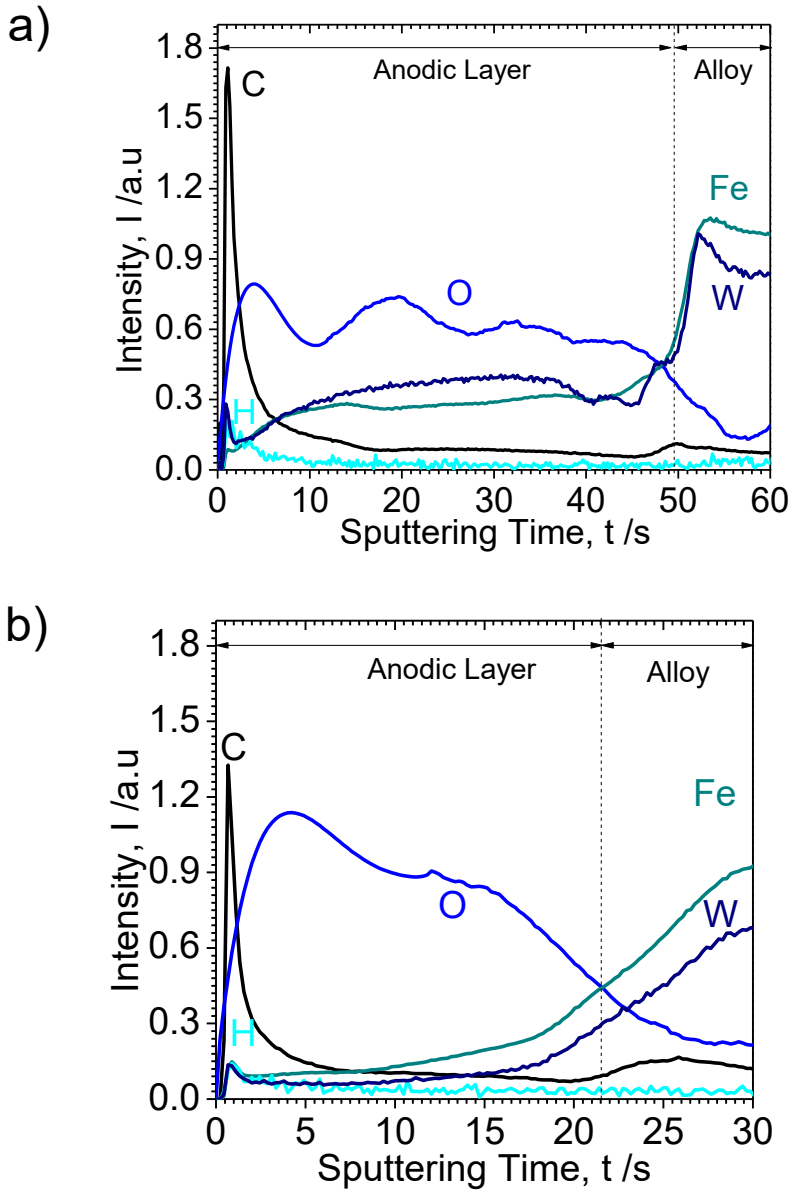

Figure 5.7 GDOES depth profiles of the anodic film grown on sputter-deposited Fe-W at 60 V anodizing in ethylene glycol containing 0.1 mol dm^{-3} NH_4F, (a) 1.5 mol dm^{-3} H_2O for 150 s and (b) 0.1 M H_2O for 10 s, and annealed for 30 min under air exposure at 450 °C.

5.3.2 Photoelectrochemical characterization

The PEC performance of a photoelectrode is strongly dependent on its optical properties. The effect of morphology on optical properties of anodic film was studied by UV-vis diffuse reflectance spectral analysis. The UV-vis diffuse reflectance spectra of barrier type with different annealing temperatures are displayed in the Fig. 3. As seen from Fig. 3, the absorption sharp edge photocatalysts are found to be around 650-750 nm, respectively.

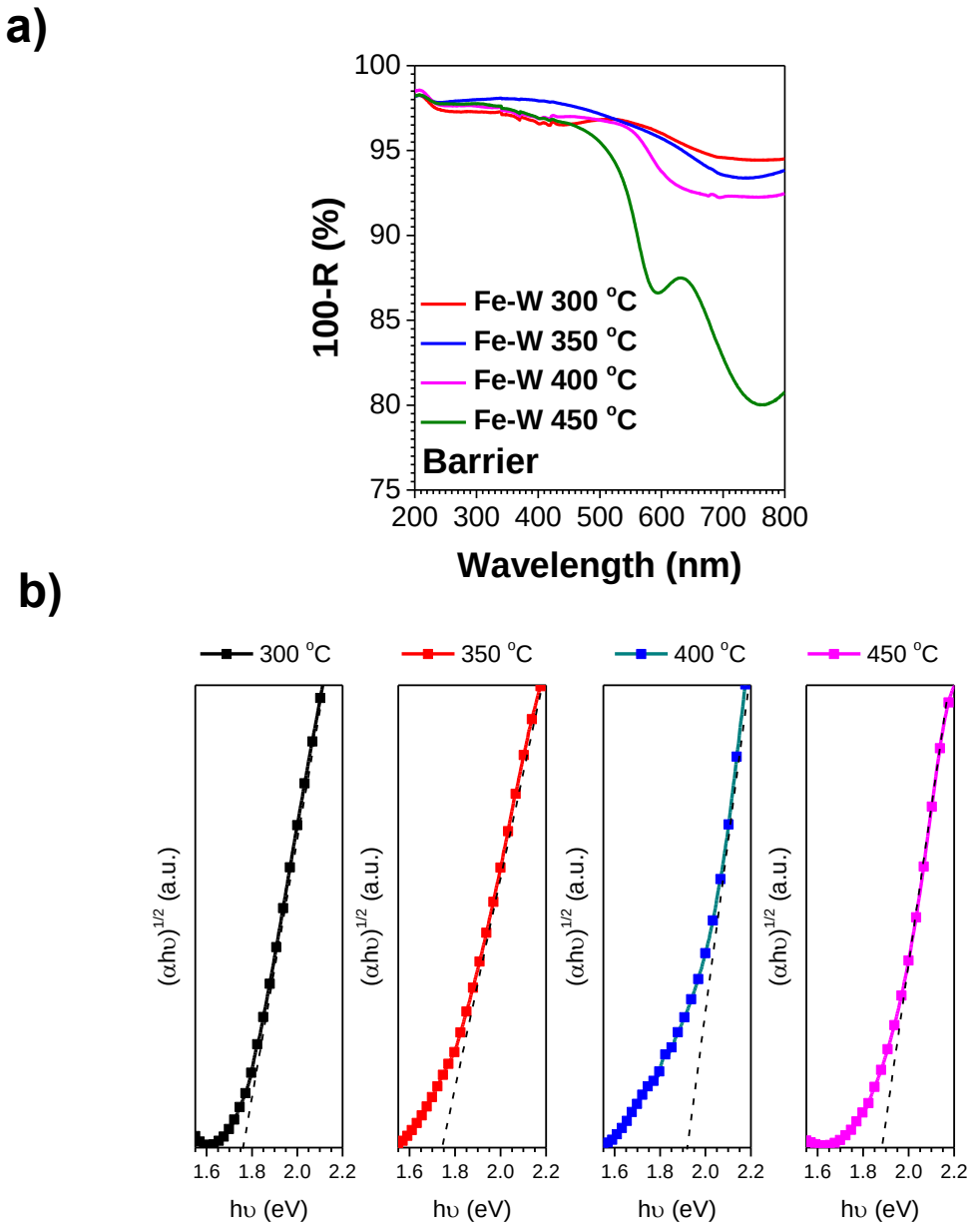

Figure 5.8 (a) UV-vis diffuse reflection spectra and (b) band gap estimate assuming indirect optical transition of the anodic film grown on sputter-deposited Fe-W at 60 V anodizing in ethylene glycol containing 0.1 mol dm^{-3} NH_4F, 0.1 mol dm^{-3} H_2O for 10 s and annealed for 30 min under air exposure at varying temperature.

From the UV-absorption data, the bandgap of the samples was calculated according to the solid band theory by using the following equation:

$$\alpha h\upsilon = A_o(h\upsilon - E_g)^n \quad (5.1)$$

where α was the absorption coefficient, E_g was the optical bandgap of the material. The value of n depended on the nature of band transition. Its value could be 1/2 or 3/2 for direct allowed and forbidden transitions, and 2 or 3 for indirect allowed and indirect forbidden transitions, respectively. The bandgap was calculated by plotting $(\alpha h\upsilon)^{1/2}$ versus photon energy $h\upsilon$. It is worth to noting that, this bandgap value follows a positive linear dependence in the temperature range. The increase of the indirect band gap with substrate temperature was also reported for sprayed, sputtered and reactive evaporation α-Fe_2O_3 thin films [2, 33, 34]. This increasing might be correlated to the crystalline structure of the anodic films.

Figure 5.9 presents the estimated bandgap of anodic Fe oxide and Fe-W oxides grown on 1.5 M of water in ethylene glycol electrolyte for 150 s and annealed at 450 ℃. Despite the fact that iron oxides exhibited favorable bandgap energy, its potential use for PEC water oxidation was limited by poor light absorption properties due to the indirect bandgap nature with a small, wavelength-dependent absorption coefficient. The calculated values of indirect bandgap for nanopores iron oxide is 1.65 eV, the reported bandgap value of Fe_2O_3 is varied from 1.3 – 2.3 eV while small bandgap of 0.1 eV was produced by Fe_3O_4 [2, 35-37]. Our values of the band gaps showed an increasing value of Fe-W barrier = 1.72 eV dan Fe-W nanotubes = 1.84 eV; this increasing value of bandgap is presence due to the addition of tungsten species in the case of anodic films. Fe_2WO_6, is an n-type semiconductor, it might be act as a photo-absorber at wavelengths below the optical absorption limit. A majority charge carrier collector of electrons generated in iron oxides due to its high conductivity, and an electron–hole recombination suppressor.

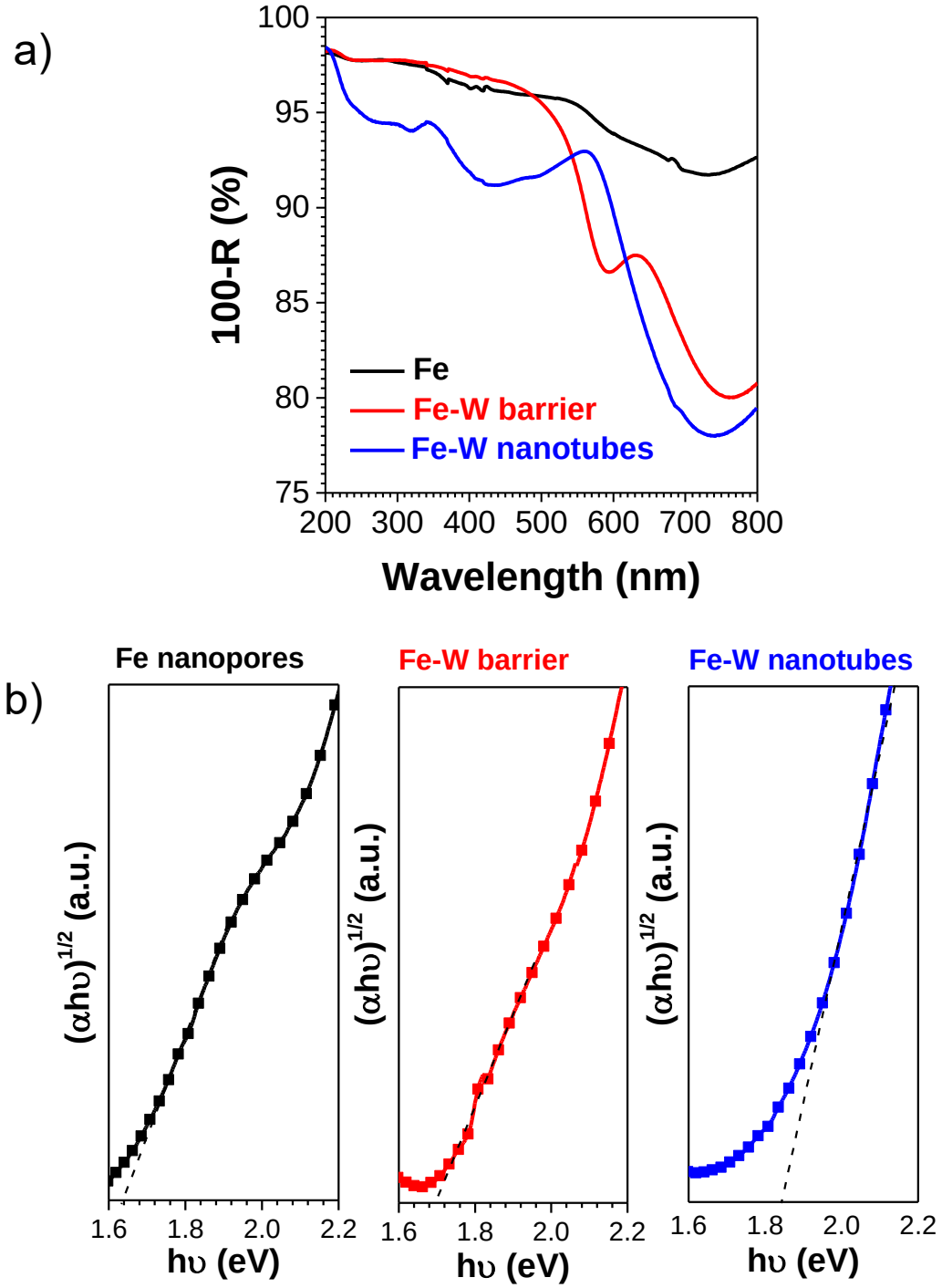

Figure 5.9 (a) UV-vis diffuse reflection spectra and (b) band gap estimate assuming indirect optical transition of the nanoporous film grown on Fe in ethylene glycol containing 0.1 mol dm^{-3} NH_4F, 1.5 mol dm^{-3} H_2O for 150 s, barrier film grown on Fe-W in ethylene glycol containing 0.1 mol dm^{-3} NH_4F, 0.1 mol dm^{-3} H_2O for 10 s, and nanotubes film grown on Fe-W in ethylene glycol containing 0.1 mol dm^{-3} NH_4F, 1.5 mol dm^{-3} H_2O for 150 s, and annealed for 30 min under air exposure at 450 °C.

In order to quantify the influence of alloying elements of the substrate on anodic iron oxides on the photocatalytic properties, the photoelectrochemical(PEC) measurements were performed in a three-electrode cell (reference, counter and working) in NaOH electrolyte, with Ag/AgCl/sat. KCl as reference. Fig. 5.10 displays the photo-electrochemical measurements which conducted under dark condition and light irradiation; this measurement was carried out to investigate the electron-hole generation on the anodic film surfaces. The photocatalytic activity of anodic Fe-W oxide films was evaluated by measuring photocurrent densities. This picture shows significant effect on alloying elements with resulting on the presents of tungsten species on the anodic films. The nanotubes structures of Fe-W oxides result on high current density of 10.8 mA cm^{-2} at 0.8 V vs Ag/AgCl/sat. KCl under visible light illumination intensity of 100 mW cm^{-2}. The onset potential of our nanopores iron is +0.4 V Ag/AgCl, which can be converted to +0.65 V vs. NHE, thus, the valance band level of our iron oxide is 2.3 V vs. NHE. Fe_2WO_6, reported to be an n-type semiconductor [38], the onset potential of Fe_2WO_6 is + 1.01 V vs. NHE with the valance band level of + 2.83 V (vs. NHE) [39], suggesting that the valance band of Fe_2WO_6 is located more positive than that of our iron oxides system 2.3 V vs. NHE.

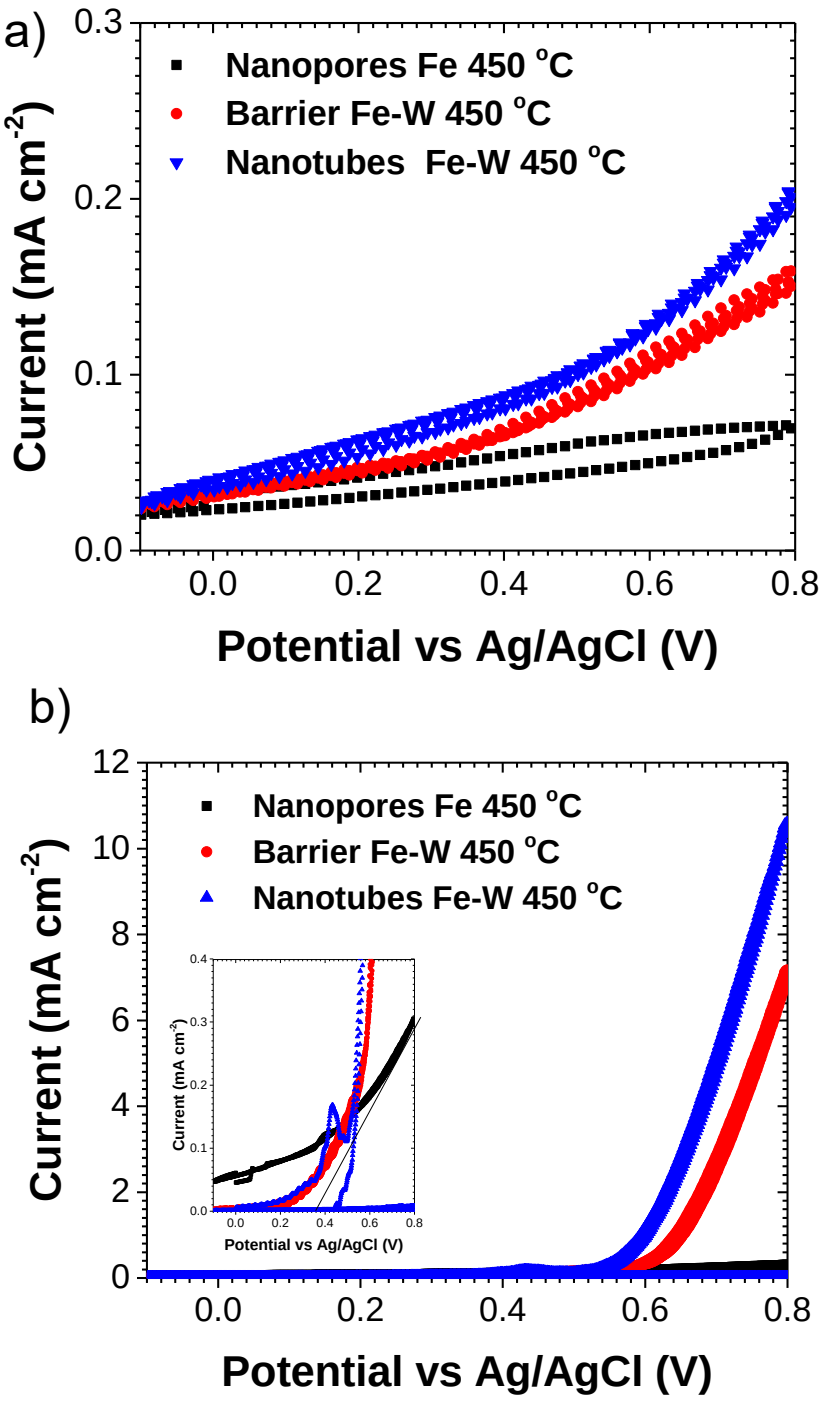

Figure 5.10 (a) Dark and (b) photo-current responses of the nanoporous film grown on Fe in ethylene glycol containing 0.1 mol dm^{-3} NH_4F, 1.5 mol dm^{-3} H_2O for 150 s, barrier film grown on Fe-W in ethylene glycol containing 0.1 mol dm^{-3} NH_4F, 0.1 mol dm^{-3} H_2O for 10 s, and nanotubes film grown on Fe-W in ethylene glycol containing 0.1 mol dm^{-3} NH_4F, 1.5 mol dm^{-3} H_2O for 150 s, and annealed for 30 min under air exposure at 450 °C.

The author uses methylene blue as model of the hazardous organic dye sample to evaluate the photocatalytic activity of the pure Fe and Fe-W oxide samples. The photocatalytic experiments were carried with definite dye concentration (1×10^{-5} mol/L), to compare the efficiency and select the most active sample. As seen from the Fig 5.11 obtained, the concentration changes C/C_0 versus time for photo-degradation of methylene blue on the anodic nanopores iron oxide exhibited a limited photocatalytic performance towards degradation with an efficiency of 9.2% after 180-min irradiation, respectively. However, on both anodic Fe-W oxides, weather barrier or nanotubes photocatalysts were found to exhibit a significantly high photocatalytic activity than that of nanoporous iron oxide. This clearly indicates that the added tungsten species had a significant influence on the photocatalytic performance of anodic films. The high adsorption capacity of the barrier-type sample can be inferred from the large amount of dye removal (40 %) under exposure to light irradiation. The enhancement in photocatalytic performance of the oxide can be contributed improved the absorption ability as well as efficient electron-hole transfer occurred at the interfaces of anodic films. Therefore, the degradation studies proved that the addition of tungsten as the alloying elements of the substrate is an effective photocatalyst material for degradation of organic pollutants from the wastewaters.

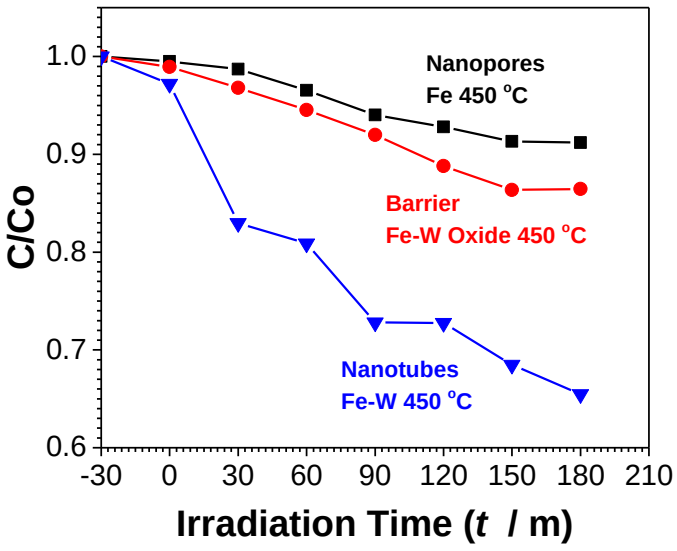

Figure 5.11 The photocatalytic activity of methylene blue degradation under visible light radiation of the anodic film grown on sputter-deposited Fe and Fe-W at 60 V anodizing in ethylene glycol containing 1.5 mol dm^{-3} H_2O for 150 s, and annealed for 30 min under air exposure at 450 °C.

Generally, the photocatalytic activity of a catalyst for the photo oxidation of organic compounds is mainly related to the position of valence band of the photocatalyst and the mobility of photogenerated carriers [40]. Fe_2WO_6 which might be present on the anodic film act as an electron acceptor. Under illuminations, photogenerated electrons in the conduction band iron oxides inclined to transfer to the conduction band of Fe_2WO_6, while the holes in the valence band move to the opposite direction from the electrons, as shown in Fig. 5.12. These processes improve the effective separation of photogenerated electron–hole pairs and prohibits their recombination, which might be ascribed to the promotion of the photocatalytic performance of the anodic Fe-W oxide.

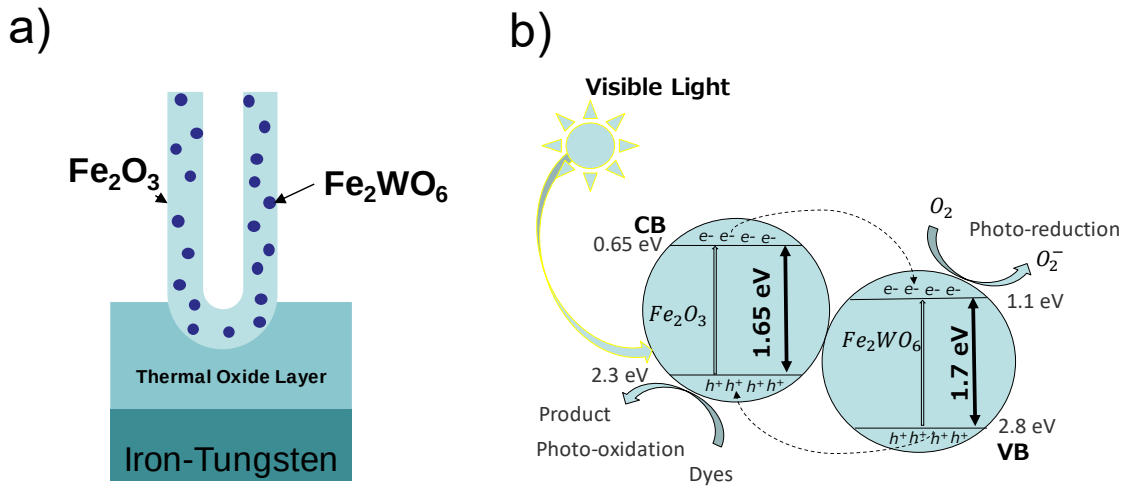

Figure 5.12 Illustrations of (a) nanotubes film grown on sputter-deposited Fe-W at 60 V anodizing in ethylene glycol containing 1.5 mol dm^{-3} H_2O for 150 s, and annealed for 30 min under air exposure at 450 °C and (b) its photogenerated electron transfer pathway.

5.4. Conclusions

This chapter present for the first time the photoelectrochemical study of well aligned Fe-W oxides system synthesized via anodizing method. Depending upon the anodization conditions, including the water content and anodizing time, the nanotubes-type with 800 nm in length and barrier-type with 540 nm length was achieved. The anodic films were annealed from 300 - 400 °C for 30 min to form crystalline structures. The barrier type has lower value of indirect bandgap compared with the nanotubular type of Fe-W oxides, due to its lower surface areas which are similar to flat electrode and provides longer distance for holes to travel hence much of the photogenerated carriers have recombined. The thermal treatment result enhances the crystallinity of the films and

simultaneously increases the concentration of defects on the anodic films results on increase of the bandgap value. The author compared the photocatalytic activity of Fe-W oxides and Fe oxides, it results on high performance with the addition of tungsten species on the anodizing substrate, the possible explanation might be attributed to the efficient separation of the photoinduced electron–hole pairs from Fe_2O_3/Fe_2WO_6 heterojunction system and large surface area of the uniform nanotubes arrays.

References:

1. Beermann, N., et al., *Photoelectrochemical Studies of Oriented Nanorod Thin Films of Hematite.* Journal of The Electrochemical Society, 2000. **147**(7): p. 2456-2461.
2. Al-Kuhaili, M.F., M. Saleem, and S.M.A. Durrani, *Optical properties of iron oxide (α-Fe_2O_3) thin films deposited by the reactive evaporation of iron.* Journal of Alloys and Compounds, 2012. **521**: p. 178-182.
3. Özer, N. and F. Tepehan, *Optical and electrochemical characteristics of sol–gel deposited iron oxide films.* Solar Energy Materials and Solar Cells, 1999. **56**(2): p. 141-152.
4. Zotti, G., et al., *Electrodeposition of Amorphous Fe_2O_3 Films by Reduction of Iron Perchlorate in Acetonitrile.* Journal of The Electrochemical Society, 2019. **145**(2): p. 385-389.
5. Wang, C. and Z. Huang, *Controlled synthesis of α-Fe_2O_3 nanostructures for efficient photocatalysis.* Materials Letters, 2016. **164**: p. 194-197.
6. Kay, A., I. Cesar, and M. Grätzel, *New Benchmark for Water Photooxidation by Nanostructured α-Fe_2O_3 Films.* Journal of the American Chemical Society, 2006. **128**(49): p. 15714-15721.
7. He, G.-H., et al., *Synthesis and visible light photocatalytic behavior of WO_3 (core)/Bi_2WO_6 (shell).* Journal of Molecular Catalysis A: Chemical, 2014. **385**: p. 106-111.
8. Bamwenda, G.R. and H. Arakawa, *The visible light induced photocatalytic activity of tungsten trioxide powders.* Applied Catalysis A: General, 2001. **210**(1): p. 181-191.
9. Martínez-de la Cruz, A., D.S. Martínez, and E.L. Cuéllar, *Synthesis and characterization of WO_3 nanoparticles prepared by the precipitation method: Evaluation of photocatalytic activity under vis-irradiation.* Solid State Sciences, 2010. **12**(1): p. 88-94.
10. Vamvasakis, I., et al., *Synthesis of WO_3 catalytic powders: evaluation of photocatalytic activity under NUV/visible light irradiation and alkaline reaction pH.* Journal of Sol-Gel Science and Technology, 2015. **76**(1): p. 120-128.
11. Xue, Q., et al., *Photocatalytic degradation of geosmin by Pd nanoparticle modified WO_3 catalyst under simulated solar light.* Chemical Engineering Journal, 2016. **283**: p. 614-621.
12. Zeng, Q., et al., *Preparation of vertically aligned WO_3 nanoplate array films based on peroxotungstate reduction reaction and their excellent photoelectrocatalytic performance.* Applied Catalysis B: Environmental, 2017. **202**: p. 388-396.
13. Mao, A., et al., *Hematite modified tungsten trioxide nanoparticle photoanode for solar water oxidation.* Journal of Power Sources, 2012. **210**: p. 32-37.
14. Kronawitter, C.X., et al., *A perspective on solar-driven water splitting with all-oxide hetero-nanostructures.* Energy & Environmental Science, 2011. **4**(10): p. 3889-3899.
15. Wang, J., et al., *Preparation and photoelectrochemical characterization of WO_3/TiO_2 nanotube array electrode.* Journal of Materials Science, 2011. **46**(2): p. 416-421.
16. Luan, P., et al., *Effective charge separation in the rutile TiO_2 nanorod-coupled α-Fe_2O_3 with exceptionally high visible activities.* Scientific Reports, 2014. **4**(1): p. 6180.
17. Sivula, K., F.L. Formal, and M. Grätzel, *WO_3– Fe_2O_3 Photoanodes for Water Splitting: A Host Scaffold, Guest Absorber Approach.* Chemistry of Materials, 2009. **21**(13): p. 2862-2867.
18. Jin, T., et al., *WO_3 nanoneedles/ α-Fe_2O_3/cobalt phosphate composite photoanode for efficient photoelectrochemical water splitting.* Applied Catalysis B: Environmental, 2014. **148-149**: p. 304-310.
19. Memar, A., C.M. Phan, and M.O. Tade, *Photocatalytic activity of WO_3/Fe_2O_3 nanocomposite photoanode.* International Journal of Hydrogen Energy, 2015. **40**(28): p. 8642-8649.

20. Memar, A., et al., *Study on photocurrent of bilayers photoanodes using different combination of WO_3 and Fe_2O_3.* Solar Energy, 2010. **84**(8): p. 1538-1544.
21. Müller, A., et al., *Dual absorber Fe_2O_3/WO_3 host-guest architectures for improved charge generation and transfer in photoelectrochemical applications.* Materials Research Express, 2017. **4**(1): p. 016409.
22. Hosseini, S., et al., *Effect of intermediate layer in photocurrent improvement of three-layer photoanodes using WO_3 and Fe_2O_3.* Journal of Environmental Chemical Engineering, 2013. **1**(4): p. 1309-1314.
23. Ramos-Delgado, N.A., et al., *Solar photocatalytic activity of TiO_2 modified with WO_3 on the degradation of an organophosphorus pesticide*. Journal of Hazardous Materials, 2013. **263**: p. 36-44.
24. Stoycheva, T., et al., *Micromachined gas sensors based on tungsten oxide nanoneedles directly integrated via aerosol assisted CVD.* Sensors and Actuators B: Chemical, 2014. **198**: p. 210-218.
25. Xu, Z., et al., *Preparation of platinum-loaded cubic tungsten oxide: A highly efficient visible light-driven photocatalyst.* Materials Letters, 2011. **65**(9): p. 1252-1256.
26. Sayed Abhudhahir, M.H. and J. Kandasamy, *Synthesis and characterization of Manganese doped Tungsten oxide by Microwave irradiation method.* Materials Science in Semiconductor Processing, 2015. **40**: p. 695-700.
27. Rashad, M.M. and A.E. Shalan, *Hydrothermal synthesis of hierarchical WO_3 nanostructures for dye-sensitized solar cells.* Applied Physics A, 2014. **116**(2): p. 781-788.
28. Walczak, J. and I.J.T.a. Rychłowska-Himmel, *Phase equilibria in the systems Fe_2O_3-WO_3 and $FeVO_4$-WO_3.* 1993. **221**(1): p. 115-121.
29. Kollender, J.P., A.I. Mardare, and A.W. Hassel, *Localized Photoelectrochemistry on a Tungsten Oxide–Iron Oxide Thin Film Material Library.* ACS Combinatorial Science, 2013. **15**(12): p. 601-608.
30. Abdi, F.F., et al., *Assessing the Suitability of Iron Tungstate (Fe_2WO_6) as a Photoelectrode Material for Water Oxidation.* The Journal of Physical Chemistry C, 2017. **121**(1): p. 153-160.
31. Khader, M.M., M.M. Saleh, and E.M. El-Naggar, *Photoelectrochemical characteristics of ferric tungstate.* Journal of Solid State Electrochemistry, 1998. **2**(3): p. 170-175.
32. León, C.P., et al., *In situ laser-induced formation of α-Fe_2O_3 from Fe^{3+} ions in a cylindrical core-shell polymer brush.* Journal of Raman Spectroscopy, 2004. **35**(2): p. 165-169.
33. Mörl, K., et al., *Optical properties of sputtered Fe_2O_3 films.* Thin Solid Films, 1979. **60**(1): p. 49-53.
34. Akl, A.A., *Influence of preparation conditions on the dispersion parameters of sprayed iron oxide thin films.* Applied Surface Science, 2010. **256**(24): p. 7496-7503.
35. Mallick, P. and B. Dash, *X-ray diffraction and UV-visible characterizations of α-Fe_2O_3 nanoparticles annealed at different temperature*. J. Nanosci. Nanotechnol, 2013. **3**(5): p. 130-134.
36. Cornell, R.M. and U. Schwertmann, *The iron oxides: structure, properties, reactions, occurrences and uses*. 2003: John Wiley & Sons.
37. Beermann, N., et al., *Photoelectrochemical Studies of Oriented Nanorod Thin Films of Hematite.* Journal of The Electrochemical Society, 2000. **147**(7): p. 2456.
38. Leiva, H., K. Dwight, and A. Wold, *Preparation and characterization of conducting iron tungstates.* Journal of Solid State Chemistry, 1982. **42**(1): p. 41-46.
39. Rawal, S.B., et al., *Fe_2WO_6/TiO_2, an efficient visible-light photocatalyst driven by hole-transport mechanism.* Catalysis Communications, 2014. **56**: p. 55-59.
40. Kim, H.i., et al., *Robust Co-catalytic Performance of Nanodiamonds Loaded on WO_3 for the Decomposition of Volatile Organic Compounds under Visible Light.* ACS Catalysis, 2016. **6**(12): p. 8350-8360.

Chapter 6 Electrochemical synthesis of 1D-Iron Oxide as Negative Electrode for Lithium Ion-Battery Microelectrode

6.1. Introduction

In the past decades, the microelectrode lithium ion batteries (LIBs) with the thickness bellow 100 µm were widely used as miniature electronic, intelligent labels, micro-electromechanical systems (MEMS), CMOS back up and implantable medical devices [1-4]. Efforts have been made to provide higher energy and power, due to requirement for emerging technology needs. 1D lithium ion batteries are introduced to maximize the energy and power densities in a small area (~1 cm^{-2}) while maintaining short lithium ion transport distances. Various fabrication methods were applied to produce 1D materials, including hydrolysis[5], precipitation[6], thermal decomposition [7] and anodizing [8]. Among of them, the anodizing is a reliable fabrication method that allows formation of ordered and free-standing oxide without the addition of binders and conductive paste. By anodizing metals using organic electrolyte containing fluoride; self-ordered anodic titania, niobia, iron oxides can be formed.

Iron oxide is one of the most interesting and important transition metal oxides for application in LIBs. Trigonal R-3C Fe_2O_3, with lattice parameters of a = b = 0.51 nm and c = 1.39 nm (Figure 6.1 a.), being the most thermodynamically stable iron oxide phase, has relatively high theoretical capacity of 1007 mAh g^{-1} [5, 9] and the theoretical capacity value of cubic Fd3m Fe_3O_4, with a = b = c = 0.602 nm (Figure 6.1 b.) is 926 mAh g^{-1} [10-12]. In addition, multiple electron valence states of Fe^0, Fe^{2+} and Fe^{3+} provide rich redox pairs, and iron has abundance and environmental friendliness, and has been studied as candidate negative electrode material since first reported as conversion-type material. In this study, the use of iron oxide thin film electrodes prepared *via* anodizing method was investigated for the first time. The objective is to investigate the influence of crystallographic structure of anodic iron oxide to the areal capacity, efficiency and stability as the negative electrode in a half cell with 1 M $LiPF_6$ in ethylene carbonate/dimethyl carbonate, EC/DMC (1:1 v/v) as electrolyte was used to control the electrochemical lithiation/delithiation process.

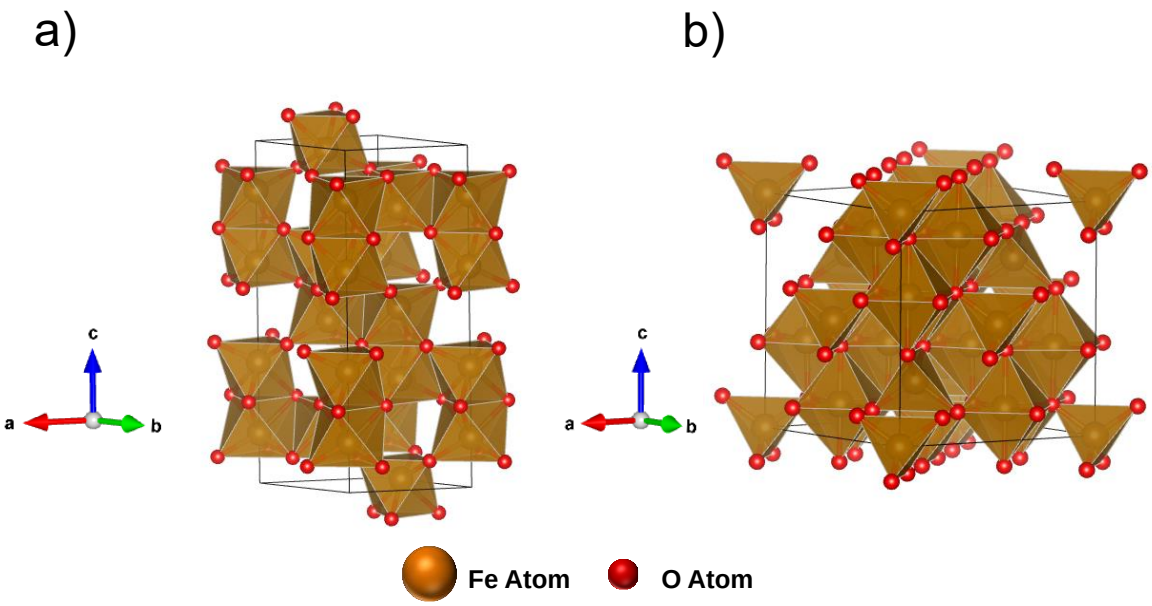

Figure 6.1 Crystallographic representation and outline of the unit cells of Fe_2O_3 and Fe_3O_4. [13]

6.2. Experimental Method

High purity of 99.9% polycrystalline iron foils; 0.3 mm thick, 1 cm^2 area (Nilaco Corp., Tokyo, Japan) was anodized at 60 V for 4 h in ethylene glycol electrolyte containing 0.1 mol dm^{-3} ammonium fluoride and 1.5 mol dm^{-3} deionized water in bath type electrochemical cell with a two-electrode system using platinum counter electrode. The distance between working and counter electrodes was kept constant at 15 mm. During anodizing the temperature of electrolyte was kept at 20 °C using circulated temperature-controlled water (Eyela CTP-1000, Tokyo Rikakikai Co, Ltd, Japan). After anodizing, the specimens were rinsed in ethylene glycol, ethanol (99,8%), and then dried in air stream. The as-anodized iron oxide layers were thermally annealed in a muffle furnace (Model FO310, Yamato Scientific Co. Ltd, Japan) at 350 ^oC, 450 ^oC and 500 ^oC in air for 30 min. In all the cases, the heating from room temperature to the selected temperatures was carried out at a rate of 10 K min^{-1}. And finally, the samples were left to cool down within the oven.

The surface morphology and cross sections of the specimens were examined by a Zeiss Sigma 500 field emission scanning electron microscope (SEM) instrument; 1 kV accelerating voltage was used to investigate the morphology. The lamella of anodic oxide were prepared by a Hitachi FB-2100 focused ion beam (FIB) system employing a Ga^+ ion beam to observe the electron distribution. Cross-sections of the anodized specimens were observed by a JEOL, JEM-ARM200F scanning transmission electron microscope

(STEM) with energy dispersive X-ray spectrometry (EDS) facilities. The phase in the anodic films identified by Rigaku, RINT-2000 Ultima X-ray diffractometer using Cu-Kα radiation (λ = 0.15418 nm) with a *2θ* range of 10–80 degrees at a scan speed of 0.5 degree/min and collected by a tube voltage of 40 kV and 20 mA tube current. For the analysis thin film, grazing incidence XRD mode was used to minimize the contribution of the substrate material.

Figure 6.2 Schematic of lithium ion battery half-cell.

The anodic iron oxide microelectrode was electrochemically tested as negative electrodes in half cell PAT-Cell (EL-cell) with constant current charge/ discharge at 20 µA cm^{-2} and the *in-situ* optic and raman spectroscopy was observed by using Optical-Cell (EL-cell) with constant current charge/ discharge at 13 µA cm^{-2} in lithium ion battery. The coin cells were assembled in argon filled glove-box using lithium foil as counter/reference electrode and 1 M $LiPF_6$ in ethylene carbonate/dimethyl carbonate, EC/DMC (1:1 v/v) electrolyte. A potential range of 2.60 to 0.05 V vs. Li reference electrode was used to extract the capacity and cyclic stability of the material. The rate capability and cycle stability were evaluated by current varied between 0.1 to 2 mA cm^{-2}. For avoiding experimental error, the term of mass of gravimetric capacity, ($mA.h.g^{-1}$) was changed to terms of areal capacity ($mA.h.cm^{-2}$) as demonstrated for other anodic systems.

6.3. Results and Discussion

6.3.1. Structural and morphological characterization

The structure of polycrystalline iron anodized at 60 V for 4 h in ethylene glycol electrolyte containing 0.1 mol dm^{-3} of ammonium fluoride and 1.5 mol dm^{-3} of deionized water at 20 °C is shown in SEM images in Fig. 6.2. The surface morphology shows nanotubular structure with average nanotube diameter of 100 ± 1 nm. The cross-section image indicates thickness of anodic layer of 7 ± 0.2 μm. The close inspection of the structure indicates that top of the structure is nanotubular (TiO_2-like) and the bottom is nanoporous (Al_2O_3-like) with the length ratio of nanotubes to nanopores of 0.4. The transition from nanopores to nanotubes is typically observed during anodizing process due to relatively slow kinetics of dissolution FeF_2 located at the cell boundary region of nanopore/nanotube [8].

Figure 6.4 shows the high angle annular dark field (HAADF) image of the focused ion beam (FIB) lamella prepared for iron anodized at 60 V. The region with lighter appearance in the micrograph corresponds to iron substrate while darker fractions to anodic film. The compositional structure of anodic film is evident from high resolution energy dispersive X-ray spectrometry (EDS) elemental maps for distribution of Fe, F and O. At the first glance, the anodic film looks nanoporous from HAADF image, however, the EDS analysis reveals that the oxide is in the form of nanotube separated by FeF_2 matrix. The formation of FeF_2 at the base of nanotube is possible due to relatively fast migration of F^- ions relative to that of O^{2-} ions under the high electric field during film growth. [14] The horizontal position of FeF_2 is changed to vertical one at the cell boundary region due to material flow at convex geometry of the pore/tube.[8, 15] The enrichment of the cell boundary region with fluorine is key in the transition of nanopores into nanotubes due to the solubility of the FeF_2 in the electrolytes already demonstrated in a previous study.[8]

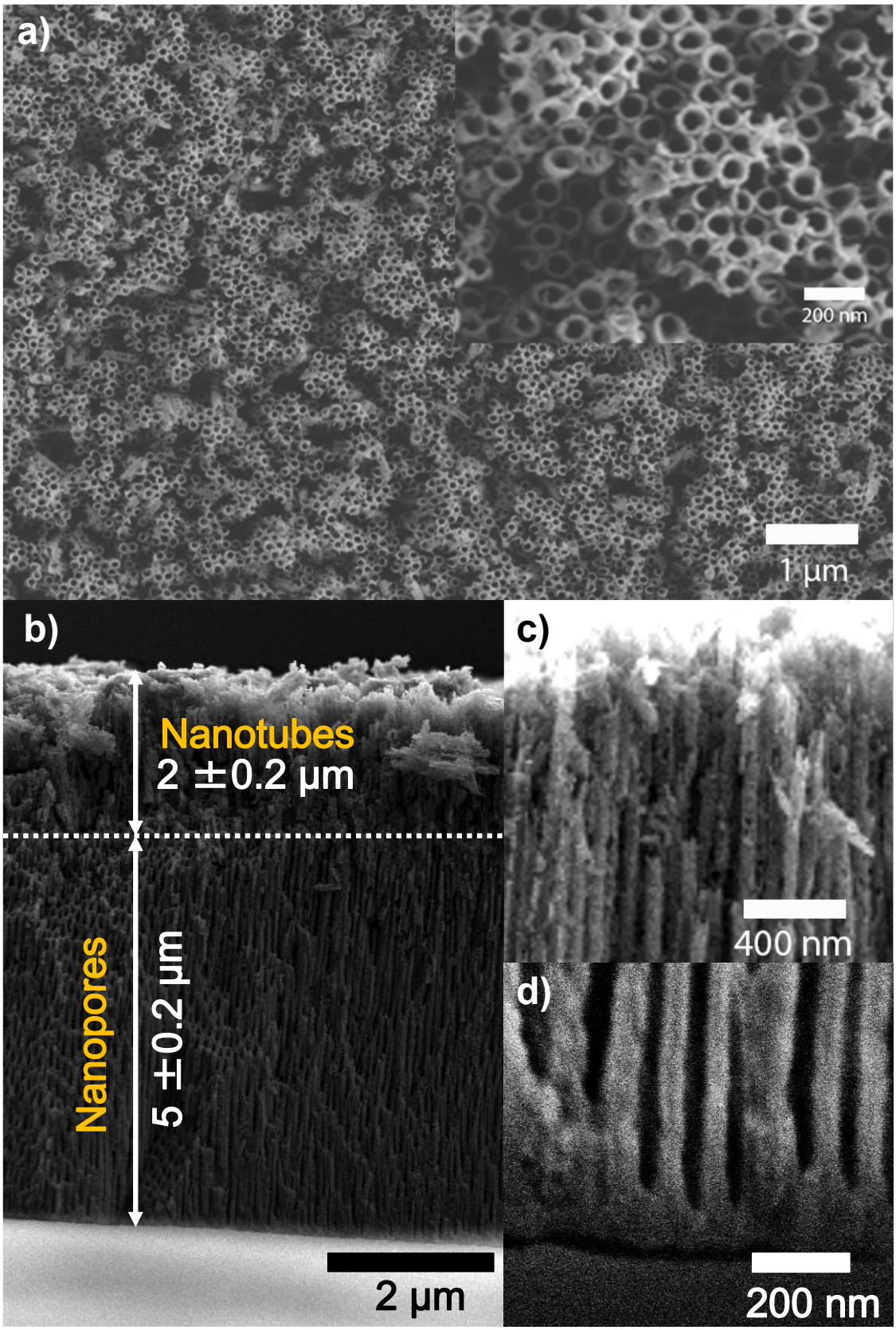

Figure 6.3 (a) Surface morphology and (b) cross-section SEM images obtained by SE mode at 3 kV; of nanopores/nanotubes formed by anodizing of Fe at 60 V in ethylene glycol electrolyte containing 1.5 mol dm^{-3} of water and 0.1 mol dm^{-3} of NH_4F at 20 ^{o}C, detail of nanotubular formation on top part and nanoporous formation on bottom part shown on (c) and (d).

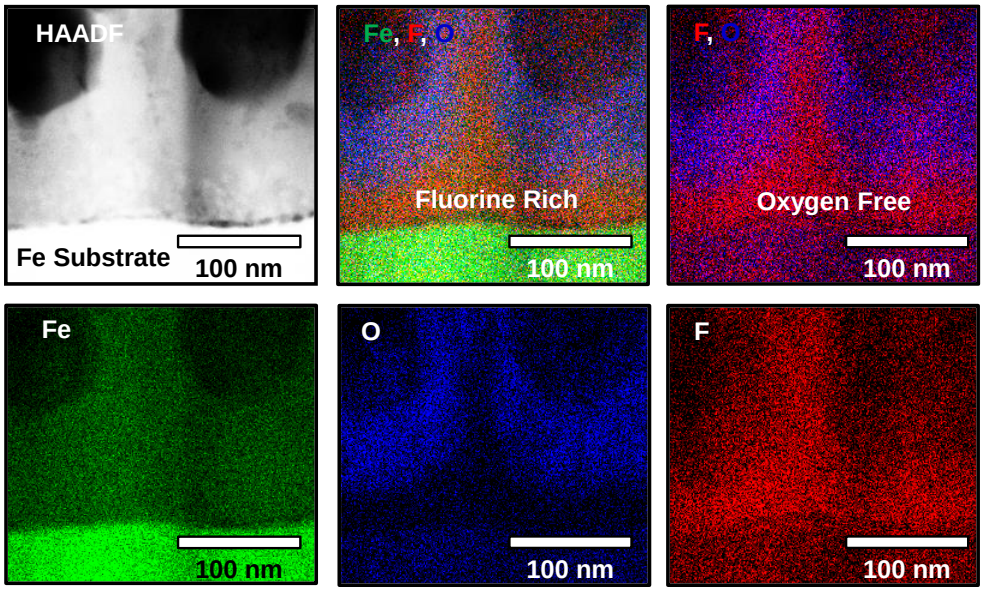

Figure 6.4 High Angle Annular Dark Field (HAADF) and Energy Dispersive X-Ray Spectrometry (EDS) mapping images for anodic layers formed on iron, anodized at 60 V in ethylene glycol electrolyte containing 1.5 mol dm^{-3} of water and 0.1 mol dm^{-3} of NH_4F at 20 ^oC.

In order to estimate the effect of crystallographic structure and chemical composition of 1D anodic nanotubes on the performance of the lithium ion battery, the specimens were subjected for thermal treatment at 350, 450, and 500 °C in the presence of oxygen and studied by means of x-ray diffraction (XRD) (Fig. 6.5) and EDS (Fig. 6.7). All of the specimens show a very intense 2θ diffraction peak at 65.20^o corresponding to 200 reflection coming from underling metal substrate. The as formed nanotubes/nanopores were generally amorphous with very low degree of crystallinity having 2θ peaks at 24.10° indexed to 012 reflection of Fe_2O_3 (ICSD no. 80-2377), 35.40° and 56.94° corresponding to 311 and 511 reflections of Fe_3O_4 (ICSD no. 75-1372) and 2θ peaks at 26.82° and 52.10° matching FeF_2 110 and 211 reflections (ICSD no. 81-2271). It is known that the tubes/porous layer can be converted to Fe_2O_3 and underlying barrier layer and thermal oxide changes to Fe_3O_4.[16] Annealing at 450 °C and 500 °C crystallizes the oxide whereby peaks of Fe_2O_3 and Fe_3O_4 are clearly observed and indexed according to the ICSD cards as mentioned above, whereas the peaks indexed to FeF_2 were not detected. By using with Rietveld refinement method using GSAS software, the ratio of Fe_2O_3 to Fe_3O_4 was roughly estimated. The specimen annealed at 450 °C appears to have 88 % Fe_2O_3, 12 % Fe_3O_4. The 500 °C annealed sample has 96% Fe_2O_3, 4% Fe_3O_4 temperature, respectively. (The Rietveld ravinement results shown on Figure 6.6).

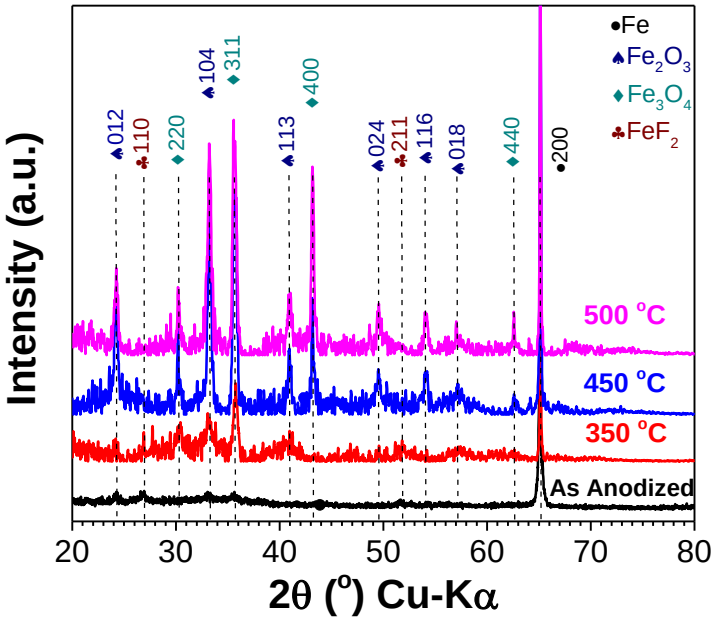

Figure 6.5 XRD patterns of the annealed and as-formed iron oxide microelectrodes formed at 60 V in ethylene glycol electrolyte containing 1.5 mol dm^{-3} of water and 0.1 mol dm^{-3} of NH_4F at 20 °C.

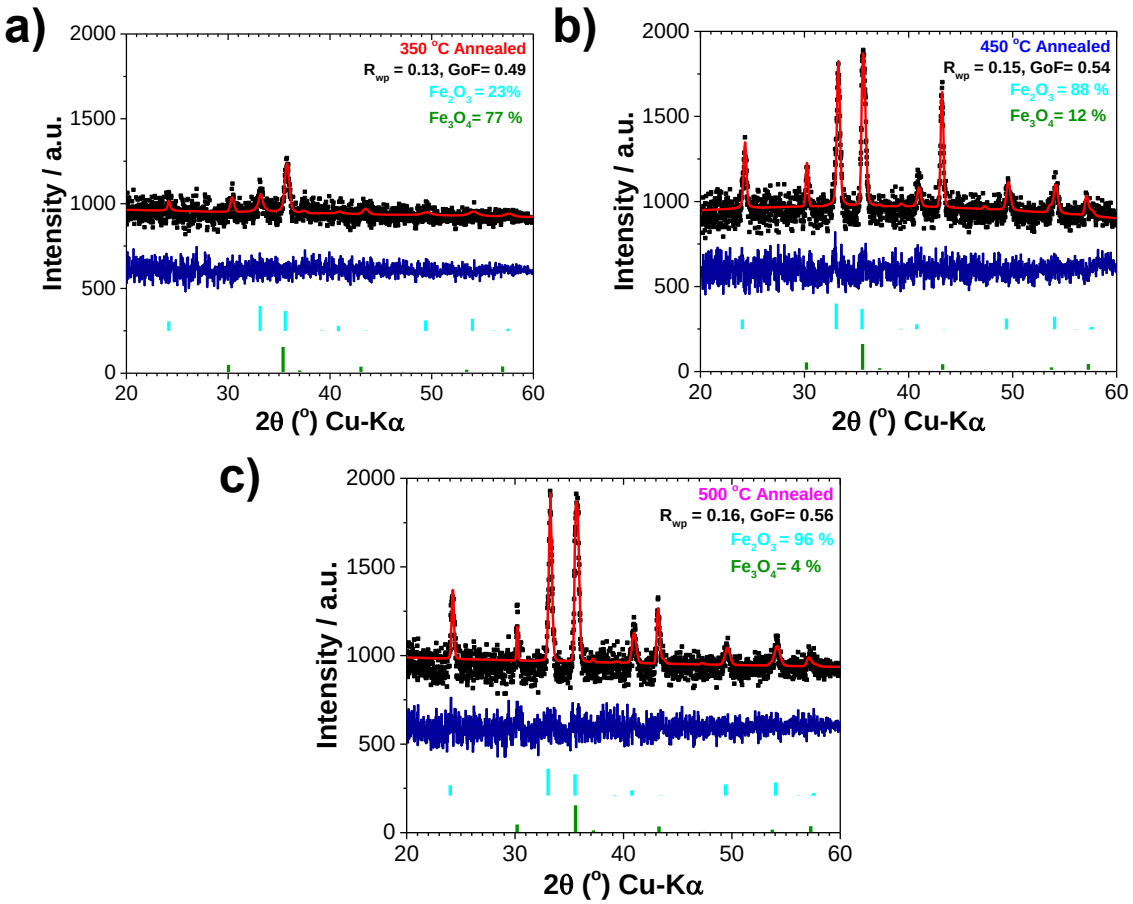

Figure 6.6 XRD refinement of the annealed iron oxide microelectrodes formed at 60 V in ethylene glycol electrolyte containing 1.5 mol dm^{-3} of water and 0.1 mol dm^{-3} of NH_4F at 20 °C after annealing at (a) 350 °C, (b) 450 °C and (c) 500 °C.

Annealing at 350 °C resulted in higher percentage ratio of Fe_3O_4 77% and 23% of Fe_2O_3. A low intensity diffraction peak corresponding to 211 reflection of FeF_2 is detected. The presence of FeF_2 is consistent with identification of fluoride-rich-layer by Shahzad et al. by means of TEM/EDS elemental mapping in the transition of anodic nanopores into nanotubes formed on bulk iron [8]. According to composition evaluated in chapter 3, as-anodized sample resulted in formation of amorphous structures with some semi crystalline phase of Fe_3O_4 and FeF_2. The anodic film composition on various spot on the surface of as-anodized and annealed iron oxides was investigated by means of EDS analysis with the atomic ratio of iron to oxygen and fluorine to iron shown in Fig. 6.7. The atomic ratio of F/Fe is high for as-anodized iron according to expected composition of $Fe_3O_4.FeF_2$ formed on high index facets of iron . The fluorine content is significantly reduced upon annealing, more specifically the trace amount of fluorine was detected for anodic film annealed at 350 °C whereas specimens annealed at 450 - 500 °C are essentially free from fluorine. The atomic ratio of oxygen to iron for as-anodized iron depends on crystallographic orientation of iron as demonstrated on single crystal studies with preferential formation of Fe_3O_4 on high index facets of iron and therefore in line with Fe_3O_4 structure of polycrystalline specimen. The ratio of oxygen to iron increases with annealing temperature revealing that specimen annealed at 500 °C has a ratio similar to hematite (Fe_2O_3), the one annealed at 450 °C shows ratio for mixed structure of hematite (Fe_2O_3) and magnetite (Fe_3O_4), whereas the oxide annealed at 350 °C ratio of magnetite (Fe_3O_4).

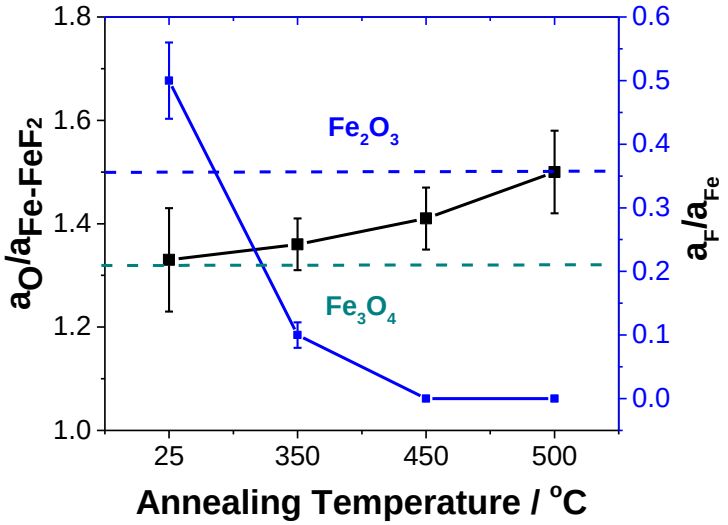

Figure 6.5 Atomic ratio of oxygen and fluorine to the iron on as formed and annealed iron oxide microelectrodes formed at 60 V in ethylene glycol electrolyte containing 1.5 mol dm^{-3} of water and 0.1 mol dm^{-3} of NH_4F at 20 °C.

6.3.2. Electrochemical characterization of iron oxides

Making an assumption Fe_2O_3 and Fe_3O_4 are the main phases of anodic nanotubes/nanopore which electrochemically active during lithiation and delithiation in the potential range of 5 mV - 2.6 V vs. Li/Li^+, the electrochemical process may be described by following the reactions: [17-19] , [20-22]

$$Fe_2O_3 + 6Li^+ + 6e^- \leftrightarrow 2Fe^0 + 3Li_2O \quad (6.1)$$

$$Fe_3O_4 + 8Li^+ + 8e^- \leftrightarrow 3Fe^0 + 4Li_2O \quad (6.2)$$

$$FeF_2 + 2Li^+ + 2e^- \leftrightarrow Fe^0 + 2LiF \quad (6.3)$$

Galvanostatic cycling with potential limitation (GCPL) was carried out to investigate in details the electrochemical activity of nanotubular/nanoporous anodic film in the lithiation process. In order to get an insight into the lithiation process the GCPL was performed at 20 $\mu A.cm^{-2}$, typical current density range of nanotubular microelectrodes, in the potential window of 5 mV – 2.6 V vs. Li/Li^+ reference electrode. Figure 6.8 shows the first lithiation of the differential capacity plot, $dQ.dE^{-1}$, for 500 ^oC annealed specimen. The first cathodic scan corresponding to initial lithiation of the nanopores/nanotubes (Fig. 6.8) shows the cathodic peaks at 0.86 V (P1) and 0.77 V (P2) vs. Li/Li^+, with P1 observed upon electrochemical reduction of Fe_2O_3 to Fe^0 with the formation of Li_2O according to reactions 6.1 and P2 is assigned the reduction of Fe_3O_4 to Fe^0 with the formation of Li_2O according to 6.2 [23].

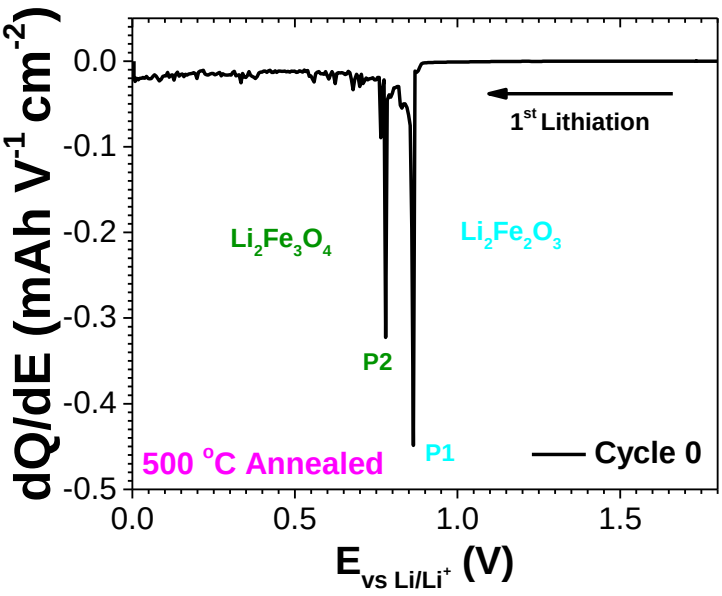

Figure 6.6 Differential capacity plot recorded for the first lithiation of 500 ^oC annealed iron oxide microelectrode.

The succeeding 1st anodic scan in Fig. 6.9 shows the broad anodic $dQ.dE^{-1}$ peak containing two components P4 and P5 at ca. 1.6 V and 1.8 V vs. Li/Li^+ corresponding to oxidation of Fe^0 to Fe_2O_3 and Fe_3O_4 [17-19] , [20-22]. For the subsequent cycles, the anodic scan of the 300 °C annealed and as-anodized samples only show one peak; this suggests that most of Fe_3O_4 may not be regenerated. The cathodic peaks of all the samples after the first cycle shifts to lower voltage due to the irreversibility of the redox reaction with decreased intensity which could be caused by crystal damage, volume expansion or shrinkage of iron oxides (Fe_2O_3/Fe_3O_4) and formation of the SEI film. The 350 °C annealed and as-anodized microelectrodes shown on Fig. 6.9 c-d exhibit similar kind of redox reaction with an additional peak in PA 2.25 V vs. Li^+/Li for the as-anodized electrode and PA 2.1 V vs. Li^+/Li at 350°C annealed electrode. The PA might be correlated to the remaining fluoride content and lower crystallinity in the samples as describe in the reaction 6.3. For the subsequent cycles, only one cathodic peak appears and shifts to P2' of 0.77 V vs. Li^+/Li for as-anodized one and P2' of 0.98 V vs. Li^+/Li for 350 °C annealed one with decreased intensity which could be caused by of the crystal damaging, volume expansion or shrinkage of $Fe_2O_3/Fe_3O_4/FeF_2$.

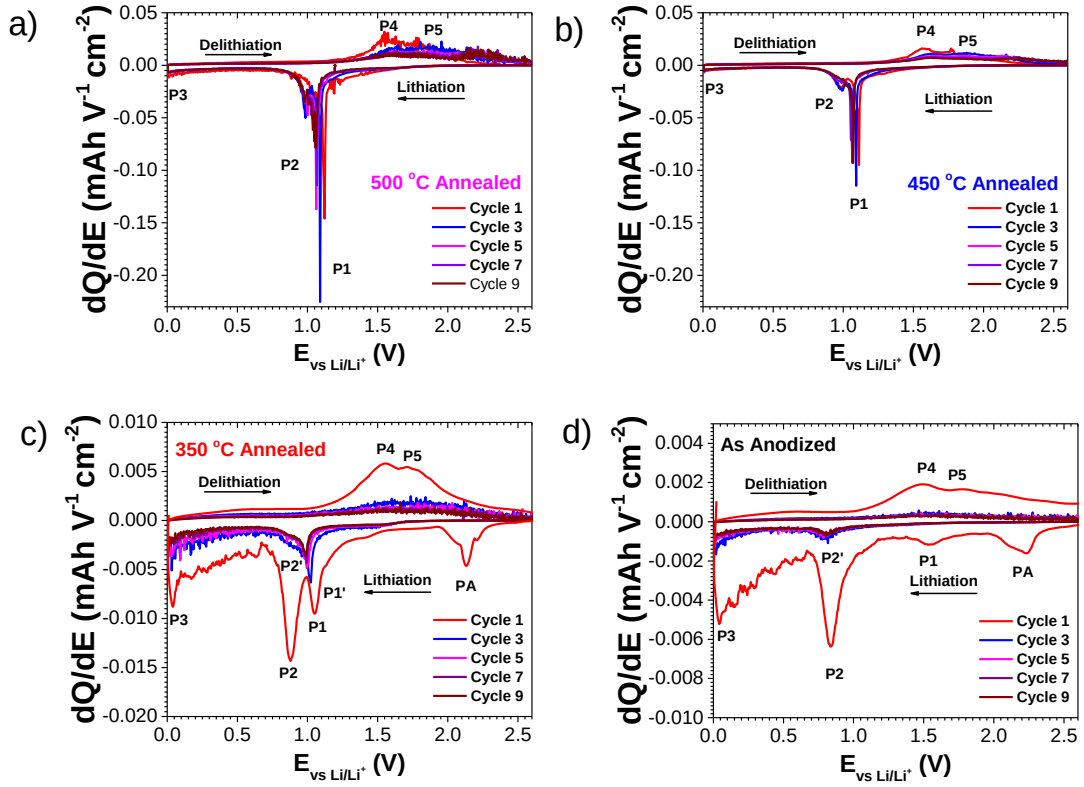

Figure 6.7 Differential capacity plots recorded for (a) as anodized, (b) 350 °C, (c) 450 °C and (d) 500 °C annealed iron oxide microelectrode in 1 mol dm^{-3} $LiPF_6$ EC:DMC 1:1 at constant current density 20 µA cm^{-2}.

In-situ Raman spectra of the iron oxide annealed at 450 ºC in the working battery during lithiation and delithiation were recorded and shown at Fig. 6.10. The Raman spectrum was collected before the charge process began, exhibiting the Raman peaks of crystalline Fe_2O_3, Fe_3O_4 and the electrolyte near 890 cm^{-1}. The Raman intensity peak stays high, followed by a sharp decrease at 1.2 V vs. Li^+/Li, due to the lithiation of the iron oxides film, in line with differential capacity plot recorded at Figure 6.9 b. The decrease of Raman intensity might be related to the conversion reaction; to the reduction of metallic Fe. After the discharge process, the intensities of Raman peaks for Fe_2O_3 and Fe_2O_3 increase at 1.7 V vs. Li^+/Li, confirming that our system is reversible.

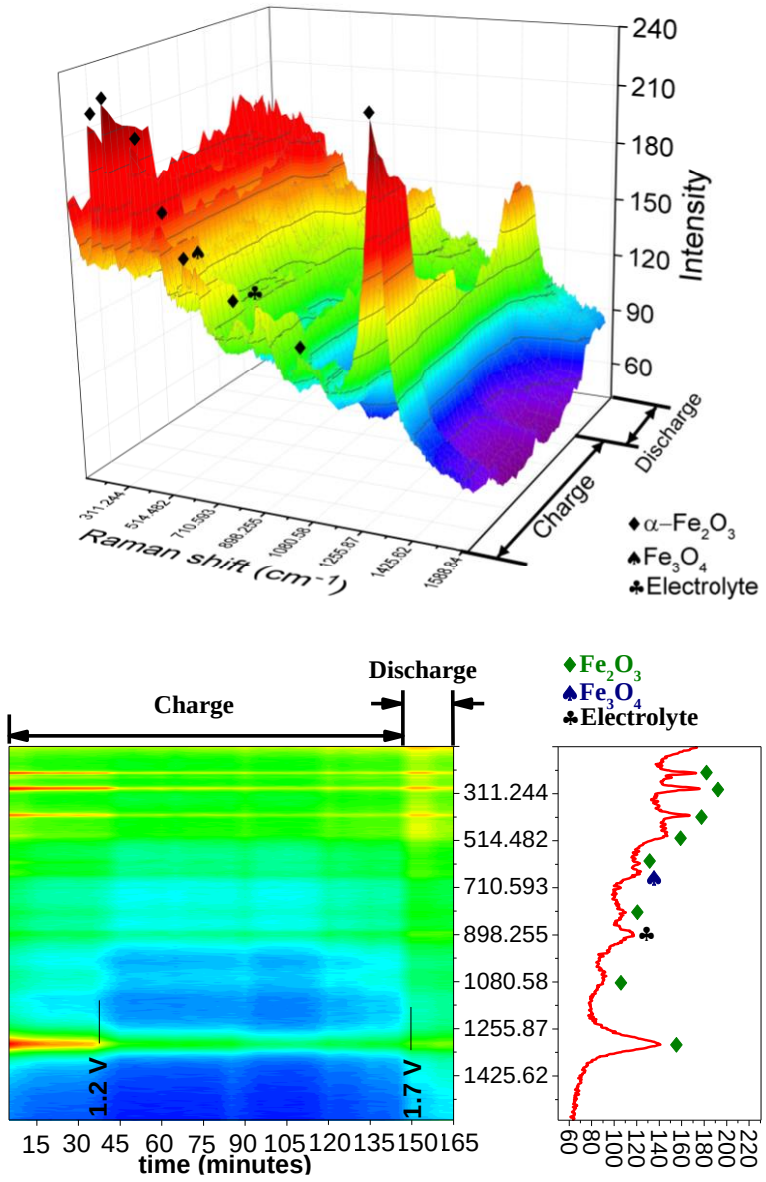

Figure 6.8 *in-situ* Raman spectroscopy recorded for 450 ºC microelectrode in 1 mol dm^{-3} $LiPF_6$ EC:DMC 1:1 at constant current density 3 µA cm^{-2}.

Fig. 6.11 compares the cycling performance of the 1st to 10th cycles of 500 °C, 400 °C, 300 °C annealed and as-anodized as the electrode. The electrochemical behavior of all electrodes is similar and in general consistency with the literature[5, 24, 25]. Fig. 6.10a shows high capacity of 3.5 mA h cm^{-2} and well-defined shape of charge–discharge capacities, a steep voltage drops from open circuit voltage to 1.2 V vs. Li^+/Li. A plateau at a potential of 1.2 V vs. Li^+/Li corresponding to the reversible reaction between $Li_xFe_2O_3$/ $Li_xFe_3O_4$ and Fe^0. Then, the plateau is followed by a voltage drop to 0.05 V correspond to the conversion from $Li_xFe_2O_3$/ $Li_xFe_3O_4$ to metal Fe^0 and the formation of Li_2O. Similar to 500 °C annealed, the cells with 450 °C annealed in Fig. 6.10b have well-defined shape of charge–discharge capacities, indicating that the annealing process is responsible for the enhancement in cycling performance. As shown in Fig. 6.11 c-d the poor defined shape, the voltage fades and the capacities of the cells with 350 °C annealed and as-anodized specimens decrease drastically after first cycle. The initial capacity loss might be attributed to the presence of small amounts of iron fluorides on the metal film interface. Iron fluorides (FeF_2) are well-known for their intrinsically poor electronic conductivity yield to stunted electron transport resulting in a very low capacity [26, 27]. The voltages fade also could be originated from the lack of crystallinity of the 350 °C annealed and as anodized microelectrodes.

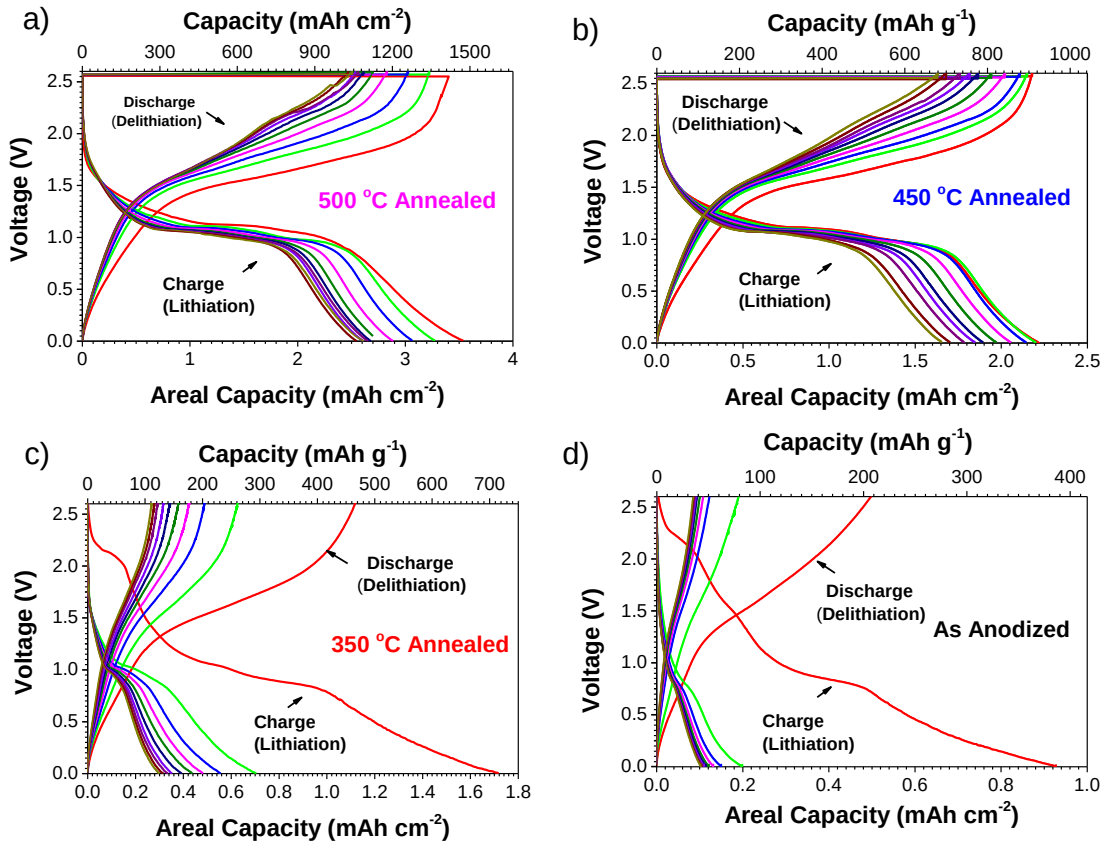

Figure 6.9 Typical charge/discharge curves for the initial 10 cycles recorded for the (a) as anodized, (b) 350 °C, (c) 450 °C and (d) 500 °C annealed iron oxide microelectrode in 1 mol dm^{-3} $LiPF_6$ EC:DMC 1:1 at constant current density 20 µA cm^{-2}.

Assuming perfect iron oxide nanotubes arrangement over the entire substrate area, with a length of 7 µm, a tube inner diameter of 55 nm and outer diameter of 110 nm. The theoretical volume of iron oxide 4.3 x 10^{-4} cm^3 is obtained from 1 cm^2 surface. The density of Fe_2O_3 and Fe_3O_4 are 5.24 g cm^{-3} and 5.17 g cm^{-3}, the estimated mass for 450 °C annealed sample is 2.2 mg cm^{-2}. The mass of the 450 °C annealed sample was also measured gravimetrically after cycling the samples for 100 times; with 2.4 mg cm^{-2}. By the data given, with approximately 10% mass experimental error; the expected capacity at 2.3 mA cm^{-2} for 450 °C annealed sample is 958 mAh g^{-1}. The theoretical capacity of Fe_2O_3 = 1000 mAh g^{-1} [5, 9] and Fe_3O_4 = 926 mAh g^{-1} [10-12], it is reasonable to assume that all the iron oxide compound was electrochemically active during lithiation and delithiation processes.

Fig. 6.12a displays the areal capacities vs. cycle number with coulombic efficiency for 500 ^{o}C, 400 ^{o}C, 300 ^{o}C annealed and as-anodized specimens. It can be seen that the cells containing the 500 ^{o}C annealed iron oxide microelectrode provided the highest initial areal capacity of 3.5 mA h cm^{-2}, followed by 2.3 mA h cm^{-2}, 1.7 mA h cm^{-2} and 0.9 mA h cm^{-2} for 400 ^{o}C, 300 ^{o}C annealed and as-anodized electrodes, respectively, using a constant current density of 20 µA cm^{-2}. After 10 cycles, 300 ^{o}C annealed and as-anodized electrodes have maintained its stability of 0.26 mA h cm^{-2} and 0.1 mA h cm^{-2} over 50 cycles, respectively. The rate capability of 500 ^{o}C, 400 ^{o}C, 300 ^{o}C annealed and as-anodized electrodes is measured by galvanostatic cycling of the cells at different current densities, as shown in Fig. 6.12b. The electrodes are first cycled at a rate as low as 0.1 mA cm^{-2}, the 500 ^{o}C annealed specimen have a capacity of 2 mA h cm^{-2}, after 22 cycles the capacity decreases to 1.4 mAh cm^{-2}. Subsequently, as the current is increased stepwise to 2.0 mA cm^{-2}, the reversible capacity pronounced to decrease progressively. This decrease in reversible capacity is mainly due to the low conductivity of the nanotubes, less participation of active material or surface of the active material only involved in the electrochemical reaction. As can be seen, the electrode delivers stable capacities of 0.06 and 0.02 mA h cm^{-2} at 0.4 and 2.0 mA cm^{-2}, respectively. As-anodized electrode shows low specific discharge capacities of 0.048, 0.035, 0.024, 0.013, 0.005, and 0.001 mA h cm^{-2} at current densities of 0.1, 0.2, 0.4, 1.0 and 2.0 mA cm^{-2}, respectively. It should be noted, after 125 cycles, with the current being again decreased back to 0.1 mA cm^{-2} from 0.4 mA cm^{-2} the cell failed to maintain the stability as the capacity fluctuate to higher value.

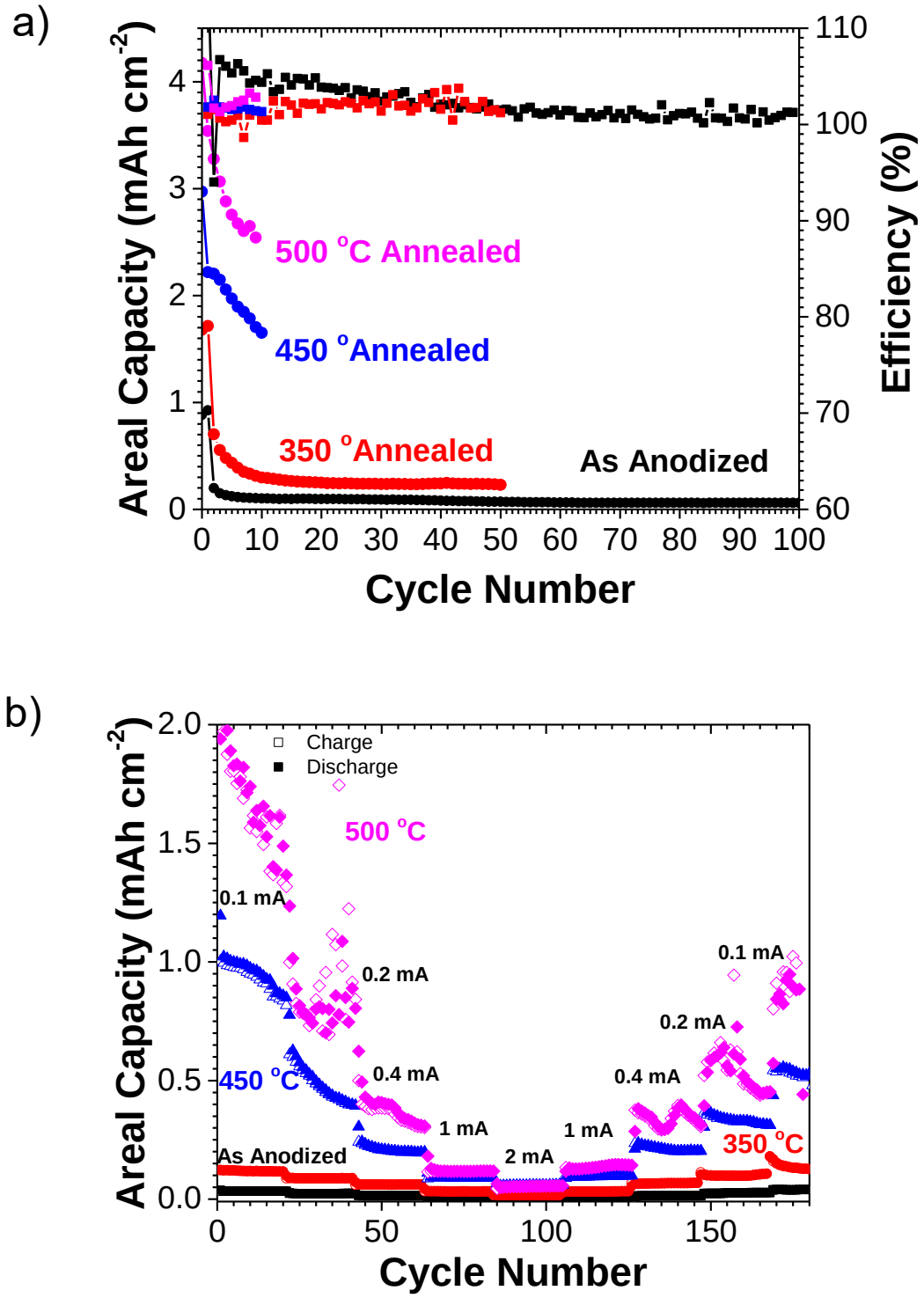

Figure 6.10 (a) Plot of capacity vs. cycle number and columbic efficiency of microelectrodes iron oxide in 1 mol dm^{-3} $LiPF_6$ EC:DMC 1:1 at constant current density 20 µA cm^{-2} and (b) rate capability for iron oxide in 1 mol dm^{-3} $LiPF_6$ EC:DMC 1:1 at different current densities from 0.04 to 2 mA cm^{-2}.

Moreover, the stability of 450 ^{o}C annealed specimen under 0.1 mA cm^{-2} in $LiPF_6$ electrolyte was measured (Fig. 6.13a).

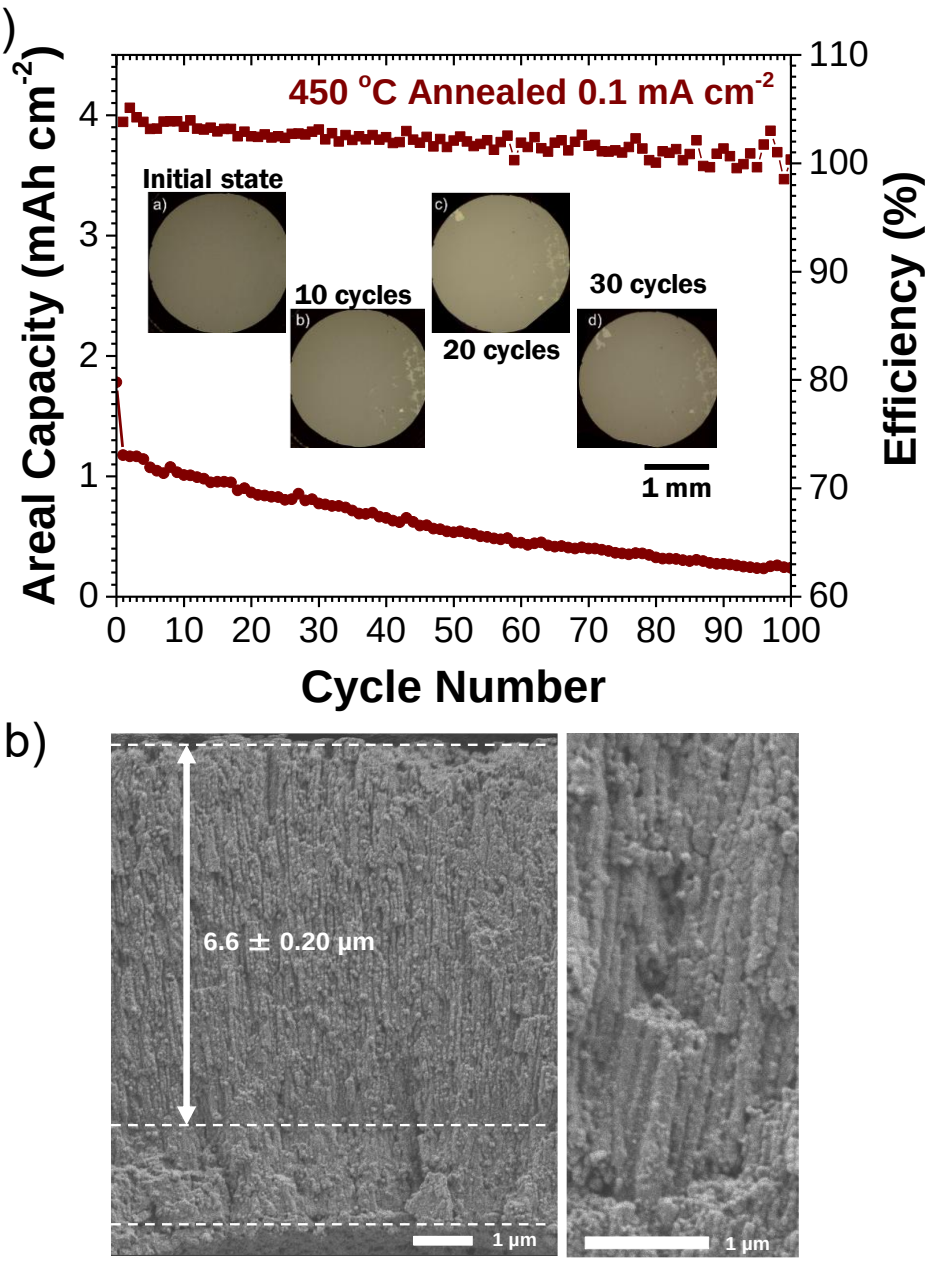

Figure 6.11 (a) Plot of capacity vs. cycle number and columbic efficiency and (b) SEM images for iron oxides annealed at 450 ^{o}C after 100 cycles of charge/discharge in 10 vol.% of FEC in 1 mol dm^{-3} $LiPF_6$ with area specific charge density of at 0.1 mA cm^{-2}, EC: DMC 1:1.

It is obvious that the capacity decreasing from 1.1 mA h cm^{-2} to 0.2 mAh cm^{-2}, the SEM images on Figure 6.13b. shows there is no deformation of nanotubes morphology after 100 cycles. However, the *in-situ* observation using optical microscopy was conducted, to have better understanding on the stability of the iron oxide nanotubes

microelectrodes. As shown in Figure 6.13 (a.), after the subsequent cycle it was obvious there are some objects floating in the electrolyte. Despite of there is no deformation of nanotubes morphology, the detachment of the iron oxides from the substrate were clearly observed which causes the capacity fade.

Taking into account that ordered nanotubular structures has beneficial role to the capacity values of the lithium ion batteries. Figure 6.14 compares the performance of our system to the recent reports on the iron based microelectrodes and nanotubular anodic oxides microelectrode; e.g.: Fe_2O_3 prepared by thermal oxidation (0.042 mAh cm^{-2} on 1st discharge, 0.026 mA h cm^{-2} after 50 cycles at 20 µA cm^{-2}) [28], electrodeposited Fe_3O_4 thin films on copper plate (about 0.3 mAh cm^{-2} at 0.01 mA cm^{-2}) [29], nanowires Fe_3O_4/ nanotubular TiO_2 (0.47 mAh cm^{-2} on 1st discharge, 0.2 mA h cm^{-2} after 45 cycles at 25 µA cm^{-2} of about 3 µm thick) [30], nanotubes TiO_2/nanowires-SnO (0.110 mA h cm^{-2} on 1st discharge, 0.095 mA h cm^{-2} after 50 cycles at 100 µA cm^{-2}) [31], Si/TiO_2 nanotubes (0.55 mAh cm^{-2} on 1st discharge, 0.2 mA h cm^{-2} after 50 cycles at 20 µA cm^{-2} of about 3 µm thick) [32], TiO_2 nanotubes (0.7 mA h cm^{-2} on 1st discharge, 0.6 mA h cm^{-2} after 100 cycles at 25 µA cm^{-2} of about 14.5 µm) [33]. Our capacity values on nanopores/nanotubes microelectrode are quite attractive, suggesting that our electrode systems might be a potential candidate for the fabrication of 1D nanostructured thin films microbatteries. The enhancement of electrochemical properties on iron oxides lithium batteries may be possible if we consider the geometrical properties of the anodic nanopores/nanotubular structures. First of all, the nanotubes can provide larger material-electrolyte contact areas, providing increased number of electrochemically active surface sites. Secondly, the space between nanotubes provides better electrolyte accessibility and can hold the structural deformation due to volume expansion during lithiation/delithiation. Finally, well align and uniformly distributed nanopores/nanotubes ensures continuous pathways for electron transports.

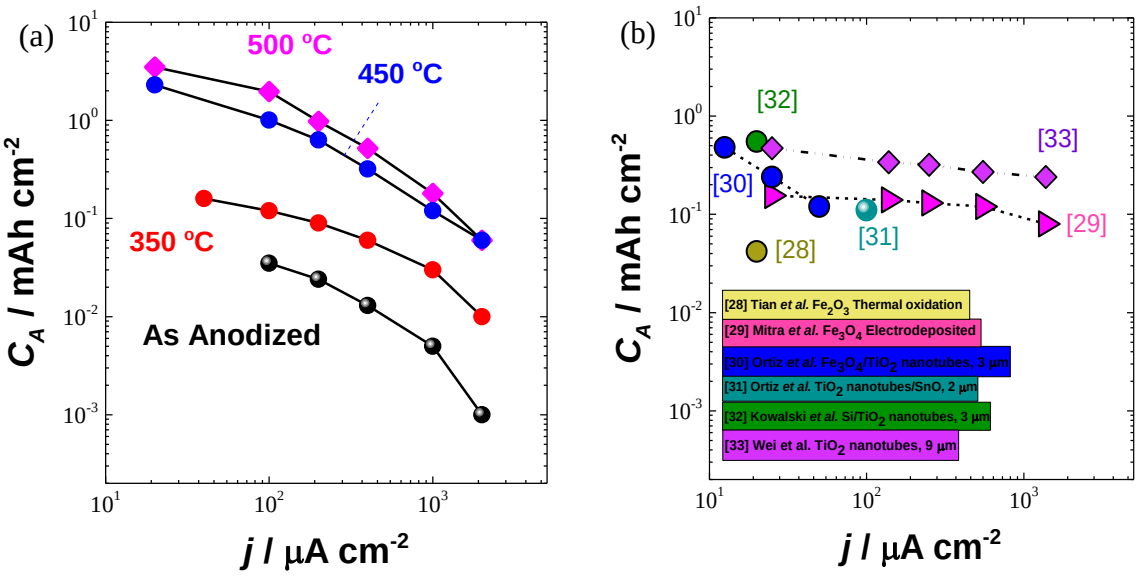

Figure 6.12 Areal capacity vs. the current density for the present iron oxide 1D nanotube microelectrode and other 1D micro-battery electrodes.

6.4. Conclusions

1D iron oxides have been synthesized by anodizing of iron foil in ethylene glycol electrolyte containing 0.1 M of ammonium fluoride and 1.5 M of water. The formation of nanopores/nanotubular structures of anodic iron oxides shows possibility to use anodic nanotubes formed on iron as a 1D negative electrode tested in the half cell of lithium ion battery. 450 °C annealed specimen can provide high areal capacities of 3.5 mA h cm^{-2} at a charge/discharge current density of 20 μA cm^{-2} in lithium ion batteries. This sample show better electrochemical performances due to the elimination of FeF_2 and higher degree for crystallinity of the iron oxides and high composition ratio of Fe_2O_3 than the as formed anodic film. Poor cycling stability and the rate capability of this system mainly caused by the detachment of oxide in the substrate observed by *in-situ* microscope optic observation.

References:

1. Bates, J., et al., *Thin-film lithium and lithium-ion batteries.* Solid state ionics, 2000. **135**(1-4): p. 33-45.
2. Julien, C. and G. Pistoia, *Lithium batteries, new materials, developments and perspectives*. 1994, Edited by: G. Pistoria, North Holland, Amsterdam, The Netherlands.
3. Jones, S. and J. Akridge, *Handbook of solid state batteries and capacitors.* Singapore: world Scientific, 1995. **2**: p. O9.
4. Souquet, J.L. and M. Duclot, *Thin film lithium batteries.* Solid State Ionics, 2002. **148**(3): p. 375-379.
5. Liu, J., et al., *Iron Oxide-Based Nanotube Arrays Derived from Sacrificial Template-Accelerated Hydrolysis: Large-Area Design and Reversible Lithium Storage*. Chemistry of Materials, 2010. **22**(1): p. 212-217.
6. Wang, Z., et al., *α-Fe_2O_3 nanotubes with superior lithium storage capability.* Chemical Communications, 2011. **47**(28): p. 8061-8063.
7. Chen, J., et al., *α-Fe_2O_3 Nanotubes in Gas Sensor and Lithium-Ion Battery Applications.* Advanced Materials, 2005. **17**(5): p. 582-586.
8. Shahzad, K., et al., *Ex situ evidence for the role of a fluoride-rich layer switching the growth of nanopores to nanotubes: A missing piece of the anodizing puzzle.* ChemElectroChem, 2018. **5**(4): p. 610-618.
9. Chen, J.S., et al., *Top-Down Fabrication of α-Fe_2O_3 Single-Crystal Nanodiscs and Microparticles with Tunable Porosity for Largely Improved Lithium Storage Properties.* Journal of the American Chemical Society, 2010. **132**(38): p. 13162-13164.
10. Muraliganth, T., A. Vadivel Murugan, and A. Manthiram, *Facile synthesis of carbon-decorated single-crystalline Fe_3O_4 nanowires and their application as high performance anode in lithium ion batteries.* Chemical Communications, 2009(47): p. 7360-7362.
11. Luo, J., et al., *Three-Dimensional Graphene Foam Supported Fe_3O_4 Lithium Battery Anodes with Long Cycle Life and High Rate Capability.* Nano Letters, 2013. **13**(12): p. 6136-6143.
12. Li, B., et al., *Superparamagnetic Fe_3O_4 nanocrystals@graphene composites for energy storage devices.* Journal of Materials Chemistry, 2011. **21**(13): p. 5069-5075.
13. A. Jain, S.P.O., G. Hautier, W. Chen, W.D. Richards, S. Dacek, S. Cholia, D. Gunter, D. Skinner, G. Ceder, K.A. Persson, *The Materials Project: A materials genome approach to accelerating materials innovation.* APL Materials, 2013, 1(1), 011002.
14. Habazaki, H., et al., *Fast migration of fluoride ions in growing anodic titanium oxide.* Electrochemistry Communications, 2007. **9**(5): p. 1222-1227.
15. Fadillah, L., et al., *Compositional variations in anodic nanotubes/nanopores formed on Fe 100, 110 and 111 single crystals.* Submitted to Electrochimica Acta.
16. Konno, Y., et al., *Corrosion protection of iron using porous anodic oxide/conducting polymer composite coatings.* Faraday Discussions, 2015. **180**(0): p. 479-493.
17. Cheng, F., et al., *Functional Materials for Rechargeable Batteries.* Advanced Materials, 2011. **23**(15): p. 1695-1715.
18. Cheng, F., et al., *Template-Directed Materials for Rechargeable Lithium-Ion Batteries.* Chemistry of Materials, 2008. **20**(3): p. 667-681.
19. Wang, Z., et al., *Assembling carbon-coated α-Fe_2O_3 hollow nanohorns on the CNT backbone for superior lithium storage capability.* Energy and Environmental Science, 2012. **5**(1): p. 5252-5256.
20. Wang, J., et al., *Nano-sized Fe_3O_4/carbon as anode material for lithium ion battery.* Materials Chemistry and Physics, 2014. **148**(3): p. 699-704.
21. He, Y., et al., *Structure and electrochemical performance of nanostructured Fe_3O_4/carbon nanotube composites as anodes for lithium ion batteries.* Electrochimica Acta, 2010. **55**(3): p. 1140-1144.
22. Wang, L., et al., *Electrospinning synthesis of C/Fe_3O_4 composite nanofibers and their application for high performance lithium-ion batteries.* Journal of Power Sources, 2008. **183**(2): p. 717-723.
23. Li, J., et al., *Phase evolution of conversion-type electrode for lithium ion batteries.* Nature Communications, 2019. **10**(1): p. 2224.
24. Wu, X.-L., et al., *α-Fe_2O_3 Nanostructures: Inorganic Salt-Controlled Synthesis and Their Electrochemical Performance toward Lithium Storage.* The Journal of Physical Chemistry C, 2008. **112**(43): p. 16824-16829.
25. Reddy, M.V., et al., *α-Fe_2O_3 Nanoflakes as an Anode Material for Li-Ion Batteries.* Advanced Functional Materials, 2007. **17**(15): p. 2792-2799.

26. Badway, F., et al., *Carbon-Metal Fluoride Nanocomposites.* Journal of The Electrochemical Society, 2003. **150**(9): p. A1209.
27. Badway, F., et al., *Carbon Metal Fluoride Nanocomposites.* Journal of The Electrochemical Society, 2003. **150**(10): p. A1318.
28. Tian, B., et al., *Aging-Induced Chemical and Morphological Modifications of Thin Film Iron Oxide Electrodes for Lithium-Ion Batteries.* Langmuir, 2014. **30**(12): p. 3538-3547.
29. Mitra, S., et al., *Growth and Electrochemical Characterization versus Lithium of Fe_3O_4 Electrodes Made by Electrodeposition.* Advanced Functional Materials, 2006. **16**(17): p. 2281-2287.
30. Ortiz, G.F., et al., *A novel architectured negative electrode based on titania nanotube and iron oxide nanowire composites for Li-ion microbatteries.* Journal of Materials Chemistry, 2010. **20**(20): p. 4041-4046.
31. Ortiz, G.F., et al., *Nanoarchitectured TiO_2/SnO: A Future Negative Electrode for High Power Density Li-Ion Microbatteries?* Chemistry of Materials, 2010. **22**(5): p. 1926-1932.
32. Kowalski, D., et al., *Electrochemical synthesis of 1D core-shell Si/TiO_2 nanotubes for lithium ion batteries.* Journal of Power Sources, 2017. **361**: p. 243-248.
33. Wei, W., et al., *High energy and power density TiO_2 nanotube electrodes for 3D Li-ion microbatteries.* Journal of Materials Chemistry A, 2013. **1**(28): p. 8160-8169.

Chapter 7 General conclusions and future suggestion

7.1. General Summary and Conclusions

In this Chapter, I will give a brief summary of each chapter, followed by a short outlook:

Chapter 3 explored the influence of grain orientation of iron substrate on the formation of nanoporous/nanotubular anodic films. Single crystalline (100), (110) and (111) facets were examined in this study. The film formation on (100) facet involved extended gas evolution upon anodizing, thus resulting in the shift of the *j*-*t* curve to the higher current density in comparison with those on higher index number facets, although the morphology and thickness of the developed anodic films were little influenced by the iron facet plane. Phases in the anodic films were dependent upon the facet. The anodic film formed on (100) facet has general chemical formula of $Fe_2O_3.FeF_2$, whereas the anodic film formed on higher index number is composed of $Fe_3O_4.FeF_2$. The anodic films formed on high index number facets are mainly amorphous or poorly crystalline whereas the one formed on (100) facet is crystalline (Fig. 7.1). Since the crystalline phase has higher electronic conductivity over the amorphous oxide resulting in enhanced gas generation on the (100) facet. Although anodizing behavior and crystallinity of the anodic films are dependent upon the iron facet, it is worth mentioning that the morphology and thickness of the nanoporous/nanotubular anodic films are similar on three facets examined in this study. Thus, it is possible to form the nanostructured anodic films with uniform morphology on polycrystalline iron substrate.

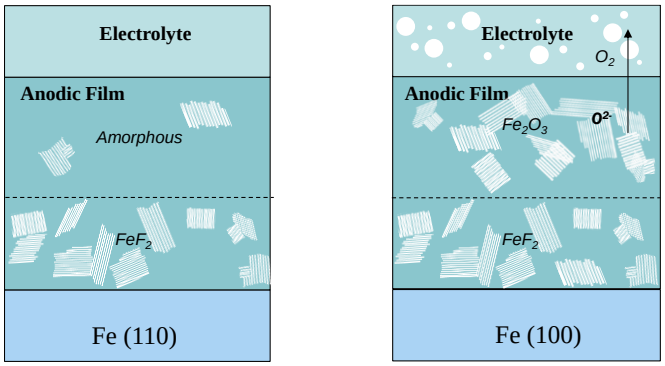

Fig. 7.1. Schematic illustrations showing the barrier layer of anodic films, beneath the porous layer, formed on the (110) and (100) iron single crystals.

Chapter 4 deals with the important question about the growth mechanism of iron oxides by alloying with tungsten. Main findings on the film growth on Fe-W alloy are as follows; i) transition of nanopores to nanotubes is observed upon anodizing of Fe-W alloy, ii) significant reduction of the cell size (nanotube diameter) is obtained on Fe-W alloy, iii) relatively thick layer is produced at Fe-W alloy/oxide interface. The primary reason of this transition to nanotubes as well as chemical changes near the metal substrate is discussed in view of effective modification of the cell boundary region with tungsten species, probably WF_6 compound, upon growth of anodic film under influence of high electric field. The possible reason of developing the space in between nanotubes is faster kinetics of WF_6 reaction with water over the presence of low solubility FeF_x species. Alloying of iron is one of the effective ways to modify the nanostructure of the anodic film on iron

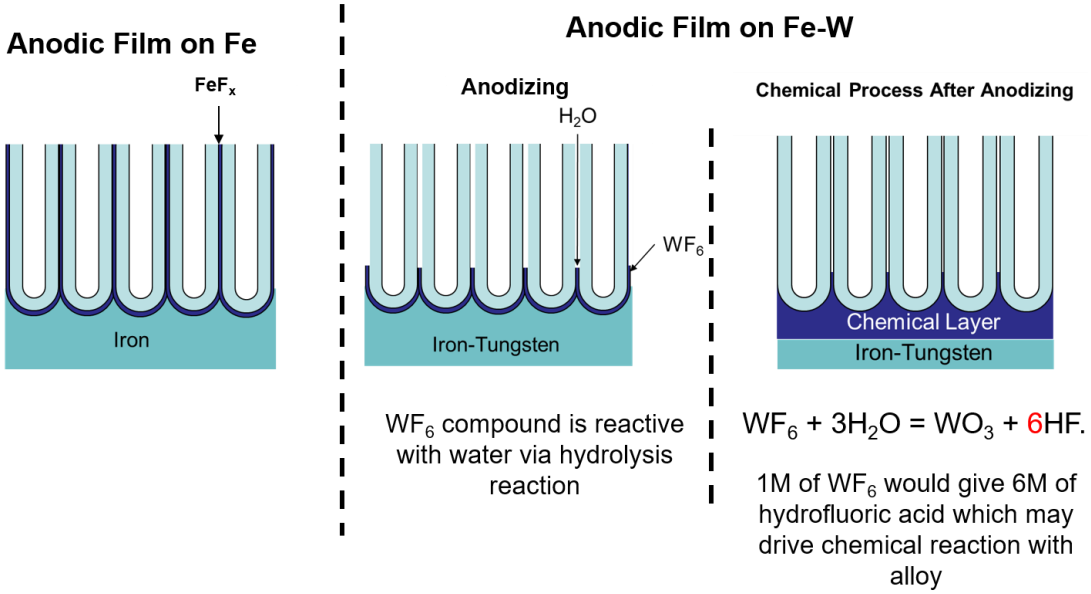

Fig. 7.2. Schematic illustrations showing the morphology of anodic films formed on iron and Fe-W alloy.

In chapter 5, the photocatalytic properties of anodized Fe-W alloy were explored. Two types of anodic films were developed on the Fe-W alloy: a barrier-type and a nanotubular-type. Their photocatalytic properties were compared with those of the nanoporous-type anodic film formed on iron. They were annealed at high temperatures to get sufficiently crystallized oxides and to remove fluorine species. The photocurrent of the Fe-W alloy specimens with the nanotubular and barrier oxide films is remarkably higher than that of the iron with the nanoporous layer. In addition, enhanced

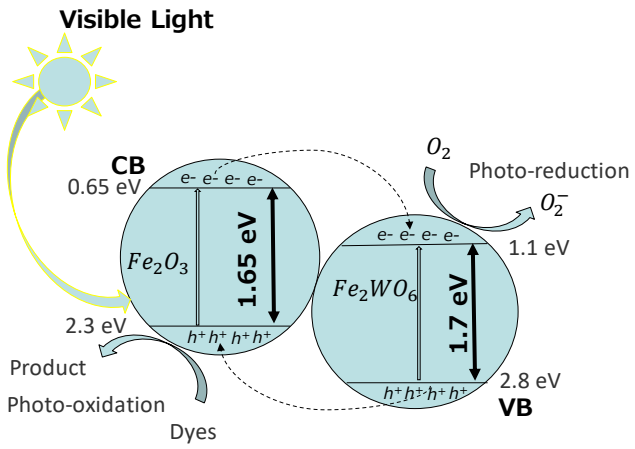

Fig. 7.3. Illustration of photogenerated electron transfer pathway of the anodic nanotubular film grown on sputter-deposited Fe-W

photodegradation of methylene blue under the presence of the anodized Fe-W alloy specimens is found in comparison with that under the anodized iron. Thus, the addition of tungsten improves markedly the photocatalytic properties. The nanotubular-type specimen shows superior photocurrent and photodegradation properties compared with the barrier-type counterpart. Although XRD patterns of the anodized Fe-W alloy specimens revealed only Fe_2O_3 and Fe_3O_4 after annealing, it is likely that $Fe_2O_3(Fe_3O_4)/Fe_2WO_6$ hybrids were developed because the solubility of tungsten species into iron oxides are very limited at equilibrium. The development of such hybrids may effectively separate the photogenerated electron-hole pairs at the heterojunction, resulting in the high photocatalytic properties. Hence, the nanotubular-type of Fe-W oxide is possible candidate for visible-light-driven photocatalysts.

Another application of nanotubular iron oxides is the 1D microelectrode for lithium ion batteries, which is described in Chapter 6. The influence of crystallinity of the electrode on the microbattery performance also investigated by annealing treatment. Compared with the as-anodized iron, the annealed iron with nanotubular anodic film revealed markedly improved charge-discharge performance. The better electrochemical performance of 1D iron oxide formed by annealing of anodized iron can be accomplished as decreasing of fluorine content and better crystallinity of the annealed electrode. The 500°C-annealed electrode with 96.3 at.% of Fe_2O_3 and 3.7 at.% of Fe_3O_4 was found to provide the best microbattery performance with areal capacities of 3.5 mA h cm^{-2} at current density of 20 μA cm^{-2}. However, cycling stability and the rate capability of this system are not sufficiently high, because of the detachment of oxide in the substrate, as observed by *in-situ* microscope optic observation. Further modification of nanostructure is needed for practical applications.

7.2. Future prospects

There are many possibilities to continue the work presented in this thesis. In Chapter 3, the author demonstrates that the crystallographic orientation of iron substrate influences the composition of the anodic films. Grain orientation effect of metal substates on passive film and anodic film growth have been studied on several metals, including aluminum, titanium and iron, and many important findings, including the present study, have been obtained. However, the reasons on the grain orientation dependence are not yet fully understood. Further fundamental study is needed to develop well controlled anodic films on polycrystalline iron and other metal substrates.

Anodizing is one of the promising techniques to develop electrode materials with high surface area and 1D morphology. The present study demonstrates that poor photocurrent and photodegradation of an organic pollutant of iron oxides formed by anodizing of iron is remarkably enhanced by the addition of tungsten. The formation of Fe_2O_3/Fe_2WO_6 heterojunction appears to improve the photocatalytic properties. Thus, this study opens up the novel approach of anodizing iron alloys to tailor the iron oxide-based photocatalysts with superior properties under the visible light irradiation. Since the study on anodizing of iron alloys is currently very limited, it is important to continue fundamental studies on the formation of nanoporous/nanotubular anodic films on a range of iron alloys as well as application studies as electrodes. Further precise control of film morphology and composition is particularly important for application to lithium ion batteries for further improving the cycle stability and improving the capacity to approach the theoretical values.

Anodizing is a unique and very promising process to form self-ordered nanostructured oxide films, which have many potential applications. The history of anodizing of iron to form nanoporous/nanotubular films is only 15 years. Further study is waited in this field for a better fundamental understanding of film growth and properties of developed nanostructured oxide

List of publications

[Publications]

(Journal) Laras Fadillah, Damian Kowalski, Yoshitaka Aoki, Hiroki Habazaki: *Compositional variations in anodic nanotubes/nanopores formed on Fe 100, 110 and 111 single crystals., Electrochimica Acta, Vol. 364, No. 137316 (2020)*

(Journal) Laras Fadillah, Kentaro Takase, Hikaru Kobayashi, Sylwia Turczyniak-Surdacka, Marcin Strawski, Damian Kowalski, Chunyu Zhu, Yoshitaka Aoki, Hiroki Habazaki : *The Role Of Tungsten Species In The Transition Of Anodic Nanopores To Nanotubes Formed On Iron Alloyed With Tungsten., Electrochimica Acta 309 (2019) 274-282,* DOI:10.1016/J.ELECTACTA.2019.03.206

[Conference Presentations]

(Oral Presentation) Damian Kowalski, Laras Fadillah, Yoshitaka Aoki, Hiroki Habazaki, *Compositional Variations in Porous Anodic Oxides Formed on Fe (100), Fe (110) and Fe (111) Single Crystals*, ECS Meeting Abstracts, 51, 2785

(Oral Presentation) Laras Fadillah, Damian Kowalski, Chunyu Zhu, Yoshitaka Aoki, Hiroki Habazaki, *Anodizing of sputter-deposited Fe-W alloy using Organic Electrolyte containing Fluorides,* Winter Meeting Hokkaido University, January 2019

(Oral Presentation) Laras Fadillah, Damian Kowalski, Chunyu Zhu, Yoshitaka Aoki, Hiroki Habazaki, *Growth of anodic nanotubular films on sputter-deposited Fe-W alloy*, Corrosion Dream Symposium, November 2018

(Oral Presentation) Laras Fadillah, Damian Kowalski, Chunyu Zhu, Yoshitaka Aoki, Hiroki Habazaki, , *Anodizing of sputter deposited iron in organic electrolytes containing fluorides*, Surf. Finish. Soc. Jpn Meeting Fall Meeting, October 2018

(Oral Presentation) Khurram Shahzad, Laras Fadillah, Damian Kowalski, Chunyu Zhu, Yoshitaka Aoki, Hiroki Habazaki: *Ex-Situ Evidence on the Transition of Anodic Nanopores into Nanotubes Formed on Iron,* The Electrochemical Society, Meeting Abstracts, 11, 598-598

[Awards]

(Best Poster Presentation) Laras Fadillah, Damian Kowalski, Chunyu Zhu, Yoshitaka Aoki, Hiroki Habazaki,: *Growth of Anodic Nanotubular Films on Sputter-Deposited Fe-W Alloy*, 3rd International Symposium on Anodizing Science and Technology, June 2019

(Best Oral Presentation) Laras Fadillah, Damian Kowalski, Chunyu Zhu, Yoshitaka Aoki, Hiroki Habazaki: *The Influence of Crystal Orientation on The Formation of Anodic Nanopores Films on Iron Single Crystals*, ECSJ Fall Meeting 2019, September 5-6, Yamanashi University, Kofu, Japan (2019).

Acknowledgments

At the last pages of this thesis, I would like to express my gratitude to all genuinely inspiring people who supported and helped me to complete my Ph.D. study.

I am deeply grateful to Professor Hiroki Habazaki, my supervisor, for his continuous support, his constant encouragement, inspiration, valuable suggestions during my Ph.D. study. I feel fortunate to have the opportunity to learn and work with him in this Laboratory of Interfacial Electrochemistry, Hokkaido University.

I also would like to sincerely appreciate Dr. Damian Kowalski as my second supervisor for his guidance and fruitful discussions. He has walked me through all the stages of my study, since I am totally a fresh student in electrochemistry field before joining this Laboratory. My gratitude also goes to Professor Kei Murakoshi, Prof Kozuhisa Azumi and Professor Yoshitaka Aoki, Prof Sho Kitano for their reading, assessment and the enjoyable discussion of this thesis.

I would gratefully acknowledge Ministry of Education, Culture, Sports, Science and Technology (MEXT), Japan and Hokkaido University for the financial support through the time period of my PhD study for their support which allowed to pursue the doctoral degree.

I give my hearty thanks to my colleagues, to all the members of Laboratory of Interfacial Electrochemistry, for the friendship and creating a very warm work atmosphere with I had pleasure working together. Dr. Ning Wang, Dr. Cheong Kim, Yoko Iwata, Yuki Sato, Seongwoo Jeong, Chunmei Tang, Ruijie Zhu, Kentaro Takase, Hikaru Kobayashi, Naohito Yamada, Miku Saito, Hajime Toriumi, and other laboratory members.

I also would like to express my heartfelt gratitude to Dr. Bambang Soegijono, who was my supervisor in master course, Dr. Faisal Budiman and Dr. Zainovia Lockman who introduced me into the field of research, Dr. Moh. Riza Iskandar for his support and discussion, and all members of BS Multiferroic Research Group.

Finally, my thanks would go to my family Mamah, Papah, Ziyyah, Nadia, Zaid, Ali, Asma, Usamah, Aisyah and also my family in Law; Mama, Papa, and Asnil. Their unwavering support, great understanding, continuous encouragement, and endless patience. The last but not least, to my beloved husband Muhamad Gusti Muharama, thank you for being understanding, and supporting during the work enabled me to complete this thesis. My wonderful son, Muhammad Reiji Muharama and my beautiful daughter, Hana Nafeesa Muharama; to them, I would like to dedicate this work and all of my achievements.